Interactions between optically-trapped circular Rydberg atoms for quantum simulation

Paul Méhaignerie

SORBONNE UNIVERSITÉ

COLLÈGE DE FRANCE 1530

THÈSE DE DOCTORAT DE SORBONNE UNIVERSITÉ

Spécialité : Physique

École doctorale n°564: Physique en Île-de-France

réalisée

au Laboratoire Kastler-Brossel

sous la direction de Jean-Michel RAIMOND

présentée par

Paul MÉHAIGNERIE

pour obtenir le grade de :

DOCTEUR DE SORBONNE UNIVERSITÉ

Sujet de la thèse :

Interactions entre atomes de Rydberg circulaires piégés pour la simulation quantique

soutenue le 6 Octobre 2023

devant le jury composé de :

M.	Benjamin HUARD	Rapporteur
Mme	Emily LAMOUR	Présidente du jury
M.	Jean-Michel RAIMOND	Directeur de thèse
M.	Clément SAYRIN	Membre invité
Mme	Juliette SIMONET	Examinatrice
M.	Shannon WHITLOCK	Rapporteur

À Gab & Rosa,

Contents

Introduction

Circular Rydberg states are probably the most peculiar atomic levels of single-valence electron elements. In circular Rydberg atoms, the outer electron's wavefunction is shaped like a torus and located extremely far away from the singly-charged ionic core [1]. More formally, circular states are defined by a high principal quantum number n and maximal orbital and magnetic angular momenta: $l = m = n - 1$. When excited to these states, atoms are thousands of times larger than a standard, ground-state atomic system. A circular atom, while behaving under the laws of quantum mechanics, can have a diameter of more than 200 nm, which is a lengthscale usually associated with classical physics phenomena. As a comparison, a regular virus – made up of tens of millions of atoms – is approximately 100 nm wide. Another way to put the circular atom's remarkable scales into perspective is to imagine its ionic core having the size of a marble. Then, its valence electron would orbit more than 30 meters away from it. The shape of circular atoms clearly sets them apart from other atomic configurations, which explains their distinctive role in the history of quantum physics.

Because of the huge distance between their outer electron and ionic core, circular states are the most hydrogen-like levels of alkali elements. The specific circular shape of their wavefunction also makes them the most "classical", and altogether simple, atomic states. It is therefore no wonder that they correspond to the levels described by Niels Bohr in his 1913 papers [2], in which he deciphered, for the first time, the hydrogen spectrum and the basic behavior of atoms. His work then allowed Einstein and Planck's theory of quantized light-matter interactions to blossom into modern quantum mechanics. More than a century ago, the notion of circular atoms, albeit at its nascent stage, was therefore essential to the birth of quantum physics.

1 From individual quantum objects to quantum technology

Although conceptually simple, circular Rydberg states require a significant amount of effort to be studied in the lab. Seventy years had to go by between Bohr's theoretical work and the first creation of circular atoms, in 1983, by Hulet and Kleppner [3]. Their work provided the technical recipe for the generation of circular states in an experimental setup. It opened the way to their extensive use, by our team, in cavity quantum-electrodynamics experiments, which fully harnessed their distinctive features [4]. Thanks to their unique size and shape, circular states indeed display

singular properties, among which long lifetimes and a high sensitivity to their environment. Taken as individual quantum systems gifted with such assets, circular atoms triggered the investigation of the most basic yet counter-intuitive principles of quantum mechanics: superposition, entanglement, field quantization, etc. Over the following decades, our team manipulated individual circular atoms and single photons to not only explore such features, but to also bring to life several thought experiments devised by the founding fathers of the quantum theory. Among the experiments successfully carried out with circular atoms, we can point out: the direct observation of the quantization of the electromagnetic field [5], the generation of Schrödinger cat states of light and the study of their decoherence [6], the creation of pairs of atoms in entangled states of the Einstein-Podolsky-Rosen (EPR) type [7], the non-destructive measurement of single photons [8], the measurement of quantum jumps of light [9] and the reconstruction of the Wigner function of non-classical states [10].

These experiments were only a small part of a wider global effort to manipulate individual quantum systems and probe the most fundamental laws of quantum mechanics. Besides circular atoms, a wide variety of other elementary quantum objects were devised and studied throughout the end of the last century. In 1976, the Young double-slit experiment was carried out for the first time with massive particles [11], using single electrons. In 1982, Alain Aspect prepared pairs of entangled photons to investigate the EPR paradox and successfully observed the violation Bell's inequalities [12]. Around the same time, Hans Dehmelt's group trapped individual ions and recorded their quantum jumps [13, 14]. David Wineland and his colleagues built upon this technique to implement fundamental quantum gates [15] and generate non-classical states of motion [16] with single ions. By the end of the 80's, John Martinis and Michel Devoret demonstrated level quantization in Josephson junctions [17, 18], thus creating an artificial individual quantum object at the macroscopic scale. Various other technical implementations of elementary quantum systems soon followed, among which we can cite optically-trapped individual neutral atoms [19] and single-photon emitters such as quantum dots [20, 21] or diamond vacancy color centers [22, 23].

By the turn of the century, the control of these individual quantum objects had become advanced enough to envision a new realm for their applications: quantum information processing. Researchers mastered the various technologies mentioned above with such craft that it soon became possible to implement assemblies of individual 2-level systems, or qubits, interacting in tailored ways. Such platforms constitute the basis for modern quantum technologies, whose goal is to tame the laws of quantum physics to outperform classical computers, communication channels and sensors. This new field of research has attracted much attention and funding in the past years – both in the public and private sectors – and can be divided into four different areas: quantum computing, quantum metrology, quantum communications and quantum simulation.

Quantum computing, at the forefront of the field but still far from practical results, aims at exploiting entanglement and state superposition to parallelize complex calculations and tackle problems such as prime factorization exponentially faster than

classical machines [24]. Quantum metrology, whose goal is to implement highly sensitive measurements of physical quantities, is currently at a much more advanced stage. Thanks to single-ions atomic clocks, it is now possible to measure time with a precision of one part in 10^{18}, which corresponds to a tenth of a second accuracy over the age of the universe [25–27]. Using similar technology, gravimeters have now reached the centimeter resolution in measuring altitudes in earth's gravitational potential [28]. The field of quantum communications deals with quantum-based protocols to transmit data in an intrinsically invulnerable manner [29, 30].

Lastly, quantum simulation is the idea of studying, on a well-controlled system of interacting and measurable qubits – a *quantum simulator* – problems that are numerically intractable. To understand the principle of a quantum simulator, consider a simple 10×10 square lattice of interacting qubits. A quantum mechanical description of this system involves a Hilbert space of dimension 2^{100}. In other words, storing a single generic state of the system requires 2^{100} units of memory, each of them having to store two real numbers, which translates into an even larger memory requirement. For comparison, *Frontier*, the world's most powerful super computer [31], "only" has around 2^{60} storage bits, making it unable to work with such a quantum state, let alone simulate the dynamics of this basic lattice. The purpose of an *analog* quantum simulator is then to mimic these interacting qubits with a synthetic quantum system, in a controlled experimental setting[1]. Recording their behavior and evolution provides direct and immediate insights into the features of the model of interest, which is rarely possible with real-life systems. With direct impact to many areas of physics, quantum simulation has gained a lot of traction over the past decades and offers promising results. This is where circular atoms could, once again, play a significant role.

2 Quantum simulations of spin systems

The idea of mimicking complex quantum systems on a controlled and measurable experimental replica was formally introduced for the first time by Richard Feynmann in 1982 [32]. An efficient quantum simulator should be made up of a large number of long-lived and measurable qubits, arbitrarily arranged, and interacting in a well-controlled and tunable manner, so as to explore various phenomena in the class of problems being addressed. Such systems would then trigger the investigation of a wide variety of intractable, strongly-correlated many-body models, ranging from fundamental physics to applied technological issues. The promised applications could be significant in high-energy physics (with the simulation of lattice gauge theories), atomic physics (via the Jaynes-Cummings Hamiltonian), quantum chemistry, cosmology and, more importantly, in condensed-matter physics [33].

[1] *Digital* quantum simulation, another paradigm for simulating physics on a quantum machine, is more closely related to quantum computers. It consists in running simulations of physical systems on a gate-based quantum architecture. We will focus here on *analog* quantum simulations only, the main purpose of this work.

Quantum simulation schemes might indeed provide deep insights into two quintessential condensed-matter physics problems: the Hubbard model and spin systems. The Hubbard model, describing interacting fermions on a lattice, is the simplest way to represent the behavior of electrons in solids. However important it may be, the Hubbard Hamiltonian has yet to be completely solved in dimensions greater than one. For instance, it is still unknown if the ground state of the system displays superconductivity when one spin sign outnumbers the other in the electron population. Several quantum simulation platforms have nonetheless already explored some of its features, such as the emergence of quantum degeneracy or the signs of long-range antiferromagnetic ordering [34].

Spins systems, the second important class of condensed-matter problems targeted by quantum simulations, cover an extremely broad variety of specific models. They are typically defined by spin-1/2 Hamiltonians of the form

$$\hat{H}_{XYZ} = \sum_{\langle i,j \rangle} J_x^{(i,j)} \hat{\sigma}_i^x \hat{\sigma}_j^x + J_y^{(i,j)} \hat{\sigma}_i^y \hat{\sigma}_j^y + J_z^{(i,j)} \hat{\sigma}_i^z \hat{\sigma}_j^z, \tag{1}$$

to which external fields can be added and where the summation runs over pairs of spins in the lattice – of arbitrary dimension. This generic Hamiltonian encompasses several well-known systems. When the interactions are uniform and verify $J_x = J_y \neq J_z$, it describes the anisotropic Heisenberg model. If $J_x = J_y = 0$, the system reduces to the famous Ising model. All of these cases lead to a surprising variety of many-body phenomena, which amount to what is called "quantum magnetism" [35].

Embryos of quantum simulators have already started tackling some of these phenomena. One famous example is the observation of the superfluid to Mott insulator transition in the Hubbard model, carried out in several platforms [36, 37]. Among the problems accessible to quantum simulations, there is also the investigation of localization and transport phenomena, through the introduction of controlled disorder [38]. In the same vein, observing spin glasses physics becomes within reach [39]. Yet another topic of interest is the frustration induced by specific geometries of spin systems, which give rise to spin liquids [40]. Topological ordering is also a feature of peculiar geometries and is being investigated [41]. Finally, much attention has recently been brought to the dynamical properties of spin systems, such as relaxation and thermalization, quantum chaos [42], quantum scars [43] and many-body localization [44]. Altogether, spin systems offer a seemingly endless playground of open questions that quantum simulations could hopefully tackle, provided that the appropriate simulators are implemented. Several platforms have already been designed for that purpose, built upon the control of individual quantum objects acquired throughout the end of the $20^{\mathbf{th}}$ century. For the sake of completeness, we provide here a brief review of the current state of spin-system-oriented quantum simulations, before diving into the purpose of this work within that context.

Trapped ions

In trapped ions quantum simulators [45], the qubits are made up of single ions, captured in radio-frequency Paul traps [46] for 1D chains or Penning traps [47] for 2D lattices. The spin states are encoded onto two long-lived internal electronic levels of the ions. The tunable, long-range interactions exhibited by the ions [45] allow the implementation of various spin systems, such as the Ising and Heisenberg models [48]. The main advantages of these platforms are the long coherence times of individual ions, which can now reach one hour [49], and their high preparation, readout and gate fidelities [50]. Trapped ions experiments have proven that they can successfully implement non-trivial spin systems. For instance, such platforms already investigated entanglement propagation in a 15-ion chain [51] and many-body localization in a transverse-field Ising system of 10 spins with tunable disorder [52]. The simulation of the Schwinger model is also a significant accomplishment of trapped ions systems [53][2]. The main drawback of trapped ions simulators is their scalability. As the number of target qubits grows, the optical and electrical techniques used to trap, cool and address individual ions get increasingly harder to deal with.

Superconducting qubits

A superconducting qubit is a micrometer-sized electrical device behaving as a 2-level quantum system. It relies on the Josephson effect [56, 57] to emulate a spin-1/2, which can take several forms depending on the qubit design. Flux, phase and charge qubits, along with their various hybridizations, are currently the most advanced qubit architectures [58], and different types of coupling modules allow them to interact. Their manufacture relies on well-established micro-fabrication techniques, which enable the efficient design of qubit assemblies with tailored frequencies and coupling strengths, but at the cost of interaction tunability and geometric flexibility. The impact of superconducting qubits has therefore been more significant in gate-based quantum computations [59] than in analog quantum simulations. Some explorations of quantum many-body effects have nonetheless been carried out on circuit-based analog simulators. Specific architectures were designed to study quantum Ising models and their phase transitions [60–62], the XXZ Hamiltonian [63] and fermionic systems [64]. The emergence of chiral currents in the ground state of a three-qubit system was also observed [65] and a chain of 8 strongly-coupled qubits was stabilized in its Mott insulator phase [66]. Through the introduction of disorder in a 9-qubit setup, the transition between thermalized and localized phases was probed [67]. However, several facets of superconducting qubits seem to limit, for now, the scope of their applications to quantum simulations. They lack exact identicality (because of unavoidable fabrication imprecision), their connectivity scales poorly with the size of the system, and they need to be operated in a cryogenic setup.

[2]Other achievements of ion platforms, though not related to spin physics simulations, are worth mentioning to underline their relevance: similar system were used to implement Shor's algorithm [54] and to carry out quantum chemistry computations [55].

Neutral atoms in optical lattices

A third important toolbox for the implementation of quantum simulations is that of cold atoms trapped in optical lattices, which has already reached a level of maturity allowing for the thorough investigation of complex many-body phenomena [68–70]. In these systems, the interference of several light beams creates large trapping lattices, which are filled with bosonic or fermionic species prepared in the quantum-degenerate regime. The spin states of the target Hamiltonian are cast into the occupation of the lattice sites, while tunneling processes provide the nearest-neighbor interactions. Additional degrees of freedom can be created using the hyperfine levels of the atoms. Through high-resolution imaging, single atoms are detected and site-resolved measurements carried out with good fidelity [71]. The first significant problem tackled by such systems was the Hubbard model, which they replicate in a straightforward manner. The superfluid to Mott insulator transition was directly observed with neutral atoms, first from collective measurements [72] and then at the single-atom level [36]. Atomic lattices also have the capacity to replicate spin models [73], which yielded insights into strongly-correlated systems [74], topological phenomena [75, 76], and artificial gauge fields [77, 78]. The addition of an optical speckle pattern introduces disorder in the lattice and led to the observation of many-body localization [38, 79]. However, cold atoms platforms still face several challenges. The large timescales involved in tunneling exchanges compared to lattice lifetimes prevent the study of long-term dynamics. Such lattices are also subject to many loss and decoherence mechanisms. Finally, single-site addressing is difficult since the lattice period is comparable with the smallest achievable laser focusing widths.

3 Rydberg atom quantum simulators

Circular atoms could soon contribute to the field of quantum simulations within a fourth category of platforms: Rydberg qubit experiments [80, 81]. Atoms placed in Rydberg states have a large principal quantum number n [82], which gives rise to properties that are promising for quantum simulation schemes. The Rydberg community currently works with low-ℓ states only, we will therefore describe their use for current quantum simulations first, before addressing the relevance of circular atoms in this context.

In Rydberg states, the large distance between ionic core and valence electron generates two important features. First, Rydberg atoms exhibit long lifetimes compared to low-lying states, in the 100 µs range for $n \sim 50$ for instance. Secondly, their large orbitals give rise to strong dipole-dipole interactions between one another, typically of tens of MHz for $n \sim 50$ at distances of around 5 µm. These properties naturally make them promising qubit encoders for quantum simulation schemes: their long lifetimes and strong, long-range interactions circumvent some of the bottlenecks inherent to other platforms.

Defect-free lattices of individual atoms

To make use of these properties, one needs to be able to deterministically position neutral atoms in a precise pattern, which was recently made possible thanks to improvements in optical control techniques. Using either spatial light modulators [83, 84], arrays of micro-lenses [85, 86] or even passive optical designs [87], it is now possible to create arbitrary lattices of tightly-focused beams, which can each trap at most a single atom in its ground state. The inter-atomic spacing in these platforms is within the 2-15 µm range. The loading of these arrays suffers from the random processes governing the atom capture, which prevent the creation of defect-free lattices of atoms. This issue was overcome in 2016 by several groups through different tactics. The teams of Mikhail Lukin at Harvard and Jaewook Ahn in Seoul dynamically moved the loaded tweezers to create 1d chains of evenly-spaced atoms [88] or two- [89] and three-dimensional [90] defect-free lattices. At Institut d'Optique, Antoine Browaeys *et al.* used an additional tweezer of tunable position to move the atoms one by one on the lattice, after the initial random loading [91]. These sets of techniques now yield near-perfect filling fractions in up to two dimensions, even with large arrays of hundreds of atoms, and offer great geometric flexibility.

Mapping onto spin Hamiltonians

Two Rydberg atoms interact through the dipole-dipole Hamiltonian $\hat{V}_{dd} \sim \hat{d}_1\hat{d}_2/(4\pi\varepsilon_0 r^3)$, where r is the inter-atomic distance and $\hat{d}_i$ the electric dipole moment of atom i [92–95]. Depending on the specific Rydberg states of the atoms, the interaction gives rise to two different kinds of effects. If the two atoms are prepared in two dipole-coupled Rydberg states, the coupling is of the first order kind, and leads to an interaction energy that goes as $\pm C_3/r^3$. If the atoms are in the same Rydberg state, the dipole-dipole interaction generally acts as a second-order process through other levels, and the interaction behaves as $\pm C_6/r^6$, in the so-called van der Waals regime. These configurations relate to two different kinds of phenomena, both of which are relevant in the context of quantum simulations.

First-order interactions

The Hamiltonian of an ensemble of atoms in the dipole-coupled Rydberg states $|\downarrow\rangle = |r\rangle$ and $|\uparrow\rangle = |r'\rangle$ and coherently driven with Rabi frequency Ω and detuning δ writes:

$$\hat{H} = \frac{\hbar\Omega}{2}\sum_i \hat{\sigma}_i^x + \frac{\hbar\delta}{2}\sum_i \hat{\sigma}_i^z + \sum_{i<j} \frac{C_3^{(i,j)}}{r_{ij}^3}\left(\hat{\sigma}_i^x\hat{\sigma}_j^x + \hat{\sigma}_i^y\hat{\sigma}_j^y\right). \tag{2}$$

This amounts to the XY spin model [96] with longitudinal and transverse fields, a sub-class of the generic Hamiltonians of equation (1). This system provides a suitable platform to study quantum magnetism, excitation transport [97] and entanglement propagation, although very few experiments have explored it in atomic lattices as of now. In [98], the team of Antoine Browaeys remarkably demonstrated the emergence of topologically-protected edge states in a chain of 14 Rydberg atoms with alternating

weak and strong couplings. This result is the first realization of a symmetry-protected topological phase in a 1d system of interacting bosons [99]. They later implemented with this configuration the XXZ Hamiltonian, by periodic applications of resonant micro-wave pulses [100].

Second-order interactions and the Ising model

However, most Rydberg platforms rely on the van der Waals interactions to study spin Hamiltonians. In this case, the qubit is encoded on a ground state and a Rydberg level: $|\downarrow\rangle = |g\rangle$, $|\uparrow\rangle = |r\rangle$. The two states are coupled via a 2-photon optical transition that, when driven at Rabi frequency Ω and detuning δ, gives rise to the following Hamiltonian for an ensemble of atoms [101]:

$$\hat{H} = \frac{\hbar\Omega}{2}\sum_i \hat{\sigma}_i^x - \hbar\delta\sum_i \hat{n}_i + \sum_{i<j}\frac{C_6^{(i,j)}}{r_{ij}^6}\hat{n}_i\hat{n}_j. \tag{3}$$

In this expression $\hat{n}_i = (1+\hat{\sigma}_i^z)/2$ is the number of excitations on site i. This Hamiltonian has the form of the quantum Ising model, another specific case of spin systems (1). The third term in the Hamiltonian describes the Rydberg blockade mechanism [102, 103], where the excitation of an atom impacts or even prevents that of its neighbors contained within the blockade radius. The effects of this interaction can be tuned via the inter-atomic distance and the driving strength, which leads to a rich variety of phases that have recently been probed in one and two dimensions. The group of Antoine Browaeys opened the way with the first realization of Hamiltonian (3), in a chain of 20 Rydberg qubits with periodic boundary conditions [104], before doing so with a square 7×7 lattice [105]. They later observed the dynamical growth of correlations in their system [106]. Jaewook Ahn *et al.* then focused on the thermalization of a chain of 10 such qubits [107] and in simple 2d geometries [108]. At Harvard, the team of Mikhail Lukin first prepared the ground state of the model in various Z_n phases via adiabatic sweeps of its parameters [109]. Among other results, they also witnessed the onset of a quantum spin liquid phase [40] in a Kagome lattice of spins frustrated by the Rydberg blockade. Recent efforts in these platforms have been dedicated to increasing their sizes, which now extend to three dimensions [110] and to over two hundred atoms in 2d [111, 112].

Although highly flexible, Rydberg-mediated simulations currently face a serious obstacle: they are severely limited by the achievable system lifetimes. First, Rydberg atoms are not trapped by optical tweezers, which actually repel them. The trapping lattice has to be turned off at the beginning of the simulation, which restricts the evolution time to a few µs. After that, the residual atomic motion destroys the chosen initial geometry and prevents any investigation of the longer-term dynamics. To bypass this issue, 2-valence species could replace alkali atoms, with one electron in the Rydberg state and the other used to keep the atoms still [113, 114]. However, the limited atomic lifetime of low-ℓ Rydberg levels (and their photo-ionization [115]) inherently restrict their study to short timescales. With a single-atom lifetime of ~ 100 µs for low-ℓ Rydberg levels, current platforms working with N atoms can only remain

defect-free for $100/N$ µs, which enforces a strong restriction on the allowed investigations. This is where circular Rydberg atoms finally come into play. Thanks to their outstanding properties, they indeed offer prospects of overcoming the limitations of current Rydberg platforms.

4 Quantum simulations with circular Rydberg atoms

A circular state of principal quantum number n, which we write $|nC\rangle$, has very few dipole-allowed transitions. It is mainly coupled to the two circular levels $|(n\pm1)C\rangle$ of the neighboring manifolds, and these transitions lie in the microwave domain. Thanks to this peculiarity, their natural lifetime is extremely large. However, it dramatically goes down as the temperature increases: at 0 K, $|50C\rangle$ has a lifetime of 29 ms, which is reduced to 9 ms at 4 K, and to 120 µs at room-temperature. Let us therefore stress right away that taking advantage of the lifetime of circular atoms comes at the cost of operating in a cryogenic environment. Moreover, circular atoms interact through the dipole-dipole coupling, in a similar fashion as low-ℓ states. Altogether, these promising features led to proposals for their use in quantum computation schemes [116] and as a new platform for quantum simulations. In 2018, our team detailed a proposal for a simulator based on circular states [117], built on our expertise in the manipulation of individual circular atoms.

An ensemble of circular Rydberg atoms can implement the spin-1/2 XXZ Hamiltonian

$$\hat{H}/\hbar = \frac{\Omega}{2}\sum_i \hat{\sigma}_i^x + \frac{\delta}{2}\sum_i \hat{\sigma}_i^z + \sum_{\langle i,j\rangle} J^{(i,j)}\left(\hat{\sigma}_i^x\hat{\sigma}_j^x + \hat{\sigma}_i^y\hat{\sigma}_j^y\right) + J_z^{(i,j)}\hat{\sigma}_i^z\hat{\sigma}_j^z, \tag{4}$$

up to lattice edge terms not written here. The qubit levels are taken to be two circular states $|nC\rangle$ and $|(n+2)C\rangle$, so that they are not dipole-coupled and the resulting van der Waals interaction leads to an $1/r^6$ dependence in all the interaction coefficients. The effective spins are driven by a microwave 2-photon transition, with Rabi frequency Ω and detuning δ, which respectively implement the fictitious transverse and longitudinal fields. This configuration covers a wide range of systems, among which the Ising model addressed by low-ℓ Rydberg simulators. Furthermore, the circular atoms offer unprecedented flexibility: the J_z coefficients can be tuned, via the static electric and magnetic fields, over a wide range of values spanning several quantum phases. However, it must be noted that, at inter-atomic distances in the range of 5-10 µm and for $n\sim50$, the interaction energies are of the order of 10 kHz i.e., about three times weaker than second-order interactions in low-ℓ Rydberg atoms for similar conditions [104]. To compensate for this issue and effectively explore spin dynamics over a large number of interaction cycles, our team proposed in [117] to further increase the lifetime of the atoms through spontaneous emission inhibition. By placing the circular atoms within a plane-parallel capacitor with a spacing lower than the radiated microwave wavelengths, one could reach individual lifetimes of the order of a minute [118], and implement $\sim 10^5$ interaction cycles. Naturally, the circular atoms also need to be

trapped throughout their evolution, which adds another difficulty in the project of building a circular-atom quantum simulator. My team decided to take on this challenge, despite its arduous nature. The project was put into motion in the beginning of 2018, following the initial proposal [117]

My PhD work started in 2018, under the supervision of Jean-Michel Raimond and shortly after the inception of the circular-atom simulator project, led by Clément Sayrin. Back then, the experimental setup dedicated to this endeavor had been used to study low-ℓ Rydberg states in a cloud of ultra-cold atoms and in the vicinity of a superconducting chip. A colossal upgrade of the setup and the installation of new systems needed to be carried out to meet the requirements of the circular-atom simulator. To spread out the workload and progressively acquire the relevant technical expertise, the project was divided into several initial tasks, which involved multiple people and were achieved throughout the five years of my PhD studies.

Demonstration of spontaneous emission inhibition. A separate experiment was initiated in order to implement, for the first time, the lifetime enhancement of circular atoms in an atomic cloud within a capacitor structure. This was conducted by Haiteng Wu, who designed, built and operated a new room-temperature setup to successfully demonstrate inhibition of black-body radiation-induced transfers. His results are detailed in [119].

Preparation of circular states out of an atomic cloud. Using our old cryogenic setup, a preliminary step of creating circular states of rubidium, from a cloud of ultra-cold atoms, was carried out. Along with Rodrigo Cortiñas and Brice Ravon, former PhD students, we successfully prepared atoms in the $|52C\rangle$ level with a purity above 80 %, measured their lifetime to be 3.7 ms, and characterized their coherence times. These results are presented in [120]. Thanks to this initial stage, we identified some key technical points in the proper free-space manipulation of ultra-cold circular atoms, the main one being a tight control of the electric and magnetic fields to reach satisfying coherence times.

Ponderomotive action on circular atoms. Still using the old version of the experiment, we then moved on to the demonstration of the effect of the ponderomotive force on circular states, with the help of Maxime Favier, a former post-doc of the team, and Yohann Machu, who had just joined us. Using a Laguerre-Gauss hollow beam, we were able to trap ensembles of circular Rydberg states along two dimensions for up to 10 ms, without any impact on their properties [121]. This work underlined the importance of proper aberration correction in shaping the trapping beams and familiarized us with the operation of spatial-light modulators.

Trapping individual circular atoms. At this point, the next step was the implementation of individual circular atom trapping. It required the preparation of arrays of ultra-cold, ground-state atoms trapped in optical tweezers. The technical necessities of these new sets of tools were no longer compatible with the old cryogenic setup, and we undertook the construction of a new experiment. It was decided that this new, intermediate-stage setup would operate at room temperature, so as to not pile up the cryogenic constraints on top of other, newer difficulties. Yohann Machu, Brice

Ravon, Maxime Favier and I built the new atomic environment, installed additional laser systems and modernized the old ones. We were eventually able to implement state-of-the-art lattices of ground-state atoms (with random loading), and to demonstrate the trapping of individual circular atoms in hollow bottle beams [122]. These results constitute the topic of Brice Ravon's dissertation [123], in which this new setup is thoroughly described.

Study of circular-circular interactions. Using the new platform, we then switched to the investigation of the dipole-dipole interactions between individually trapped circular atoms. To do so, we needed to be able to fill our atomic lattices in a deterministic manner. With the help of Andrés Durán-Hernández, a younger PhD student, we added a moving tweezer to the setup, in order to create defect-free geometries of trapped circular atoms. It allowed us to eventually characterize the dipole-dipole coupling within pairs of circular atoms. In doing so, we investigated the interaction-induced atomic motion appearing within the individual traps, and eventually learned how to mitigate these effects. These results make up the heart of my thesis and are presented here.

Future steps. In the near future, the experiment will be switched back, in its current state, to a cryogenic environment. In doing so, it should already allow the exploration of some interesting quantum simulation schemes. The final step will be the addition of the spontaneous-inhibition structure, at which point the circular-atom simulator should reach its full capacity and allow the study of unexplored regimes in many-body spin systems. Hopefully, circular atoms will then once again be at the forefront of modern quantum physics, more than a century after Niels Bohr's first intuition of these fascinating states.

5 Outline

This dissertation is split into four chapters. In the first one, we present the formal notions governing the physics of circular atoms. We introduce the appropriate framework for their description and, by doing so, pave the way for a good understanding of their manipulation in our setup. We point out the relevant properties of individual circular atoms but mainly center the discussion on the description of their interactions, specifically in the first-order regime we investigated in our experiments. We also address the expected interplay between motion and interactions in a system of two individually trapped circular atoms. Through analytical models and numerical simulations carried out in collaboration with Guillaume Roux, we exhibit several regimes of spin-motion coupling tailored to various applications.

The second chapter is dedicated to the presentation of our experimental setup and to the description of the preparation of deterministic arrays of ultra-cold atoms, the first cornerstone of our experiments. The technical discussions will be kept short, as the new setup is already detailed in Brice Ravon's thesis [123], to which we refer the reader for more in-depth explanations of the apparatus. We nonetheless take the time to address here the moving tweezer, the newest addition to the setup, designed and optimized to create defect-free arrays of atoms.

The excitation of the atoms to circular states and their individual trapping rely on complex protocols and techniques, which we present in the third chapter. We characterize there the successive steps of the *circularization* procedure, the second cornerstone of our manipulations. The individual trapping of circular atoms is also explained in this chapter, along with the properties of the trapped atoms. These results rely on the site-resolved, optical detection of circular states, a key element in the future operation of the full-scale simulator.

In the fourth chapter, we tackle the experimental investigation of resonant dipole-dipole interactions between circular atoms, our newest results, which make up the core of this work. By focusing on pairs of circular atoms, we thoroughly characterize their interaction energy, that we probe by microwave spectroscopy. In strongly interacting regimes, we witness the emergence of unwanted atomic motion. Through a refined preparation procedure, we show how to inhibit this motion, so as to implement fully controlled, unperturbed circular-circular interactions. We then demonstrate their tunability via the study of their geometric dependence, which perfectly matches the theoretical expectations. We conclude with the observation of spin exchange between two circular atoms, a significant milestone and my last contribution in the long-term project of a circular-atom quantum simulator.

Chapter I

Elements of theory

The first chapter focuses on the key concepts and phenomena that underlie the experimental results of this thesis. By going over formal notions and numerical estimates, we provide here the set of tools that are useful to understand and explain the data discussed throughout this work.

We begin by introducing the single-atom framework in which circular atoms are best described. Our experiments are based on the manipulation of rubidium-87, an alkali atom with a single valence electron. As such, when elevated to Rydberg levels, i.e. levels with a large principal quantum number n, and in particular to circular Rydberg levels, rubidium can be accurately described by the simple model of the hydrogen atom. Through this analogy, of which the limitations are addressed here, we outline the main properties of individual alkali Rydberg atoms. This discussion leads to the definition of *circular* Rydberg levels, the center of focus of this thesis. Owing to their large principal quantum number and maximal orbital angular momentum, circular Rydberg atoms exhibit remarkable properties, among which long lifetimes and very large dipole moments. An additional useful feature of Rydberg atoms is their sensitivity to the ponderomotive force, which enables their optical trapping in individual traps. This last point concludes the theoretical description of the single-atom physics relevant to this thesis.

The second part of this chapter tackles the subject of interactions between circular atoms. We restrict the analysis to a pair of interacting atoms, as it is the case in our experimental investigations. Due to their electric polarizability, circular atoms exhibit important dipole-dipole interactions. A perturbative approach distinguishes two interaction regimes: the first-order direct dipole case and the second-order van der Waals interaction. By a formal re-writing of the general dipole-dipole Hamiltonian, we can identify the pair of atoms with two spins that interact via tunable transverse and longitudinal terms. Depending on the specific circular levels involved, two different situations emerge. Either the resonant, first-order spin-exchange term dominates the physics of the system, or all terms are second-order, van der Waals contributions and exhibit the same order of magnitude. We narrow down our focus to the first case, that of the resonant exchange, which we study experimentally in this work. In this regime, where two atoms approximately 10 µm apart evolve between two circular states dis-

tant by a single quantum of angular momentum ($\Delta n = 1$), the interaction is in the MHz range and only depends on the geometry of the system. The case of the van der Waals interactions regime, where $\Delta n = 2$, displays richer physics and is the end goal for quantum simulations with circular atoms, but has not been investigated in our experiments as of yet.

To predict the dynamics of a pair of interacting circular atoms as thoroughly as possible, we conclude this theoretical part by discussing the interplay between the spin and motional states of the atoms in their traps. This auxiliary study [124], carried out in collaboration with G. Roux, characterizes the spin-motion coupling in a pair of individually trapped interacting atoms and yields several interesting insights. On the one hand, there are regimes of experimental parameters in which the spin-motion entanglement should not be detrimental to the second-order van der Waals dynamics for quantum simulations. On the other hand and more interestingly, it is possible to take advantage of this interplay in strong coupling regimes: either to indirectly measure the temperature of the circular atoms in their traps, or to create motional Schrödinger cat states. Unfortunately, due to lack of time, this last section on spin-motion entanglement describes purely theoretical results for now, as we lacked the time during my PhD to explore these regimes in real experiments.

I.1 Individual Rydberg atoms

I.1.1 Rydberg states of alkali atoms

Rubidium 87, the atomic species used in our experiments, has a single valence electron. Its atomic energy levels are therefore solutions of Schrödinger's equation [125] for this electron in the potential $V(\mathbf{r})$ created by the atomic core:

$$\left(-\frac{\hbar^2}{2m_e}\Delta + V(\mathbf{r})\right)\psi(\mathbf{r}) = E\psi(\mathbf{r}), \tag{I.1}$$

where $\hbar$ is the reduced Planck constant and m_e the electron mass. Qualitatively, we expect that when its wavefunction lies far away from the nucleus and other electronic shells, the electron sees the potential $V(\mathbf{r})$ as a point-like, single charge distribution:

$$V(\mathbf{r}) \underset{r\to\infty}{\sim} -\frac{e^2}{4\pi\varepsilon_0}\frac{1}{r}, \tag{I.2}$$

with e the elementary charge and ε_0 the vacuum permittivity. In such a highly-excited state, rubidium can then behave as a hydrogenic atom, in which a single electron orbits a single point charge. The hydrogen model is therefore a good starting point to dive into single-atom Rydberg physics. Going over its solutions provides the right framework for the study of the Rydberg states of rubidium.

The bound states of a single electron in a Coulomb potential are described by the wavefunctions [126]:

$$\psi_{n\ell m}(r,\theta,\phi) = a_0^{-3/2}\frac{2}{n^2}\sqrt{\frac{(n-\ell-1)!}{(n+\ell)!}}F_{n\ell}\left(\frac{2r}{na_0}\right)Y_\ell^m(\theta,\phi), \tag{I.3}$$

where a_0 is Bohr's radius $a_0 = 4\pi\varepsilon_0\hbar^2/m_e e^2$. These states are labeled by three quantum numbers: $n \in \mathbb{N}^*$, $\ell \in \{0,...,n-1\}$ and $m \in \{-\ell,...,\ell\}$. The principal quantum number n describes the energy of the state via the Rydberg constant $\mathrm{R_y}$ and the fine-structure constant α:

$$E_n = -\frac{\mathrm{R_y}}{n^2}, \quad \mathrm{R_y} = \frac{\alpha^2 m_e c^2}{2} = \frac{e^2}{8\pi\varepsilon_0 a_0}. \tag{I.4}$$

The electron orbital angular momentum is written ℓ and its projection along the z-axis m. The radial and angular parts of the wavefunction, $F_{n\ell}$ and Y_ℓ^m, are analytically defined using the Laguerre polynomials and spherical orbitals.

This state classification does not completely account for all the transition frequencies measured in hydrogen. To perfectly describe its energy levels, one must also take into account [126]:

- relativistic corrections,
- the nucleus mass, accounted for by replacing m_e with the reduced mass of the 2-body system, i.e. a 10^{-5} correction to m_e,
- the electron spin $s = 1/2$ and its projection $m_s = \pm 1/2$ [127], which interacts with its own orbital angular momentum (fine structure),
- the spin-orbit and spin-spin interactions between the nucleus and the electron (hyperfine structure).

These four contributions lead to various energy shifts in this first simple level structure. To study Rydberg levels, i.e., levels with large principal quantum number, we need to retain only one of these deviations [128], the *spin-orbit coupling*, which arises from the interaction between the electron's intrinsic magnetic moment and its orbital angular momentum. Indeed, in Rydberg levels the electron lies rather far away from the nucleus and evolves slowly compared to low-lying levels: the relativistic corrections and coupling to the nucleus spin are always negligible. The spin-orbit term in the atomic Hamiltonian writes, for the hydrogen atom [126]:

$$\hat{H}_{\mathrm{SO}} = \frac{\hbar\alpha g_S}{2m_e^2 c}\frac{\left(\hat{\mathbf{S}}\cdot\hat{\mathbf{L}}\right)}{r^3}, \tag{I.5}$$

with g_S the electron g-factor, $\hat{\mathbf{S}}$ and $\hat{\mathbf{L}}$ its spin and orbital angular momentum observables. To compute quantities associated to this term, the total electron angular momentum $\mathbf{J} = \mathbf{L} + \mathbf{S}$ is introduced, which leads to the definition of new quantum numbers: $j = \ell \pm 1/2$ and m_j its projection on the quantization axis. The proper

basis in which to consider the hydrogenic energy levels is then (n, j, m_j). This fine structure formalism is relevant for low-ℓ states only, independently of the principal quantum number. It arises from relativistic effects and, as such, becomes negligible when ℓ grows: the electron evolves further away from the nucleus, in a weaker potential and with reduced momentum [128]. As stated previously, other corrective terms are ignored in our study of Rydberg states, as they lead to insignificant or constant energy shifts [123].

With these notions in mind, we can now properly define Rydberg states of rubidium and estimate their proximity to the hydrogen model. Qualitatively, we expect that deviations from the hydrogenic model will emerge when the electron is close to the ionic core and the potential differs from the Coulomb one. This situation is encountered whenever ℓ is small. Throughout this study, we will therefore make sure to carefully distinguish the two cases: low ℓ or $\ell \gg 1$.

To estimate the similitude between rubidium Rydberg levels, i.e., states with $n \gg 1$ (around 50 in the experiments) and hydrogenic states, we can start by computing from equation (I.3) the size $\langle r \rangle$ and spread $\Delta r = \sqrt{\langle r^2 \rangle - \langle r \rangle^2}$ of the generic hydrogenic wavefunctions:

$$\langle r \rangle = \frac{a_0}{2}\left[3n^2 - \ell(\ell+1)\right], \quad \Delta r = \frac{a_0}{2}\sqrt{n^2(n^2+2) - \ell^2(\ell+1)^2}. \tag{I.6}$$

We now consider two limit cases. First, for hydrogenic states with maximal orbital angular momentum ($\ell = n-1$), we obtain

$$\frac{\Delta r}{\langle r \rangle} \sim \frac{1}{3}\sqrt{\frac{2}{n}}. \tag{I.7}$$

Here, the relative spread of the wavefunction goes to zero as n grows. In such states with high n and maximal angular momentum, the electron remains located at a large distance $\sim a_0 n^2$ from the core and we anticipate close proximity between the hydrogen model and the corresponding levels in rubidium.

However, in a zero orbital angular momentum level ($\ell = 0$), equation (I.3) yields:

$$\frac{\Delta r}{\langle r \rangle} \sim \frac{1}{3}, \tag{I.8}$$

which shows that, in this case and independently of n, the electron always gets close to the ionic core. Large deviations from the hydrogen model are then expected in low-ℓ Rydberg states of rubidium, due to the interaction between the electron and the complex ionic structure of the core.

In figure I.1 (a), we represent the electron probability distribution computed for two Rydberg states of rubidium that match the two limit cases: $|52D, j = 5/2, m_j = 5/2\rangle$ (a low-ℓ state) and $|52, l = 45, m = 44\rangle$ (high-ℓ state). These images make it visually clear that in the low-ℓ orbitals of rubidium, the electron interacts with the ionic core,

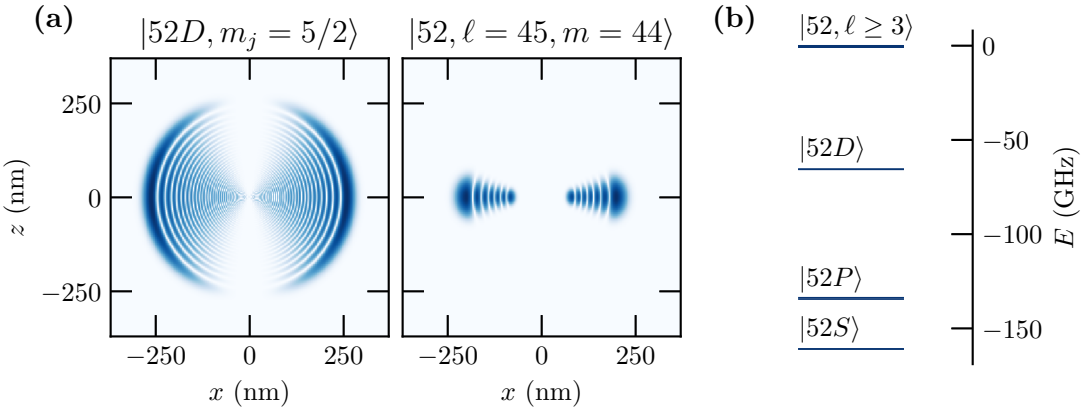

Figure I.1: **(a)** Probability density distribution $|r\psi(\mathbf{r})|^2$ (logarithmic scale) in the $x-z$ plane, for the $|52D, m_j = 5/2\rangle$ (left panel) and $|52, \ell = 45, m = 44\rangle$ (right panel) rubidium levels, z being the quantification axis. The core penetration is clear for the low-ℓ level and nonexistent in the high-ℓ level. **(b)** Level scheme for the whole $n = 52$ rubidium manifold. Low-ℓ states are energy-shifted by several tens of gigahertz due to their quantum defects. High-ℓ levels ($\ell \geq 4$) all stand at the same energy, taken as the origin. The $\ell = 3$ states, have a -0.8 GHz quantum defect, which is not visible in the figure. The fine structure splitting of each level is also taken into account but barely visible at this scale.

as the electronic density is non-zero near the nucleus. However, in high-ℓ levels the electronic density is zero for a large volume around the ionic core and the electron therefore sees it as a simple far-away point-charge.

In rubidium, the electron penetration in the complex atomic core structure results in energy deviations from the hydrogenic model that are called *quantum defects* [129]. These shifts are accounted for by empirically introducing a non-integer, effective principal quantum number in the radial part of the wavefunction, which yields the new energies:

$$E^*_{n\ell j} = -\frac{\mathrm{R_y}}{n^{*2}} = -\frac{\mathrm{R_y}}{(n - \delta_{n\ell j})^2}, \tag{I.9}$$

where the quantum defect $\delta_{n\ell j}$ can be expanded as a power series for more detailed analyses: $\delta_{n\ell j} = \delta^{(0)}_{\ell j} + \delta^{(2)}_{\ell j}/(n-\delta^{(0)}_{\ell j})^2 + \ldots$ [82]. For ℓ up to 4, its first terms have been measured experimentally in rubidium [130–132]. The energy shift due to the quantum defect in the $|52D\rangle$ levels is -65.6 GHz with respect to the unperturbed levels in the $n = 52$ manifold. That of the $|52F\rangle$ levels is -0.8 GHz.

These energy shifts are depicted in figure I.1 (b) for the $n = 52$ rubidium manifold. The quantum defect lifts some of the manifold's degeneracy by lowering the energy of low-ℓ levels by several tens of gigahertz. For higher values of ℓ ($\ell \geq 4$), the quantum

defect scales as ℓ^{-5} [82], which quickly makes it irrelevant as ℓ grows. For $\ell \geq 4$, we can consider that that the quantum defects vanish and all states are degenerate.

Overall, Rydberg states of rubidium can be well-described by the simple hydrogen atom model. However, extra caution has to be taken when dealing with low-ℓ Rydberg levels, for two reasons. First, their spin-orbit coupling is often non-negligible. Cases in which the fine structure has to be considered will be detailed when addressing the coupling of the atom to static fields. Secondly, low-$^\ell$ levels are also subject to quantum defects, the main difference between hydrogen and Rydberg states of alkali atoms. High-ℓ levels ($\ell \geq 4$) in the degenerate subspace, however, behave exactly as a hydrogenic system. They can be accurately studied as an electron in a Coulomb potential. We will use this analogy throughout the rest of section to introduce the Rydberg states of rubidium and their properties, while making sure to underline the deviations in low-ℓ states when necessary.

I.1.2 Coupling to static fields

As a hydrogenic system in which an electron is loosely held around the ionic core, any electric field will greatly deform a Rydberg atom: it is said to have a large electric polarizability. Furthermore, a directing static field, whether it be electric or magnetic, will couple differently to different levels in a given manifold and thus will lift its degeneracy. Accordingly, understanding the coupling of Rydberg atoms to static fields is essential for their manipulation.

Magnetic field: Zeeman and Paschen-Back effects

We begin with the simpler case of the interaction with the magnetic field, which acts on the spin and orbital angular momenta of the atom via the Hamiltonian

$$\hat{H}_B = \frac{\mu_B}{\hbar}\left(g_L\hat{\mathbf{L}} + g_S\hat{\mathbf{S}}\right)\cdot\mathbf{B}, \tag{I.10}$$

where g_L and g_S are the orbital and spin g-factors of the electron, and μ_B the Bohr magneton [133]. We consider the quantization axis to be along $\mathbf{B}$. This Hamiltonian leads to different effects depending on its strength vis-à-vis the bare spin-orbit coupling described in equation (I.5). We focus on the two straightforward limit cases $H_B \gg H_{SO}$ and $H_B \ll H_{SO}$, which are sufficient to describe the relevant experimental conditions.

In the strong field situation, the magnetic field de-couples the spin and orbital angular momenta of the electron: both $\mathbf{S}$ and $\mathbf{L}$ precess around $\mathbf{B}$. The fine structure then becomes irrelevant, ℓ, m, m_s remain the good quantum numbers and the energy contribution of the magnetic field coupling writes, in the state $|n,\ell,m,m_s\rangle$,

$$\langle\hat{H}_B\rangle = \mu_B\left(g_L m + g_S m_s\right)B. \tag{I.11}$$

This regime is called the Paschen-Back effect. Given the limited magnitude of the magnetic fields in our experiments, (around 10 G), the strong-field limit typically arises as soon as the spin-orbit coupling becomes small, i.e., when considering Rydberg states with $\ell \geq 3$ [128].

With low-ℓ states however, we are in the opposite situation: the spin-orbit coupling is large and $H_B \ll H_{SO}$. Here, the magnetic field can be treated as a perturbation to the spin-orbit coupling. We keep the $|\ell, j, m_j\rangle$ basis, in which we get the Zeeman level shifts:

$$\langle \hat{H}_B \rangle = \mu_B g_J m_j B, \tag{I.12}$$

where g_J is the Landé factor, defined as

$$g_J = g_L + \frac{j(j+1) - \ell(\ell+1) + 3/4}{2j(j+1)}(g_L - g_S). \tag{I.13}$$

In summary, in both cases the magnetic field linearly shifts the Rydberg levels. The value of the orbital angular momentum determines if the fine-structure basis provides the appropriate description or not. In our experimental conditions, the shift is ruled by m_j if $\ell \leq 2$ and by m and m_s if $\ell \geq 3$. We recall that, on top of this distinction, quantum defects have to be considered for $\ell \leq 3$.

Electric field: Stark shift

The effects of the electric field on Rydberg states are a bit trickier to tackle. The coupling between the atom and the static field $\mathbf{F}$ is described by the Stark Hamiltonian [133]:

$$\hat{H}_F = -\hat{\mathbf{d}}.\mathbf{F}, \tag{I.14}$$

where $\hat{\mathbf{d}} = -e\hat{\mathbf{r}}$ is the dipole operator. As opposed to the Zeeman Hamiltonian, this Stark term impacts the radial motion of the electron, which causes a more complex mixing of subspaces. A few results can nonetheless be derived from basic considerations without diving into the full Hamiltonian diagonalization. We consider the field $\mathbf{F}$ to be along (Oz), taken as the natural quantization axis in this context.

The Stark term can then be re-written using spherical harmonics:

$$\hat{H}_F = -e\hat{z}|\mathbf{F}| = -e\hat{r}\sqrt{\frac{4\pi}{3}}Y_1^0|\mathbf{F}|, \tag{I.15}$$

where Y_1^0 is the $(\ell = 1, m = 0)$ spherical harmonic. Through this expression, it comes out that the electric field only mixes states having the same m and orbital angular momenta that differ by a single unit, yielding the formal static dipole selection rules between two states $|n\ell m\rangle$ and $|n'\ell' m'\rangle$:

$$\ell' = \ell \pm 1, \tag{I.16}$$

$$m' = m. \tag{I.17}$$

Let us note that per these selection rules (or because $\langle\psi_{n\ell m}|\hat{r}|\psi_{n\ell m}\rangle = 0$) the Stark term does not couple a state to itself, i.e., its diagonal matrix elements are zero.

The presence of the static electric field also breaks down the spherical symmetry of the bare atom. Because of the dipole operator in the Stark Hamiltonian, the $\hat{\mathbf{L}}^2$ operator does not commute with the full Hamiltonian anymore, which means that ℓ is no longer a good quantum number (as it was suggested by the mixing of states with $\Delta\ell = 1$). However, the system retains a cylindrical symmetry around (Oz). The projection m of $\mathbf{L}$ along this axis therefore remains a good quantum number.

As we have seen, the low-ℓ levels are non-degenerate and shifted far away from the manifold by the quantum defects (see figure I.1 [b]). In the case of a weak electric field, perturbation theory can therefore be applied to estimate the effects of the Stark term on these states. Since the Stark Hamiltonian does not couple a state to itself, it only generates a second-order, quadratic shift on these low-ℓ levels. In the degenerate manifold however (when $\ell \geq 4$), the dipole operator couples states that have the same bare energy and non-degenerate perturbation theory should be replaced by the degenerate one[1]. We then expect a first order, linear shift on these levels. Figure I.2 (a) depicts the Stark shift on the $n = 52$ subspace, for $\ell \geq 2$ in the weak field regime. The data was computed by brute-force numerical diagonalization of the full Hamiltonian. We indeed observe a second-order shift on the low-ℓ levels and a linear splitting of the manifold under the action of the static electric field. The behavior of the $|52F\rangle$ level, which quadratically joins the base of the manifold as $\mathbf{F}$ is increased, will be relevant in the description of the experimental processes.

As suggested, since ℓ is no longer an appropriate quantum number, a change of basis is required to make the general study of the linear Stark shifts in the manifold more straightforward. Since we want to focus on the states of the degenerate manifold (i.e, without quantum defects), which follows the behavior of the hydrogen model, we will proceed within this simplified context and directly extrapolate the results to rubidium.

The most convenient way to proceed is by introducing the symmetric Runge-Lenz vector [134]:

$$\hat{\mathbf{A}} = \frac{n}{cm_e\alpha}\left[\frac{1}{2}\left(\hat{\mathbf{p}}\wedge\hat{\mathbf{L}} - \hat{\mathbf{L}}\wedge\hat{\mathbf{p}}\right) - \frac{e^2 m_e}{4\pi\varepsilon_0}\frac{\hat{\mathbf{r}}}{r}\right], \tag{I.18}$$

where $\hat{\mathbf{p}}$ is the electron momentum. This vector allows us to define the two operators

$$\hat{\mathbf{J}}_a = \frac{1}{2}(\hat{\mathbf{L}} - \hat{\mathbf{A}}), \quad \hat{\mathbf{J}}_b = \frac{1}{2}(\hat{\mathbf{L}} + \hat{\mathbf{A}}). \tag{I.19}$$

These operators commute with the full Hamiltonian and with each other, and define two angular momenta of size $\hat{\mathbf{J}}^2_{a(b)} = \hbar^2(n^2-1)/4$ [135]. A given state in the n-

[1]The states in this subspace actually have very slightly different energies because of the various corrections, such as the fine structure, that we considered negligible. However, even at low field strengths, the effect of the Stark Hamiltonian is always much larger than these bare energy differences. In that sense, we consider these states to be degenerate when applying an electric field.

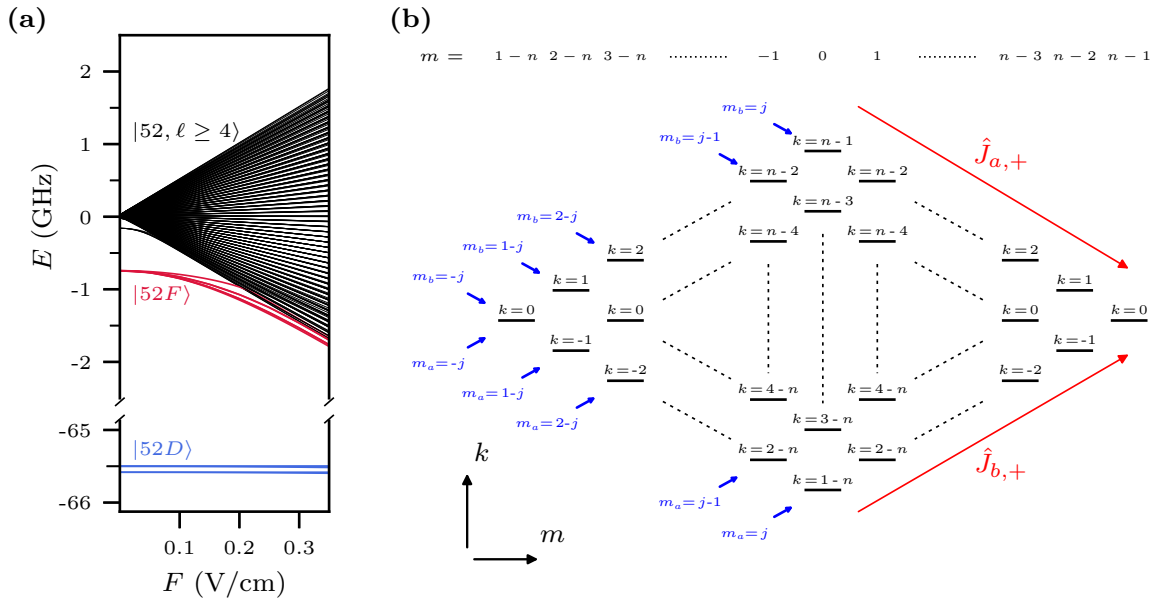

Figure I.2: **(a)** Stark map of the $n = 52$ manifold in rubidium 87, depicting the energy of the atomic levels as a function of the electric field strength. $|52S\rangle$ and $|52P\rangle$ are not shown here; $|52D\rangle$ and $|52F\rangle$ exhibit a quadratic, second-order Stark shift, whereas the levels within the manifold spread apart linearly when $\ell \geq 5$ under the action of the electric field. **(b)** Stark diagram of the manifold levels, in the hydrogen model, labeled in the parabolic basis $|n, m, k\rangle$. This classification and depiction remain mostly valid for Rydberg states of rubidium within a given manifold: only its low-ℓ levels deviate from this picture.

th manifold can then be unequivocally labeled via $j_i = J = (n-1)/2$ and $m_i \in \{-j_i, -j_i + 1, ..., j_i - 1, j_i\}$, with $i = a, b$. The actions of $\hat{\mathbf{J}}_a$ and $\hat{\mathbf{J}}_b$ are straightforward in this basis:

$$\hat{\mathbf{J}}^2_{a(b)}|J, m_a, m_b\rangle = \hbar^2 J(J+1)|J, m_a, m_b\rangle, \quad \hat{J}_{a(b),z}|J, m_a, m_b\rangle = \hbar m_{a(b)}|J, m_a, m_b\rangle, \tag{I.20}$$

which leads to the standard definition of the ladder operators $\hat{J}_{a(b),\pm} = \hat{J}_{a(b),x} \pm i\hat{J}_{a(b),y}$. Given the expression of $\hat{\mathbf{J}}_a$ and $\hat{\mathbf{J}}_b$ in equations (I.19), we also have $m_a + m_b = m$. Finally, it can be shown [136] that the two angular momenta relate to the dipole operator $\hat{\mathbf{d}}$ via

$$\hat{\mathbf{d}} = \frac{3}{2} nea_0(\hat{\mathbf{J}}_a - \hat{\mathbf{J}}_b)/\hbar. \tag{I.21}$$

This last relation hints at the definition of a new quantum number $k = m_a - m_b$, directly linked to an observable. Each state can be written unambiguously $|n, m, k\rangle$ under this new representation, that we call the *parabolic* basis. Even though this is strictly valid for the hydrogen model only, we will apply this classification to rubidium

while keeping in mind that, in low-ℓ states, j_a and j_b are actually not good quantum numbers.

The dipole matrix elements of the Stark Hamiltonian are easier to compute in this new basis. Through a perturbative approach, one can show [133] that the Stark shift writes, for a given state $|n, m, k\rangle$:

$$\Delta E_S = \alpha^{(1)} F + \alpha^{(2)} F^2 + \alpha^{(3)} F^3 + ... \tag{I.22}$$

with the first coefficients $\alpha^{(i)}$ expressed as:

$$\alpha^{(1)} = \frac{3kn}{2} e a_0, \tag{I.23}$$

$$\alpha^{(2)} = -\frac{n^4}{32}(17n^2 - 9m^2 - 3k^2 + 19)\frac{(ea_0)^2}{\mathrm{Ry}}, \tag{I.24}$$

$$\alpha^{(3)} = \frac{3kn^7}{128}(23n^2 + 11m^2 - k^2 + 39)\frac{(ea_0)^3}{\mathrm{Ry}^2}. \tag{I.25}$$

We indeed recover a first order linear shift of the degenerate levels, which depends only on k. In figure I.2 (b) we give a representation of the hydrogenic manifold under a static electric field, classified in this new basis by order of m and k, for the hydrogen model. The end result for rubidium would be very similar, with only slight additional displacements for low-m levels and some missing levels at the center of the manifold, due to the quantum defects shifting them far away out of this scale. In this representation of the manifold, the action of the ladder operators $\hat{J}_{a(b),\pm}$ are easily understood and shown in red arrows in the diagram. They raise or lower $m_{a(b)}$ by a single unit, which corresponds to transfers along the diagonals of the manifold.

We wrap up this section by discussing the atomic state evolution in static field within this formalism. We consider $\mathbf{F}$ and $\mathbf{B}$ to be static and along (Oz). We neglect the irrelevant spin coupling to the magnetic field, i.e., we consider only the first term of the Hamiltonian (I.10), where we set the orbital g-factor $g_L = 1 - m_e/M \simeq 1$ (M being the mass of rubidium 87). The coupling to the static fields then writes:

$$\hat{H}_{B,F} = \frac{\mu_B}{\hbar}\hat{\mathbf{L}} \cdot \mathbf{B} - \hat{\mathbf{d}}.\mathbf{F}. \tag{I.26}$$

Using the definitions (I.19) of the two angular momenta $\hat{\mathbf{J}}_a$ and $\hat{\mathbf{J}}_b$, the Hamiltonian can be recast as

$$\hat{H}_{B,F} = -(\omega_S - \omega_Z)\hat{J}_{a,z} + (\omega_S + \omega_Z)\hat{J}_{b,z}, \tag{I.27}$$

where $\omega_Z = \mu_B B_z/\hbar$ and $\omega_S = (3nea_0/2)F_z/\hbar$ are respectively the Zeeman and Stark frequencies. To get a sense of the atomic dynamics, we focus on the expectation values of the two angular momenta, which we write $\langle \mathbf{J}_{a(b)} \rangle$. Through Ehrenfest equation and the usual commutation relations $[\hat{J}_{a(b),\alpha}, \hat{J}_{a(b),\beta}] = i\hbar\epsilon_{\alpha\beta\gamma}\hat{J}_{a(b),\gamma}$, we get the evolution of the expectation values:

$$\frac{d\langle \mathbf{J}_a \rangle}{dt} = -(\omega_S - \omega_Z)\mathbf{u}_z \times \langle \mathbf{J}_a \rangle, \tag{I.28}$$

$$\frac{d\langle \mathbf{J}_b \rangle}{dt} = (\omega_S + \omega_Z)\mathbf{u}_z \times \langle \mathbf{J}_b \rangle. \tag{I.29}$$

Both precess around the quantization axis, with their norms being preserved. $\langle J_{a(b),z}\rangle$ remains constant, while the transverse components along x and y rotate, with a pulsation that depends on the strength of the fields. Since the Stark frequency dominates at regular field values, both pre-factors $\omega_S - \omega_Z$ and $\omega_S + \omega_Z$ are positive, and the two angular momenta rotate in opposite directions.

For later purposes, we finally consider the application of a radio-frequency field, of frequency ω_{RF}, which couples the manifold levels via the ladder operators $\hat{J}_{a(b),\pm}$. If the field is σ^+-polarized, its action on the atom, combined with the effect of the static fields, boils down to the Hamiltonian [136]:

$$\hat{H}_{\mathrm{RF}} = -\omega_a \hat{J}_{a,z} - \Delta_b \hat{J}_{b,z} + \Omega_b(\hat{J}_{b,+} + \hat{J}_{b,-}), \tag{I.30}$$

where $\Delta_b = -\omega_b + \omega_{\mathrm{RF}}$ and $\Omega_b \propto F$ is the Rabi frequency of the $\hat{J}_{b,\pm}$ transitions. Under the right frequency and power conditions, the σ^+ RF field drives the transitions along the lower-left to top-right diagonals of the manifold. It keeps m_a constant, while acting on m_b only. This feature will be helpful when addressing the state evolution towards the circular level in the experiments.

I.1.3 Circular Rydberg states

The parabolic basis provides the right framework to properly define *circular* Rydberg states and their neighboring levels within a given n manifold. For a fixed n, the circular levels are the two states with maximal angular momentum: $\ell = n-1, \quad m = \pm(n-1)$. In the Stark diagram of figure I.2 (b), they are located at both lateral ends of the manifold. As levels with maximal angular momentum, circular states are not subject to quantum defects and the hydrogen model perfectly applies to their study. We focus on the circular state with positive m (one for each n – the right-most level in the figure) and denote it $|nC\rangle$. Accordingly, its definition in the parabolic basis representation is $|n, k = 0, m = n-1\rangle$. In the $\mathbf{J}_a$, $\mathbf{J}_b$ formalism, this circular level is $|m_a = +J, m_b = +J\rangle$. In this state, the two angular momenta are aligned and parallel to the quantization axis.

The circular state wavefunction writes, from equation (I.3):

$$\psi_{|nC\rangle}(r,\theta,\phi) = \frac{1}{\sqrt{\pi a_0^3}} \frac{1}{nn!} \left(-\frac{r}{na_0} e^{i\phi} \sin\theta\right)^{n-1} e^{-\frac{r}{na_0}}. \tag{I.31}$$

Figure I.3 (a) depicts the electron probability density in $|52C\rangle$, seen in the $x-z$ plane. This specific circular state is the one we prepare and manipulate in the experiments. Its electron is located on a torus approximately 200 nm away from the nucleus, and its phase winds up $n-1$ times along its orbit. More generally, the radius of circular atoms goes as

$$\langle r\rangle_{|nC\rangle} \sim a_0 n^2. \tag{I.32}$$

The parabolic basis is particularly convenient to define the levels closest to the circular state in the Rydberg manifold, called the *elliptical* states. They differ from

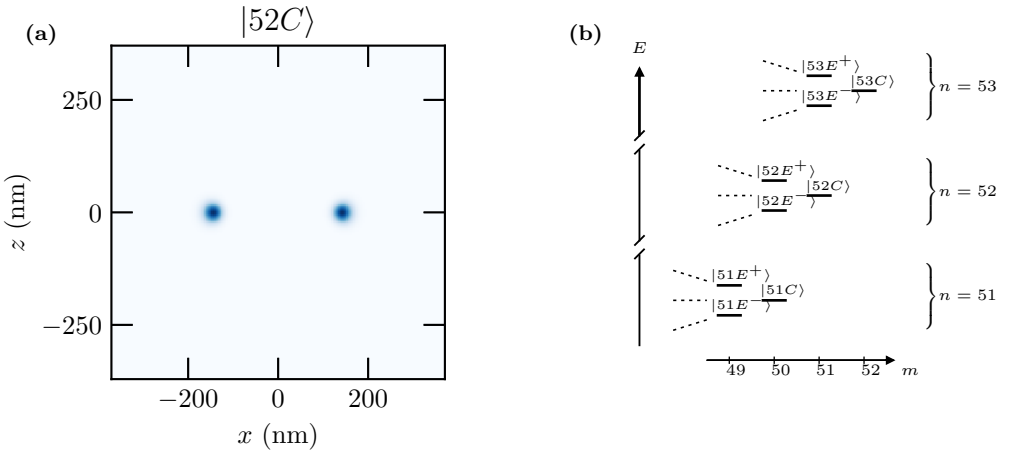

Figure I.3: **(a)** Electron probability density in the circular state $|52C\rangle$. **(b)** Level scheme for the circular states and their elliptical neighbors of three adjacent manifolds.

$|nC\rangle$ by a single quantum of angular momentum and are written:

$$|nE^{\pm}\rangle = |n, m = n-2, k = \pm 1\rangle. \tag{I.33}$$

Figure I.3 (b) illustrates this level structure by focusing on the right-most part of the Stark diagram, for three neighboring n manifolds. We consider here the directing electric field to be of the order of 1 V/cm, so that we can get an idea of the energy scales involved in typical experimental conditions. In this case, the energy difference between $|52C\rangle$ and $|52E^{\pm}\rangle$ is around 100 MHz, whereas the $|52C\rangle$-$|51C\rangle$ and $|52C\rangle$-$|53C\rangle$ distances are of approximately 50 GHz, i.e, orders of magnitude larger.

Dipole matrix elements

One important feature of Rydberg atoms is, due to their great size, their large dipole matrix elements on the allowed transitions. This is especially true for circular levels. Using the same formalism as the one introduced to describe the static Stark shifts, the generalized dipole selection rules (i.e. for non-necessarily static electric fields) between two levels $|n, \ell, m\rangle$ and $|n', \ell', m'\rangle$ write [137]:

$$\ell' = \ell \pm 1, \tag{I.34}$$

$$m' = m + q, \tag{I.35}$$

where $q = 0$ corresponds to a π-polarized transition, and $q = \pm 1$ to σ^-- or σ^+-polarized transitions, depending on whether a photon is absorbed or emitted. These dipole matrix elements are numerically tractable [95]. The one associated to the σ^+ microwave transition $|52C\rangle \rightarrow |51C\rangle$ is $1846(ea_0)$ and scales as n^2. For comparison, the one between $|52S_{1/2}\rangle$ and $|52P_{3/2}\rangle$ is $1574(ea_0)$ and the dipole matrix element for the D_2 line transition $|5S_{1/2}\rangle \rightarrow |5P_{3/2}\rangle$ is about $4.2(ea_0)$ [138]. The huge dipole matrix elements between neighboring circular states imply that these transitions are strongly coupled

to the electromagnetic field, in the microwave range. This makes for an easy manipulation of the circular levels using standard microwave technology.

Lifetime

Another important characteristic of circular atoms is their lifetime. To spontaneously decay, the only channels available to a circular state (allowed by the general dipole transition rules) are towards the underlying elliptical state $|nE^-\rangle$ and towards the lower circular state $|(n-1)C\rangle$. Their rates are given by the Einstein coefficients [139]:

$$A_{if} = \frac{4\alpha\omega^3}{3c^2}|\langle i|\hat{\mathbf{r}}|f\rangle|^2, \tag{I.36}$$

where $|i\rangle$ and $|f\rangle$ are the initial and final levels involved in the radiative decay and $\omega/(2\pi)$ the transition frequency. Given the ω^3 dependency in this expression and the frequencies of the two allowed transitions in an experimentally standard electric field – MHz radio-frequency towards $|nE^-\rangle$ and GHz micro-wave towards $|(n-1)C\rangle$ – the $|nC\rangle \rightarrow |nE^-\rangle$ decay is completely negligible. The resulting spontaneous emission rate yields a 0 K natural radiative lifetime of 35 ms for $|52C\rangle$, our circular state of interest. For comparison, low-ℓ Rydberg states, with many decay channels in the optical domain to low-lying or ground state levels, have a radiative lifetime at 0 K of a few hundred microseconds [82].

As previously explained, dipole-accessible transitions from circular states are strongly coupled to the electromagnetic field in the microwave range. At non-zero temperature, it is therefore crucial to take into account absorption and stimulated emission processes to estimate the real lifetime of circular atoms [139]. Stimulated emission occurs over the same $|nC\rangle \rightarrow |(n-1)C\rangle$ transition as spontaneous emission, but absorption can occur for several allowed transitions to the upper $n+q$, $q \geq 1$ manifolds. Both mechanisms are described by the enhanced Einstein coefficients

$$B_{if} = \overline{n}(\omega)A_{if}, \tag{I.37}$$

where $\overline{n}(\omega)$ is the average number of photons in mode ω at a given temperature:

$$\overline{n}(\omega) = \frac{1}{e^{\hbar\omega/k_BT} - 1}. \tag{I.38}$$

Altogether, these various contributions yield a lifetime of about 10 ms for $|52C\rangle$ at 4 K (accessible using standard cryogenic technology [120]). At 300 K, the temperature of our current setup, this lifetime drops to about 140 µs. In the first part of appendix A, we detail the numerical model we use to estimate the circular atom lifetimes. It will be used throughout the rest of the text in various discussions of the experimental results. It can finally be shown that the spontaneous emission lifetime scales as n^5 for circular atoms at low temperature [82].

The properties outlined here, of large *circular-circular* dipole matrix elements and long lifetimes, make circular atoms good candidates on which to encode spin states

for quantum simulation. However, in order to make use of these features, one has to be able to individually trap these atoms to immobilize them over extended durations. This is thankfully made possible by the ponderomotive force, described in the next section.

Ponderomotive energy

The ponderomotive energy arises from the interaction between the Rydberg electron and an oscillating inhomogeneous electromagnetic field [140, 141]. In a quickly oscillating field, charged particles undergo a quiver motion: to minimize their kinetic energy, the particles are attracted to low-intensity regions of space. In a Rydberg atom, the valence electron can be subjected to this force if the atom is placed in such an inhomogeneous field distribution, typically using frequencies in the optical domain. The force also applies to the ionic core, but its large mass makes this effect negligible. The electron then drives the whole atom to low-intensity regions, thus creating a 3-dimensional potential distribution for the Rydberg atom.

The ponderomotive effect can be derived from the general atom-field interaction Hamiltonian, using the classical electromagnetic four-vector $(\Phi/c, \mathbf{A})$ in the Coulomb gauge and where we set $\Phi \equiv 0$ since there are no sources:

$$\hat{H}_I = \frac{e}{m_e}\mathbf{A}(\hat{\mathbf{r}},t).\hat{\mathbf{p}} + \frac{e^2}{2m_e}\mathbf{A}^2(\hat{\mathbf{r}},t) + \frac{\mu_B}{\hbar}g_S\hat{\mathbf{S}}.\mathbf{B}(\hat{\mathbf{r}},t). \tag{I.39}$$

In this expression, we can drop the magnetic term, as it is much smaller than others. We can also discard the $\mathbf{A}.\hat{\mathbf{p}}$ contribution: in Rydberg states, as n increases, $\mathbf{p}$ gets smaller and that part vanishes. We end up with the quadratic term only, which we re-write in terms of field intensity $I(\mathbf{r})$ via $\mathbf{F} = -\partial_t\mathbf{A} = -i\omega\mathbf{A}$, to obtain a classical potential [142], written as a function of the light frequency $\omega/(2\pi)$ and position r:

$$V(\mathbf{r}) = \frac{e^2}{2m_e c\varepsilon_0\omega^2}I(\mathbf{r}) = h\beta(\omega)I(\mathbf{r}). \tag{I.40}$$

To give an idea of the energy scale involved, we compute the proportionality coefficient $\beta(\omega)$ in the case of our trapping light of 821 nm wavelength:

$$\beta(\omega) = 1.52\ \frac{\text{MHz}}{\text{mW}\,\mu\text{m}^{-2}}. \tag{I.41}$$

Rydberg atoms are low-field seekers in such a distribution. It is then possible to trap individual circular atoms in this ponderomotive potential, provided that one can create, in the optical domain, a low-intensity region surrounded by high intensity regions in all 3 dimensions. It is also important to mention that circular atoms are insensitive to photo-ionization [117, 121], an essential property that low-ℓ states lack.

Having now covered the properties of individual Rydberg atoms, and more specifically those of circular Rydberg atoms, we can turn to the matter of their interactions, at the heart of this work.

I.2 Interactions between circular Rydberg atoms

As large antennas strongly coupled to the electromagnetic field, (circular) Rydberg states exhibit significant interactions with one another. In this section, we cover the general description of two interacting circular atoms. After introducing the necessary formalism to understand the underlying physics, we focus on two specific configurations which lead to different interaction regimes: either a first-order resonant exchange or a second-order van der Waals interaction which can emulate the XXZ Hamiltonian.

I.2.1 Two interacting circular atoms

We consider two circular atoms, indexed 1 and 2, in states $|nC\rangle$ and $|n'C\rangle$, with dipole moments $\mathbf{d}_i$ and at a fixed distance r (treated classically). The inter-atomic vector is written $\mathbf{r} = r\mathbf{n}_{1\to 2}$ and static parallel electric and magnetic fields define the quantization axis, which allows us to use the parabolic basis depicted in figures I.2 (b) and I.3 (b) of the previous sections. The two atoms interact via the dipole-dipole Hamiltonian [143]:

$$\hat{V}_{dd}(\mathbf{r}) = \frac{1}{4\pi\varepsilon_0\, r^3}\left[\hat{\mathbf{d}}_1.\hat{\mathbf{d}}_2 - 3(\hat{\mathbf{d}}_1.\frac{\mathbf{r}}{r})(\hat{\mathbf{d}}_2.\frac{\mathbf{r}}{r})\right]. \tag{I.42}$$

This operator gives rise to couplings between the pair state $|nC, n'C\rangle$ and other pair levels $|a, b\rangle$ via dipole-allowed transitions, i.e.

$$\Delta\ell_i = \pm 1, \quad \Delta m_i \in \{-1, 0, 1\}, \tag{I.43}$$

for each atom i. The dipole-dipole couplings should also conserve the projection of the total angular momentum $m = m_1 + m_2$, so that $\Delta m = 0$. Without additional details, we expect these dipole-dipole matrix elements to scale as $1/r^3$, given the expression of $\hat{V}_{dd}$. We treat the action of this operator perturbatively, in orders of $1/r^3$. The first-order, $1/r^3$ terms are referred to as the "direct" dipole interaction, whereas the second-order, $1/r^6$ ones are the van der Waals interactions.

Two atoms in the same circular state

In the simplest $n = n'$ case, the selection rules impose $\langle nC, nC|\hat{V}_{dd}|nC, nC\rangle = 0$. The dipole-dipole interaction then acts as a second order perturbation. It induces a distance-dependent energy shift in the uncoupled $|nC\rangle|nC\rangle$ state that goes as [143]:

$$E_{nC-nC}(r) = \sum_{|ab\rangle} \frac{\langle nC, nC|\hat{V}_{dd}|ab\rangle\langle ab|\hat{V}_{dd}|nC, nC\rangle}{2E_{nC} - E_a - E_b} = \frac{C_{6,nC-nC}}{r^6}, \tag{I.44}$$

where E_g is the energy of the individual level $|g\rangle$. The main contribution in this sum comes from the coupling to the state $(|nE^+, nE^-\rangle + |nE^-, nE^+\rangle)/\sqrt{2}$ (see figure I.3 for the position of the elliptical levels with respect to $|nC\rangle$). The linear Zeeman shift (eq. (I.11)) and quadratic Stark shift (eq. (I.22)) ensure that this symmetric level

is non-degenerate with $|nC, nC\rangle$, so that the denominator of this term does not diverge and non-degenerate perturbative expansion stands. The next significant allowed couplings are with $|nE^+, nE^+\rangle$ and $|ne^-, ne^-\rangle$, but these two contributions actually cancel each other out [144]. By brute-force diagonalization, in fields of $F = 2$ V/cm and $B = 10$ G, we compute this van der Waals coefficient for $|52C\rangle$ in two configurations, with the inter-atomic axis either parallel or orthogonal to the quantization axis:

$$C^{\parallel}_{6,52C-52C}/h = 7.8\ \text{GHz.µm}^6, \quad C^{\perp}_{6,52C-52C} = 6.3\ \text{GHz.µm}^6. \tag{I.45}$$

The second-order, $1/r^6$ van der Waals behavior holds true for large-enough distances, when the perturbative treatment remains valid. Through the numerical diagonalization, we find that the perturbative approach and the $1/r^6$ scaling are accurate for $r > 3$ µm.

Two atoms in different circular states

We now consider the interaction between atoms in two different circular levels: $n' > n$. We restrict our study to the two most interesting and relevant cases $n' = n+1$ or $n' = n + 2$. Once again, the selection rules (eq. (I.43)) impose

$$\langle nC, n'C|\hat{V}_{dd}|nC, n'C\rangle = \langle n'C, nC|\hat{V}_{dd}|n'C, nC\rangle = 0. \tag{I.46}$$

These diagonal terms in the general $\hat{V}_{dd}$ operator are therefore 0. The interaction-induced energy shift on the bare $|nC\rangle|n'C\rangle$ and $|n'C\rangle|nC\rangle$ levels is a second-order, van der Waals contribution via the mixing to other states. We can nonetheless take these contributions into account in diagonal terms [145] by writing an effective Hamiltonian:

$$\hat{V}/\hbar = \begin{array}{c} \begin{array}{cc} |nC, n'C\rangle & |n'C, nC\rangle \end{array} \\ \begin{pmatrix} C_{nC-n'C} & A_{nC-n'C} \\ A_{nC-n'C} & C_{nC-n'C} \end{pmatrix} \begin{array}{l} |nC, n'C\rangle \\ |n'C, nC\rangle \end{array} \end{array}. \tag{I.47}$$

The diagonal component writes

$$C_{nC-n'C}(r) = \sum_{|ab\rangle} \frac{\langle nC, n'C|\hat{V}_{dd}|ab\rangle\langle ab|\hat{V}_{dd}|nC, n'C\rangle}{E_{nC} + E_{n'C} - E_a - E_b} = \frac{C_{6,nC-n'C}}{r^6} \tag{I.48}$$

and it describes the second-order shift on the bare levels $|nC\rangle|n'C\rangle$ and $|n'C\rangle|nC\rangle$. Technically, this amounts to turning the full $\hat{V}_{dd}$ matrix into a block-diagonal matrix, where we extract the block corresponding to the subspace $\{|nC, n'C\rangle, |n'C, nC\rangle\}$. The off-diagonal terms $A_{nC-n'C}$ govern an exchange interaction $|nC, n'C\rangle \leftrightarrow |n'C, nC\rangle$ and are written, up to second order:

$$\begin{aligned} A_{nC-n'C}(r) &= \langle nC, n'C|\hat{V}_{dd}|n'C, nC\rangle + \sum_{|ab\rangle} \frac{\langle nC, n'C|\hat{V}_{dd}|ab\rangle\langle ab|\hat{V}_{dd}|n'C, nC\rangle}{E_{nC} + E_{n'C} - E_a - E_b} \\ &= \frac{A_{3,nC-n'C}}{r^3} + \frac{A_{6,nC-n'C}}{r^6}. \end{aligned} \tag{I.49}$$

If the $|nC, n'C\rangle \leftrightarrow |n'C, nC\rangle$ transition is dipole-allowed, $A_{nC-n'C}$ is a first-order, direct exchange and scales as $1/r^3$, since the first term in the expansion dominates. If not, only the second-order term in the perturbative treatment is non-zero and we recover, for the off-diagonal terms, a van der Waals interaction scaling as $1/r^6$ via the coupling to other pair states.

To cover the more general case where the two atoms can be in the same state, we write the effective interaction operator as:

$$\hat{V}/\hbar = \begin{array}{c} \begin{array}{cccc} |nC,nC\rangle & |nC,n'C\rangle & |n'C,nC\rangle & |n'C,n'C\rangle \end{array} \\ \begin{pmatrix} C_{nC-nC} & 0 & 0 & 0 \\ 0 & C_{nC-n'C} & A_{nC-n'C} & 0 \\ 0 & A_{nC-n'C} & C_{nC-n'C} & 0 \\ 0 & 0 & 0 & C_{n'C-n'C} \end{pmatrix} \end{array} \begin{array}{l} |nC,nC\rangle \\ |nC,n'C\rangle \\ |n'C,nC\rangle \\ |n'C,n'C\rangle \end{array}. \tag{I.50}$$

In $\hat{V}$, according to the above discussion, the distance dependence goes as

$$\hat{V}/\hbar \sim \begin{pmatrix} 1/r^6 & 0 & 0 & 0 \\ 0 & 1/r^6 & 1/r^3 \text{ or } 1/r^6 & 0 \\ 0 & 1/r^3 \text{ or } 1/r^6 & 1/r^6 & 0 \\ 0 & 0 & 0 & 1/r^6 \end{pmatrix}, \tag{I.51}$$

depending on whether or not the $|nC\rangle \leftrightarrow |n'C\rangle$ transition is dipole-allowed.

Spin Hamiltonian

It is actually easier to make sense of the circular-circular interaction dynamics by rewriting the previous Hamiltonian in terms of spins [117]. We identify the space $\{|nC\rangle, |n'C\rangle\}$ with a spin-1/2 so that the pair of atoms evolves in $\{|\downarrow\downarrow\rangle, |\downarrow\uparrow\rangle, |\uparrow\downarrow\rangle, |\uparrow\uparrow\rangle\}$ under Hamiltonian (I.50). In order to write $\hat{V}$ using the usual spin formalism, we introduce the following quantities:

$$\begin{cases} \delta E_0 = (C_{nC-nC} + 2C_{nC-n'C} + C_{n'C-n'C})/4 \\ \delta\zeta = (C_{nC-nC} - C_{n'C-n'C})/2 \\ J_z = (C_{nC-nC} - 2C_{nC-n'C} + C_{n'C-n'C})/4 \\ J = A_{nC-n'C}/2. \end{cases} \tag{I.52}$$

According to equation (I.51), δE_0, $\delta\zeta$ and J_z scale as $1/r^6$, but J scales as either $1/r^3$ or $1/r^6$ depending on whether or not the $|nC\rangle \leftrightarrow |n'C\rangle$ transition is allowed. Thanks to this transformation, we can write the interaction Hamiltonian as

$$\hat{V}/\hbar = \begin{pmatrix} \delta E_0 + \delta\zeta + J_z & 0 & 0 & 0 \\ 0 & \delta E_0 - J_z & 2J & 0 \\ 0 & 2J & \delta E_0 - J_z & 0 \\ 0 & 0 & 0 & \delta E_0 - \delta\zeta + J_z \end{pmatrix}. \tag{I.53}$$

By dropping the constant energy offset δE_0 and introducing the standard Pauli matrices, we finally write the dipole-dipole interaction Hamiltonian between two atoms restricted to two circular levels as:

$$\hat{V}/\hbar = \frac{\delta\zeta}{2}(\sigma_1^z + \sigma_2^z) + J_z(\sigma_1^z\sigma_2^z) + J(\sigma_1^x\sigma_2^x + \sigma_1^y\sigma_2^y). \tag{I.54}$$

We recognize here three terms:

- the single-atom frequency shift $\delta\zeta$, related to edge effects that are more explicitly understood in larger ensembles of atoms,
- the longitudinal "Ising-like" interaction J_z, pertaining to the alignment or anti-alignment of the spins,
- the transverse term J, which characterizes the energy exchange between the two spins.

From the definition of the C coefficients in equations (I.44) and (I.48), we expect that $\delta\zeta$ and J_z vary with $\mathbf{F}$ and $\mathbf{B}$, due to the Stark and Zeeman shifts induced on all the levels involved in the summation. Numerical diagonalization indicates that these three coefficients are at most of the order of 1-10 kHz. The situation is a bit more complex with J. If the $|nC\rangle \leftrightarrow |n'C\rangle$ transition is allowed, i.e., if $n' = n + 1$, then J ($\propto 1/r^3$) is proportional to $\langle nC, n'C|\hat{V}|n'C, nC\rangle$ and its value is in the MHz range: it dominates all other terms. If the transition is not allowed however, i.e., if $n' = n + 2$ for instance, then perturbation expansion is involved and J ($\propto 1/r^6$) is of the same order of magnitude as the other terms (i.e. in the kHz range). Interestingly, in both cases J is nearly independent of F and B, the fields' amplitudes, contrary to the other coefficients. The details of the dynamics in these two different regimes (J dominant and direct exchange vs. all coefficients of similar magnitude and van der Waals interactions) are detailed in the next sections.

I.2.2 Resonant spin-exchange interaction

Our experimental investigations led us to focus on the $n' = n+1$, direct exchange case. As we currently work with a room-temperature setup, the limited lifetime of the circular atoms (a few hundred µs) prevented us from properly characterizing the slow van der Waals interactions (in the kHz range). We therefore decided to focus on the direct exchange interaction, which lies in the MHz range and is accessible to our experimental capabilities. Following the formalism introduced in the previous section, we detail here the spin dynamics of two circular atoms, each in $\{|\downarrow\rangle = |51C\rangle, |\uparrow\rangle = |52C\rangle\}$, the levels we work with in the lab. This section provides the theoretical context with which the results of chapter 4 are coupled. Figure I.4 (a) represents the geometry of the system. We write r the distance between the two atoms and θ the angle between the quantization axis and the inter-atomic axis. We consider here that the atoms have infinite lifetimes and no motion.

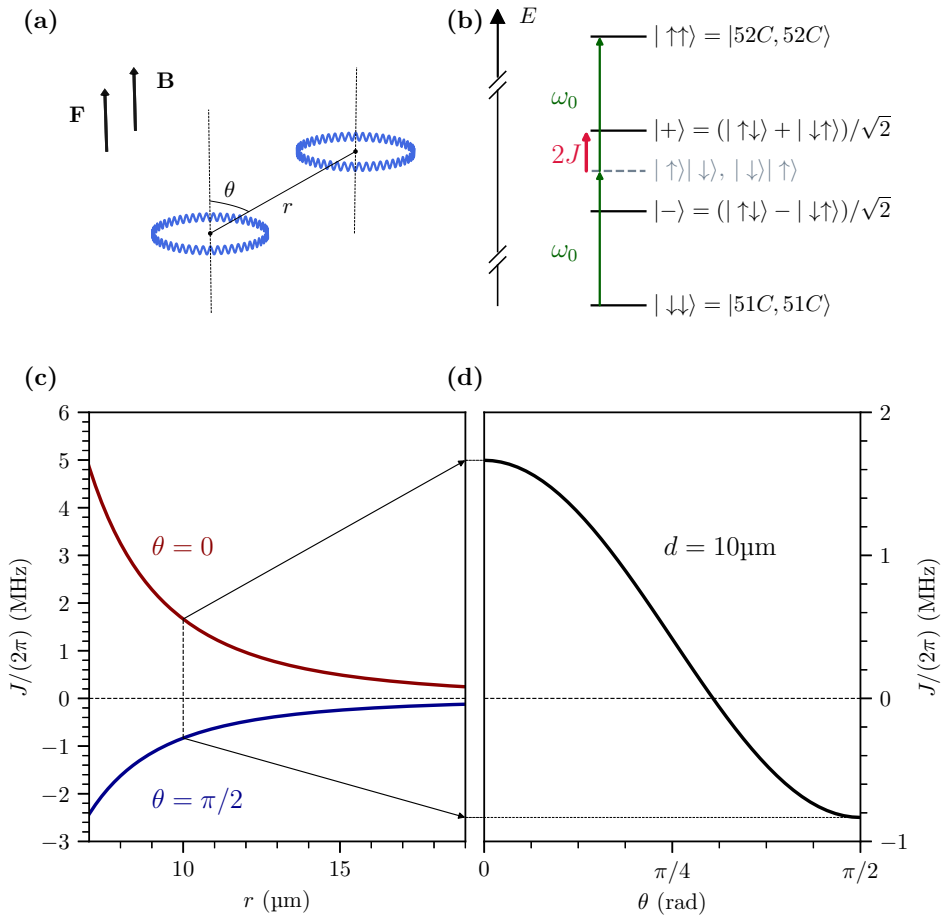

Figure I.4: **(a)** Geometry and parametrization of the system. The fields are taken to be $F = 2$ V/cm and $B = 10$ G for the energy computations. **(b)** Level scheme for the interacting pair states: the energy splitting between $|+\rangle$ and $|-\rangle$ is given by $2J$. The two other states $|\uparrow\uparrow\rangle$ and $|\downarrow\downarrow\rangle$ lie tens of GHz away from them due to the bare atomic energies: ω_0 is the single spin-flip energy, between $|51C\rangle$ and $|52C\rangle$. **(c)** Variation of J with the distance r, for both $\theta = 0$ (red) and $\theta = \pi/2$ (blue). **(d)** Variation of J with the angle θ, at a distance of 10 µm. For $\theta = \theta_0 \simeq 54.7°$, $J = 0$ and the two atoms do not interact.

Numerical computations give, for a distance of 10 µm and at an angle $\theta = \pi/2$ (i.e. atoms placed like two plates next to each other on a table), in fields of 2 V/(cm) and 10 G, the following interaction coefficients:

$$J = -2\pi \times 832 \text{ kHz}, \quad J_z = 2\pi \times 1 \text{ kHz}, \quad \delta\zeta = -2\pi \times 0.4 \text{ kHz}. \tag{I.55}$$

As expected from the previous section, J (which goes as $1/r^3$ here) is much larger than the other terms (in $1/r^6$). It then is safe to neglect all terms except J to study the dynamics of the pair of atoms, and we end up with the simplified interaction Hamiltonian:

$$\hat{V}/\hbar = \begin{array}{c} \begin{array}{cccc} |\downarrow\downarrow\rangle & |\downarrow\uparrow\rangle & |\uparrow\downarrow\rangle & |\uparrow\uparrow\rangle \end{array} \\ \begin{pmatrix} -\omega_0 & 0 & 0 & 0 \\ 0 & 0 & 2J & 0 \\ 0 & 2J & 0 & 0 \\ 0 & 0 & 0 & \omega_0 \end{pmatrix} \end{array}, \tag{I.56}$$

where we also account for the bare atoms' energies via ω_0, the pulsation difference between $|51C\rangle$ and $|52C\rangle$, which is of the order of $2\pi \times 50$ GHz. The diagonalization of this operator is straightforward and its eigenvectors are

$$\left\{ |\downarrow\downarrow\rangle, \quad |+\rangle = (|\uparrow\downarrow\rangle + |\downarrow\uparrow\rangle)/\sqrt{2}, \quad |-\rangle = (|\uparrow\downarrow\rangle - |\downarrow\uparrow\rangle)/\sqrt{2}, \quad |\uparrow\uparrow\rangle \right\}. \tag{I.57}$$

Figure I.4 (b) depicts the level scheme in this basis. The interaction coupling J appears in the splitting between the symmetric and anti-symmetric levels. Probing the interaction strength is then possible via microwave spectroscopy. The frequency of the transition from $|\uparrow\uparrow\rangle$ (or $|\downarrow\downarrow\rangle$) to $|+\rangle$, compared to that of the bare $|\downarrow\rangle \rightarrow |\uparrow\rangle$ transition, gives a direct measurement of J. Since J lies in the MHz range, the linewidth constraints for these measurements should not be too demanding. It is also worth noting that, due to symmetry conservation, the transition from $|\uparrow\uparrow\rangle$ (or from $|\downarrow\downarrow\rangle$) to the anti-symmetric state $|-\rangle$ is forbidden. We also expect a pair of atoms initialized in $|\uparrow\downarrow\rangle$ to undergo spin-exchange oscillations $|\uparrow\downarrow\rangle \leftrightarrow |\downarrow\uparrow\rangle$ at a frequency $4J/(2\pi)$.

Furthermore, the interaction strength is tunable via the geometry of the system. Using numerical diagonalization, we plot in figure I.4 (c) J as a function of distance, for angles θ of 0 and $\pi/2$. Figure I.4 (d) represents the variation of J as a function of θ, at a distance of 10 µm. As shown in these plots, J is proportional to $1/r^3$ and tuning θ changes the sign of the interaction: for values of θ below $\theta_0 \simeq 54.7°$, J is positive and the interaction in $|+\rangle$ is repulsive. For $\theta \in [\theta_0, \pi/2]$ however, $J < 0$ and the interaction in $|+\rangle$ is attractive. Importantly, for $\theta = \theta_0$ the interaction energy vanishes. We make use of this important property in the experiments to inhibit interactions when needed.

This behavior can be understood via a geometrical interpretation of the system in terms of real electric dipoles. When the pair is in the symmetric level $|+\rangle$, each atom evolves in superposed states, according to the decomposition:

$$|+\rangle = \frac{1}{2}\left\{(|\uparrow\rangle + |\downarrow\rangle) \otimes (|\uparrow\rangle + |\downarrow\rangle) - (|\uparrow\rangle - |\downarrow\rangle) \otimes (|\uparrow\rangle - |\downarrow\rangle)\right\}. \tag{I.58}$$

The wavefunction of the electron in the superposition $|\uparrow\rangle + |\downarrow\rangle$ makes a real dipole emerge, because of the phase winding numbers that differ by a single unit between $|\uparrow\rangle$ and $|\downarrow\rangle$, as illustrated in figure I.5 (this is only true in this present case, where $n' = n + 1$). This dipole rotates in the plane of the atom at the angular frequency ω_0, the energy difference between the two circular levels involved, since the superposition evolves in time as $|\downarrow\rangle + e^{-i\omega_0 t}|\uparrow\rangle$. In this symmetric state, one can therefore see each atom as a clock with a single hand that points in the direction of the dipole and

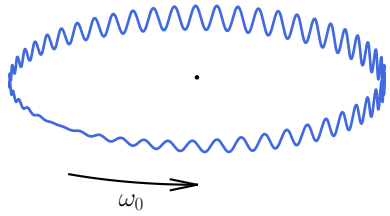

Figure I.5: Wavefunction of the electron in the superposition $|51C\rangle + e^{-i\omega_0 t}|52C\rangle$, illustrating the emergence of a real electric dipole rotating around the quantization axis.

rotates over times. The two hands always point in the same direction, according to equation (I.58) and since the two atoms' states can both be decomposed in exactly the same way.

When the two atoms are on top of each other (i.e., $\theta = 0$), the two clock hands rotate in sync above one another around the quantization axis. Their respective orientation never changes and they classically repel each other, with a strength that goes as $1/r^3$. When the two atoms are next to each other ($\theta = \pi/2$), the two clock hands rotate in the same plane, going from an attractive interaction when aligned with the inter-atomic axis to a repulsive interaction when perpendicular to the inter-atomic axis. However, on average over a full rotation (i.e averaging $1 - 3\cos^2\omega_0 t$), this interaction is attractive - and obviously still varies as $1/r^3$. In the anti-symmetric state, decomposition (I.58) changes and the two dipoles point in opposite directions, leading to the opposite interactions. We therefore recover from this simple geometrical picture the behavior expected from the numerical simulations.

From the discussed numerical computations, we can roughly estimate the trap depth needed to experimentally probe these interactions. We consider individual traps based on the ponderomotive energy described in section I.1.3. To counteract the typical interaction strength in the $\{|51C\rangle, |52C\rangle\}$ subspace described here, trap depths of several MHz are required, according to figure I.4. From the proportionality factor of equation (I.41), the domain walls of the intensity distribution should be around 5 mW µm^{-2} in order to probe interactions of up to a few MHz.

To sum up, this exchange configuration constitutes the most basic and straightforward system in which to probe interactions between circular Rydberg atoms. It exhibits elementary dynamics governed by a single dominant and geometrically tunable term in the MHz range, which is measurable via microwave spectroscopy. The

experimental investigation of this rudimentary system constitutes a natural – but nonetheless significant – milestone on the way to full scale quantum simulations with circular atoms.

I.2.3 Quantum simulation of a tunable XXZ Hamiltonian

The end goal of mastering interactions between circular atoms is to implement quantum simulation schemes [117]. In the case $n' = n+2$, interacting circular states display much more complex behaviors. In this configuration, J scales as $1/r^6$, just like the other coefficients of the spin Hamiltonian (I.54). All terms are van der Waals, second order contributions of the same order of magnitude and no single one dominates the dynamics of the system. To get an idea of the new energy scales involved here, we give the values of the three interaction coefficients in this new configuration, with $|\downarrow\rangle = |50C\rangle$ and $|\uparrow\rangle = |52C\rangle$. these levels were identified in [117] as convenient for the implementation of simulation schemes. We keep here the parametrization of the previous section (figureI.4 [a]), we still consider the fields to be 2 V/(cm), 10 G and $\theta = \pi/2$ but we choose a distance of 5 µm (the $1/r^6$ dependence requires shorter distances to make the interactions significant):

$$J = -2\pi \times 28 \text{ kHz}, \quad J_z = 2\pi \times 69 \text{ kHz}, \quad \delta\zeta = -2\pi \times 51 \text{ kHz}. \tag{I.59}$$

Apart from the comparable strengths of the three coefficients, the other advantage of this configuration compared to the $n' = n+1$ direct exchange is its tunability. Since J_z is sensitive to the values of the static fields, the ratio between the longitudinal term J_z and the transverse term J can be tuned over a wide range of values, both positive and negative, without changing the geometry. Figure I.6 (a) shows the extent of the variations of J_z/J in various fields, with the same geometrical parameters as previously stated. The tunability suggests the possibility to explore different regimes of spin physics in such a system. By adding a microwave drive resonant on the $|\downarrow\rangle \leftrightarrow |\uparrow\rangle$ transition (2-photon process of Rabi frequency Ω and detuning δ) and extending the spin Hamiltonian (I.54) to a 1D chain of atoms (neglecting edge effects and next-nearest-neighbor interactions), we end up with the XXZ Hamiltonian [146–150]:

$$\hat{V}/\hbar = \sum_i J_z \sigma_i^z \sigma_{i+1}^z \; + \; J(\sigma_i^x \sigma_{i+1}^x + \sigma_i^y \sigma_{i+1}^y) + \frac{\Omega}{2}\sigma_i^x + \frac{\delta}{2}\sigma_i^z. \tag{I.60}$$

The wide tunability of the system, through J_z/J, δ and Ω and at arbitrary timescales[2], should therefore allow to explore a large range of many-body physics phenomena [151–155]. The XXZ Hamiltonian exhibits a rich phase diagram, reproduced in figure I.6 for a chain of atoms in the $\delta = 0$ case. Four different phases of spin physics and their corresponding phase transitions [155–160] can be studied in such a system, by simply tuning the parameters of the circular atoms via the static fields and the microwave drive power. At high microwave drive, the ensemble of spins is in a paramagnetic phase: the drive dominates the dynamics of the atoms, there is no spontaneous ordering. At low microwave drive and large negative values of J_z (when $J_z/J < -1$),

[2]In our experiment, the electric field strength can be changed in under one microsecond, while the microwave drive power is tunable over tens of nanoseconds.

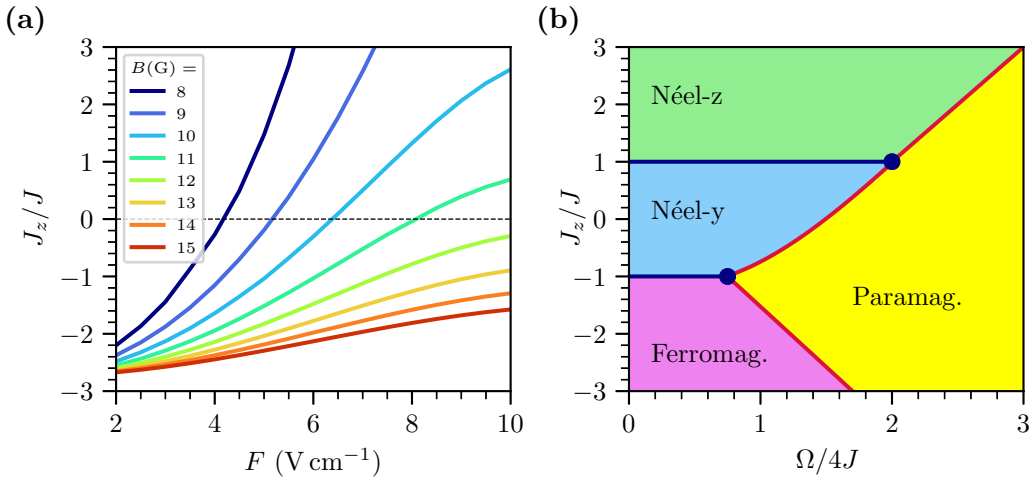

Figure I.6: **(a)** Ratio J_z/J as a function of the electric field, at an inter-atomic distance of 5 µm, with $\theta = \pi/2$ and $\delta = 0$, for magnetic fields ranging from 8 G (dark blue) to 15 G (red). **(b)** Phase diagram of the XXZ Hamiltonian, showing the 4 phases of the system. The red lines indicate Ising transitions and the blue ones Luttinger liquid phases.

the system reaches a ferromagnetic phase and exhibits spontaneous magnetization. As J_z increases via zero to positive values, the atoms go through two Néel phases. For $|J_z| < 1$, the spins tend to anti-align along y (Néel-y phase) and for large values of J_z (for $J_z/J > 1$), the spins anti-align along z (Néel-z).

Such a platform would also enable the investigation of quantum scars [161, 162], quenches and thermalization (through the dynamic control of the Hamiltonian) [107, 163], localization (by adding disorder) [52, 164] and topological effects (with specific lattice geometries) [165, 166]. However, getting to these implementations requires additional experimental features that have yet to be developped in our setup. It should first and foremost be switched back to a cryogenic environment to make the most of the atoms' black-body-sensitive lifetimes and kHz interaction frequencies. Additional control over the system, such as single-site spin manipulation, will also be required for state initialization. That is why we focused, in this thesis, only on the direct exchange configuration in pairs of atoms, which nevertheless constitutes a first step towards full-scale quantum simulations schemes.

I.3 Spin-motion coupling in interacting circular atoms

Throughout the previous part, we completely neglected the motion of the atoms. However, in a real experiment, even though the atoms are individually trapped, they are not perfectly still. The traps necessarily have some spatial extension and the atoms have a certain amount of kinetic energy due to their non-zero temperature. They therefore oscillate around the traps minima and the inter-atomic distance changes over time. Since the interaction coefficients strongly depend on this distance (as $1/r^3$ or $1/r^6$, depending on the configuration), we expect them to change over time, which might alter the spin dynamics of the interaction. Perhaps more importantly, the interaction in itself, whether it be attractive or repulsive, could induce some extra motion. If the atoms are initially not interacting and lying at their equilibrium positions, switching on the interactions can generate motion in the traps. The next section therefore describes the interplay between the spin and motional dynamics for two trapped, interacting circular Rydberg atoms. It presents the main results of a theoretical study, published in [124], born out of the Covid lockdowns, when we used the time away from the lab to answer this question: could the motion in the traps impede the proper investigation of circular atoms interactions?

I.3.1 System definition

In the following, we consider two circular atoms individually trapped by the ponderomotive force. The discussion is based on the trapping setup suggested in the original proposal for quantum simulations with circular atoms [117]. The quantization axis (Oz) is perpendicular to the inter-atomic axis (Ox), the atoms are trapped in the periodic minima of a sinusoidal intensity pattern along (Ox) and tightly confined in the other directions (achievable with a set of laser beams described in [117, 124]). We therefore neglect the transverse motion and consider that the atoms only have a one-dimensional motion along the inter-atomic axis. The distance between the two sites' minima is written d and is adjustable. The trapping frequency associated to the harmonic approximation of the sine traps is ω, which is also freely tunable by varying the beam powers. Using readily available laser systems, trap depths of several MHz can be achieved[3]: as long as the motional energy remains small compared to that, we consider the trap to be harmonic. All these geometrical quantities are depicted in figure I.7 (a), where we also display the spatial extension x_0 of the motional ground states in the traps.

Spin-phonon Hamiltonian

Using the same framework as in the previous part and considering the atoms to be in the circular states $\{|\downarrow\rangle = |nC\rangle,\ |\uparrow\rangle = |(n+\Delta n)\rangle\}$, with $\Delta n \in \{1, 2\}$, we still write the interaction Hamiltonian as

$$\hat{H}_S/\hbar = \frac{\delta\zeta}{2}(\sigma_1^z + \sigma_2^z) + J_z(\sigma_1^z\sigma_2^z) + J(\sigma_1^x\sigma_2^x + \sigma_1^y\sigma_2^y) + \delta E_0, \tag{I.61}$$

[3]We reach these values in our own experimental setup but with a different optical trapping scheme.

where the four coefficients depend on r, the inter-atomic distance, as $1/r^m$ ($m = 3$ or 6, not necessarily the same for all coefficients). We restrict our study to the case where there is no microwave field driving the transitions between the two levels. This simplification still allows us to tackle the goals of this project, namely the impact of motion on the pair-state's spin oscillations. We therefore focus on the subspace $\{|\downarrow\uparrow\rangle, |\uparrow\downarrow\rangle\}$, i.e. the 2×2 block in the center of matrix (I.53). We will consider situations where the atomic levels are initialized in one of the subspace's states and are left to evolve freely. Introducing the set of Pauli matrices $\hat{\Sigma}_{X,Y,Z}$ standardly associated to this subspace, the Hamiltonian reads:

$$\tilde{H}_S/\hbar = 2J\hat{\Sigma}_X - \Delta, \tag{I.62}$$

where $\Delta = J_z - \delta E_0$. According to the different configurations discussed in subsection I.2.1, if $\Delta n = 1$, J goes as $1/r^3$ and dominates all other terms, which we can discard by setting $\Delta = 0$ to carry out the analytics. If $\Delta n = 2$, all contributions are comparable and scale as $1/r^6$.

The atomic positions in the traps are described by $\hat{x}_1$ and $\hat{x}_2$, taken with respect to the traps minima. Thanks to the harmonicity of the wells, we can actually eliminate the un-coupled center of mass motion and describe the dynamics using the relative position $\hat{x} = \hat{x}_2 - \hat{x}_1$ and the reduced mass $\mu = M/2$, which is subjected to the same harmonic potential as each atom. We will use the regular quantization formalism to describe the motion in terms of phonons, i.e., occupation numbers of the discretized levels of the harmonic oscillator (of frequency ω). The spatial extent of the motional ground state is given by $x_0 = \sqrt{\hbar/(2\mu\omega)}$ and we write d the fixed distance between the traps' centers. The full Hamiltonian of the system is then:

$$\hat{H} = \frac{\hat{p}}{2\mu} + \frac{1}{2}\mu\omega^2\hat{x}^2 + \hat{U}_m(\hat{x}) \otimes \hbar(2J\hat{\Sigma}_X - \Delta), \tag{I.63}$$

where

$$U_m(\hat{x}) = \left(1 + \frac{\hat{x}}{d}\right)^{-m} \tag{I.64}$$

accounts for the distance dependence of the interaction coefficients. Once again, we recall that if $m = 3$ i.e., $\Delta n = 1$), we can set $\Delta = 0$. Throughout this study, we will compute both the expectation value of the relative position $x(t) = \langle\hat{x}\rangle(t)$ and the spin level probability $P_{\uparrow\downarrow}$ over time, starting from $|\uparrow\downarrow\rangle$ and a given motional state.

To further simplify the Hamiltonian, we introduce the dimensionless quantity $\hat{\xi} = \hat{x}/x_0$ and the coupling factor $g = x_0/d \ll 1$. Using the standard phonon number $\hat{n} = \hat{a}^\dagger\hat{a}$, with $\hat{a}^\dagger$ and $\hat{a}$ the creation and annihilation operators for the harmonic levels of the relative displacement, we end up with the spin-phonon Hamiltonian:

$$\hat{H}/\hbar = \omega(\hat{n} + \frac{1}{2}) + (1 + g\hat{\xi})^{-m} \otimes (2J\hat{\Sigma}_X - \Delta). \tag{I.65}$$

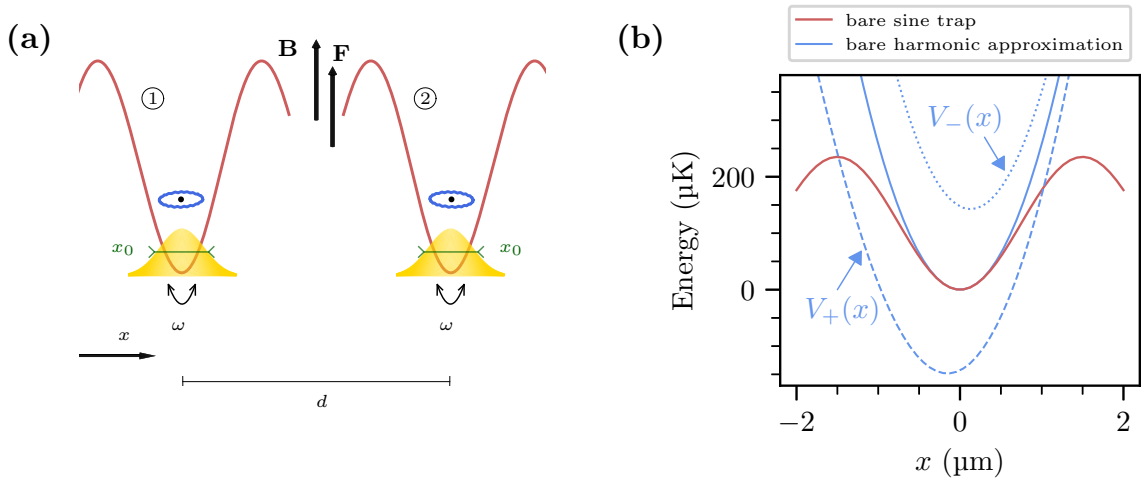

Figure I.7: **(a)** Schematic view of the geometrical configuration for the study of the spin-motion entanglement in a system of two trapped, interacting circular atoms indexed 1 and 2. The spatial extent of the motional ground state (in yellow) is x_0 and the inter-atomic distance d. The trapping potentials are schematically shown in red. **(b)** Potential energies as functions of the relative displacement $x = x_2 - x_1$ in a strong interaction regime. The bare sine potential is plotted in red, its harmonic approximation in blue (solid line). The two effective potentials V_+ and V_- exerted on states $|X\rangle$ and $|-X\rangle$ are the dashed and dotted lines respectively. They illustrate the $\sim \pm 2J$ spin-dependence of the system's energy.

Geometric picture and effective potentials

The spin dependence of the motion can be made more explicit by using the projectors on the two eigenstates of $\hat{\Sigma}_X$, $|\pm X\rangle = (|\uparrow\downarrow\rangle \pm |\downarrow\uparrow\rangle)/\sqrt{2}$, through which we decompose the Hamiltonian as follows:

$$\hat{H} = \left(\frac{\hat{p}^2}{2\mu} + V_+(\hat{x})\right) \otimes |X\rangle\langle X| + \left(\frac{\hat{p}^2}{2\mu} + V_-(\hat{x})\right) \otimes |-X\rangle\langle -X|, \tag{I.66}$$

where V_+ and V_- are the two effective potentials exerted on the two different spin states:

$$V_\pm(\hat{x}) = \frac{1}{2}\mu\omega^2\hat{x}^2 + \hbar U_m(\hat{x})(\pm 2J - \Delta). \tag{I.67}$$

These two effective potentials are plotted in figure I.7 (b) as functions of the relative displacement x, for a strong interaction regime that clearly separates them: $n = 48$ and $\Delta n = 1$ (so that $m = 3$ and $J \simeq -2\pi \times 3$ MHz dominates), $d = 6$ μm and $\omega = 2\pi \times 50$ kHz. The bare sine trap and its harmonic approximation are also shown here. The effect of the interaction is to shift, both spatially and energetically, the bare harmonic potential. In state $|X\rangle$, the interaction is attractive ($J < 0$, see figure I.4 [b]) so the minimum is shifted to lower values of x, the spin energy is low and therefore the effective potential is lowered. In $|-X\rangle$, the interaction is repulsive, so x is shifted to higher values, with a positive global offset on the potential because of the positive

spin energy. For very strong attractive interaction, the hyperbolic behavior of $U_m(x)$ can dominate the harmonic trap. In that extreme case, the confining potential is not robust enough to keep the atoms apart and the system becomes unstable: the effective potential no longer traps the atoms. This issue, which we avoid in the rest of this work by focusing on weak-enough interactions, is discussed in more details in appendix B.

We can thus see the motion as two uncoupled movements related to the two spin components: if the initial state is $|\Psi(t=0)\rangle = |\psi_0(x)\rangle|\uparrow\downarrow\rangle$, the evolving state then reads:

$$|\Psi(t)\rangle = \frac{1}{\sqrt{2}}(|\psi_+(x,t)\rangle|+X\rangle + |\psi_-(x,t)\rangle|-X\rangle), \tag{I.68}$$

$|\psi_\pm(x,t)\rangle = e^{-i\hat{H}_\pm t}|\psi_0(x)\rangle$ being the evolution under the two effective potentials ($\hat{H}_\pm = \hat{p}^2/2\mu + V_\pm(\hat{x})$). The motional ket associated to the $|\uparrow\downarrow\rangle$ spin component in the wavefunction is then $(|\psi_+\rangle + |\psi_-\rangle)/\sqrt{2}$. The resulting spin level probability $P_{\uparrow\downarrow}$ is derived from the interference between these two paths.

Linear coupling

The first, simplified way of computing the effect of motion on the interaction dynamics is to consider the linear coupling limit, which amounts to developing $(1+g\xi)^{-m}$ in equation (I.65) to first order in g. Using $\eta = gm$, we get

$$\hat{H}/\hbar = \omega(\hat{n} + \frac{1}{2}) + (1 - \eta\hat{\xi}) \otimes (2J\hat{\Sigma}_X - \Delta). \tag{I.69}$$

Again, let us recall that if $\Delta n = 1$, i.e. $m = 3$, we can consider $\Delta \sim 0$. Following the previous discussion, the two spin-dependent effective potentials read:

$$V_\pm(\hat{x}) = \frac{1}{2}\mu\omega^2(\hat{x} - x_0^\pm)^2 \pm \frac{\hbar\Omega}{2} - \hbar\Delta - \hbar\omega(\alpha^2 + \alpha_z^2). \tag{I.70}$$

The displacements of the minima of both potentials are made explicit via $x_0^\pm = 2x_0(\pm\alpha - \alpha_z)$, where we introduce the two dimensionless shifts in phase space:

$$\alpha = \eta\frac{2J}{\omega}, \quad \alpha_z = \eta\frac{\Delta}{\omega}. \tag{I.71}$$

The energy difference between the minima of the two effective potentials is written

$$\Omega = 4J\left(1 + 2\eta^2\frac{\Delta}{\omega}\right). \tag{I.72}$$

Under this form, it is possible to diagonalize the Hamiltonian using a unitary polaron transformation via the displacement operator $\hat{D}(\beta) = \exp\left(\beta\hat{a}^\dagger - \beta^*\hat{a}\right)$:

$$\hat{\mathcal{U}}(\alpha,\alpha_z) = \hat{D}(\alpha\hat{\Sigma}_X - \alpha_z) = e^{\alpha(\hat{a}^\dagger - \hat{a})\otimes\hat{\Sigma}_X - \alpha_z(\hat{a}^\dagger - \hat{a})\otimes\mathbb{1}}. \tag{I.73}$$

In the transformed Hamiltonian $\hat{\tilde{H}} = \hat{\mathcal{U}}^\dagger(\alpha,\alpha_z)\hat{H}\hat{\mathcal{U}}(\alpha,\alpha_z)$ the spin and positions are decoupled:

$$\hat{\tilde{H}}/\hbar = \omega(\hat{n} + \frac{1}{2}) + \frac{\Omega}{2}\hat{\Sigma}_X - \Delta - \omega(\alpha^2 + \alpha_z^2). \tag{I.74}$$

In this linear coupling limit, we can therefore analytically compute the state of equation (I.68). We assume that the initial motion is described by a coherent state $|\alpha_0\rangle$ and that the spins start in $|\uparrow\downarrow\rangle$.

The spin oscillation then writes:

$$P_{\uparrow\downarrow}(t) = \frac{1}{2}\left[1 + e^{-4\alpha^2(1-\cos\omega t)}\cos\left(\Omega t - \Theta(t)\right)\right], \tag{I.75}$$

with

$$\Theta(t) = 4\alpha(\alpha_z + \alpha_0)\sin(\omega t). \tag{I.76}$$

The pair state undergoes oscillations between $|\uparrow\downarrow\rangle$ and $|\downarrow\uparrow\rangle$ at the Rabi frequency Ω, which corresponds to the energy difference between the two effective minima. This is in agreement with the wavefunction of (I.68): the two spatial components $|\psi_\pm(x,t)\rangle$ evolve with a phase difference of Ω, due to the energy imbalance between their two effective Hamiltonians. Since $P_{\uparrow\downarrow}$ is derived from the interference between these two paths, as stated previously in the beginning of this section, we get the emergence of spin Rabi oscillations at this frequency Ω. It amounts to a first-order correction of the bare Rabi frequency $4J$, as suggested by equation (I.72). The oscillation is phase-shifted by the periodic function Θ, which is small compared to Ω because α, $\alpha_z \ll 1$. The contrast of the oscillations is also periodically modulated over time, at a frequency $\omega/(2\pi)$. For a small displacement α (i.e. for a small coupling g), the contrast is barely affected but, for a large value of α, it periodically collapses to zero with a period $T_{\text{trap}} = 2\pi/\omega$.

We also show that, starting from the coherent state $|\alpha_0\rangle$, the $|\psi_\pm(x,t)\rangle$ wavefunctions remain coherent states throughout the evolution. Indeed, we derive from the polaron transformation in the linear regime:

$$|\psi_\pm(x,t)\rangle = |\alpha_0 + \alpha_\pm e^{-i\omega t}\rangle, \tag{I.77}$$

with $\alpha_\pm = \pm\alpha - \alpha_z$ and up to time-dependent global phases that differ between the two wavefunctions.

The two components of the motional state rotate along circles centered around $\alpha_\pm$ in phase space, at the angular frequency ω and with opposite orientations. Figure I.8 illustrates these trajectories in the oscillator phase space. The initial state splits into two components that evolve separately before reuniting periodically, with a period T_{trap}.

The collapse of the Rabi oscillations and the splitting of the motional wavefunction, which both evolve with the same time period, hint at a full entanglement of the spin and motional degrees of freedom when α in non-negligible. When the two coherent states reunite in $|\alpha_0\rangle$, the spin oscillates with perfect contrast. When the two motional components are maximally separated, the envelope of the average Rabi signal is reduced.

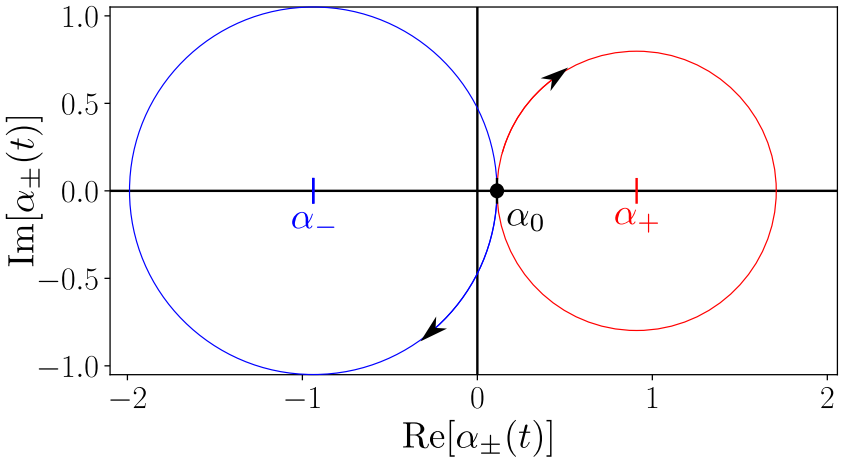

Figure I.8: Phase-space trajectories of the two spatial components $|\psi_\pm(x,t)\rangle$ in the linear regime, starting from an initial coherent state $|\alpha_0\rangle$.

The linear approach gives a first glimpse of the possible effects of the atomic motion on the spin dynamics, which could range from no impact to a total collapse of the Rabi oscillations depending on the strength of the coupling. Thanks to the polaron transformation, which decouples the spin and motion dynamics, all observables can be analytically computed in this regime. In the next sections, we detail the analysis of this system in three different specific configurations, serving various purposes. We use exact numerical simulations to compute observables when needed, in order to go beyond the linear coupling limit.

I.3.2 Spin-motion coupling in the XXZ Hamiltonian parameters

The first concrete application of this study is the estimation of the contrast loss in the spin dynamics of the XXZ simulator that could be induced by the motional degree of freedom of the circular atoms. Since the circular atoms allow for simulations over long timescales, we need to scrutinize the spin-motion entanglement over many interaction cycles. We can tackle this problem either via analytical solutions in the linear coupling regime or using numerical computations at higher orders. To do so, we consider here an atomic configuration similar to the initial simulator proposed in [117].

We set a high trapping frequency to minimize the spin-motion coupling and consider the atoms to be placed next to each other, again as two plates on a table[4]:

$$\begin{gathered} n = 48,\ n' = 50,\ d = 6\ \mu\mathrm{m},\ \omega = 2\pi \times 50\ \mathrm{kHz}, \\ F = 9\ \mathrm{V/cm},\ B = 12\ G. \end{gathered} \tag{I.78}$$

[4]This configuration differs a bit from that of section I.2.3 on the presentation of the XXZ simulator: the levels involved are not the same, the distance is slightly larger and F is smaller, so that the interactions are weakened and the spin-motion coupling is further reduced.

With these parameters, we compute the following interaction coefficients and other relevant quantities:

$$\begin{aligned} J = -2\pi \times 5.8 \text{ kHz}, \quad \Delta = -2\pi \times 73.2 \text{ kHz}, \\ g = 0.008, \quad x_0 = 48 \text{ nm}, \quad \Omega = 2\pi \times 22.8 \text{ kHz}. \end{aligned} \tag{I.79}$$

To estimate the effect of temperature as realistically as possible, we now take the initial motional state to be a thermal distribution

$$\hat{\rho}_T(0) = \frac{1}{1+\overline{n}} \sum_{n=0}^{\infty} \left(\frac{\overline{n}}{1+\overline{n}} \right)^n |n\rangle\langle n|, \tag{I.80}$$

where the average phonon number $\overline{n}$ is related to the atomic temperature T via the Bose-Einstein distribution $\overline{n} = 1/(e^{\hbar\omega/k_B T} - 1)$, with $\hbar\omega/k_B = 2.4$ µK the natural temperature scale of the harmonic well. The initial spin level is taken to be $|\uparrow\downarrow\rangle$, so that the system starts in:

$$\hat{\rho}(0) = \hat{\rho}_T(0) \otimes |\uparrow\downarrow\rangle\langle\uparrow\downarrow|. \tag{I.81}$$

We implement the numerical simulations in this context and present the results in figures I.9 (a) and (b), respectively the displacement $\xi(t)$ and the spin probability $P_{\uparrow\downarrow}$ over tens of interaction cycles. The computations shown here are carried out to infinite order in the spin-phonon coupling but the terms up to second order actually already account for all the features seen on the resulting graphs.

These simulations reveal some significant contrast loss over time in the spin dynamics of the system, even though the motion remains limited, with an amplitude for the relative position x of less than 15 nm (to be compared with the extent of the motional ground state, 48 nm, and the inter-atomic distance of 6 μm).

To get more insight into this phenomenon, we compute the state energies up to second-order in the coupling. We consider the eigenenergies of the linear Hamiltonian of equation (I.69) to be known, via the polaron transformation described above. The second-order coupling term $7/12\ \eta^2\hat{\xi}^2(2J\hat{\Sigma}_X - \Delta)$ is then treated as a perturbation on that linear Hamiltonian, which allows us to effectively obtain the energies $E(n,s)$ for the states $|n\rangle \otimes |s\rangle$ to second-order in η, with s the spin state ($|+X\rangle$ or $|-X\rangle$) and $|n\rangle$ a motional Fock state. By computing the energy difference between the two spin eigenstates $|n\rangle|+X\rangle$ and $|n\rangle|-X\rangle$, we retrieve the spin Rabi frequency Ω_n associated to this Fock state and show that it depends linearly on the phonon number:

$$\Omega_n = \Omega + \frac{7}{3}\eta^2 J \times n, \tag{I.82}$$

with $\Omega = 4J(1 + 2\eta^2\Delta/\omega)$ the Rabi frequency in the linear regime. Altogether, each motional level $|n\rangle$ involved in the thermal distribution (I.80) induces its own spin Rabi frequency Ω_n. These different frequencies lead, over a few ms, to a progressive loss of contrast in the average Rabi oscillation signal. However, since we consider the system to be closed, we expect the evolution to remain coherent, so that the different contributions are brought back in phase after some delay, a phenomenon quite reminiscent

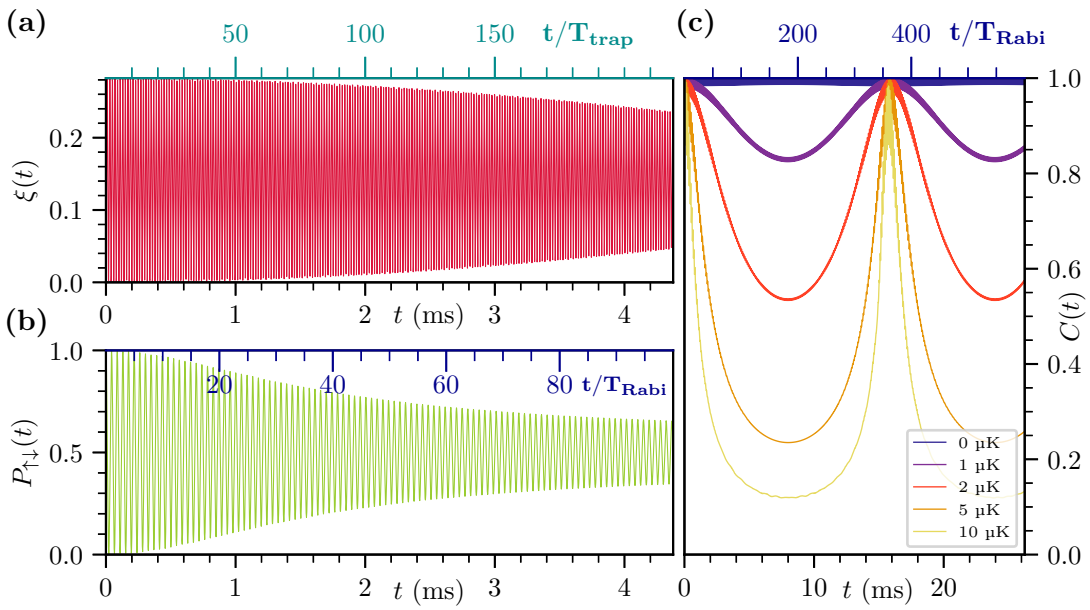

Figure I.9: **(a)** Displacement $\xi(t) = x(t)/x_0$. We recall that $x_0 = 48$ nm here, so that the total amplitude of the oscillations of $x_2(t) - x_1(t)$ is less than 15 nm. The top axis (in blue) gives the evolution in numbers of trap periods $T_{\text{trap}} = 2\pi/\omega$. **(b)** Spin-state probability $P_{\uparrow\downarrow}(t)$ over 100 spin oscillations, showing the loss of contrast due to the spin-phonon entanglement. The top axis (in dark blue) shows the number of cycles $T_{\text{Rabi}} = 2\pi/\Omega$. **(c)** Envelope $C(t)$ of the Rabi oscillations over time, computed for various temperatures and over several hundred cycles of interactions.

of the quantum revivals observed for the Rabi oscillation of a two-level system in a coherent quantum field [167]. We show this result in figure I.9 (c), where we plot the envelope of the Rabi oscillations over long timescales and for various temperatures. We observe that, as the temperature grows, the contrast loss becomes more severe. There is nonetheless always a revival of the oscillations after some amount of time, which corresponds to approximately 350 oscillations (or 17 ms).

Two conclusions can be drawn from these results:

- First, the contrast loss is highly sensitive to the temperature of the atoms: even at 2 μK, the contrast is already diminished by half. Lowering the atomic temperature is therefore key to limiting these effects. With standard optical and adiabatic cooling mechanisms, temperatures of a few μK can be reached. More advanced mechanisms, such as side-band Raman cooling [168], should be considered to fully prevent these effects by forcing the atomic temperature to be small compared to T_{trap}.[5]

[5]Increasing the trapping frequency ω would also limit this effect but might not be a viable long-term solution appropriate for large number of traps.

- Secondly, since this contrast loss results from a mere dephasing of different Rabi frequencies and not from irremediable decoherence, it could in principle be canceled out by echo techniques, that have yet to be detailed.

We therefore get the answer to the original question that spawned this study: under the right circumstances, spin-motion coupling should not be detrimental to the realization of a circular atom quantum simulator. The system does not exhibit any irreversible motional-induced decoherence. We should only expect some preventable contrast loss that highly depends on the temperature of the atoms.

I.3.3 Application to thermometry

The temperature dependence of the spin dynamics incidentally suggests that one could use the Rabi oscillations to directly probe the motion of the atoms. More specifically, by making the spin-phonon interplay as large as possible within reasonable bounds, could this effect be put to use to make the circular levels a thermometer for the atomic motion? To investigate this question, we keep the atomic parameters of the previous section but lower the trap frequency from $2\pi \times 50$ kHz to $2\pi \times 15$ kHz, such that we reach the coupling strength $g = 0.015$ (versus 0.008 for the XXZ simulator), which should exacerbate the effects of the motion on the spin evolution. The linear coupling results should remain valid for low temperatures, as g is still small and validates the perturbative treatment of the problem.

Figure I.10 (a) shows the results of exact simulations of the spin evolution in this system, over a few periods and for various temperatures. As expected, the contrast decays much faster than in the previous part (see figure I.9 [b] and [c]) as soon as the temperature is non-zero, because of the lower trapping frequency. The quick decay allows for an efficient probe of the temperature: measuring the spin level after half of an oscillation (i.e. after ~ 23 µs) already yields information on the motional state of the atoms.

In figure I.10 (b) we detail this feature by plotting the population at half of the Rabi period $P_{\uparrow\downarrow}[T_{\text{Rabi}}/2]$ as a function of temperature, both using the analytics of the linear case (blue dotted line) and the numerical simulations for exact resolution (red solid line). The two are in good agreement for low temperatures (under 10 µK). In that range, the slope is approximately 2% /µK: a measurement of the spin population with a 1% error therefore gives a temperature estimation with a 1 µK precision.

To go further, we study the variation of this sensitivity with the geometric parameters of the system. We write $P^*_{\uparrow\downarrow}$ the spin population at half the Rabi period and derive, from the linear regime results, the sensitivity $dP^*_{\uparrow\downarrow}/d\overline{n}$ (equivalent to $dP^*_{\uparrow\downarrow}/dT$ but more straightforward to compute), using $\varphi_R = \pi\omega/(4J)$, the phase halfway through the first spin oscillation:

$$\frac{dP^*_{\uparrow\downarrow}}{d\overline{n}} = 4\alpha^2(1-\cos\varphi_R)\cos(4\alpha\alpha_z\sin\varphi_R)e^{-4\alpha^2(1-\cos\varphi_R)(2\overline{n}+1)}. \tag{I.83}$$

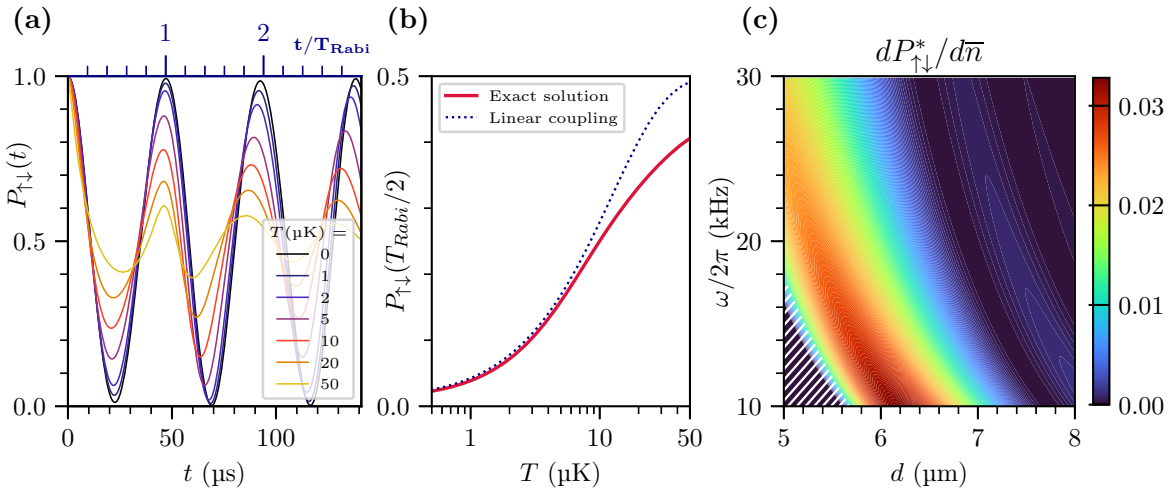

Figure I.10: **(a)** Rabi oscillations in the XXZ atomic parameters but with a low trapping frequency of 15 kHz. The motion-induced contrast decay occurs over a few oscillations and strongly depends on the temperature. **(b)** Spin expectation value at half the Rabi period as a function of temperature. The solid red line depicts the result of exact numerical simulations, while the blue dotted line is derived from the linear coupling results. The two approaches remain comparable for temperatures below 10 µK. **(c)** Thermometer sensitivity, in %/phonon, as a function of ω and d, for $\overline{n} = 1$. The lower left part of the plot (white hatched area) where $dP^*_{\uparrow\downarrow}/d\overline{n}$ decreases to zero should be ignored, as it corresponds to configurations where the trapping depth is not enough to counteract the strong interactions.

Figure I.10 (c) plots this quantity as a function of ω and d, taking $\overline{n} = 1$ (i.e., with always the same phonons in the motional states of the harmonic well). At $\omega = 2\pi \times 15$ kHz, this condition corresponds to $T \simeq 1.5$ µK and at $\omega = 2\pi \times 50$ kHz to $T \simeq 3$ µK. For low values of ω and d, the interaction is too strong to keep the atoms in their shallow traps: it overcomes the trapping potential and the traps open up. The lower left part of the plot I.10 (c), hatched in white and where the sensitivity abruptly drops, should be ignored. It corresponds to instabilities previously mentioned and addressed in appendix B. The graph clearly exhibits a region of sensitivity maxima, where we expect the spin population to vary by 3% per phonon. The parameters used in this section ($d = 6$ µm and $\omega = 15$ kHz) were not far from that optimum. Although this is computed using the linear coupling results, we expect these considerations to hold true for the system as long as the temperature is not too high, as shown in panel (b) of figure I.10.

With the right set of parameters, the precise measurement of the spin population therefore provides a sensitive temperature estimation for the initial atomic motion. It is most appropriate for small oscillation frequencies and low average phonon numbers, conditions in which other methods (release and recapture after thermal expansion, measurement of motional side-bands) tend to fall short. Furthermore, the

short timescales involved here (half a Rabi oscillation) also make this method applicable to ordinary low-ℓ, short-lived Rydberg states, already in use in several quantum simulation platforms.

I.3.4 Motional Schrödinger cat states

We described so far the impact of the atomic movement on the spin dynamics of the pair of atoms: the motion-induced contrast loss should not be detrimental to simulation of spin physics and could actually be used to probe the temperature of the system. In this last section, we scrutinize the motional states of the atoms themselves. As explained from equation (I.68), we expect the displacement associated to the spin level $|\uparrow\downarrow\rangle$ to be $(|\psi_+\rangle + |\psi_-\rangle)/\sqrt{(2)}$, i.e., a Schrödinger cat state, where $|\psi_\pm\rangle$ are the evolutions under the two effective potentials of equation (I.67) (or (I.70) in the linear coupling limit). In order to investigate the formation of these states, we switch to the set of parameters of the direct exchange[6], with $\Delta n = 1$:

$$\begin{gathered} n = 48,\ n' = 49,\ d = 8\ \mu\text{m},\ \omega = 2\pi \times 50\ \text{kHz}, \\ F = 9\ \text{V/cm},\ B = 12\ \text{G}. \end{gathered} \tag{I.84}$$

These parameters lead to a large interaction term J, and therefore a large motional displacement $\alpha = 2\eta J/\omega$, while keeping the coupling $g = x_0/d$ small so that the linear regime results remain accurate:

$$\begin{gathered} J = -2\pi \times 1277\ \text{kHz}, \quad \Delta = -2\pi \times 9\ \text{kHz}, \\ g = 0.006, \quad x_0 = 48\ \text{nm}, \quad \Omega = 2\pi \times 5106\ \text{kHz}. \end{gathered} \tag{I.85}$$

This configuration is notably close to that detailed in section I.2.2 on the pure direct-exchange interaction, and the fact that we focused on this scheme in our experiments adds a layer of relevance to the investigation of its spin-motion dynamics. Although we use different circular levels here, $\Delta n = 1$ guarantees that the fast direct exchange term J dominates the spin evolution and Δ can be discarded.

We proceed as in the last two sections: the system is initialized in $\hat{\rho}(0) = \hat{\rho}_T \otimes |\uparrow\downarrow\rangle\langle\uparrow\downarrow|$, with $\hat{\rho}_T$ a thermal distribution of temperature 2 µK. We compute the exact evolution numerically, although the linear regime analytics yield the same results quite accurately thanks to the low g value. To properly characterize the spin-phonon entanglement and the motional states, we compute two additional quantities besides $P_{\uparrow\downarrow}(t)$ and $\xi(t)$: the von Neumann entropy [169] and the Wigner function [167] of the displacement.

The von Neumann entanglement entropy, which quantifies the "mixed" or "pure" character of the spin state, is defined as:

$$\mathcal{S}_{\text{vN}}(t) = -\text{Tr}\left(\hat{\rho}_S(t) \ln \hat{\rho}_S(t)\right), \tag{I.86}$$

where $\hat{\rho}_S(t)$ is the spin density matrix, obtained by tracing over the harmonic oscillator part of the full density matrix $\hat{\rho}_S(t) = \text{Tr}_{HO}\left(\hat{\rho}(t)\right)$. This quantity is always positive.

[6]The only differences with the set of parameters of section I.3.2 on the contrast loss in the XXZ simulator are Δn and d, taken to be a bit larger (8 µm instead of 6 µm)

In the limiting case of the spin being in a pure state, $\mathcal{S}_{\mathrm{vN}} = 0$. When the spin is in a maximally mixed state, i.e., fully entangled with the motion, the von Neumann entropy is $\ln(2)$, its maximal value.

The Wigner function of the motion is a function defined in phase space, using the number parity operator $\hat{\Pi} = (-1)^{\hat{n}}$, the displacement operator $\hat{D}(\beta) = e^{\beta\hat{a}^\dagger - \beta^*\hat{a}}$ and the motion density matrix $\hat{\rho}_{HO} = \mathrm{Tr}_S(\hat{\rho})$:

$$W(q) = \frac{1}{\pi}\mathrm{Tr}\left\{\hat{\rho}_{HO}\hat{D}(q)\hat{\Pi}\hat{D}^\dagger(q)\right\}, \tag{I.87}$$

in which we use $q = (r + ip)/\sqrt{2}$. We also compute the projected Wigner function

$$\overline{W}(q) = \frac{1}{\pi}\mathrm{Tr}\left\{\langle\uparrow\downarrow|\hat{\rho}|\uparrow\downarrow\rangle\hat{D}(q)\hat{\Pi}\hat{D}^\dagger(q)\right\}, \tag{I.88}$$

where the oscillator density matrix is conditioned on the spin state $|\uparrow\downarrow\rangle$, to specifically probe the motional entanglement associated to that state. Indeed, we recall that we expect the evolution from a pure motional state to go as

$$\propto [|\psi_+\rangle + |\psi_-\rangle] \otimes |\uparrow\downarrow\rangle + [|\psi_+\rangle - |\psi_-\rangle] \otimes |\downarrow\uparrow\rangle. \tag{I.89}$$

We introduce $\overline{W}$ to examine the displacement starting from the mixed thermal state and when projecting the spin in $|\uparrow\downarrow\rangle$.

We present the evolution of all these quantities, in the current direct-exchange configuration, in figure I.11. The spin dynamics display a total collapse of the envelope after ~ 15 oscillations and an almost perfect revival after one trap period T_{trap}, when the contrast nearly grows back to 1. The normalized von Neumann entropy in panel (c) explicitly indicates that, when $P_{\uparrow\downarrow}$ stagnates at 0.5, the entanglement between spin and motion is maximal. Regarding the motion, we witness in panel (b) much slower oscillations of the displacement $\xi = (x_2 - x_1)/x_0$ at the trap frequency ω. In terms of phonons, this leads to an evolution of n, the average phonon number, between its initial value of ~ 0.4 (corresponding to 2 µK) and 4, which amounts to a 10 µK temperature. The exchange interaction in this trap thus induces a non-negligible "heating" of the atoms.

The standard Wigner function $W(q)$ (top row of panel (e) in figure I.11) splits into two components that evolve along circles in phase space, in opposite directions (drawn in green in the figure) and with angular frequency ω. They each correspond to the motion in the effective potentials V_+ and V_- predicted in the linear regime and already illustrated in figure I.8. The projected Wigner function $\overline{W}(q)$, on the other hand (bottom row of the same panel), displays negative regions that appear over half of a trap oscillation and rotate as the features of $W(q)$. These indicate a non-classical evolution and are characteristic of a cat state [167]. Throughout the plateau of the spin oscillations, the motion is in a two-component Schrödinger cat state of the harmonic oscillator.

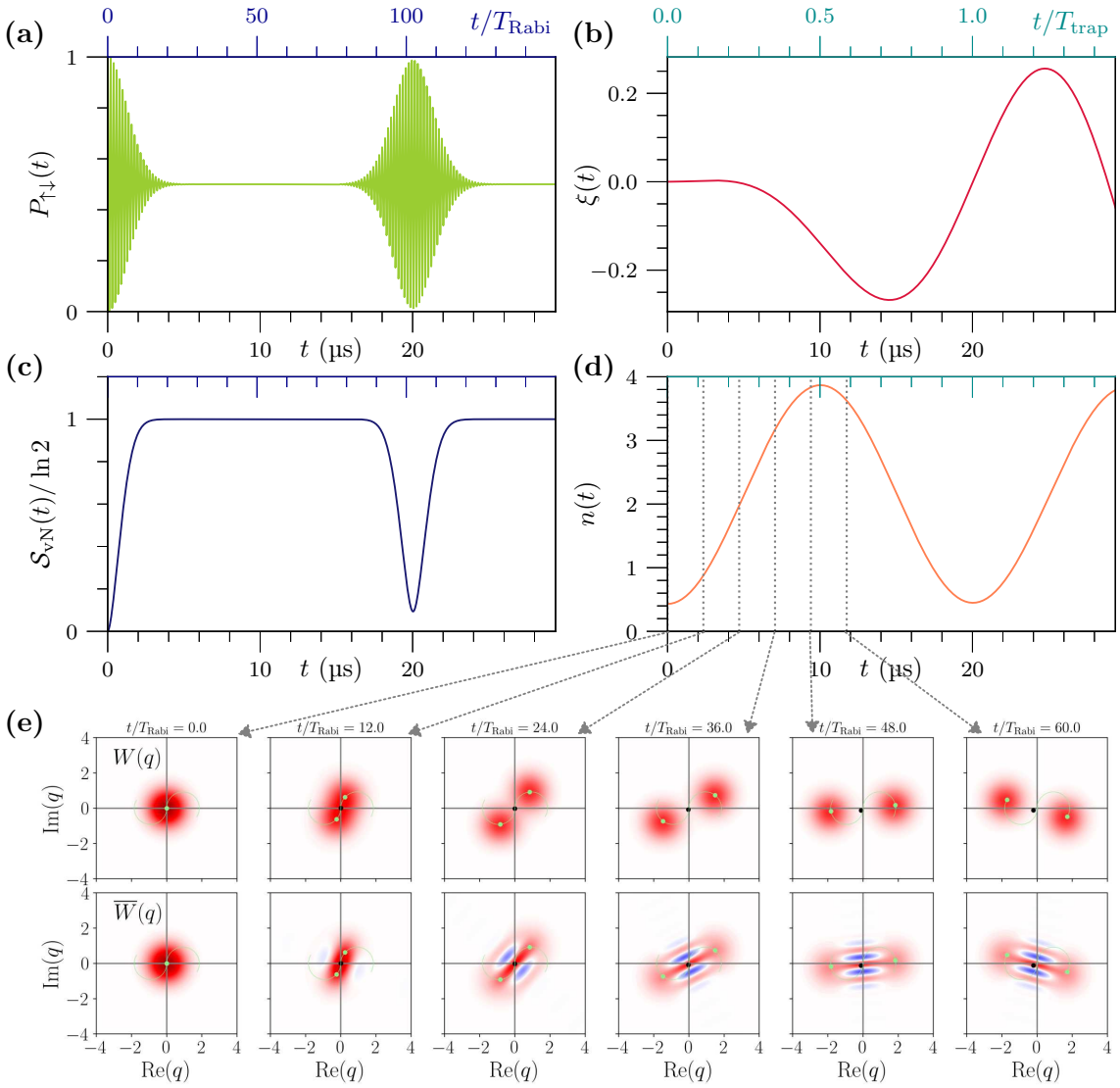

Figure I.11: Evolution of the system observables in the $\Delta n = 1$ configuration, computed to infinite order coupling. **(a)** Rabi oscillations of the spin state $P_{\uparrow\downarrow}$, showing a total collapse and a revival of the contrast after one trap period. **(b)** Displacement $\xi(t)$, oscillating much slower than the spins, due to the large imbalance between J and ω. **(c)** Evolution of the normalized von Neumann entropy, reaching 1 over a large span of time and thus indicating maximal entanglement between the spin and motion degrees of freedom. **(d)** Average number of phonons $n(t)$, starting from a thermal state of $T = 2$ µK. **(e)** Standard (top row) and projected (bottom row) Wigner functions computed at various times over half a trap period. The negative values of $\overline{W}$ (blue regions) reveal a clear Schrödinger cat state during the collapse of the spin Rabi contrast.

We have explored in the last part of this first chapter several consequences of the coupling between motion and atomic states in a system of two trapped, interacting circular Rydberg atoms. We showed that, in the tight trapping regime, the motion degree of freedom does not lead to an irreversible damage to the spin oscillations: although the low-phonon number regime is key to limiting the reduction of the contrast, motion-induced effects could be canceled out via additional echo techniques, and quantum simulation should remain accessible over long timescales. Moreover, it is possible to take advantage of the spin-phonon coupling to precisely and quickly probe the motional states of the atoms. In the strong coupling regime, we showed that the spin and motion become fully entangled, leading to interesting, non-classical motional states, which should be realistically observable in accessible experimental conditions. These first results constitute only a first step in the exploration of these phenomena and can obviously be further detailed. To explore the full XXZ dynamics, a resonant microwave drive could easily be added to the spin Hamiltonian in the simulations. The extension of the model to more than two atoms would also be an interesting development. A more refined description of the trapping could finally be implemented: the two circular states involved have different sizes and therefore do not perceive exactly the same trap shape.

Conclusion of chapter 1

We presented in this first chapter the main properties of individual and interacting circular Rydberg atoms that pertain to the scope of this thesis. The hydrogenic model was used to introduce the features of Rydberg states of Rubidium, the alkali species used in our experiments. The theory of quantum defects accounts for corrections to the hydrogen model that have to be taken into account to describe low-ℓ Rydberg states. Their coupling to static fields and their classification within a given n manifold were detailed, so as to provide the tools and formalism required to understand the experimental excitation of Rubidium from its ground state to circular states, on which our results are based. We outlined the remarkable properties of these specific states: long lifetimes, large dipole matrix elements and their sensitivity to the ponderomotive force, which allows their individual trapping in hollow beams of light.

Such features hinted at the use of circular states as spin-encoding levels in quantum simulation schemes. This idea ultimately led to the experimental results presented in this thesis, on the interactions between trapped circular atoms. The second part of this chapter therefore discussed the framework in which we study these interactions, going from the perturbative treatment of the dipole-dipole interactions to their description using the toolbox of spin physics. We focused on the case of two atoms restrained to circular states separated by a single quantum of angular momentum and thoroughly described the interactions and their geometrical dependence in this case. We also examined the more complex paradigm envisioned for the realization of a tunable XXZ Hamiltonian using circular atoms, which should open up prospects of rich and complex experimental investigations.

The third part focused on the more specific problem of spin-phonon coupling in pairs of trapped, interacting circular atoms. Although highly sensitive to the atomic temperature, the interplay between the atomic and motional degrees of freedom is far from being detrimental to the implementation of quantum simulations, and could actually be used to probe the temperature of the atoms or to generate interesting Schrödinger cat states of motion.

Chapter II

Defect-free arrays of ultracold atoms

The main goal of this thesis is to measure and characterize, for the first time, interactions between circular Rydberg atoms. Since interacting circular atoms are a new field of investigations for our team, we decided to simplify our endeavor by the following means. First, we chose to conduct the experiments in a room-temperature setup, even though one of the main assets of circular atoms is their long lifetimes in a cryogenic environment. Albeit constraining us to the study of interaction dynamics over short timescales because of the reduced lifetimes, this choice allowed us to get rid of the experimental layer of complexity that comes with a cryogenic setup. We were therefore able to focus on mastering techniques that were new to us, especially in the optical trapping domain. The setup was designed to eventually be easily transferred into a cryostat, once it is deemed acceptable to add this constraint, with which our team has years of experience [170, 171]. Secondly, and partly because of the reduced lifetimes, we decided to focus on the investigation of the direct exchange interaction. As we have seen in chapter 1, it involves short timescales and can easily be probed via microwave spectroscopy thanks to the energy distance of several MHz between the pair states. We focused on interactions within pairs only, as a first step towards the realization of more complex geometries. All in all, the experimental prerequisites to reach the goals of this thesis were the deterministic creation of pairs of trapped circular states and the ability to measure the state of the atoms within said pairs.

This second chapter presents the main features of our new experimental setup and details the "ground-state" part of the atomic manipulations. We introduce here the ultra-high vacuum chamber that hosts the experiment. Within that chamber, we manipulate the atoms in a hollow sapphire cube holding electrodes for precise electric field control. We also detail the crucial optical trapping apparatus, which consists in three different beams to (i) trap the ground-state atoms in tweezers, (ii) move them around to create deterministic arrays and (iii) trap the Rydberg atoms in hollow beams once the excitation process has been carried out. The optical traps are shaped thanks to spatial light modulators, in a process that involves careful algorithmic optimizations.

We then describe the preparation and characterization of arrays of ultra-cold atoms, individually trapped in optical tweezers loaded in a probabilistic manner. These first points were conducted alongside Brice Ravon, with whom I worked on the design, con-

struction and operation of this new setup. A more detailed account of these features can be found in his own PhD manuscript [123], the first to present this setup and its capacities.

The third section of this chapter finally discusses its most recent development, the addition of the rearranger beam, used to create deterministic atomic arrays by spatially reordering the atoms in each experimental run.

II.1 Experimental setup

We start with the technical description of the key features of the experimental setup. To give an idea of the mechanical configuration of the experiment, we present the chamber in which we manipulate the atoms and the relevant elements in its vicinity. We then describe the setup inside the chamber, designed to precisely control the electromagnetic fields. We also choose to detail the optical setup put in place to trap the atoms, both in their ground and Rydberg states, as it constitutes a new and crucial element in the success of our achievements. The description of the other laser systems is left out of the main text and presented in appendix D. Other components of the setup, such as the field ionization system or the single-atom imaging scheme, will only be mentioned, since they consist in standard technology and do not involve any new technical implementations.

II.1.1 The ultra-high vacuum chamber

Our experiments take place in a ultra-high vacuum (UHV) chamber, where the residual pressure is kept at 3×10^{-10} mbar by an ion pump. Figure II.1 depicts the chamber and its surrounding optical table, which accommodates all the components used to bring the various laser beams to the experiment through eight optical windows. Under the chamber is a structure that holds a bi-dimensional magneto-optical trap (2D-MOT, developed by the SYRTE laboratory), in which a rubidium cell continuously releases atoms. Its operation is described in details in [172]. The 2D-MOT is directly connected to the chamber via a tube. It provides a vertical stream of slow (10–20 m/s) atoms fed into the experiment that we control by switching on or off the 2D-MOT laser beams. The 2D-MOT has two advantages: to allows to enable or disable the source of cold atoms at the ms scale, and is compatible with a cryogenic setup. The UHV chamber and 2D-MOT [2]are shown in figure II.1 (a), where we also define the coordinate system (x, y, z) that will be used throughout the rest of the text. The whole structure is supported by a frame, on which large magnetic coils are placed to cancel out earth's and other stray magnetic fields in the region of the experiment (shown in the inset of panel [a]).

The heart of the experiment, where we manipulate the atoms, is made of a hollow sapphire structure located in the cylindrical center of the UHV chamber, which is shown in beige in figure II.1 (b). The sapphire structure appears in the center of panel

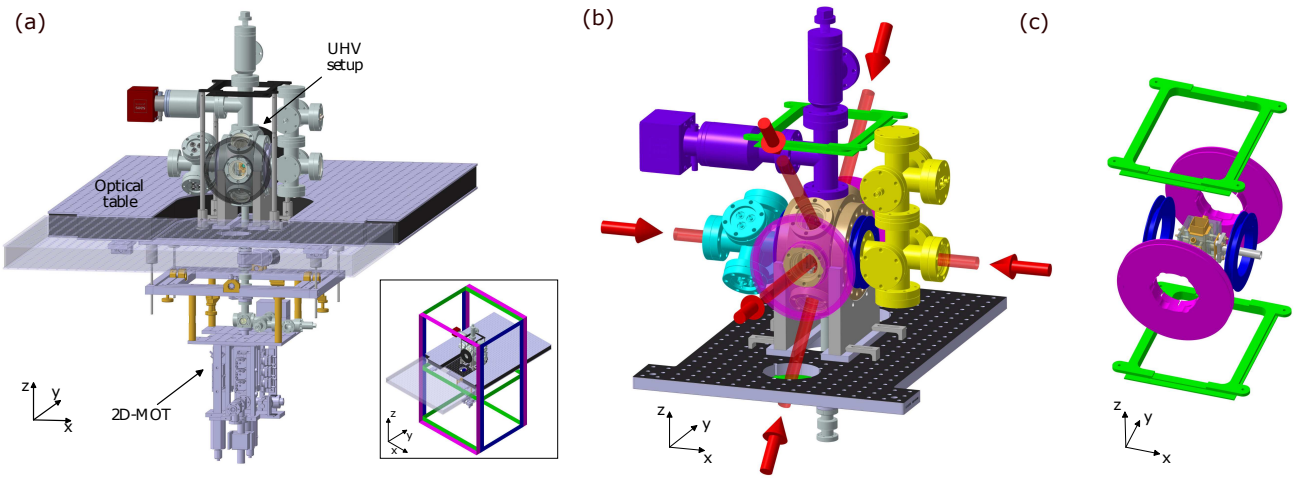

Figure II.1: Main elements of the experimental platform, adapted from [123]. **(a)** Depiction of the largest components of the setup, showing the UHV chamber, the surrounding optical table and the atom source (2D-MOT) right under them. The compensation coils are drawn in the inset: in blue for B_x, pink for B_y and green for B_z. **(b)** Close-up on the main parts of the UHV chamber: the heart of the experiment where the atoms are manipulated is shown in beige, the ion pump and associated tubing in purple, the ion channeling and detection setup in yellow and the electrical feedthroughs in cyan. The optical access directions used to shine beams onto the atoms are illustrated with red arrows. The one coming from $+y$ is hidden behind the chamber. **(c)** Coil holders shown around the sapphire cube that hosts the heart of the experiment. The colors are the same as for the compensation coils.

(c) of that figure, and in more details in figure II.2 of the next sub-section, where we thoroughly discuss its design. The hollow sapphire cube holds various electric-field-control electrodes, designed to precisely tune the static and radio-frequency fields in the region of the experiment, at its center. The UHV chamber is equipped with several electrical feedthroughs to control the electrodes. A total of 8 windows allow optical access to the center of the UHV chamber, along 4 axes: x, y, and at angles of $\pm 45°$ in the $y-z$ plane (all drawn with red arrows in II.1 [b]). One of its sides (in $+x$) also hosts the ion detection setup, designed to be compatible with an optical access along that axis. A microwave horn antenna, not shown in the figures, is placed close to the 45° $(-y, +z)$ window to shine microwave radiation onto the atoms when needed.

A set of 3 pairs of coils allow for precise, time-resolved control of the magnetic field in the region of the atoms, at the ms scale. The coils are placed on holders secured onto the UHV chamber, and are shown in panels (b) and (c) of figure II.1. The B_x coils are positioned as close as possible to the atoms in order to create the field gradient for the magneto-optical trap and the strong directing magnetic field used to carry out the Rydberg experiments. The less critical B_y and B_z coils are placed further away from the atoms and help fine-tune the magnetic field.

II.1.2 Sapphire cube and electric-field control

The individual trapping and manipulation of the atoms, from their ground state to circular levels, takes place in the center of the hollow, custom-made sapphire structure.[1] Having dimensions of $50 \times 50 \times 55$ mm, it will from now on be simply referred to as the sapphire cube. A picture of it, attached to one of the UHV chamber flanges, is shown in figure II.2 (c). A 26×26 mm vertical opening throughout the cube allows for the loading of the atoms from below, coming from the 2D-MOT under the chamber (represented in figure II.1 [a]). Eight additional holes, drilled in the sapphire structure and aligned with the eight windows of the chamber, ensure the optical access to the atoms along the four different axes previously mentioned. The four holes along the diagonal directions in the $y-z$ plane have a diameter of 8 mm, when that of the pairs of holes along x and y is 12 mm. Two aspheric lenses are placed inside the openings of the $\pm y$ holes into the center of the cube. They are used to tightly focus the trapping beams onto the atoms and are depicted in light blue in the drawings of figure II.2.

As we have seen in the first chapter, Rydberg atoms are highly sensitive to static electric fields; a fine control of them throughout the experiments is essential to their manipulation. The inner dielectric surfaces of the cube are therefore covered with gold-plated, brass electrodes, shown in pink, yellow, blue and red in figure II.2. These ten electrodes, whose potentials can be individually set, allow for a very precise control of the electric field and its gradients in all three directions. We split the ten electrodes into four groups:

- The two electrodes along x, used to define the quantization axis when manipulating high-ℓ Rydberg states, by maintaining $\mathbf{F}$ parallel to x. Drawn in pink in figure II.2, they are called the Stark electrodes. We also use them to ionize the atoms for state-selective detection by applying high voltages to them. They each have a 6 mm diameter hole in their center to allow optical access along x.
- The two additional electrodes along the x axis, pictured in blue in the figures, which are used to cover the sapphire surface to avoid stray fields. They are called the Stark holder electrodes.
- The four electrodes placed on the $+y$ and $-y$ sides of the atoms, with tubes going up the diagonal holes in the cube and drawn in yellow in the figure: these electrodes generate the radio-frequency field needed to reach, starting from the bottom of the Rydberg manifolds, the circular states. Called the RF electrodes, they are also used to apply static fields to the region of manipulation of the atoms to finely tune the three components F_x, F_y and F_z of the electric field.
- The lens holder electrodes, placed between each aspheric lens and the sapphire structure. They maintain electrical contact with the lenses, which are made conductive thanks to an indium tin oxide coating on their surfaces. This set of

[1] Sapphire was chosen as the building material for the heart of the setup because it is both a good electrical insulator and thermal conductor: it can hold various high-voltage electrodes and dissipate the heat potentially induced by stray light from intense laser beams. This last property is crucial for a transfer of the experiment to a cryogenic setup.

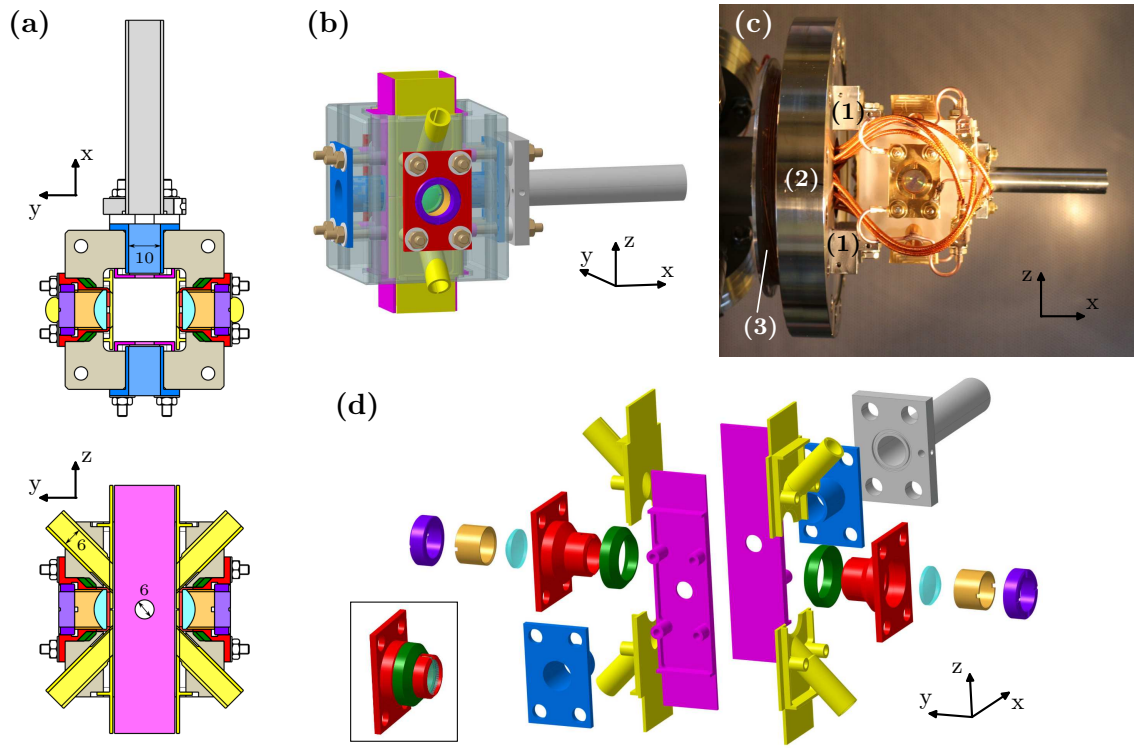

Figure II.2: Sapphire cube and its electrodes, adapted from [123]. **(a)** Views of the cube and its electrodes from the top and from the $-x$ side. **(b)** 3D rendering of the sapphire structure and electrodes. The grey tube is grounded and used to guide the ions for Rydberg state-selective detection. **(c)** Picture of the sapphire cube secured onto a flange (2) of the UHV chamber; a support for one of the B_x coils (3) is also visible. One of the aspheric lenses can be seen in the center of the image. **(d)** Exploded view of the 10 electrodes surrounding the region of the experiment: the 2 Stark electrodes responsible for the directing field F_x (pink), the 2 Stark holders (blue), the 4 RF electrodes (yellow) and the 2 lens-holding electrodes (red). The 2 aspheric lenses and their supports (pictured assembled in the inset) also appear in the panel.

electrodes adds an additional layer of control over F_y, especially to reduce its gradient.

We therefore have in this new setup an environment in which we can manipulate atoms in precisely controlled electric and magnetic fields. In appendix C, we detail how we predict, measure and calibrate the electric field in three dimensions. The electrode setup, although substantial, is designed to allow numerous optical accesses to the atoms. Among these optical paths, one is specifically designed to tightly focus the trapping beams via the two aspheric lenses placed in the sapphire structure.

II.1.3 Optical trapping setup

To trap the atoms throughout the experiments, we work with three different trapping beams:

- the tweezers: an array of tightly focused gaussian beams, designed to trap individual ground state rubidium atoms through the dipole force,
- the rearranger: a single gaussian beam whose intensity and position can be quickly tuned to move single atoms from one site to another on the tweezer lattice,
- the bottle beams ("BoBs"): an array of hollow traps, devised to trap individual Rydberg atoms via the ponderomotive force.

Optical system

All three of these trapping beams emanate from the same laser, a Toptica TA Pro system, set to 821 nm with 2 W of output power. The initial laser beam is split in three via two acousto-optic modulators (AOM). Each of these beams is sent via distinct optical fibers to the UHV chamber optical table, where they are overlapped and sent to the experiment after having been shaped separately for their respective purposes. The top inset of figure II.3 shows the arrangement used to split the laser output between the three trapping beams. If the atoms are in Rydberg states, a first AOM sends all of the laser intensity to the BoBs path, as there is no need for tweezers or the rearranger. If the atoms are in their ground state, this AOM is turned off and all the light goes to a second AOM, which splits it between the rearranger and the tweezers. Its first diffraction order is sent to the tweezers fiber, and the residual, non-diffracted light goes to the rearranger. Tuning the diffraction efficiency of this AOM changes the power balance between the tweezers and the rearranger. This scheme ensures that a maximal amount of light is always allocated to the traps independently of which ones are being used (as opposed to having power divisions of fixed ratios).

On the UHV chamber optical table, three different spatial light modulators (SLMs) shape each of the trapping beams to create the desired intensity patterns in the region of the experiment and correct for aberrations induced by the optical paths. We detail this crucial process in this section. Moreover, an acousto-optic deflector (AOD) is placed on the rearranger path. It allows to control its position and intensity over fast timescales in order to move single atoms around the tweezer lattice. We will discuss that specific part of the setup in the last section of this chapter. All of these optical elements are pictured in figure II.3, where the trapping beams are colored in green. We also show in this figure, for future reference, the other optical systems involved in the experiment, such as the magneto-optical trap beams, the Rydberg excitation lasers, the "Raman" beams and the imaging setup. After reflecting on their respective SLMs, the three trapping beams are overlapped via polarization-dependent cubes and sent into the UHV chamber and sapphire cube along the y axis. They are tightly focused by the aspheric lens (Asphericon AFL12-15-S-U-285), of focal length 16.3 mm,

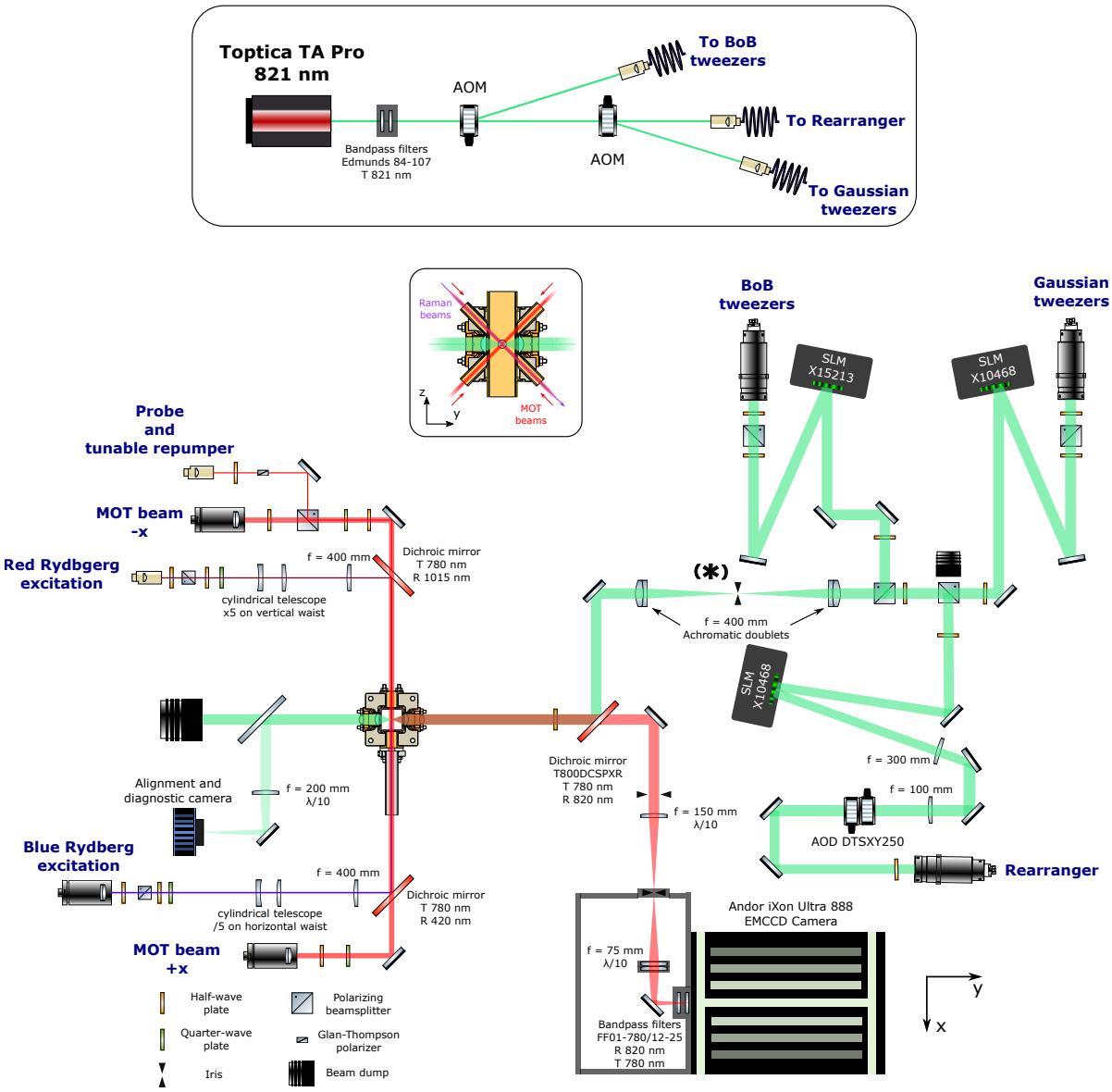

Figure II.3: Schematic view of the optical systems involved in the experiment. All of them lie on the optical table surrounding the UHV chamber. The top inset represents the scheme for power distribution between the three trapping paths. Shown in green, the trapping beams are each reflected on an SLM before being overlapped and sent into the experiment. The * symbol indicates the position where spatial filtering is carried out. We also represent here the other optical systems involved in the experiments. The cooling lasers ("MOT beams", two along x and four in the $y-z$ plane) are shown in red. The two Rydberg excitation beams, in dark red and in blue, propagate along x. The imaging system, which collects the atomic fluorescence signal and sends it to the EMCCD camera, is represented in red. Other beams, such as the "probe", "tunable repumper" and "Raman" beams also appear on the figure. The various uses of these systems are addressed throughout the rest of the text, using this figure as reference for the geometry of the system.

to create the required traps at the position of the atoms. The second identical aspheric lens then re-collimates the beams. After exiting the chamber, a small fraction of the intensity is sent to a camera for alignment and beam shaping purposes.

Spatial light modulation

The SLMs we use are Hamamatsu "liquid crystals on silicon" phase modulators, models X10468 for the tweezers and the rearranger and X15213 for the BoBs (the latter has higher resolution and is used for more complex beam shapes). Each SLM is made of a dielectric mirror covered by a matrix of independent phase modulators, that can be seen as elementary "pixels". Every single pixel has a tunable refractive index. Upon reflection on the SLM, an arbitrary discrete phase pattern, or "phase mask", is applied to the light beam. The diffraction by this phase mask is what allows us to arbitrarily shape the trapping beams. To briefly explain the SLM operation, we denote u and v the transverse coordinates in the SLM plane, $\varphi(u,v)$ the phase pattern applied (with values in $[0, 2\pi[$), and consider the light field in this plane to be that of a gaussian beam of waist w and wavelength $\lambda = 2\pi/k$. The beam, that we suppose to propagate along y as in the experiment, is subsequently focused by a lens of focal length f. The resulting field distribution then writes, close to the lens' focal plane $y = 0$, in the paraxial approximations and up to global constants [173]:

$$F(x,y,z) \propto \int e^{i\varphi(u,v) - \frac{u^2+v^2}{w^2}(1+iwky/f)} \times e^{-i\frac{k}{f}(ux+vz)} \mathrm{d}u\mathrm{d}v \tag{II.1}$$

We recognize here the Fourier transform of a function related to the phase mask. We write this function

$$f_y(u,v) = e^{i\varphi(u,v) - \frac{u^2+v^2}{w^2}(1+iwky/f)}, \tag{II.2}$$

which amounts to the transparency function of the phase mask, multiplied by the beam's gaussian profile and by a function that depends on the observation position. The field in the focal plane of the lens is then simply:

$$F(x,y,z) \propto FT\left[f_y\right]\left(\frac{kx}{f}, \frac{kz}{f}\right). \tag{II.3}$$

Creating the desired intensity profile F in the focal plane of the lens is however not as simple as applying, on the SLM, the phase mask derived from the inverse Fourier transform of F. The inverse Fourier transform of a target field would impose not only a phase, but also an amplitude distribution in the SLM plane. However, we have no control over the incoming intensity profile, as it is always that of a gaussian beam of 4-mm waist. As we will see, the procedure we implement to properly shape the traps is much more involved than that. We go over this scheme rather quickly: a more detailed discussion will be found in Y. Machu's upcoming PhD dissertation. We focus here on a single SLM as a generic example: the procedure is exactly the same for each of the three trapping beams, the only difference being the target intensity distributions that are specific to each trapping system. The process is divided into three steps, each producing a phase mask: (i) positioning and spatially filtering the

trapping beam, (ii) generating the desired trapping intensity pattern, (iii) correcting optical aberrations. The end result is the addition, modulo 2π, of the three created phase masks.

(i) Position and spatial filtering

The first step consists in getting rid, in the trapping beam, of the unwanted stray light that is not diffracted by the SLM (of imperfect diffraction efficiency). We do so with a simple grating pattern in the phase mask. In a disk-shaped region in the center of the SLM, of radius 5.5 mm and corresponding to the area of illumination (all three beams have a waist of 4 mm), we implement a vertical grating using the allowed phase modulation. Over the rest of the SLM surface, an horizontal grating is applied. The top left image of figure II.4 (a) shows such a phase mask. We also install a first focusing system before the UHV chamber, using two lenses of focal lengths 400 mm and as pictured in the region labeled with a * in figure II.3. In the focal plane of these lenses we place a small pinhole, positioned such that it only lets the desired diffracted light go through. Thanks to the grating patterns, in this focal plane the light diffracted by the vertical grating of the central region of the SLM is shifted horizontally with respect to the non-diffracted, zero-order light (always present due to the technical imperfections of the SLM), which is itself blocked by the pinhole. Moreover, the light diffracted by the edges and corners of the SLM outside of the central disk is shifted vertically and is also blocked by the pinhole. This operation allows us to remove the stray, zero-order light which could damage the intensity patterns seen by the atoms. It also restores a cylindrical symmetry around the propagation axis in spite of the rectangular SLM frame, thanks to the disk-shaped intensity selection that we call from now on the "diffracting pupil". Tuning the central grating of the pupil will also enable the fine adjustment of the traps' positions in the plane of the atoms by global shifts of the intensity pattern in the $x - z$ plane. This spatial filtering is implemented in the same manner for all three of the trapping beams.

(ii) Trapping pattern definition

The decisive point in the definition of the final phase mask is finding the SLM phase pattern that will generate the desired intensity profile seen at the atoms' position, in the focal plane of the entrance aspheric lens. To do so, we implement an adaptation of an algorithm devised by Gerchberg and Saxton [174]. Given an input intensity profile I_0 (in the SLM plane, measured from the incoming beam) and a target output pattern I_t (in the focal plane), it enables the retrieval of a phase mask that will yield the desired result. It proceeds iteratively as follows, writing $A_k e^{i\phi_k}$ the field profiles in the plane of the SLM and $B_k e^{i\psi_k}$ those in the focal plane of the focusing lens:

- initialization: the field in the SLM plane is defined as $A_0 e^{i\phi_0} = \sqrt{I_0} e^{i\phi_0}$, with ϕ_0 a random phase mask or an educated guess.
- n^{th} iteration:
  - compute the field in the focal plane $B_{n-1} e^{i\psi_{n-1}} = FT\left[\sqrt{I_0} e^{i\phi_{n-1}}\right]$,

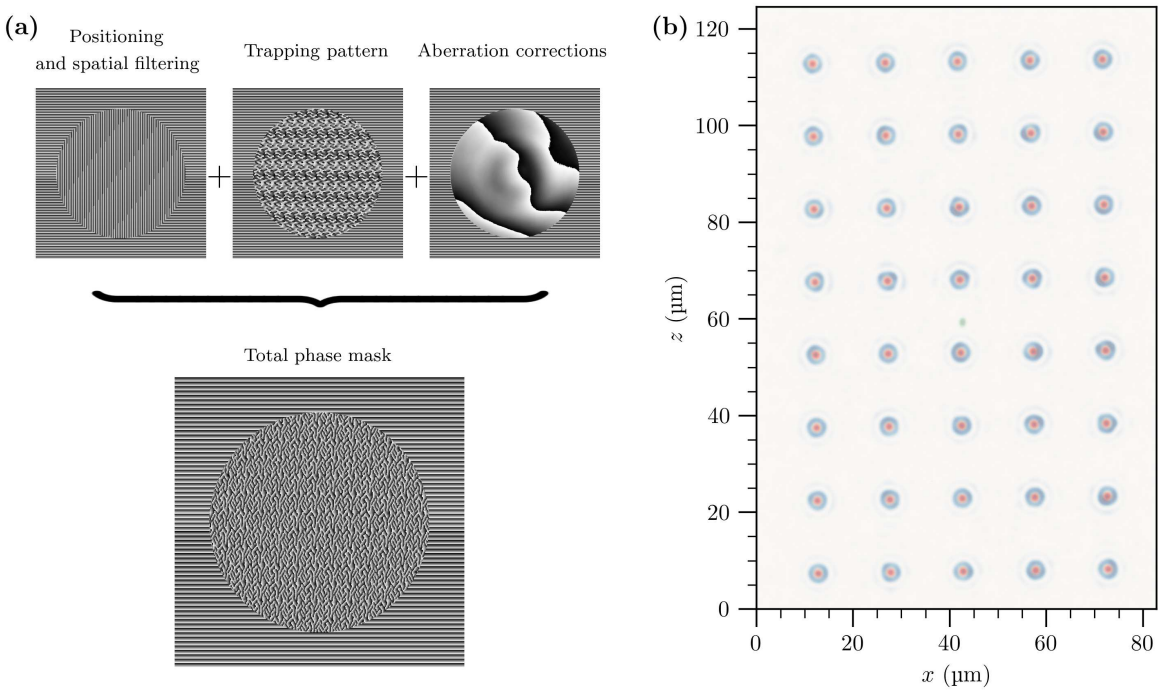

Figure II.4: **(a)** Illustration with real SLM phase profiles of the three components in the definition of the phase mask: a first phase layer made of gratings ensures spatial filtering and removes stray light (the central vertical grating is at a slight angle to fine-tune the traps position), a second layer computed from the Gerchberg-Saxton algorithm imprints the phase that will lead to the target intensity in the image plane, a third layer corrects optical aberrations. The grating used to discard the light hitting the edges of the SLM is always present. The addition modulo 2π of the three layers yields the final phase mask. **(b)** Real image of the three trapping beams as they typically exist in the experiment: BoBs (blue), tweezers (red) and rearranger (green, center of the image). The image is taken on the diagnostics camera after re-focusing at the exit of the UHV chamber but the distance scale shown is that of the corresponding lattices in the experiment at the position of the atoms.

  - replace the obtained amplitude with the target intensity profile: $B_{n-1}e^{i\psi_{n-1}} \rightarrow \sqrt{I_t}e^{i\psi_{n-1}}$,
  - derive the corresponding field in the SLM plane vie the inverse Fourier transform: $A_n e^{i\phi_n} = FT^{-1}\left[\sqrt{I_t}e^{i\psi_{n-1}}\right]$,
  - replace the SLM field amplitude with the imposed intensity: $A_n e^{i\phi_n} \rightarrow \sqrt{I_0}e^{i\phi_n}$.

- conclusion: stop the iterations after a fixed number of loops or once B_n is close enough to the target $\sqrt{I_t}$. We keep ϕ_n as the phase mask to apply on the SLM to get the target trapping pattern in the focal plane of the focusing lens.

The resulting phase-mask, an example of which is given in figure II.4 (a) (center image of top row), is then simply added modulo 2π to the diffracting pupil. We carry

out this algorithmic procedure to create arrays of tweezers with arbitrary geometries. To make sure that we implement homogeneous lattices, the procedure is run a first time, with an array of identical tweezers as the target. We then measure the power of each tweezer in the result, using the diagnostics camera. The resulting power distribution shows some fluctuations across the array. We then re-run the algorithm, this time taking as the target the array of tweezers with single-site intensities adjusted to cancel out the measured spatial variations. The result is now an array with very homogeneous single-site powers, with deviations across the lattice of the order of 0.4% around an average value. The number of traps we can effectively implement is only limited by the trade-off between the available laser power and the power per site required to efficiently trap ground-state atoms.

To create arrays of hollow beams (BoBs) that trap individual Rydberg atoms, an additional ingredient is needed. Considering a target geometry for a lattice of BoBs, we run the Gerchberg-Saxton algorithm as if wanting to create the same array but with tweezers. We then take the output phase mask and add to it a π phase-shift over a disk of radius 3.35 mm centered on the diffracting pupil. We recall that the beam waist is 4 mm and the diffracting pupil has a radius of 5.5 mm. Thanks to the π phase shift applied to the inner part of the beam only, each site of the resulting lattice will be a hollow beam instead of a simple tweezer. Indeed, in the focal plane, the inner and outer parts of each single trap of the lattice interfere destructively, producing a small region of space devoid of any intensity surrounded by light in all directions [175]. This distribution corresponds to the geometry required to trap Rydberg atoms through the ponderomotive force, as discussed in the first chapter. The precise geometry of the bottle beam trap will be discussed further down when we address the trapping of individual circular atoms. Concerning the rearranger, we do not need to run the Gerchberg-Saxton algorithm to conceive its trap-shaping phase mask, as it consists in a single elementary tweezer. For that beam only, this step is skipped in the phase mask definition process.

Figure II.4 (b) shows the results of this process with an image of the three overlapped trapping systems, taken on the diagnostics camera after re-focusing. The BoB and tweezer lattices have the same 5×8 geometry. The former are shown in blue and the latter in red. The axes are scaled to show the distances as they appear in the UHV chamber, in the focal plane of the aspheric lens. Let us mention that, although meticulously calibrated, a minor uncertainty is not impossible in the optical system's magnification. In other words, distances in the lattice could be very slightly smaller or bigger than we program them to be. This remark will become important in the exploration of the circular-circular interactions.

(iii) Aberration correction

The purpose of the third and final layer of phase definition is to correct optical aberrations induced by the imperfect optical paths. Without any correction, the traps created following the Gerchberg-Saxton procedure would have many defects and efficient trapping of the atoms, especially in the BoBs, would be arduous. This step is divided in two components: the aberrations of the UHV components (its windows and the aspheric lenses), and the aberrations of the rest of the optical path (various mirrors, lenses and wave-plates).

The aberrations induced by the chamber's windows and by the aspheric lenses were all measured prior to their definitive installation in the setup. By comparing the wavefront of a beam before and after going through each of these components, we obtained the transverse phase pattern that each of them induces. Adding the opposite of that phase to the SLM phase mask then cancels the corresponding aberrations. Thanks to these measurements, we are able to correct the aberrations associated either to the entrance into the setup ($+y$ window and $+y$ aspheric lens) or to the full crossing of the UHV chamber (both windows and both aspheric lenses), which is useful to properly reconstruct the expected image intensity pattern on the diagnostics camera.

To counter the aberrations created by all the other optical elements, another algorithmic optimization routine is run *in situ*, using the diagnostics camera. Roughly speaking, it consists in a 3-dimensional version of the Gerchberg-Saxton algorithm aiming for a single perfect gaussian beam. Fresnel lenses are added to the SLM phase masks to reconstruct the beam profile at various positions along its optical axis. The Gerchberg-Saxton algorithm is then run for each of these positions, so as to obtain a perfect gaussian profile both in the transverse and longitudinal planes of the beam. Once achieved, the resulting phase mask is a correction for all the aberrations induced by the optical path and can be added to the diffracting pupil and trap-shaping layers to create the final phase mask (see figure II.4 [a]). This sensitive procedure is run once every couple of months and whenever one of the beam gets slightly misaligned in the optical setup. More details regarding its principle will be discussed in Yohann Machu's PhD thesis, as he is the one who devised the process. The homogeneity, both in shape and in intensity, of the traps in the image of figure II.4 shows that the aberration correction is efficient.

The three steps described here allow us to create state-of-the art trap arrays. We are able to generate ensembles of traps highly homogeneous both in depth and shape, over an area of ~ 100 µm $\times 100$ µm in the focal plane of the aspheric lens. The quality of the produced arrays will be analyzed in the next section of this chapter through atomic signal measurements.

II.2 Arrays of ultra-cold atoms in optical tweezers

Now that we covered the main technical components of the setup, we present the preparation and characterization of the trapped ground-state atoms. This is the first step towards the manipulation of circular states. In this next section, we describe the experimental process implemented to create arrays of ultra-cold rubidium atoms individually trapped in optical tweezers. We start by discussing the sequence designed to load the traps with single atoms, cool them and image the resulting array, filled in a probabilistic manner. The optical detection and subsequent data analysis method are detailed here, as they are central to the measurements presented throughout this work. Through atomic signals, we then characterize the individual traps by measuring their depths and waists. We also present here some properties of the trapped ground-state atoms, namely their temperature and lifetime in the tweezers.

II.2.1 Atomic preparation: trapping, cooling and imaging

The initial preparation of trapped ground-state rubidium-87 atoms relies on usual notions and experimental techniques: magneto-optical trapping and optical molasses are used to cool them down, while their trapping in optical tweezers is based on the dipole force. Without going over the theoretical principles behind these standard concepts and mechanisms [176], we describe here their specific use and implementation in our setup for the purpose of creating arrays of individual, ultra-cold atoms, prepared for Rydberg excitation. All the relevant laser systems and their locking scheme are described in appendix D. I personally oversaw the installation of the Rydberg lasers, the design and implementation of the locking schemes and the overall alignment and operation of most laser systems.

Optical trapping in individual tweezers

The dipole force is the phenomenon that allows the trapping of ground-state rubidium atoms in optical tweezers [177]. Each tweezer of the array, created by a specific SLM phase mask and corrected for aberrations (cf. subsection II.1.3), is a tightly-focused gaussian beam. We use linearly-polarized light at 821 nm to create the traps. Each tweezer has a power of approximately 2 mW and an estimated 1.2 µm waist.[2] With these parameters, the light is red-detuned with respect to the $|5S_{1/2}\rangle \rightarrow |5P_{1/2}\rangle$ and $|5S_{1/2}\rangle \rightarrow |5P_{3/2}\rangle$ transitions (at respectively 795 and 780 nm) and in a negligible saturation regime. Accordingly, the intensity pattern $I(\mathbf{r})$ of each tweezer creates an attractive well $V(\mathbf{r}) = \beta_0 I(\mathbf{r})$ for ground-state atoms, where they can be trapped in the region of highest intensity [177]. The energy scale can be computed via second-order perturbation theory [95]:

$$\beta_0 = -18.2 \text{ MHz}/(\text{mW}\,\mu\text{m}^{-2}). \tag{II.4}$$

This attractive well amounts to a negative light-shift induced on $|5S_{1/2}\rangle$, almost independently of its hyperfine sub-levels. For one of the experiments discussed further

[2] These estimations, derived from the laser power and designed phase masks, will be quantitatively characterized later through atomic measurements.

down, we also make use of the light-shift induced on $|5P_{3/2}, F' = 2\rangle$, for which we have the positive coefficient $\beta_1 = 5.7$ MHz/(mW µm^{-2}). The total light-shift on the $|5S_{1/2}\rangle \rightarrow |5P_{3/2}, F' = 2\rangle$ is then $\beta_1 - \beta_0 = 23.9$ MHz/(mW µm^{-2}).

Thanks to their extremely small trapping volume, each tweezer implements the collisional blockade mechanism [178]. A combination of effects due to the cooling light and reduced trapping volumes allows to trap at most a single ground-state atom at the focus of each tweezer, where the intensity is highest [19].

Experimental sequence

In each repetition of a typical experimental sequence, the 2D-MOT is activated during 10 ms. The atoms sent upwards during this delay are collected 50 cm above, in the central region of the sapphire cube, by a tri-dimensional magneto-optical trap (3D-MOT) [176, 179]. The general arrangement of these elements is shown in figure II.1 (a). The 3D-MOT is made of three pairs of counter-propagating, circularly-polarized cooling beams: one pair along the x axis and two along the diagonal directions in the $y-z$ plane (see figure II.1 [b] to visualize the axes involved). The three pairs of coils around the center of the UHV chamber (figure II.1 [c]) create a magnetic quadrupole along x, with the B_x coils set in an anti-Helmholtz configuration. B_y and B_z help finely adjust the position of the field zero at the center of the quadrupole. The cooling beams are red-detuned by 14.8 MHz with respect to the natural $|5S_{1/2}, F = 2\rangle \rightarrow |5P_{3/2}, F' = 3\rangle$ cycling transition. This amounts to a -2.5Γ detuning, $\Gamma = 2\pi \times 6.06$ MHz being the natural linewidth of the transition [138]. The intensity in each beam is ~ 10 mW/cm^2, when the saturation intensity of the transition is $I_{sat} = 3.5$ mW/cm^2 [138]. These parameters are illustrated in the first part of figure II.5 (a). During the MOT cooling process, atoms are sometimes sent to $|5P_{3/2}, F' = 2\rangle$ and from there can then decay to the dark state $|5S_{1/2}, F = 1\rangle$. The atoms that do end up in this dark state are pumped back to $|5P_{3/2}, F' = 2\rangle$ by a "repumper" laser, set on resonance with this transition and co-propagating with four of the six cooling beams. Figure II.5 (b) depicts the energy levels involved in the cooling mechanism of the 3D-MOT. This stage lasts for about 150 ms in each repetition of the experimental sequence. It creates, from the rising beam of rubidium, a cold atomic cloud positioned at the center of the sapphire cube.

The optical tweezers are turned on throughout the 3D-MOT stage. As stated above, some of the optical traps get filled with a single atom during this initial cooling period. The trapped atoms experience a large light-shift of approximately +30 MHz (i.e., around 5 Γ) on the cycling transition: the MOT cooling beams become ineffective on these atoms. After the 150 ms MOT duration, we switch the MOT frequency during ~ 5 ms to a blue-detuned value of $+0.5\Gamma$ with respect to the cycling transition of the free atoms, which pushes them away from the region of the trapping array without affecting the already trapped atoms. We end up at this point with an array of tweezers partially filled with single atoms and no residual atomic cloud around them.

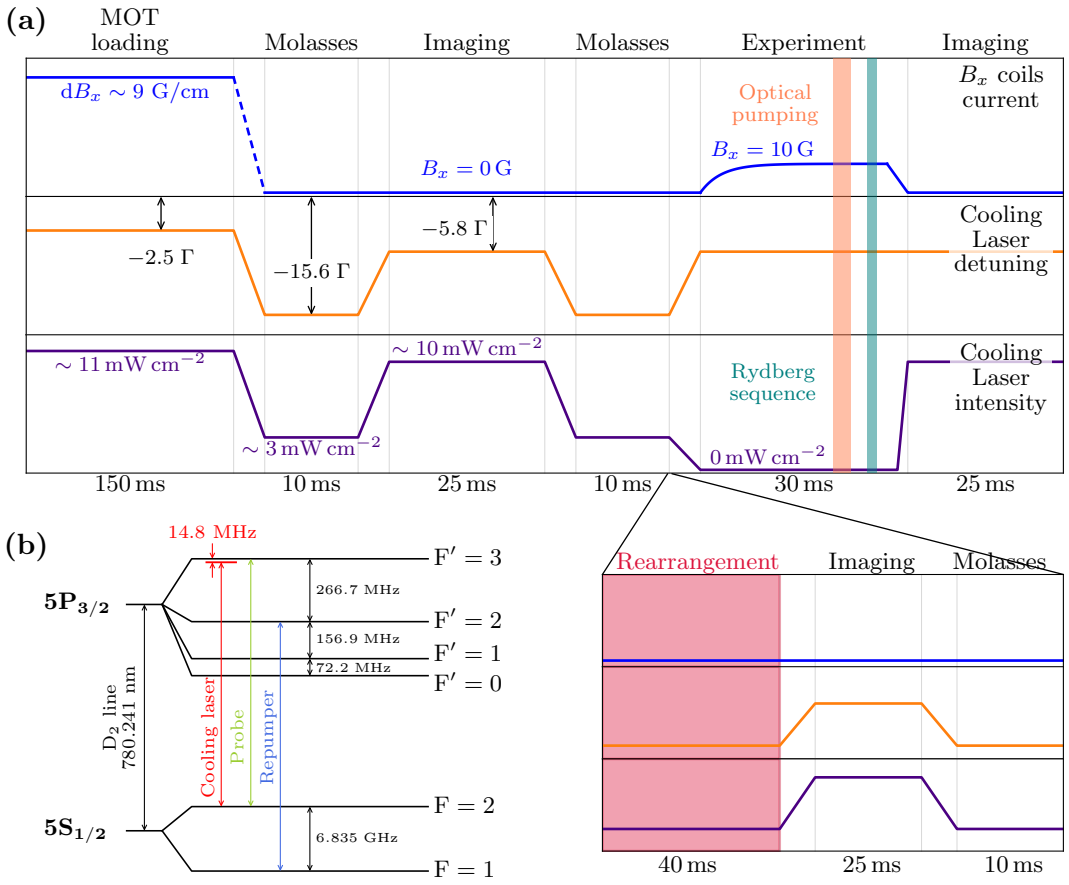

Figure II.5: Preparation of trapped ultracold atoms. **(a)** Schematic representation of the experimental steps implemented to prepare arrays of trapped, ultracold ground state atoms. The trapping beams are on throughout the sequence. The magnetic field is switched from a quadrupole configuration for the MOT to a Helmholtz one for the molasses, imaging and experiment stages. The cooling laser detuning is shown with respect to the natural $|F = 2\rangle \rightarrow |F' = 3\rangle$ transition. Importantly, the trapped atoms experience a $\sim$ 30 MHz light-shift on this transition. This value, which amounts to $\sim 5\Gamma$, should be added to the indicated detuning in the molasses and imaging phases to understand the real action of the cooling beams on the trapped atoms. The inset shows the steps we can add to deterministically rearrange the array (the details of the rearrangement itself are not depicted here). **(b)** Rubidium 87 atomic levels (D_2 line) involved in the cooling and imaging mechanisms. The detuning of the cooling beams shown here is that of the MOT.

Further manipulations are then still required to fully prepare the trapped atoms for Rydberg experiments. The complete sequence subsequently implemented (and including the initial MOT) is schematically drawn in figure II.5 (a). An optical molasses stage is carried out to further cool the trapped atoms [176, 180]: the detuning of the cooling beams is brought to 15.6Γ and their power is decreased to 3 mW/cm^2, while the B_x coils are switched to a Helmholtz configuration (by inverting the current po-

larity in one of them) to cancel the magnetic field in the whole region of the atoms. A repumping beam of adjustable frequency, the "tunable repumper" (see fig. II.3) is used to avoid loosing atoms in the dark state during the optical molasses. A first pre-experiment, reference image of the trapped atoms is then taken. To do so, the detuning of the cooling beams is reduced to -0.8 MHz for the trapped atoms, and their power increased so as to make the trapped atoms fluoresce. Some of the photons scattered by the atoms are collected through the $+y$ aspheric lens. With a numerical aperture of 0.36, the fraction of collected photons is approximately 3% of all the scattered light. These photons are sent to an Andor iXon EMCCD camera following the optical path shown in figure II.3. The camera records the fluorescence intensity and converts it to photon numbers for each pixel. Examples of recorded images are shown further down in figure II.6 (a), when presenting the data-processing protocol. A second stage of optical molasses is then carried out after the first image acquisition to re-cool the atoms.

The cooling parameters for the imaging step, along with those of the optical molasses, are optimized through atomic measurements. We try to get a good fluorescence signal while minimizing their temperature resulting from these manipulations. The atomic temperature measurement will be detailed in the next section of this chapter.

The preparation of the trapped atoms ends with a final step of optical pumping [181]. Its purpose is to prepare the atoms in the hyperfine sub-level $|5S_{1/2}, F = 2, m_F = +2\rangle$ for later optical excitation to Rydberg levels in an efficient manner. To do so, the magnetic field is first ramped up to 10 G to mitigate the light-shifts and decoherence induced by the spatially-varying polarization within each tweezer [182]. The trapped atoms are then illuminated during 400 µs by two beams: the "tunable repumper" and the "probe" beam. They co-propagate along x (see fig. II.3 for their position in the optical setup) and are both σ^+-polarized with respect to the applied magnetic field. Their intensities are 0.02 mW.cm^{-2} for the "probe" and 200 mW.cm^{-2} for the "tunable repumper". Their frequencies are set on resonance, for the trapped atoms, with the $F = 2 \rightarrow F' = 3$ ("probe") and $F = 1 \rightarrow F' = 2$ ("tunable repumper") transitions. Their tunable frequencies allow us to adapt this process to various trapping powers. During this procedure, with each $F = 2 \rightarrow F' = 3$ cycle, the hyperfine m_F sub-level occupied by the atom grows approximately by one, via the σ^+ excitation from the probe beam and random spontaneous σ^-, π or σ^+ de-excitation. The "tunable repumper" avoids the loss of atoms in the dark state $F = 1$. We characterize the efficiency of this process through a 2-photon Raman spectroscopy, which probes the population in the $F = 2$ sub-levels. Its principle is detailed in appendix E. Through this characterization, we measure an optical pumping efficiency of $\eta_{\mathrm{OP}} = 0.97 \pm 0.01$ in optimal conditions. In other words, at the end of the process, only 3% of the atoms remain in states with $m_F < 2$. However, this level of performance is arduous to maintain on a day-to-day basis in the experiment. The tweezers exhibit slow intensity drifts, which detune the transition frequencies over time. Moreover, the very low "probe" power is subject to fluctuations. The re-optimization of these parameters is unfortunately too time-consuming to be conducted daily, and the optical pumping efficiency is closer to

90% in typical experimental runs.

The optical pumping concludes the preparation of the trapped atoms for actual experiments, which cover a wide range of situations discussed in dedicated parts of this work. We can manipulate the ground state atoms or their traps for various diagnostics, or bring them to Rydberg and circular states for other purposes. A second, post-experiment image is finally taken after these manipulations: its comparison with the first image will constitute the results of the investigations.

Let us only mention for now that additional steps can be added to this sequence right before the optical pumping to rearrange the array in a deterministic manner, as shown in the inset of figure II.5. Once the rearrangement of the atoms is performed, another image of the filled target array is taken to be the pre-experiment reference and an optical molasses stage re-cools the atoms. The full rearrangement procedure and its dedicated hardware and software, the most recent additions to the setup, will be detailed in the last section of this chapter.

Imaging and data processing

For clarity in further discussions, we wrap up this atomic preparation section by describing the digitization of the fluorescence signals for data analysis purposes. Examples of images of a loaded array (7×6 sites) are presented in figure II.6 (a). The axes of the setup with respect to the array are indicated in the first image. The optical components used to collect the fluorescence induce a slight angle in the imaging optical path, which makes the orientation appear tilted on the recorded images.

By averaging together many images of the trapped atoms, we can precisely define the locations of the trapping sites in a given array, and therefore define a "region of interest" (ROI) for each trap. These ROIs are squares of 3 pixels width, over which we integrate the recorded photon number for each acquired image. Once every day, before proceeding with actual experiments, we acquire a large number (typically 1000) of images of the loaded, cooled array. We then plot the distribution of each integrated ROI signal over the many frames in the form of histograms, as shown in figure II.6 (b). In each ROI histogram, the horizontal axis corresponds to the recorded photon numbers while the vertical axis is the frequency of such occurrences, over the series of acquired images and in this ROI only. Each histogram displays two clearly separated peaks: the background signal, when no atom is in the trap (photon number around 50), and the fluorescence signal, when an atom is in the trap (photon number around 250). We then fit a sum of two gaussian peaks on each histogram. For a site i, the amplitudes ($A_b^{(i)}$ for the background and $A_f^{(i)}$ for the fluorescence) and centers ($\mu_b^{(i)}$ and $\mu_f^{(i)}$) of both peaks allow us to define two key quantities:

- $p_i = A_f^{(i)}/(A_b^{(i)} + A_f^{(i)})$, the loading probability of the site, which we assimilate with the fraction of the total signal corresponding to the fluorescence peak,
- $t_i = 0.55\mu_b^{(i)} + 0.45\mu_f^{(i)}$, the threshold that will be used to determine, for a single

image and in real time, whether or not an atom is present in site i. If, in a given image, the recorded number of photons in the ROI is lower than t_i, then no atom is trapped. If it is higher, then an atom is present. This threshold is empirically defined and shifted towards the fluorescence peak, in order to reduce the number of false positive events in the "atom" and "no atom" discrimination.

The MOT, molasses and imaging parameters are chosen to maximize all p_i (for a good loading of the array) and $\mu_f^{(i)} - \mu_b^{(i)}$ (for a good discrimination fluorescence signal), while keeping the atomic temperature as low as possible. In our standard experimental conditions, we get an average loading probability per site between 60 and 65%, with deviations from this value over the lattice of the order of 1%. We therefore have state-of-the-art loading of the lattice (independently of its size), and this loading is very homogeneous across the array.

We use the thresholds to discriminate the "atom" and "no atom" events in each site for two different purposes:

- For data analysis: to extract information from the optical measurements, we compare, for each repetition of the full sequence, the pre- and post-experiment images. Figure II.6 (c) illustrates this process: using the thresholds t_i, each of the two frames is converted into a binary matrix representing the filling of the array, before and after conducting the experiment. The comparison between these two matrices yields four possible outcomes for each site (see fig. II.6 (c) for an example):
  - *null* event: no atom in either frame,
  - *appearance* event: no atom in the first frame and an atom in the second frame (rare event caused by some residual background atoms, occurring typically with a probability of less than 0.1% in each site),
  - *loss* event: an atom in the first frame but no atom in the second frame,
  - *recapture* event: an atom in both frames.

  Computing statistics on these events over many repetitions of a sequence provides the desired conclusions on the experiments carried out. We obtain loss and recapture probabilities for each site of the array, most often as a function of a scanned parameter.

- For the rearrangement: when implementing deterministic rearrangement of the atoms, the initial image of the randomly filled array is processed by the acquisition software, in real time and using the thresholds, so as to determine how the atoms should be moved on the lattice to reach the target geometry.

I personally designed and coded the acquisition software that controls the camera, acquires the images, defines the thresholds and analyses the optical data accordingly. It also comprises, as we will see later, the rearrangement module which computes in real time the movements to implement and controls the hardware that executes them.

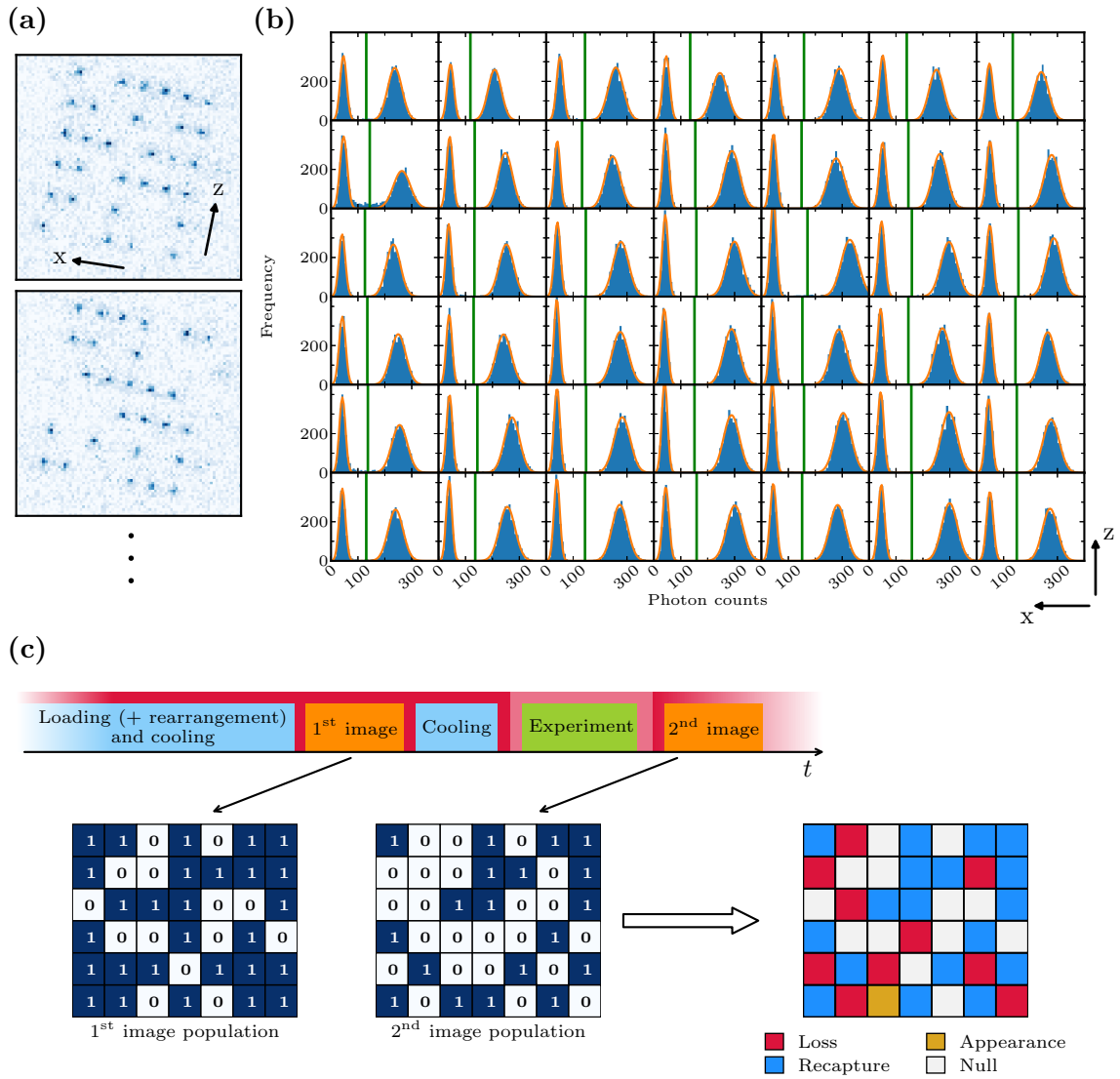

Figure II.6: Image processing for binarization of the optical signal. **(a)** Two frames of a series of images acquired for the calibration of the digitization process. **(b)** Histograms of the recorded photon numbers in each region of interest, onto which we fit two gaussian peaks. The thresholds defined accordingly are plotted as vertical green lines. **(c)** Illustration of the image binarization for data analysis. In the representation of the sequence, the red band represents the activation of the optical tweezers: its color is dimmed during the experiment as the sequence can involve turning the tweezers off. The comparison between the pre- and post-experiment images yields one of four events for each site: loss of the atom (red), recapture (blue), appearance of an atom (orange) and *null*.

It only takes a few ms to retrieve the image from the camera and convert it to a digital filling matrix.

With this overview of the fundamental steps of the atomic preparation in mind, we can move on to the description of the experimental investigations *per se*. From now on, we will focus on the "experiment" part of the sequence (shown in green in figure II.6 [c]) and on its results derived from the data treatment process. Let us address here the notations that will be used throughout the rest of the text. We take for example a sequence designed to measure a quantity X, either in each site or over the whole array. The measurement yields a dataset d_i for each site i (most often the recapture probability as a function of a scanned parameter). Two data analysis procedures are then possible. On the one hand, to get the site-resolved result, we can extract from each dataset the desired quantity X_i. The spatial average of these results is then written $\langle X_i \rangle$, and its error bar refers to spatial fluctuations of X over the array. On the other hand, if we are interested in a global estimation of X, we can first average the individual datasets together to obtain what we write $\overline{d}$. From this average data, we can then extract the mean quantity of interest, written $\overline{X}$. Its error bar refers, in this case, to the error in the estimation of $\overline{X}$ from $\overline{d}$, via fitting routines or numerical computations and simulations.

II.2.2 Characterization of the tweezers and trapped atoms

We present here the various measurements we carried out to fully characterize the properties of both the gaussian tweezers array and of the individual trapped atoms. In all the experiments described in this section, the preparation sequence is implemented as previously discussed, we do not conduct any rearrangement, and the outcome of the manipulations is the recapture probability in each site.

Tweezer characteristics

As a gaussian beam, each tweezer i is fully characterized by two parameters: its power P_i and its waist w_i. To access these quantities and assess the quality and homogeneity of the array, we measure the tweezers peak intensities I_i and transverse trapping frequencies ν_i. Assuming that the traps have perfect gaussian profiles[3], all these quantities are related as follows [177]:

$$w_i = \sqrt{\frac{h\beta_0 I_i}{\pi^2 M \nu_i^2}}, \quad P_i = \frac{\pi}{2} I_i w_i^2, \tag{II.5}$$

where M is rubidium 87's mass, h is the Planck constant and β_0 the intensity-energy conversion coefficient previously introduced in equation (II.4). We will compute the traps properties in one of the arrays used for our Rydberg experiments and shown in II.6 (a): a lattice of 7×6 sites, of dimensions 70 µm $\times$ 60 µm.

To obtain the peak intensity of each trap, we perform a spectroscopic measurement on the $|5S_{1/2}, F = 1\rangle \rightarrow |5P_{3/2}, F' = 2\rangle$ transition. The experimental sequence, its

[3]The quality of the aberration correction process ensures that the traps differ very little from perfect gaussian beams.

corresponding level evolution and its results are presented in figure II.7 (a). Once the atomic preparation is done and a pre-experiment image has been acquired, the manipulation of the trapped atoms goes as follows:

- We apply the cooling beams, without the repumper, during 20 ms, to pump the atoms to $F = 1$, so that they are all initialized in $|5S_{1/2}, F = 1\rangle$. This initialization is not shown in the figure, where we focused on the following steps.
- A repumping pulse of 8 µs duration is applied, using the "tunable repumper", propagating along x (see figure II.3) and whose frequency is scanned. We run this experiment with the traps either on or off during this pulse. When they are off, the pulse effectively repumps the atoms into $F = 2$ when it is at resonance with the natural $F = 1 \rightarrow F' = 2$ transition frequency. When the traps are on during the pulse, the atoms are repumped in $F = 2$ only when the laser is at a higher frequency, because of the light-shift induced on the $F = 1 \rightarrow F' = 2$ transition by the traps ($\beta_0 = 3.877$ MHz/(mW µm^{-2})).
- A "kick" pulse of 4 µs is applied, with the traps off, using the "probe" beam (see figure II.3) resonant on the $F = 2 \rightarrow F' = 3$ (non light-shifted) transition. Two possibilities then arise. If the atoms had been repumped into $F = 2$, this pulse kicks them away and they are not recaptured when we turn the traps back on. If the atoms had not been repumped into $F = 2$, the "kick" pulse has no effect on them, they do not move away and are recaptured when the traps are turned back on.

We plot in figure II.7 (b) the recapture probability as a function of the "tunable repumper" frequency, averaged over all the sites and in the two cases: tweezers on or off during the repumping pulse. The frequency origin is set at the center of the resonance measured with the traps off. The position of the line in the "traps on" case indicates the average light-shift exerted by the traps on the repumping transition. We also plot in this graph the Lorentzian fit of the averaged data. The "traps on" line is wider than the "traps off" one because it was measured with a slightly more powerful kick pulse. By fitting the spectrum obtained for each ROI, we can compute the light-shift and therefore the peak intensity of each trap, as illustrated in the spatial map (mosaic) of the same figure, which matches the actual geometry of the array. We therefore get the precise intensity distribution over the traps of the lattice. The spatial average of the intensity, which we can also write in terms of trap depths U_i, is:

$$\langle I_i \rangle = 1.07 \pm 0.05 \text{ mW}\mu\text{m}^{-2}, \quad \langle U_i \rangle = 1220 \pm 62 \text{ µK}. \tag{II.6}$$

We recall that the error estimations presented here refer to the spatial distribution of the results across the array. Although two deficient sites clearly differ from this average value and indicate some local defects, we have a pretty homogeneous array intensity-wise, with only a 5% spread in this distribution over the whole lattice. This is not as good as the power dispersion of 0.4% mentioned in the description of the phase mask design, indicating that the system was in need of some slight aberration correction at the time of this measurement.

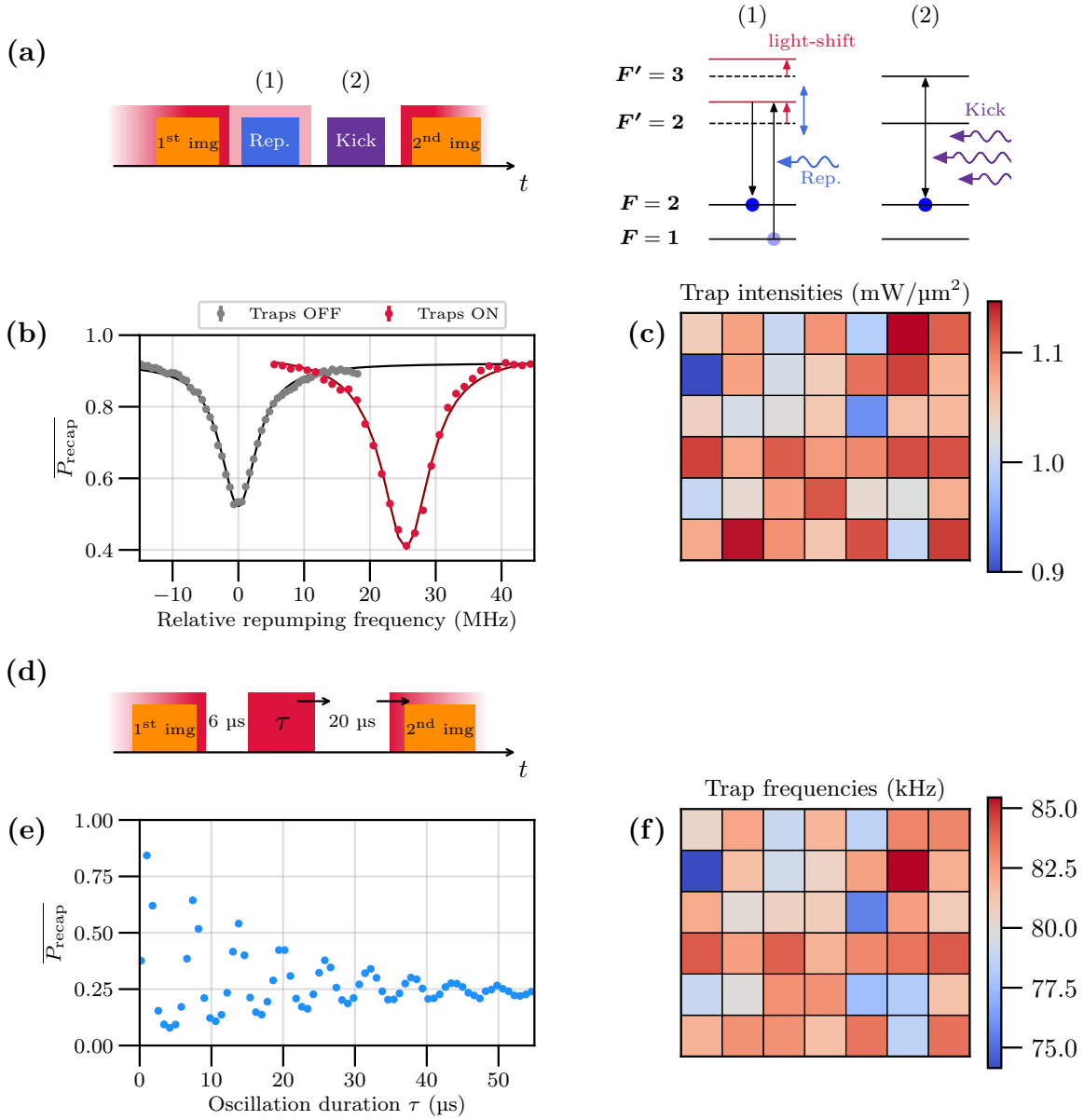

Figure II.7: Tweezer characterization. **(a)** Sequence of events and level evolution. The tweezer activation in shown in red, with the traps ON or OFF (dimmed red part in the experimental sequence) during the repumper pulse to measure the light-shift induced by each trap on the $F = 1 \rightarrow F' = 2$ transition. The fading red in the sequence indicates links with previous (preparation) and subsequent (re-initialization) manipulations of the trapped atoms. **(b)** Recapture probability averaged over all sites, with and without the tweezers, and fitted with Lorentzian peaks. The averaged data yields the mean intensity $\overline{I} = 1.065 \pm 0.003$ mW/μm². **(c)** Site-by-site result of peak intensity for each trap. **(d)** Release-recapture experiment to measure the transverse trapping frequencies of the tweezers. **(e)** Averaged signal, displaying oscillations at 166 KHz. **(f)** Site-resolved transverse trapping frequencies.

The measurement of the trapping frequencies relies on a different experiment and is shown in part (d) of figure II.7. It consists in a "release-recapture" experiment:

- The atoms are released a first time for 6 µs. Due to their thermal velocity, atoms move slightly away from the center of each trapping site.
- We turn the traps back on for a variable duration τ. The atoms are recaptured but now oscillate within their traps, all in sync, since they had moved away from their centers.
- The traps are turned off a second time, for 20 µs, which probes the atoms' oscillations. The instant at which we open the traps this second time varies according to τ. If it occurs as the atoms are moving quickly in the middle of their traps (high kinetic energy, low potential energy), the fast momentum they have will prevent recapture when turning the traps back on after 20 µs of free evolution. If the traps extinction happens when the atoms are slower but further away from the traps centers (low kinetic energy but high potential energy), the recapture probability will be high after the 20 µs extinction, as they won't have enough momentum to move away from the trapping region. The end result is a periodic evolution of the recapture probability, as a function of τ, at twice the trapping frequency. Indeed, recapture spikes up when this second trap extinction happens as atoms are at both ends of their oscillations in the traps.

The recapture probability, averaged over all 42 sites, is plotted in the lower left part of figure II.7 (e). Although technically not sinusoidal, a damped sine fit of each site data provides its trapping frequency with good accuracy. Individual site results are given in the mosaic spatial map (f), which shows the distribution of trapping frequencies across the array. The average value is

$$\langle \nu_i \rangle = 81.3 \pm 2.3 \text{ kHz}. \tag{II.7}$$

Again, we have a very homogeneous distribution over the whole array: apart from the same outliers as in the intensity distribution, all traps have the same transverse trapping frequency, up to 3% differences.

From these two measurements, we can now recover the distributions of the traps' powers and waists across the array, according to equation (II.5):

$$\langle P_i \rangle = 2.3 \pm 0.1 \text{ mW}, \quad \langle w_i \rangle = 1.16 \pm 0.01 \text{ µm}. \tag{II.8}$$

The uniformity of these distributions confirms the efficiency of the array creation and aberration-correction procedures. We are able to create very homogeneous gaussian traps over the a 100 µm×100 µm area in the field of the aspheric lenses. This confirms, in a quantitative manner, the expectations of section II.1.3 on the optical trapping setup and the design of the arrays.

Atomic characteristics

The two main properties of the trapped atoms we can easily access are their lifetime and temperature. Again, these measurements are conducted after the standard loading and cooling sequence and the results are derived from the average recapture probability in each site, computed from the images.

The measurement of the atoms lifetime in the tweezers is straightforward. We scan the delay between the pre- and post-experiment image acquisitions, while keeping the tweezers on in-between. We then compute the survival probability of the atoms as a function of the delay. To reduce the heating of the atoms due to their scattering of the trapping light and to potential traps fluctuations in intensity and position, we apply the cooling beams (and static repumper) in their molasses configuration during the waiting delay. This basic sequence is shown in figure II.8, where we also plot the survival probability, averaged over all of the sites, as a function of the delay. We fit the averaged data with a simple exponential decay model, which yields the mean atomic lifetime:

$$\overline{\tau_{\mathrm{at}}} = 12.6 \pm 0.2 \text{ s}. \tag{II.9}$$

The indicated error refers to that of the fit of the average data, and not to variations over the array. Individual site results (not shown here) do not display any significant heterogeneity. This simple model accounts for losses over time due to collisions with residual, untrapped atoms surrounding the array, which occur with a rate $1/\tau_{\mathrm{at}}$. The agreement between the experimental data and the fit is not perfect: a more refined analysis, taking into account the possibility of loading empty traps with residual background atoms during the waiting delay, can be carried out to explain the deviations from a basic exponential decay [123]. This result is nonetheless satisfactory: the qualitative estimation of the lifetime τ_{at} indicates low losses at the sub-second timescales over which we want to manipulate the atoms. Indeed, the estimated lifetime for the full array of N atoms is $\tau_{\mathrm{array}} = \overline{\tau_{\mathrm{at}}}/N$. In a 100-site array filled with around 50 atoms, the first loss will occur after 240 ms on average. We will make use of such estimations when discussing the success rates of the rearranging procedure, which is carried out in a fraction of a second.

A more sensitive measurement, conducted daily in our setup, is that of the atomic temperature. The experimental sequence consists in a simple release-recapture process, where we release the atoms by turning the tweezers off for a variable delay τ, as shown in figure II.8 (b). We then compute, over many repetitions and for each site i, the recapture probability $p^{(i)}_{\mathrm{recap}}(\tau)$. The higher the recapture, the lower the atomic temperature: cold atoms have a low kinetic energy and therefore escape less during the opening of the traps. The recapture probability, averaged over all sites, is plotted in the lower part of the panel.

To extract the value of the temperature from the data, we carry out numerical Monte-Carlo simulations of the evolution. Given a trap depth and waist (we use the measured values of figure II.7), we simulate the release-recapture evolution, as

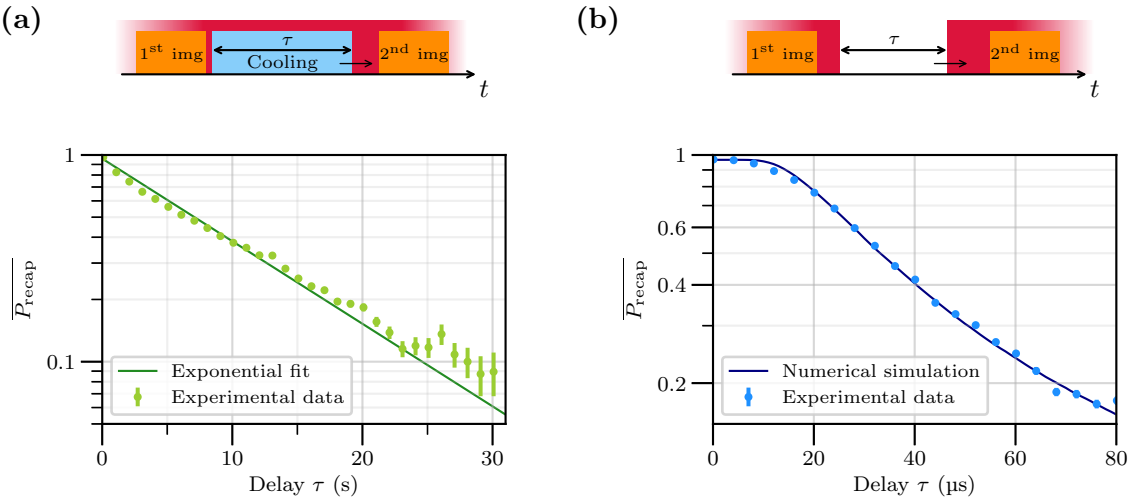

Figure II.8: Characterization of the atomic properties. **(a)** Lifetime measurement: the survival probability over a variable waiting time yields an atomic lifetime of approximately 12 seconds in the tweezers, limited by collisions with background gas. **(b)** Temperature measurement, yielding $\overline{T} = 19$ µK.

implemented in the sequence, for several temperature values $\{T_k\}$. For a single T_k, we thus generate a simulated recapture probability $p_{\text{sim, k}}(\tau)$. We then compute the distance between the experimental result p_{recap} (single site or average over all traps) and the simulated evolution $p_{\text{sim, k}}$ through

$$\chi^2(T_k) = \sum_{\tau} \frac{(p_{\text{recap}}(\tau) - p_{\text{sim, k}}(\tau))^2}{\sigma^2_{\text{recap}}(\tau)}, \tag{II.10}$$

where σ_{recap} is the standard deviation in p_{recap} (measurement error if single site, spread over sites if averaged value). The sum runs over all the scanned values of the delay τ. We finally perform a polynomial fit of $\chi^2(T_k)$ near its minimum, so as to extract a temperature $T = \arg\min \chi^2(T)$, where the data fits closest to the simulation, i.e., the most likely real temperature of the atoms. We can perform the simulation and fitting routine for the data on each site: the result is a temperature distribution over the lattice

$$\langle T_i \rangle = 18.7 \pm 2.3 \text{ µK}. \tag{II.11}$$

We get here significant deviations across the array, with atoms on the $\pm x$ edges being hotter than those in the center of the array. This might be explained by the geometrical 3D-MOT configuration and beam waists, although no further investigation was conducted to mitigate this dispersion. The temperature estimation is nevertheless precise enough to optimize all of the molasses and imaging parameters, which are chosen to minimize its value. Some re-optimization of these parameters are required once every few weeks because of drifts.

The main contribution to the temperature of the atoms comes from the optical pumping, which significantly heats them: without it, we measure temperatures around

9 µK. We can further reduce the temperature of the atoms through an adiabatic ramp-down of the tweezer intensities right before conducting experiments. By exponentially decreasing their power to 10% of its initial value in 500 µs, we lower the energy of the motional states in the traps while their population remains unchanged, leading to an effective cooling of the atoms [183]. Through this technique, we reach temperatures of less than 5 µK for all trapped atoms, regardless of the implementation or not of the optical pumping beforehand. The implementation of adiabatic cooling is not always necessary in the experiments. Since it does not directly relate to the essential atomic preparation and characterization, the data presented thus far was acquired without this additional process, for clarity purposes in these first experimental results.

A third measurement concludes the characterization of the trapped ground-state atoms: the Raman spectroscopy of the hyperfine levels population. As previously mentioned in the global description of the sequence, it analyses the efficiency of the optical pumping procedure. Its presentation is left out of the main text and addressed in appendix E, dedicated to the hyperfine manipulation of the atoms. We only retain here the important value it provides: the maximal efficiency of the optical pumping procedure, measured at $\eta_{\mathrm{OP}} = 0.97 \pm 0.01$ in optimal conditions.

We presented in this section the standard techniques implemented to load, cool and image arrays of individually trapped ground-state atoms. Thanks to the highly homogeneous properties of the lattices and to careful optimization of the preparation process, we reach high loading probabilities, excellent imaging signals, low temperature and good hyperfine population control in all individual trapping sites. All of these preparation steps provide a good basis for the excitation of the trapped atoms to Rydberg and circular states.

II.3 Deterministic array rearrangement

As such, the preparation of lattices of trapped, ultra-cold ground state atoms has a significant drawback: the random, $\sim 65\%$ loading of the tweezers prevents any deterministic study of interactions between circular states. Ideally, to characterize the pair interactions described in the first chapter, we need to work with arrays of isolated pairs of atoms and not with randomly filled lattices. More generally and for the longer-term goals of quantum simulations [117], we would like to deterministically implement filled arrays of arbitrary geometry: each repetition of the experimental sequence should yield exactly the same filled array. To do so, we recently added a "rearranging beam" (the *moving tweezer*) to the setup: a gaussian tweezer similar to the static ones but of tunable intensity and position, able to move atoms from one site to another in the lattice of traps. The moving tweezer can trap ground-state atoms exactly as the static tweezers, via the dipole force. For a given target sub-lattice of the full array of static tweezers, the rearranger operation is inserted into the sequence

as follows, for each repetition:

- a randomly-filled array of ultra-cold atoms is prepared in the static tweezers and a first image is acquired,
- an algorithm computes which atoms need to be moved where to fill the target sub-lattice,
- the rearranging beam executes the moves and discards the extra unnecessary atoms by moving them away from the lattice,
- a second image is taken to check that we are left, as required, with the filled target array.

We describe in this section the working principle of the moving tweezer, the hardware and software it relies on and the way we optimized its parameters. The end result of this new tool is the deterministic creation of atomic arrays of arbitrary geometries, which will be presented and characterized here. This additional feature opens the way for the proper study of interactions in our setup.

II.3.1 The moving tweezer

Technical setup

The implementation of the rearranging beam setup is shown in figure II.9. The goal of this system is to create, at the position of the trapping array, a gaussian tweezer focused in the plane of the lattice, whose depth and (x,z) position can be tuned over short timescales (in the µs range). This trapping beam is generated from the same 821 nm laser used to create the static traps (cf. figure II.3). To be able to control its position and intensity, we use two crossed Acousto-Optic Deflectors (AODs - DTSXY250 from AA Opto-Electronics): each one handles the position of the beam in one of the two directions x and z.

A single AOD deflects an incoming beam via the diffraction induced by the sound wave excited in its crystal, generated by an input radio-frequency signal. The RF frequency tunes the deflection angle, while its power adjusts the deflection efficiency. The AODs each have a deflection range of 49 mrad, for an input RF bandwidth of 36 MHz centered on 100.5 MHz. We discard the non-diffracted light thanks to a diaphragm, which only allows the light effectively diffracted by both AODs to reach the setup. The two radio-frequency input signals $(\mathrm{RF}_x, \mathrm{RF}_z)$ thus completely control the output direction and power of the beam after the diaphragm. The beam is then expanded by a telescope to reach a size compatible with the subsequent beam shaping. An SLM is used for aberration correction, as described in the first section of this chapter. We also use this SLM to finely adjust the position of the moving tweezer, in a static manner. We make sure that the beam waist is close to that of the tweezer array beam, shaped on its own SLM, so that the moving tweezer in the setup has a size comparable with

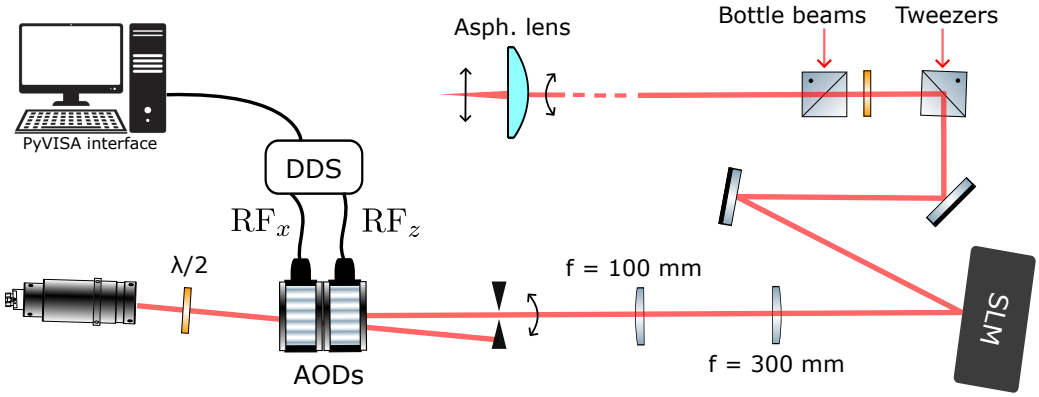

Figure II.9: Illustration of the technical system implementing the moving tweezer. The intensity and (x,z) position of the moving tweezer is set by tuning the frequency and power of the two radio-frequency signals sent into the two AODs with orthogonal axes. These signals are generated by a DDS, numerically controlled from our homemade acquisition software.

that of the static tweezers, after focusing by the aspheric lens. The moving tweezer is superimposed with the other two trapping beams (tweezers and bottle beams) via polarization-dependent cubes, before being sent into the setup. Given the deflection range of the AODs, the magnification of the beam and the focal length of the aspheric lens, we obtain a 250×250 µm^2 position range for the moving tweezer in the (x, z) focal plane of the lens, which is more than enough considering the 100×100 µm^2 extent of the static arrays. The position of the moving tweezer in the setup then varies linearly, in each direction, with the input RF frequencies. The intensity of the beam is set by the RF$_z$ signal only, as RF$_x$ is always tuned to maximum diffraction efficiency (at 33 dBm). This choice mitigates the thermal effects occurring in the AODs when switching the RF on and off [91].

A two-channel Direct Digital Synthesizer (DDS, FlexDDS-NG DUAL – Wieserlabs Electronics) generates the input RF signals. It is digitally controlled from the acquisition software and outputs, from digital orders, an analog sinusoidal signal of tunable amplitude, frequency and phase[4]. The DDS output frequency ranges from 0.3 to 400 MHz, with a 0.23 Hz precision and a 0.005° phase resolution. The digital commands of the DDS are carried out by lists of instructions sent from the computer through the PyVISA python library and an ethernet connection. This enables the control, over microseconds, of the moving tweezer's position and intensity. The low-level, technical encoding protocols and complex DDS operation proved to be challenging. We however leave their discussion out of this work, as they are irrelevant to the implementation of the experiments.

[4]The DDS output waveform is actually an approximation of a sine wave, generated using evenly spaced voltage steps at its 1 GHz internal clock rate. The steps' amplitudes and durations are however small enough to consider, for our purposes, the output signal to be a perfect sine oscillation.

Characteristics and calibration of the moving tweezer

We conducted, with the moving tweezer, the same experiments as those used to characterize the array of static tweezers, i.e., light-shift spectroscopy to obtain the intensity at its focus and a release-recapture sequence to compute its transverse trapping frequency. We use RF amplitudes of 33 and 22 dBm in the x and z channels respectively. We limit the RF_z power here to reduce the optical power and aim for a light-shift in the same range as that of the static tweezers. The two RF frequencies are set to position the moving tweezer in the center of the aspheric lens' focal plane without moving (i.e., at the center of the static lattices). In this configuration, we measure in these single-atom experiments a light-shift of 23.6 MHz and a trapping frequency of 74.7 kHz. From these values, we derive the waist of the moving tweezer:

$$w = 1.21 \text{ µm}. \tag{II.12}$$

This waist is therefore very close to that of the static tweezers (1.16 µm on average), as expected from the design of the optical setup. The power computed from these experiments is 2.3 mW. Although measured in a specific RF power configuration, it allows us to extrapolate the maximal power available in the setup at full amplitude in both RF channels: 27.3 mW. This corresponds to a depth of 13 mK, i.e., about 10 times more than the static tweezers. This is more than enough to capture a single atom efficiently from a static tweezer without switching off the array [91].

To be able to carefully position the moving tweezer over the static array, we need to convert the RF frequencies to actual positions in the lattice. We do so through the diagnostics camera (see fig. II.3). We image the focal plane of the aspheric lens onto it, and thus obtain an image of the traps as they appear in the setup. The scaling factor between the trapping plane in the setup and that of the camera is know with good precision. Formally, the goal of the process is then to map the RF frequencies (ν_x, ν_z) onto positions (x, z) in the setup:

$$x = x_0 + \alpha_x \nu_x, \quad z = z_0 + \alpha_z \nu_z. \tag{II.13}$$

To determine the proportionality factor, we precisely pinpoint the position of the moving tweezer on the camera for various RF frequency couples. A linear regression of the positions then provides the proportionality coefficients, measured to be $\alpha_x = \alpha_z = 6.8$ µm/MHz. This measured value matches very well the 250 µm range estimated from the optical design for the full 36 MHz AOD bandwidth. This calibration was done once and its result is stable in time.

Dealing with the (x_0, z_0) offset is more sensitive. We actually impose its value, not through the AOD, but using the moving tweezer's SLM. To do so, we first remove the array-defining phase mask layer of the static tweezers SLM, so that it outputs a single gaussian beam, identical to the moving tweezer. The position of this single static tweezer is taken as the origin O of the $(x - z)$ plane of the setup, thus completely defining a reference frame (O, x, z). From the definition of the tweezer arrays, we know the position (x_i, z_i), in this frame, of any site i in the lattice we want to work

with. Then, using finely tuned phase gratings on the moving tweezer SLM, we overlap it with the single static tweezer on the diagnostics camera. While doing so, the RF frequencies are fixed and at the center of the AOD bandwidth $(\nu_x^{(0)}, \nu_z^{(0)})$. When the two beams are perfectly overlapped, we end up with the moving tweezer positioned at the origin of the plane in the setup. We keep the corresponding grating on its SLM. This effectively imposes the (x_0, z_0) offset, which is therefore set to $(0, 0)$ in the defined reference frame. Once the static tweezer array is re-implemented, the moving tweezer can be placed at any site position in the lattice (x_i, z_i) via the conversion to RF frequencies $(\nu_x^{(0)} + x_i/\alpha_x,\ \nu_z^{(0)} + z_i/\alpha_z)$. The offset adjustment, which boils down to tuning the phase grating on the moving tweezer SLM, is carried out daily via an automated procedure. It allows us to overcome the independent drifts of each trapping beam.

Moving a single atom

Now that we have described the technical implementation and characteristics of the moving tweezer, we can go over its actual operation to move atoms on the lattice. The execution of a single elementary displacement of an atom from a filled trap to an empty one is depicted in figure II.10 (a). We illustrate this process in one dimension only, taking z as the direction of the movement, and we schematically plot the relevant RF_z parameters as functions of time in (b) and (c). The full procedure goes as follows:

1. the moving tweezer, initially at zero or low intensity (low RF_z amplitude), is brought at the position of the filled static tweezer by ramping its frequency,

2. its depth is increased by a linear ramp-up of the RF_z amplitude, from t_1 to t_2, until its intensity is (much) higher than that of the static tweezer: the moving tweezer catches the atom,

3. the RF_z frequency is linearly changed over a duration $t_3 - t_2$ to place the moving tweezer at the position of the empty static trap,

4. the moving tweezer releases the atom in the empty trap via a decrease of the RF_z amplitude from t_3 to t_4,

5. a final change in the RF frequency shifts the moving tweezer away.

Let us mention here that we can also catch an atom from a filled static tweezer and release it away from the lattice site to discard it. We will implement these elementary moves many times in each realization of the arrays of ground-state atoms, so as to reach a target geometry from initial random fillings. The elementary displacement therefore needs to be highly effective to avoid unwanted errors and deterministically generate the target lattice with good success rates.

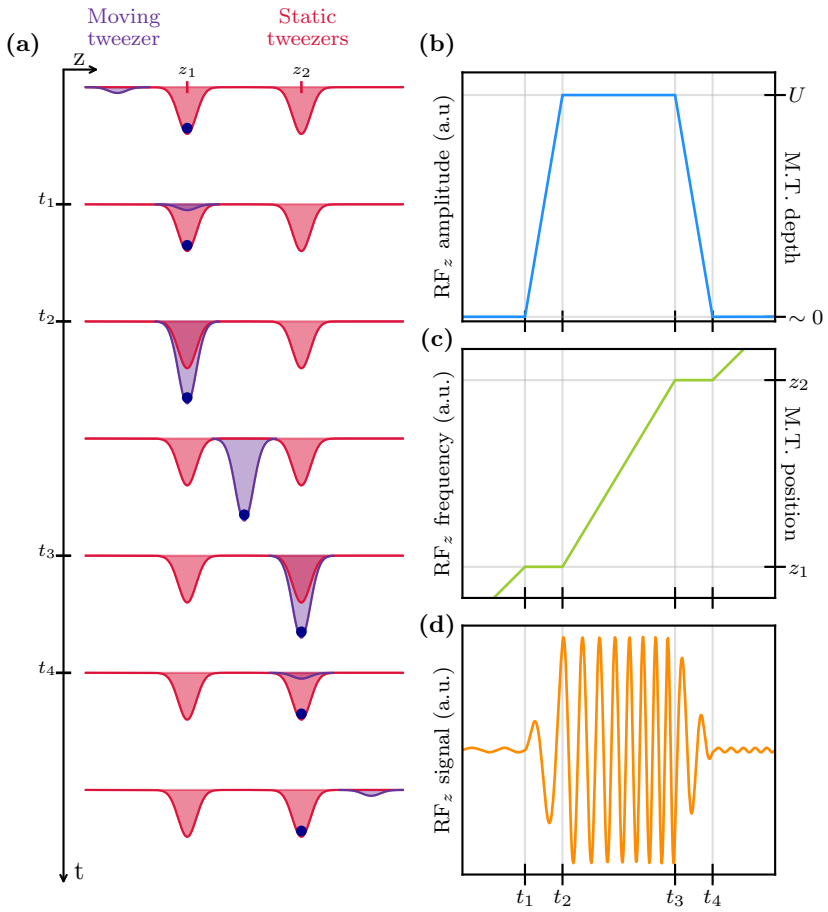

Figure II.10: Schematic illustration of the displacement, using the moving tweezer (M.T.), of a single atom from a static tweezer to another. **(a)** Representation of the full procedure in one spatial dimension. **(b)** Moving tweezer depth, proportional to the power of RF_z, ramping from a low to high value and back. **(c)** Evolution of the RF_z frequency over time, directly proportional to the position of the moving tweezer. **(d)** Indicative plot of the RF signal over time, varying both in amplitude and frequency. The frequencies used here for illustration purposes are not representative of the actual timescales of the experimental implementation.

II.3.2 Optimization of the elementary displacement

We present here the approach we took to optimize the elementary displacement of atoms. The goal is to maximize its probability of success by finding the optimal values of the following parameters:

- The catch time t_c over which the moving tweezer intensity is increased to grab the atom: $t_c = t_2 - t_1$ as per the notations of the previous subsection and figure II.10.

- The trapping depth U, i.e., the moving tweezer intensity kept constant when moving the atom, controlled via the power in RF_z.

- the moving speed v, defined in the case of the previous illustrative example as $v = (z_2 - z_1)/(t_3 - t_2)$. We work with a constant moving speed; it should be as high as possible so as to rapidly implement many successive displacements, but not so high that it induces losses or significant heating due to the movement.

- The drop time t_d over which we release the atom in the target tweezer.

To optimize these parameters, we worked with a square 6×6 array of static tweezers with 15 µm spacing. We operate the rearranger to study elementary moves within pairs of sites: the full lattice can be seen as an array of 18 horizontal pairs, arranged in three columns of six pairs each, as depicted in figure II.11 (a). We prepare the atoms via the standard MOT-molasses-image-molasses sequence, with random filling of the array. We then operate the moving tweezer in a pre-defined sequence of moves, using a fixed set of parameters (t_c, U, v, t_d) for elementary moves. For simplicity purposes, we set $t_c = t_d$. The sequence of moves goes as follows:

1. In each pair, we apply an elementary move from the left site to an empty region of the plane: if an atom was initially in the left site, it is discarded.

2. We implement, in each pair, a move from right to left and then a move from left to right; we repeat this back-and-forth displacement a total of five times. If an atom was initially in the site on the right and the elementary moves are efficient, it ends up in the right site again at the end of the ten moves.

3. We perform one last move from right to left in each pair, for measurement purposes. We want the result to be a transfer probability, from right to left.

We then take a second image and finally compute the success rate of the full process within each pair, over 200 repetitions of the total sequence. We define the total, 11-move success probability within each pair as:

$$P_{\text{move}}^{(\text{tot})} = P\left[\,(\bullet\ \circ)_2 \,|\, (\times\ \bullet)_1\,\right]. \tag{II.14}$$

It corresponds to the probability of finding, in the second image, the configuration $(\bullet\ \circ)_2$, i.e., the left site filled and the right side empty, conditioned on the realization of the configuration $(\times\ \bullet)_1$ in the first image, i.e., an atom in the right site and either an atom or no atom in the left site (made irrelevant thanks to the first step in the sequence, which discards any left atom). We work here with numerous (eleven) repetitions of the elementary move to exacerbate its inefficiencies: if the success probability of a single elementary move is P_{move}, then we have[5] $P_{\text{move}}^{(\text{tot})} = (P_{\text{move}})^{11}$.

The measurement of the total success probability, averaged over all 18 pairs, as a function of the displacement parameters are plotted in the three panels (b), (c) and (d)

[5]This is technically an approximation, as an 11-move process could be considered successful even if several of the elementary moves it comprises were unsuccessful in catching the atom. However, we witnessed that the failures come almost exclusively from the motion itself and the release of the atom. Cases where, in several successive moves, the atom is not caught are extremely rare. We also neglect here the probability of capturing a background atom at any time during the process. These model refinements are not necessary to the optimization of the parameters.

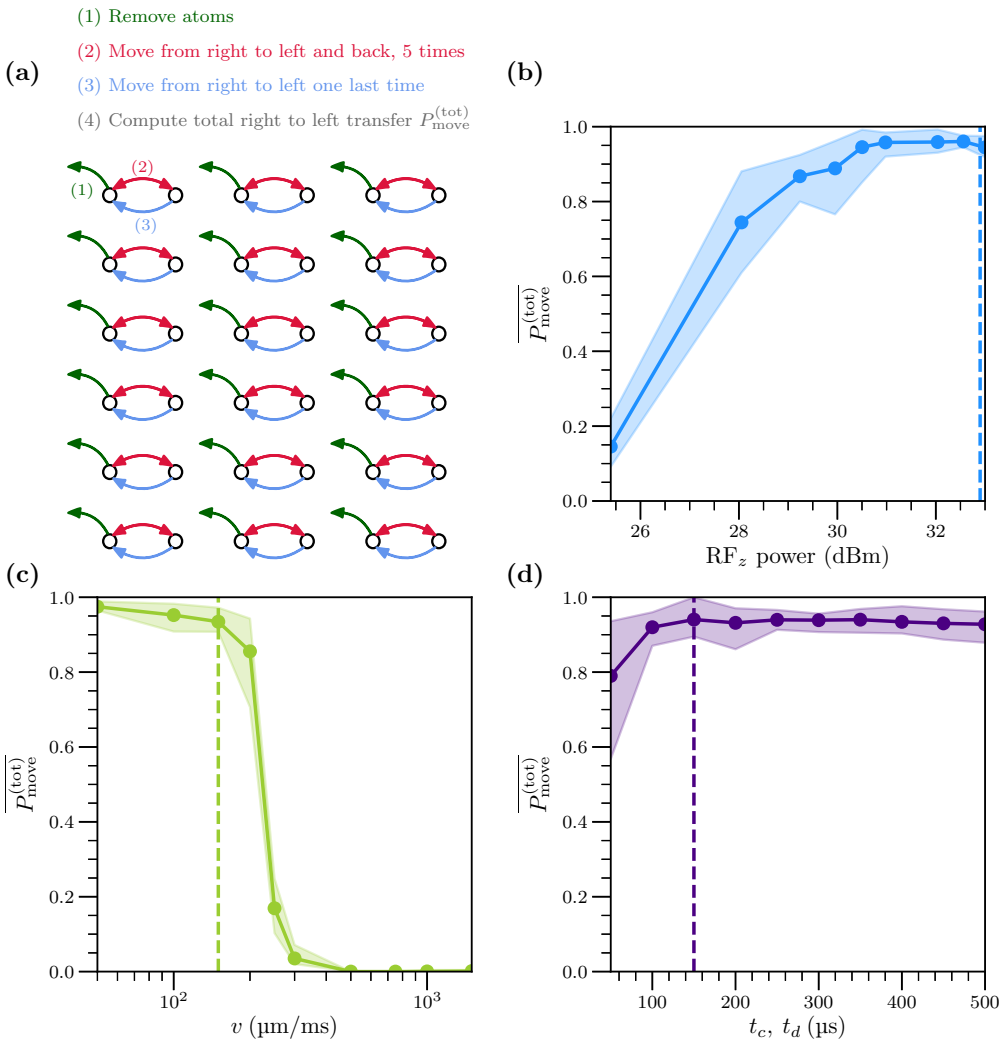

Figure II.11: Optimization of the elementary displacement. **(a)** Sequence of elementary moves deterministically implemented within each pair of sites, detailed in the main text. **(b-d)** Total 11-move success rate $P_{\text{move}}^{(\text{tot})}$, averaged over all 18 pairs, as a function of **(a)** the moving tweezer depth during the motion (via the RF power), **(b)** the moving speed v and **(d)** the catch and drop times t_c and t_d, taken equal to each other. The dots are the average success rate, while the shaded area is delimited by the minimal and maximal probabilities, among all individual pairs, for each scanned value. Vertical dashed lines correspond to the values kept as optimal.

of figure II.11. We remind that we chose to implement ramps with the same catch and drop times: their values are kept identical and scanned at the same time in graph (d). The success rate dependency on each parameter is clear and allows us to select optimal values:

$$v = 150 \text{ µm/ms}, \quad t_c = t_d = 150 \text{ µs}, \quad P_{\text{RF}_z} = 33 \text{ dBm}, \tag{II.15}$$

with the maximal RF power P_{RF_z} corresponding to a trapping depth of ~ 13 mK. The speed v is chosen as a trade-off between efficiency and execution speed. It corresponds

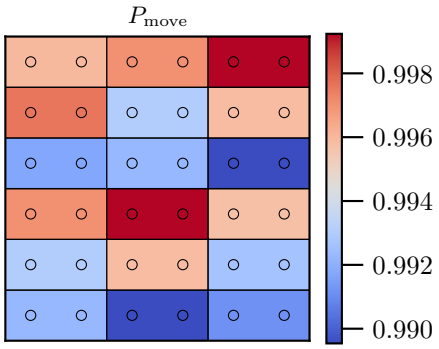

Figure II.12: Outcome of the optimization process: spatial map of the elementary move success rate over the 18 pairs.

to the highest value deemed acceptable in terms of success performance. These parameters lead to an estimated $94 \pm 3\%$ 11-move success rate over all pairs. We therefore extrapolate the elementary move success probability:

$$\langle P_{\text{move}} \rangle = 99.44 \pm 0.29\%. \tag{II.16}$$

where the standard deviation is related to spatial dispersion across the array of pairs.

Figure II.12 displays the spatial map of the elementary success over the 18 pairs. Two lines of pairs seem to exhibit lower success probabilities, but no general tendency appears over the full array. We also checked that the same procedure implemented within vertical pairs leads to the same results, without any clear spatial dependency of the success rate. Overall, we reach a very satisfactory level of efficiency, which should be enough to implement full rearrangement of the arrays without too many errors, as discussed in the next section.

We presented here the optimization of the physical process in which we move a single atom from a site to another. We left aside most of the low-level technicalities that were also overcome to make this process work correctly. Let us only mention here that careful attention was brought to the continuity of the RF phase. Phase jumps in the input signal generated by the DDS initially prevented us from reaching good displacement efficiencies, as the atoms were kicked out of the moving tweezer by these discontinuities. Fine tuning of the delays between successive displacements and of the DDS discretization steps were also carried out to remove unwanted deficiencies.

II.3.3 Complete rearrangement procedure

With an efficient elementary move process, we now have the means to fully rearrange the arrays of trapped atoms so as to implement arbitrary, defect-free geometries in each repetition of the experiment. The goal is to reach, for any initial random filling of the full array, a pre-defined target arrangement of the atoms on a sub-lattice, via successive elementary moves that relocate or discard the atoms. The full preparation sequence then goes as shown in figure II.5, where the inset dedicated to the rearrangement is now taken into account. We remind that its successive steps are, in the following order:

$$\text{loading} \rightarrow \text{cooling} \rightarrow \text{image 1} \rightarrow \text{cooling} \rightarrow \textit{rearrangement} \rightarrow \text{image 2} \rightarrow \text{cooling},$$

where the loading and cooling steps are done respectively in the MOT and molasses configurations. From that preparation, we can then proceed with the actual experiments in the same fashion as before and perform optical detection with a third, final imaging step. We focus here on the *rearrangement* phase of the full process. We estimate its efficiency through the comparison of image 1 with image 2 over many repetitions.

Atom-sorting algorithm

The computation of an optimal series of elementary moves to reach the target lattice from the initial filling is key: it should return a minimal number of moves, computed in a minimal amount of time. This corresponds to the NP-hard "pebble motion on a graph" problem; we take a heuristic approach, based on known algorithms [91], to find efficient though approximate solutions to this problem. We restrict our method to rectangular lattices but it could easily be extended to any regular lattice geometry. For simplicity purposes, we also impose that the algorithm only outputs moves along the axes of the lattice or along the directions of its main diagonals (those of a square of $n \times n$ sites).

To present the implemented algorithm, we need to introduce some relevant notations. The full array of sites is indexed from 1 to N, each site having real-space coordinates (x_i, z_i). We derive from the sites coordinates the distance matrix $D = (d_{ij})_{1 \leq i,j \leq N}$, where $d_{ij} = (x_i - x_j)^2 + (z_i - z_j)^2$ is the squared euclidean distance between sites i and j. A random atomic filling of the array is written $(\sigma_i)_{1 \leq i \leq N} \in \{0,1\}^N$, while $(t_i)_{1 \leq i \leq N}$ (also in $\{0,1\}^N$) is the fixed target arrangement.

The algorithm takes as inputs the initial filling $(\sigma_i)_{1 \leq i \leq N}$ and the target $(t_i)_{1 \leq i \leq N}$, and it outputs an ordered list of allowed moves $\{(a \rightarrow b), (c \rightarrow d), ...\}$. It proceeds with the following successive sub-tasks:

1. Assignment: finding in which site each atom of the initial filling should end up. We solve this task through the Jonker-Volgenant algorithm [184]. Using the sub-matrix of D that only links the filled sites $\{i \mid \sigma_i = 1\}$ to the target sites $\{j \mid t_j = 1\}$, it derives the sorting that minimizes the total distance traveled by the atoms: the atom initially in site i should end up in site j, the one in site

k should go to l, etc. This solution does not take into account the physical constraints of the movements: it can lead to two or more atoms being placed in the same site during the procedure, which we want to avoid. It also does not take into account the fact that atoms cannot be moved over already filled sites. We then have to compute, from this initial assignment, the actual atomic paths.

2. Reordering: pre-processing of the assignment solution. The prescribed assignments are re-ordered to prevent sending several atoms in the same site. For instance, the series of assignments $(1 \to 3), (2 \to 3), (3 \to 4)$ is changed to $(1 \to 3), (3 \to 4), (2 \to 3)$.

3. Path-finding: translation of the ordered assignment into real atomic moves. Each element of the ordered assignment is converted, through Bresenham's line algorithm [185], into a series of real steps on the lattice. Bresenham algorithm selects, from two sites, the series of lattice points that most closely approximates the straight line between the two input points. An assignment is therefore converted into a sequence of elementary moves on the lattice, along its axes or its main diagonals. These elementary moves are then re-ordered to avoid collisions: if we need to do $(i \to j)$ but a filled site k is in the way, we find the next displacement that moves k and place it before $(i \to j)$ (the move involving k necessarily exists, otherwise k would have been assigned to j, being closer to it than i).

4. Merging: we combine the moves that can be merged. If two successive moves can be combined, we do so. For instance, $(a \to b), (b \to c)$ becomes $(a \to c)$, provided that the two moves are along the same direction.

5. Removal: the moves required to discard the extra, unwanted atoms are added to the result. They consist in taking an atom and dropping it in its neighboring empty space, away from its own or other tweezers.

We assess the performance of the full algorithm by running it in numerical simulations, written in Python and run on our standard acquisition computer. The full array is taken to be a square 144-site lattice, while the target lattice contains 72 sites. The lattice filling is initialized with 72 randomly placed atoms. The loading of the real arrays being above 60%, we simulate here a conservative 50% estimation of the actual filling. In this configuration, the average computing time needed to find a solution is around 50 ms, while the output number of steps is ~ 50. For this number of atoms, these estimations are independent on the geometry of target.

Taking into account the duration of the optimized elementary move, we estimate the total rearrangement procedure to last approximately 75 ms (50 ms computation time and 50×500 µs moving time). This is less than half of the predicted lifetime for the full array of ground state atoms: $\tau_{\text{array}} = 166$ ms in a 72-atom array, according to the single-atom 12 s lifetime. Moreover, given the single-move 99.44% efficiency, a 50-move process should have a total success rate of about 75%. These estimations are quite satisfactory for the scope of our experiments on circular interactions, where we actually use smaller arrays which require around 25 moves to be rearranged. When

increasing the number of atoms and size of the arrays in the simulations, the number of moves and computation times grow in various fashions and start depending a lot on the target geometry. We leave these considerations aside, as our work focuses on arrays of reduced size, 72 atoms already being higher than the amount involved in most of our experimental conditions. We typically work with 40-site lattices which contain less than 25 atoms.

Rearranged arrays and success rate

The rearrangement procedure is operated by a homemade Python code, embedded in the imaging and data-processing software. In each repetition of the experimental sequence, the software acquires the first image of the random filling, computes the atomic positions using the pre-defined thresholds, and runs the sorting algorithm with that input. The generated list of moves is then converted to successive frequency and amplitude ramps to be sent to the AODs. This conversion uses the daily AODs calibration, converting positions in the lattice to RF frequencies. The ramps are then encoded into signals readable by the DDS and sent to it, which finally feeds them to the AODs, thus executing the computed moves. In regular lattices of around 50 static sites, the whole process always takes less than 60 ms, in good agreement with the estimations discussed above. Figure II.13 shows single-shot images of rearranged arrays, with four different target geometries. The full underlying array of static tweezers is a 5×8 lattice with regular 15 µm spacing.

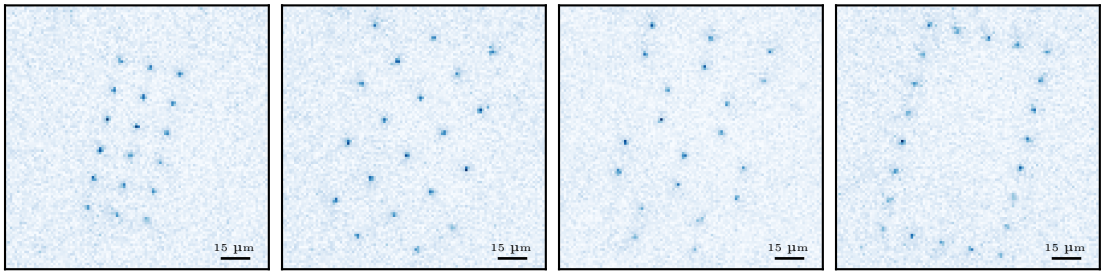

Figure II.13: Single-shot frames of rearranged arrays, showing different target geometries reached from the same 5×8 initial rectangular lattice.

To precisely estimate the success rate of the rearrangement, we work with a target array used for experiments on circular atom interactions. The full lattice now has 6×8 sites and the target sub-array is a set of nine pairs of traps. Single shot images of the array, before and after the rearrangement, are shown in figure II.14 (a). We run 1000 repetitions of the rearranging sequence and compute, for each one, the number of errors in the rearranged array with respect to the target. The results are plotted in figure II.14 (b). On average, the rearranging sequence involves 7 ± 3 atomic moves between sites and 14 ± 5 moves to discard extra atoms. We expect, from the number of moves between sites (considering that discarding atoms is always successful) and from the collective lifetime of the 18 atoms compared to the duration of the process, a

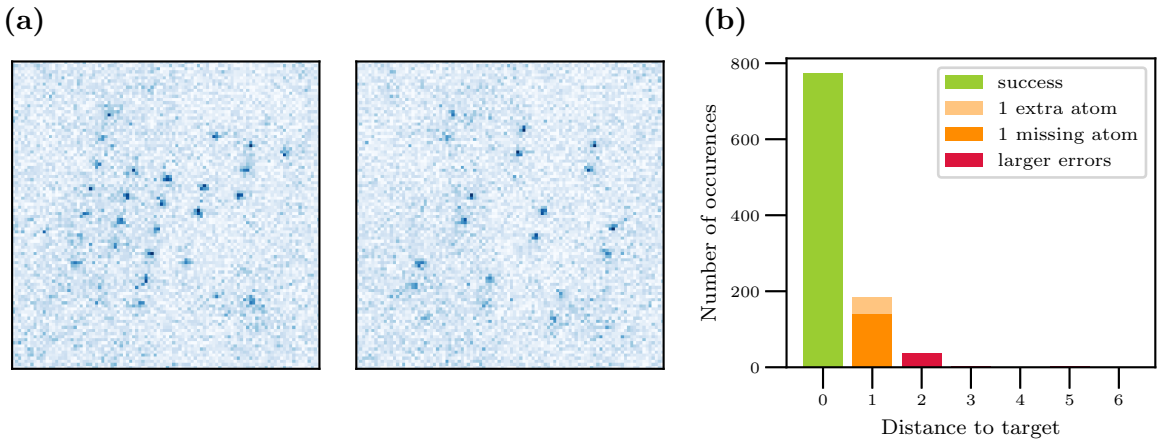

Figure II.14: **(a)** Single-shot images of the atoms, before and after a successful rearrangement. The target array, realized in the second frame, is designed to study interactions within pairs of atoms. **(b)** Histogram of the distance to the target array, in 1000 repetitions of the sequence. In 774 cases, the target array is perfectly realized, with no missing or extra atoms.

success rate of 86%. The measured value is 77.4%, indicating unexpected inefficiencies in the process. In 14% of all repetitions, an atom is missing from the target array, while the presence of an extra atom on a site that should be empty occurs with a 4% rate. Unsuccessful realizations with two errors are rarer, and rearranged arrays with a distance to the target larger than 2 happen in less than 0.5% of the repetitions. Further investigations would need to be conducted to reach the theoretical rearranging efficiency, but the overall success rate is nonetheless satisfactory for the experiments presented in this work: a single pair has a 98% probability of being successfully created in each repetition of the experiments.

We therefore properly implemented the rearrangement of arrays of ultra-cold atoms to work on Rydberg experiments with deterministic geometries. The moving tweezer, controlled through AODs and aberration-corrected via an SLM, can move atoms from one trap to another with state-of-the-art efficiency. The full rearrangement of the arrays, based on a heuristic algorithm that computes the moves for each repetition of the sequence, yields correct success rates, though not as high as expected. With the example of an array of pairs devised to study atomic interactions (18 atoms), the setup outputs a defect-free geometry in more than 3 out of 4 repetitions. We checked that the rearrangement procedure does not affect the properties of the atoms: once recooled by optical molasses, atoms in a rearranged array have the same temperature of ~ 9 µK (prior to the optical pumping phase) as those in the non-rearranging sequences.

Conclusion of chapter 2

We presented in this second chapter our new experimental setup, designed, built and put into operation over the past few years. Though currently running at room-temperature, the heart of the setup is set to be moved from the UHV chamber to a cryogenic environment for future experiments, once some first measurements on circular Rydberg interactions have been performed with it in the current system. Such experiments start with the preparation ultra-cold, defect-free arrays of individual ground-state rubidium atoms. Several coils and various optical accesses enable the use of standard techniques to load and cool the arrays of single atoms, trapped in optical tweezers. The optical traps are created through a careful design of phase patterns on an SLM, which allows us to implement arbitrary arrays of traps over a wide 100 µm × 100 µm area in the focal plane of the aspheric lens that focuses the trapping beams. The correction of aberrations via the SLM ensures that the tweezers are homogeneous both in shape and intensity throughout the lattice. This is checked via atomic measurements. Spectroscopy and release-recapture experiments reveal the power and waist distribution over a 42-site, 70 µm-wide array:

$$\langle P_i \rangle = 2.3 \pm 0.1 \text{ mW}, \quad \langle w_i \rangle = 1.16 \pm 0.01 \text{ µm}. \tag{II.17}$$

Good control on the loading, cooling and imaging parameters of the setup yields state-of-the-art atomic properties in the arrays. Their initial random filling is around 65%, while we measure their lifetime and temperature to be:

$$\overline{\tau_{\text{at}}} = 12.6 \pm 0.2 \text{ s}, \quad \langle T_i \rangle = 18.7 \pm 2.3 \text{µK}. \tag{II.18}$$

The hyperfine level of the trapped atoms is also controlled, via an optical pumping stage that, while somewhat heating the atoms, populates the $|5S_{1/2}, F = 2, m_F = +2\rangle$ sub-level with $\eta_{\text{OP}} = 97\%$ efficiency.

The moving tweezer, controlled by AODs and shaped by an SLM, finally allows us to deterministically rearrange the atoms on the arrays. The optimization of its parameters led to a rearranging efficiency of 77% in creating $\sim$ 20-atom target geometries, designed for the study of circular Rydberg interactions. More precisely, in the tested geometry of 9 pairs of atoms, the rearranging process has a 97% success rate for each pair.

Thanks to these various setup features and techniques, the atoms are properly prepared for Rydberg experiments. The excitation to Rydberg states, detailed in the next chapter, will always start from arrays that we prepare as described here: individually trapped, ultra-cold atoms, optically pumped to $|5S_{1/2}, F = 2, m_F = +2\rangle$, either randomly filling the array or rearranged to fit our needs.

Chapter III

Arrays of trapped circular atoms

The preparation of deterministic arrays of trapped, ultra-cold ground-state atoms constitutes the groundwork for experiments on interacting circular Rydberg states. The end goal of this thesis is the characterization of interactions between circular states, and our longer-term aim is the implementation of quantum simulations based on circular atoms. Efficiently bringing the atoms to circular levels is therefore key in our experiments. The process which elevates ground-state atoms to circular levels, with its specific technical tools and methods, constitutes the second pillar of the setup and has been mastered for a long time in our team. To properly study circular-circular interactions, we also need to individually trap the Rydberg atoms at fixed distances from one another. This level of control was successfully achieved for the first time in our setup quite recently [122], and is now implemented daily in our experiments.

In this third chapter, we first tackle the *circularization* procedure itself, which excites the atoms to $|52C\rangle$. We work with this specific state due to a combination of historical reasons and motivations related to the simulator project. From the scaling laws of the circular atom properties with respect to n, levels with $n \sim 50$ were identified as the most promising spin-encoding states [117]. These levels coincide with the ones we are used to working with in the lab, although exciting the atoms to other manifolds require little additional effort and could easily be implemented in a similar manner. All of the results presented here are therefore based on the creation and study of $|52C\rangle$ exclusively.

We also describe here the trapping of these states in individual optical bottle beams, based on the ponderomotive energy discussed in the first chapter and the optical system introduced in the second one. A more detailed account of these results and methods can be found in Brice Ravon's dissertation [123], as the trapping of circular atoms made up the central results of his thesis, and in the corresponding publication [122]. We focus here on the general description of these processes, with the study of interactions in sight. For the purpose of this chapter, we mostly use non-rearranged arrays, in order to maximize the number of atoms present in each repetition of the Rydberg experiments. When dealing with circular atoms, the lattice geometry is specifically chosen to minimize interactions: all the results presented here still pertain to single-atom physics.

III.1 From ground-state atoms to Rydberg states

III.1.1 Overview and ionic detection

The *circularization* process constitutes a crucial part of the experiments: a good circularization efficiency is key to the preparation of defect-free arrays of circular atoms. Its principle has been extensively discussed in previous works from our team [123, 144]. We present here its specific implementation in this new setup, starting from a non-rearranged array of ultra-cold atoms optically pumped to $|5S_{1/2}, F = 2, m_F = 2\rangle$, with a directing magnetic field B_x defining the quantization axis along x kept constant throughout the sequence. The adiabatic cooling through the exponential ramp-down of the tweezer intensity is always implemented, so that the trapped atoms have a < 8 µK temperature. The electric field is initially zero. The full procedure consists in three main steps, illustrated in figure III.1 (a) with the relevant atomic levels involved. The three successive stages are:

1. Two-photon laser-excitation process to reach, via the intermediate level $6P_{3/2}$, the Rydberg state $|52D_{5/2}, m_j = 5/2\rangle$.

2. Microwave transfer to $|52F, m = 2\rangle$. The electric field is then ramped up to lift the degeneracy of the $n = 52$ manifold and branch 52F onto one of its low-lying levels (cf. Stark map of the $n = 52$ manifold in fig. I.2).

3. Radio-frequency adiabatic transfer. The successive absorption of many σ_+-polarized RF photons while the electric field strength is ramped up brings the atom to the circular state $|52C\rangle$. In this work, two slightly different implementations of the adiabatic passage were used. The first one, that will be referred to as "adiabatic passage A", relies on a historical set of parameters and is carried out in a magnetic field of 10 G. In the second one, called "adiabatic passage B", the parameters were recently re-optimized to further improve its efficiency, and it is performed in 14 G.

We discuss each of these processes and their respective efficiencies in the following subsections.

To manipulate Rydberg states, we rely on yet another feature of the setup: the ionic detection. Specifically designed to measure the state of the atoms when in Rydberg levels, it consists in applying a large ramp of electric field to the atoms, over approximately 100 µs. Rydberg states, being close to the ionization threshold, ionize at fields around 100 V/cm, reachable with standard electronic tools. In the setup, the two Stark electrodes (in pink in fig. II.2 of chapter 2) can apply such voltages. The details of the electrical system enabling, through the Stark electrodes, both the implementation of precise low fields for atomic manipulation and the creation of intense electric fields for ionization, are discussed in appendix C. After their ionization, the Rb^+ ions are guided, thanks to various electrodes, to the channeltron, a charge-amplifying device that counts the incoming ions [123]. The different voltages to which the guiding electrodes are set maximize the number of ions that reach the channeltron.

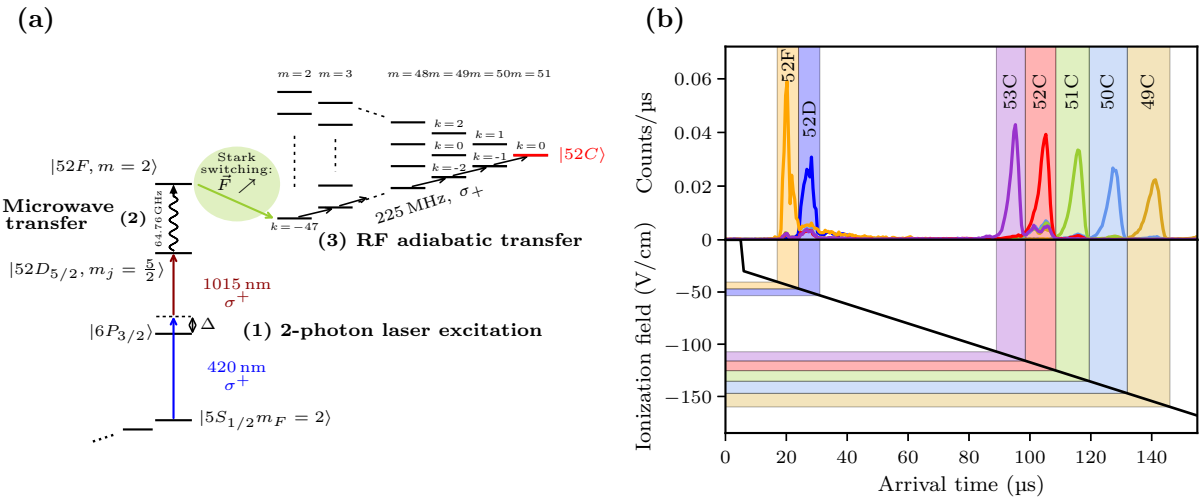

Figure III.1: (a) Schematic representation of the full circularization process, starting with a 2-photon excitation to the $|52D\rangle$ level of the $n = 52$ Rydberg manifold, followed by a microwave transfer and a RF adiabatic passage to finally reach $|52C\rangle$. The energy scales shown here do not reflect the real ones. (b) Ionic detection signals recorded for various Rydberg levels, superimposed on the same graph to show the state discrimination. The ionization threshold depends on both n and m. $|52D\rangle$ and $|52F\rangle$ ionize at smaller fields than $|52C\rangle$, while the ionizing field and arrival time of circular states grow with decreasing n. The corresponding electric field ramp is plotted under the atomic signals. It is chosen here to be slower than those implemented in most experiments, in order to clearly illustrate the level discrimination it enables.

Different Rydberg states ionize at different electric fields, and therefore at different times during the electric field ramp. By precisely recording the arrival time of the ions, we can deduce which Rydberg level the atoms were in at the time of the ionization. This is schematized in figure III.1 (b), where we plot both the electric field over time and the corresponding ionic signal recorded for various Rydberg levels. The ionic detection scheme therefore allows us to discriminate between the different states involved in the circularization process. Triggering this detection technique gives a snapshot of the Rydberg level populations present at a given time in the experiment. We use the ionic detection to optimize parts of the circularization process and to diagnose the outcome of the manipulations of circular levels between different manifolds. Its main drawback is that it does not provide site-resolved results, as opposed to the optical detection scheme discussed so far. When possible, both techniques are implemented to provide complementary information on the state of the atoms.

III.1.2 Laser excitation to $|52D\rangle$

We perform the excitation to Rydberg levels with a two-photon optical transition, from $|5S_{1/2}, F = 2, m_F = 2\rangle$ to $|52D_{5/2}, m_j = 5/2\rangle$, the highest laser-accessible state in the $n = 52$ manifold, via the intermediate state $|6P_{3/2}\rangle$. To do so, we use two counter-propagating beams aligned on the x axis of the setup (cf. fig. II.3), one at 420 nm and the other at 1015 nm.[1] Both are σ_+-polarized with respect to the quantization axis, defined by the magnetic field $B_x = 10$ G, which splits apart[2] the $|52D_{5/2}\rangle$ sub-levels and allows us to aim for $m_j = +5/2$. The detuning with the intermediate level is set to approximately +500 MHz.

The beams originate from two titanium-sapphire lasers (Equinox-SolsTiS systems, M-Squared). One of them is frequency-doubled through a cavity doubler (ECD-X, M-Squared) to reach 420 nm. Both lasers are locked onto a Fabry-Perot etalon cavity and output around 1.5 W of light at their respective wavelengths. The lasers systems, which I set up and optimized, are detailed in appendix D. Each beam is shaped by a system of cylindrical lenses before reaching the atoms, in order to elongate them along the vertical direction z while decreasing their size along y. We do so to maximize and homogenize the intensity focused in the plane where the atoms are, and to not lose light in the $y \neq 0$ regions of the experiment. Their measured waists are

$$w_y^{(420)} = 80\ \mu\text{m}, \quad w_z^{(420)} = 372\ \mu\text{m}, \tag{III.1}$$

$$w_y^{(1015)} = 46\ \mu\text{m}, \quad w_z^{(1015)} = 214\ \mu\text{m}. \tag{III.2}$$

Given the optical power in each beam, 100 mW for the infrared laser and 190 mW for the blue one, we expect single-photon Rabi frequencies to be

$$\Omega_{420} = 2\pi \times 192\ \text{MHz}, \quad \Omega_{1015} = 2\pi \times 20\ \text{MHz}. \tag{III.3}$$

The detuning with respect to the intermediate level is large compared to these Rabi frequencies: we can treat the excitation as the addressing of a two-level transition, from the ground-state to the Rydberg level. The two-photon Rabi frequency is then [186]:

$$\Omega = \frac{\Omega_{420}\Omega_{1015}}{2\Delta} = 2\pi \times 3.8\ \text{MHz}, \tag{III.4}$$

where $\Delta = 2\pi \times 500$ MHz is the detuning with respect to the intermediate level.

The characterization of the excitation is shown in figure III.2. The experiment is carried out after the preparation of the trapped cold atoms, as described in chapter 2. A first reference image is taken, the atoms are re-cooled and optically pumped to $m_F = +2$, the adiabatic cooling is carried out, and the tweezers are then turned off for a few µs while the excitation lasers are turned on. The optical traps are off during the

[1] We remind that the atom arrays lie in the (x, z) plane of the experiment.

[2] In these conditions, the spin-orbit coupling of $|52D\rangle$ is still large compared to the effect of the magnetic field. As per the discussion of chapter 1, the fine structure remains relevant for $|52D\rangle$ and the field shifts its m_j sub-levels according to the Zeeman effect.

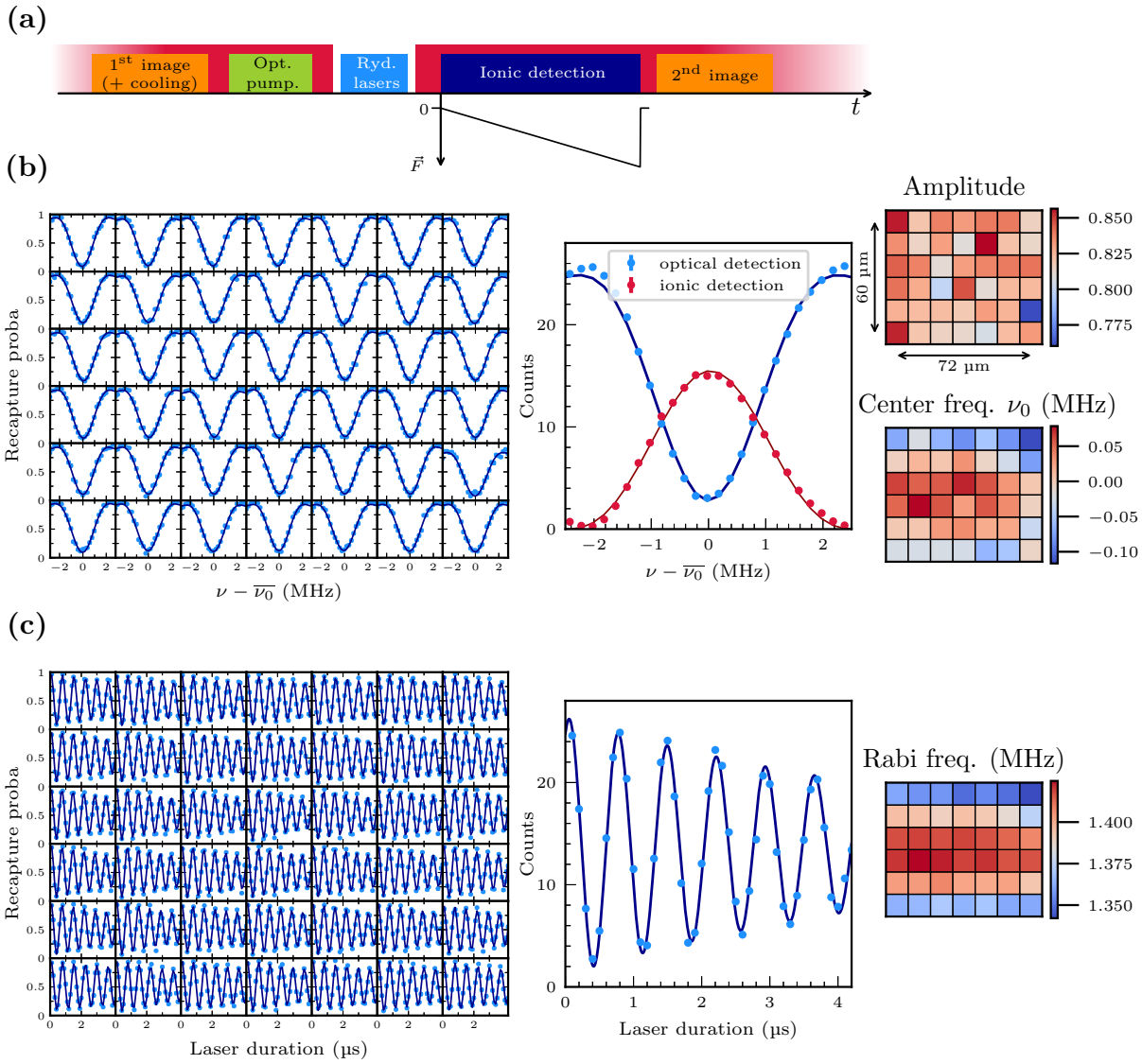

Figure III.2: Two-photon excitation to $|52D\rangle$. **(a)** Sequence used to characterize the laser excitation. Both detection methods, optical and ionic, are implemented. **(b)** Spectrum of the laser excitation for a 0.4 µs pulse. The x-axes are centered on $\overline{\nu_0}$, the peak frequency of the average optical signal. Left panel: site-resolved data. Center panel: optical signal averaged over all sites and converted to counts, overlapped with the ionic signal. Right panel: spatial maps of the amplitude and central frequencies, obtained from the fits of the individual spectra. The dispersion in central frequencies reflects the spatial variation of the lasers' intensities. **(c)** Rabi oscillation signal: the measured average Rabi frequency is lower than the theoretical 3.8 MHz value but shows good homogeneity across the array, thanks to the cylindrical shape of the beams. The measured residual variations in Rabi frequencies across the vertical direction are in good agreement with the spatial profile of the two lasers.

excitation to avoid unwanted inhomogeneous light-shifts on the 2-photon transition across the array. We also keep the electric field at zero during the whole sequence, in order to reduce the Stark broadening of the transition induced by field gradients. The traps are switched back on right after the end of the laser pulse. Atoms that have been excited to $|52D\rangle$ get repelled from the trapping region due to the ponderomotive force exerted on them by the tweezers, while the atoms that stayed in the ground-state are recaptured in their traps. We then proceed with our two measurements techniques. First, we trigger the ionic detection. A $\sim$100 µs electric field ramp ionizes the excited atoms, which we count via the scheme presented above. A second image is finally acquired and we compute, from the two frames, the recapture probability in each site of the array. If the laser excitation is efficient, the recapture probability is low and the ion counts are high. Panel (a) of figure III.2 schematically represents the successive steps involved in the sequence.

The optical detection allows us to have site-resolved characterization of the excitation, as shown in the spectra on the left side of fig. III.2-(b). The data presented here was acquired with a non-rearranged 6×7 array, with 12 µm spacing and a laser pulse duration of 0.4 µs. Each spectrum is well approximated by the theoretical line shape of a 2-level excitation by a square pulse of duration τ and frequency ν [186]:

$$P(\nu) = y_0 + A \,\mathrm{sinc}^2 \left[\pi(\nu - \nu^{(0)})\tau)\right], \tag{III.5}$$

where P is the transition probability and $\nu^{(0)}$ the resonant frequency. We extract, for each site i, the excitation efficiency A_i and the central frequency $\nu_i^{(0)}$, which we map in fig. III.2 (b). The direction of propagation of the excitation lasers corresponds to the horizontal axis of the grids. The excitation amplitude is rather homogeneous across the array, and yields the overall efficiency (amplitude of the site-averaged optical signal):

$$\overline{\eta_{52D}} = 0.83 \pm 0.02. \tag{III.6}$$

This data reflects a combination of both the optical pumping efficiency (usually about 90%) and that of the laser pulse itself (around 93% according to the damping of the Rabi oscillations), in standard, day-to-day operations. With extra care on the optimization of the optical pumping process and precise re-alignment of the excitation lasers, we can reach a global efficiency of about 90% with any array of the same dimensions. These parameters are not re-optimized daily, and we end up with usual excitation efficiencies closer to 85%.

The spatial variations in the central frequencies of the spectra reflect the laser intensity distribution across the array. The blue 420 nm beam light-shifts the addressed transition, so that atoms closer to its center experience a higher resonant frequency than those on the top and bottom edges of the array. This dispersion, of the order of 0.1 MHz, is nonetheless small compared to the $1/\tau = 2.2$ MHz fitted width of the spectra. Let us note here that this width is in good agreement with the 0.4 µs pulse duration and confirms that the excitation is Fourier-limited: no unwanted process broadens the excitation spectrum.

The signal averaged on all sites and converted to counts is also plotted in figure III.2 (b), along with the ionic data. The counts derived from the optical detection are computed using the 64% loading probability measured in this experiment. At resonance, $n_{\text{opt}} = 22.1$ atoms are on average excited to $|52D\rangle$ and not recaptured (difference between baseline and resonance). However, the ionic signal indicates that, on average at resonance, $n_{\text{ion}} = 14.3$ atoms are detected (we integrate all the counts measured over the ramp). The discrepancy between the two numbers comes from the 150 µs lifetime of $|52D\rangle$, which is ionized ∼65 µs after its excitation by the lasers. Given these numbers, we expect the losses measured with the optical detection to translate into $n_{\text{opt}} \times e^{-65/150} = 14.3$ ionic counts, in excellent agreement with the measured value. We therefore have near-perfect ionic detection efficiency. It is worth noting that, for the ionic measurement, we summed up all the detected ions, regardless of their arrival time. The signal is however spread over a rather large time window, maybe because of the Coulomb interaction between the charged particles during their flight to the channeltron, or because of atomic interactions and level crossings when the field is ramped up. This trick will not be possible when dealing with several Rydberg states at a time, as precise level-specific time windows will have to be defined.

We also show in figure III.2 (c) the Rabi oscillation on the laser excitation. In the same fashion, we present the site-resolved results, the average optical detection signal translated into atomic counts, and the spatial map of the Rabi frequencies. The first main information from these results is the spatial distribution of the individual Rabi frequencies obtained over the array:

$$\langle \Omega_i \rangle = 2\pi \times (1.39 \pm 0.03)\ \text{MHz}. \tag{III.7}$$

This value is much lower than the theoretical 3.8 MHz expectation. This could be explained by poor estimations of the laser powers effectively involved in the pulses, as the pulse peak powers might be lower than the continuous-operation values we measured. The polarizations of the beams might also not be as pure as we expect them to be. Although less probable, the low Rabi frequency could maybe indicate an erroneous alignment of the lasers in the system. The second notable feature of the Rabi signals is the spatial variation of the frequencies, explained by the intensity profile of the laser beams along the vertical direction z. Taking the measured vertical waists $w_z^{(420)}$ and $w_z^{(1015)}$, we expect the ratio between the 2-photon Rabi frequencies at the center and at the top and bottom edges of the array to be $\Omega(z = 30\ \mu\text{m})/\Omega(z = 0\ \mu\text{m}) = 0.95$. We indeed measure a ratio of 0.94 between the smallest and largest measured frequencies, indicating a good understanding of the spatial profile of the excitation. The spatial map of the Rabi frequencies is actually used to cautiously align the two excitation lasers onto the array.

Regardless of the unexpected average Rabi frequency, we overall implement an efficient and homogeneous excitation of the ground-state atoms to $|52D_{5/2}, m_j = 5/2\rangle$, with a mean $\overline{\eta_{52D}} = 83\%$ efficiency and limited dispersion in the excitation properties over the full array. The two detection methods provide complementary diagnostics, with the main advantage of the optical detection being the site-resolved data. The

same methods will be implemented in the next steps of the process to reach circular states.

III.1.3 Microwave transfer to $|52F\rangle$

Because of its large quantum defect, $|52D\rangle$ is much lower in energy than the $n = 52$ sub-manifold where the high-ℓ states, and specifically $|52C\rangle$, are located (as shown in the Stark map of figure I.2-[a]). The next step in reaching circular atoms is therefore the transfer to a state closer in energy to the high-ℓ levels, from which we will then be able to climb the "ladder" of states (depicted in fig. I.2-[b]) to reach $|52C\rangle$.

We do so through a one-photon microwave transfer to a sub-level of $|52F\rangle$. We address this transition in the same field conditions as the laser excitation: zero electric field (to minimize transition broadening) and a 10 G directing magnetic field along x, which defines the quantization axis. As explained in chapter 1, $|52D\rangle$ and $|52F\rangle$ exhibit two different behaviors with these field parameters. On the one hand, the spin-orbit coupling in $|52D\rangle$ still overcomes the effect of the magnetic field: the fine structure basis remains its relevant description and its m_j sub-levels are linearly shifted by B_x. On the other hand, the spin-orbit coupling in $52F$ is much weaker, so that it is subjected to the Paschen-Back effect. In 10 G, its coupling to the magnetic field dominates its behavior and its appropriate quantum numbers are l, m and m_s. Starting from $|52D_{5/2}, m_j = +5/2\rangle$, also written $|52D, m = 2, m_s = +1/2\rangle$, we can excite the atoms to any of the three states $|52F, m, m_s = +1/2\rangle$, $m \in \{1, 2, 3\}$, according to the selection rules of the electric dipole transition. For reasons that will be explained later, $|52F, m = 2\rangle$ is the most convenient level to then reach $|52C\rangle$. We therefore choose to address the $\Delta m = 0$ transition, as drawn in figure III.3-(b) within the relevant level structure. In a magnetic field of 10 G, the frequency of this transition is 64.754 GHz. In the experimental setup, a signal generator (MG3692C, Anritsu) generates microwave at 16.19 GHz, which is then amplified and quadrupled (AMC-15-RFH00, Militech) before being shone by a horn onto the atoms through one of the chamber's windows. A PIN diode allows us to digitally control the activation and extinction of the microwave sent to the atoms, in order to implement square pulses with 0.1 µs time resolution (limited by the National Instruments card controlling the PIN diode).

We present in figure III.3 the full characterization of the transition. The sequence, pictured in panel (a), implements both detection methods. After the initial cold-atoms preparation, the tweezers are turned off and a first laser π-pulse sends the atoms to $|52D\rangle$. The microwave pulse, of tunable frequency and duration, is then applied. A second laser π-pulse lowers the remaining $|52D\rangle$ atoms back to their ground-state, after which the tweezers are turned back on. The atoms transferred to $|52F\rangle$ by the microwave pulse are kicked out of the trapping region by the tweezers and not recaptured. We count them via ionic detection, while optical detection computes the recapture probability for each set of microwave parameters, related to the number of $|52D\rangle$ atoms after the microwave pulse. We show here the spectrum of the transition

(panel [c]), obtained with a 0.6 µs pulse. We also plot the Rabi oscillation signal at resonance the resonance frequency (panel [d]).

The site-resolved spectra obtained from optical detection are well approximated by the theoretical shape of equation (III.5). The individual resonant frequencies ν_0 are very homogeneous, with only a 25 kHz dispersion across the lattice. The baselines, lower than 1, reflect the imperfect laser π-pulse efficiency. In this experiment, the tweezers are turned off for 2.6 µs, which is small with respect to the atomic temperature: recapture losses induced by the free flight during that time are negligible. The mosaic representing the individual amplitudes over the array shows some spatial variations. Atoms in the top-left corner have higher microwave transfer than the rest of the array. One deficient site, already outlying in the laser excitation, has a significantly lower amplitude than the rest. This specific tweezer might have an imperfect shape and therefore recapture less efficiently.

The averaged optical signal is also converted into counts. Through the 64% initial loading of the array, we initialize $n_{\mathrm{GS}} = 26.7$ ground-state atoms. On average, at resonance, we recapture 1.9 atoms. These include the atoms unaffected by both laser pulses (0.8 atoms) and those excited to $|52D\rangle$, not transferred to $|52F\rangle$ and then brought back to the ground-state. Knowing the laser pulse efficiency, we compute from these numbers the mean microwave succes rate:

$$\overline{\eta_{52F}} = 0.94 \pm 0.01. \tag{III.8}$$

The ionic signals of both $|52D\rangle$ and $|52F\rangle$ are trickier to analyze, and are presented here for indicative purposes only. Indeed, the arrival time windows of both levels exhibit some overlap. Even at microwave resonance, we count ions in the $|52D\rangle$ window, which biases the results. The overlap can bee seen in the ionic signals of fig. III.1-(b), where a residual $|52F\rangle$ orange signal appears in the blue $|52D\rangle$ time window. Some non-negligible ion counts also occur after the two peaks, indicating some spreading of the flight times which are difficult to take into account to analyze level populations.

The Rabi oscillation of this microwave transition, presented in panel (b) of figure III.3, displays one noteworthy feature. The single-site Rabi frequencies exhibit a noticeable gradient across the array, with a 5% difference in value between the top-left and bottom-right corners of the lattice. We attribute this phenomenon to a gradient of microwave power across the array. With various gilded electrodes covering the inside of the sapphire structure, a microwave standing wave emerges during the pulse (of 4.6 mm-wavelength) and one of its nodes happens to be near the lattice. The spread in Rabi frequencies seems to explain the spatial variations of the spectra's amplitudes. In the spectrum sequence, not all sites experienced a π pulse, leading to reduced amplitude in some regions of the array.

Overall, we retain from this characterization an efficient transfer of population from $|52D_{5/2}, m_j = 5/2\rangle$ to $|52F, m = 2, m_s = 1/2\rangle$. Even though we witness a gradient in Rabi frequencies across the array, we reach an overall efficiency of $\overline{\eta_{52F}} = 94\%$, which is satisfactory and allows us to proceed with the circularization.

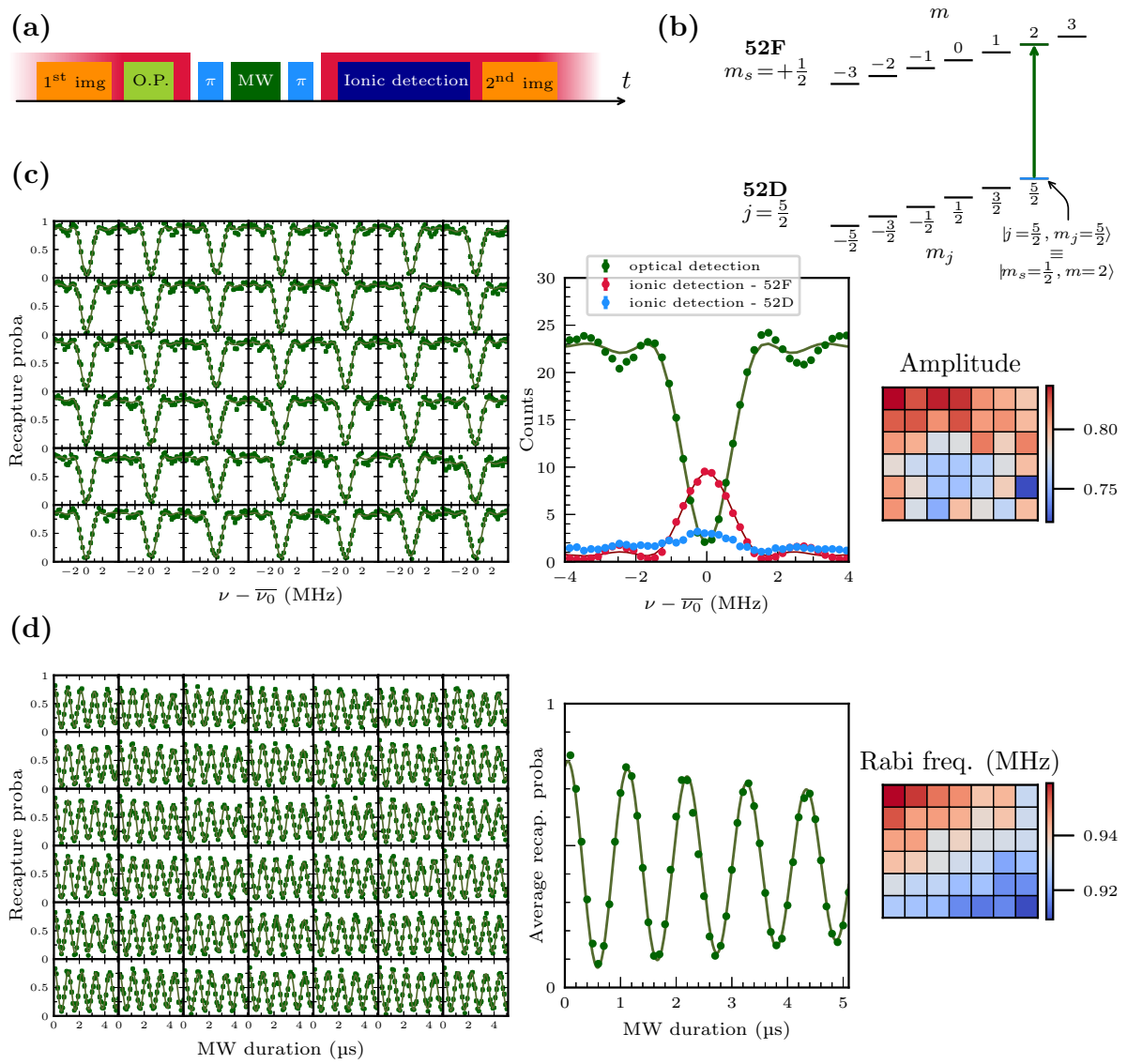

Figure III.3: Microwave transition to $52F$. **(a)** Experimental sequence. **(b)** Level structure, highlighting the selected atomic transition. **(c)** Spectrum of the transition, with the horizontal axes centered on $\overline{\nu_0}$, the central frequency of the average optical signal. Site-resolved data are fitted with the theoretical sinc line shape and yield the spatial distribution of amplitudes plotted in the mosaic. The optical recapture signal, averaged over all sites, indicates that, on average, 20.8 atoms are excited to $|52F\rangle$ at resonance. The ionic signals are presented for comparison, but overlap between the detection windows of the two levels involved make them harder to analyze. **(d)** Rabi oscillations, exhibiting a gradient of Rabi frequencies across the array linked to inhomogeneity in the microwave power, probably explained by a nearby node in the microwave standing wave pattern.

III.2 Circularization to $|52C\rangle$

The final part in the preparation of circular atoms is the transfer of population from the low-ℓ $|52F\rangle$ state to the circular state $|52C\rangle$. Its purpose is the absorption of many quanta of angular momentum by the atoms, in a well-controlled manner, in order to reach the state $|52, m = 51, k = 0\rangle = |52C\rangle$. This procedure is not as straightforward as the optical and microwave transitions previously addressed. We rely on a rapid adiabatic passage induced by a σ_+-polarized radio-frequency field. The adiabatic passage carries the atomic population up the lower-right diagonal of states in the Stark multiplicity (cf. fig. I.2 of chapter 1). This method has been used for a long time in our team, and its robustness and efficiency were demonstrated in numerous results [170, 171, 187]. Since it has been described extensively in previous works [123, 135, 144, 145], we only recall here its basic general principle and its application to the $n = 52$ manifold of rubidium 87. We then discuss in more details its technical implementation, in its recently improved, "adiabatic passage B" version, and show the results it leads to in the setup.

III.2.1 The adiabatic passage procedure

To go over the basics of the circularizing adiabatic passage, we consider a hydrogenic Rydberg manifold with principal quantum number n. A fixed electric field $\mathbf{F}$ lifts its degeneracy and defines the quantization axis. The purpose of the procedure is to climb the lower-right ladder of the manifold: we therefore only consider the atomic states $|n, m, k = m + 1 - n\rangle$ along this diagonal, written in the parabolic basis introduced in chapter 1. Such states are unambiguously defined by m, or equivalently by $k = m+1-n$, so that we write them $|m\rangle$. The end goal is to reach, from a low-m/high-k state, the circular level where $m = n - 1$ and $k = 0$. To do so, we couple these states with one another through a pure σ_+-polarized radio-frequency field. We denote its frequency ω and write N the number of photons in its mode. Moreover, the atomic states have – considering their linear Stark shifts only – evenly-spaced bare energies $E_m = k \times \hbar\omega_0$, where $\hbar\omega_0 = 3nea_0F/2$ according to equation (I.23) of chapter 1.

The adiabatic passage is best understood in the dressed-atom formalism [188]. We describe the full atom-field system by state vectors $|m, N\rangle$. The radio-frequency field couples the neighboring states via single-photon transitions. More specifically, a state $|m, N\rangle$ is coupled to both $|m + 1, N - 1\rangle$ (absorption of a photon) and $|m - 1, N + 1\rangle$ (emission of a photon). We can thus restrict the analysis to the subspace of fixed total energy $\{|m, N_0 - m\rangle\}$, where $m \in \{0, ..., n - 1\}$ and $N_0 \gg 1$ (high-intensity limit). We introduce the detuning $\Delta = \omega_0 - \omega$ and coupling strength $\Omega = 3nea_0\mathcal{E}_{\mathrm{RF}}/\sqrt{2}$, where $\mathcal{E}_{\mathrm{RF}}$ if the field amplitude. The Hamiltonian of the system can then be written [189],

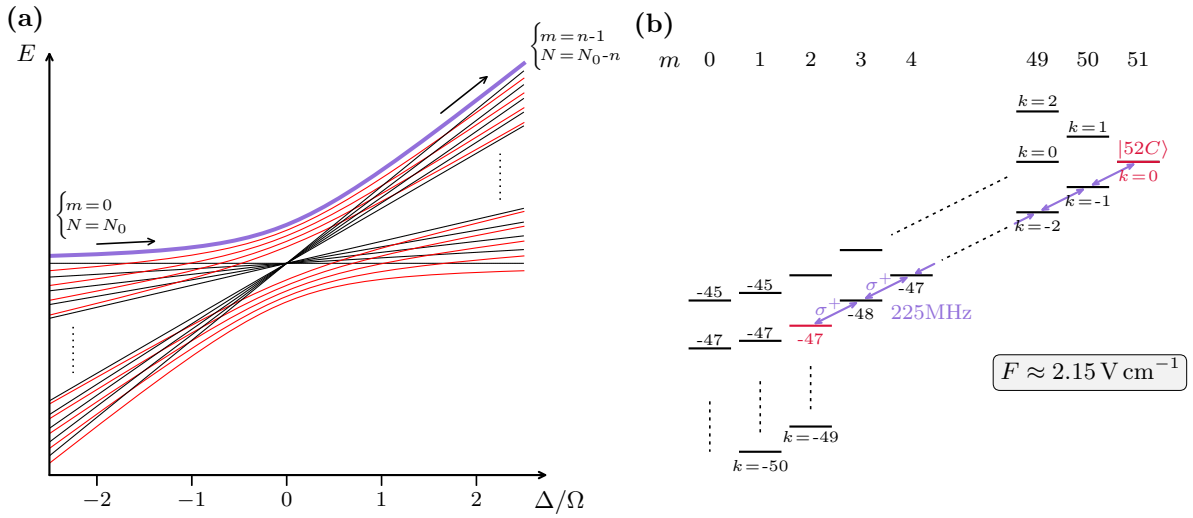

Figure III.4: Adiabatic passage for circularization. **(a)** Eigenenergies of the atom-field system, in the hydrogenic model and for a generic n, as a function of the detuning between the RF field frequency and the atomic level spacing. Black lines represent the eigenenergies without atom–radio-frequency coupling, while the coupled states are shown in red. The highest-energy level, plotted in purple, evolves from $|m = 0\rangle$ to $|m = n - 1\rangle$ as the detuning is ramped up. **(b)** Level structure involved in the adiabatic passage for rubidium. In 2.15 V/cm, the state $|m = 2, k = -47\rangle$ happens to lie, thanks to its quantum defect, on the lower ladder of the manifold, at an energy that matches the ladder spacing. Starting from this level, the successive absorption of 49 σ_+ photons through the adiabatic passage leads to $|52C\rangle$.

in matrix form:

$$H = \hbar \begin{bmatrix} \ddots & \ddots & \ddots & & 0 \\ \ddots & (m-1)\Delta & -i\Omega\, a_{m-1} & 0 & \\ \ddots & i\Omega\, a_{m-1} & m\Delta & -i\Omega\, a_m & \ddots \\ & 0 & i\Omega\, a_m & (m+1)\Delta & \ddots \\ 0 & & \ddots & \ddots & \ddots \end{bmatrix}, \tag{III.9}$$

where a_m depends only on m. Its eigenenergies are analytically tractable for any field configuration (Ω, Δ).

In the large detuning limit $|\Delta/\Omega| \gg 1$, the effect of the field coupling on the bare atomic energies becomes negligible. Two possibilities then arise:

- if $\Delta > 0$, the eigenenergies are ordered with m, and $|m = 0\rangle$ has the lowest energy,
- if $\Delta < 0$, the order of the energies are reversed: $|m = n - 1\rangle$ now has the lowest energy among atomic states.

The principle of the adiabatic passage is now clear: it consists in ramping the detuning from a large negative value to a large positive value[3]. If this is done in an adiabatic way, an atom initially in $|m = 0\rangle$ ends up in $|m = n - 1\rangle$, i.e., in the circular state. This procedure is illustrated in figure III.4 (a), where we plot both the bare (in black) and dressed (red) eigenenergies of the system as a function of the detuning. The anti-crossing of the coupled states is clearly visible, and the level followed by the atom is during the ramp is highlighted in purple.

The complete adiabatic procedure then splits into three parts, starting from an atomic population in $m = 0$ and zero field amplitude:

1. the radio-frequency is turned on progressively, with a fixed large negative detuning, so as to dress the atoms: this is done adiabatically provided that $|d\Omega/dt|/\Delta^2 \ll 1$,

2. the detuning is ramped up: the atoms remain in the highest-energy eigenstate if $|d\Delta/dt|/\Omega^2 \ll 1$ [190],

3. the field amplitude is brought back to zero, under the same condition as the first step.

Following these steps in the right adiabatic conditions should therefore lead to a perfect population transfer to the circular state.

III.2.2 Technical implementation

In practice, carrying out the adiabatic passage with non-Hydrogen atoms requires to address some additional details. Indeed, as described in chapter 1, low-ℓ Rydberg states of rubidium are affected by quantum defects: the ladder of states used for the adiabatic transfer only exhibits regular spacing for $m \geq 3$. We circumvent this issue with a careful choice of electric field and initial level: at 2.15 V/cm, the $|52, m = 2, k = -47\rangle$ state happens to be 225 MHz below $|m = 2, k = -48\rangle$, while the spacing in the ladder is also 225 MHz. Figure III.4 (b) shows the relevant level structure in this specific field. The $|m = 2, k = -47\rangle$ level is highlighted in red. It will be the starting point of the atoms in the adiabatic passage. $|52F, m = 2\rangle$ was specifically selected as an intermediate level in the full excitation procedure because it branches to $|m = 2, k = -47\rangle$ when the electric field is switched on. In the experiment, we therefore ramp up the electric field right after the 52D-52F microwave transfer. We do so fast enough (in 0.2 µs) so that anti-crossings with other levels are avoided and no purity losses are induced by the process. We keep **F** aligned with the magnetic field while doing so to preserve the quantization axis along x.

To proceed with the adiabatic transfer, we scan the detuning by actually ramping the electric field, instead of changing the RF frequency. We keep the RF frequency

[3]In adiabatic passage A, the detuning was ramped from a positive to a negative value.

at 225 MHz, while the static electric field strength sets the actual detuning: the resonance condition is fulfilled when $F = 2.15$ V/cm. At this field strength only, the ladder effectively extends from $|m = 2, k = -47\rangle$ to the circular state and its spacing matches the RF frequency, as pictured in fig. III.4-(b). A field ramp from 2.05 to 2.25 V/cm is then enough to go from a large negative detuning to a large positive one and implement the adiabatic passage. Through this process, the atoms absorb a total of 49 photons and end up in $|52C\rangle$.

The radio-frequency field is created by four dedicated electrodes within the sapphire cube, shown in yellow in figure II.2 of chapter 2. Specific RF circuitry allows us to control the amplitude and relative phases of the signals emitted by each of the four electrodes, numbered from 1 to 4. Due to some malfunction with electrode 3, we actually only use the 1-2 pair to create the σ_+ field. A signal generator (Synth-300, Acquitek) creates the 225 MHz signal, which is split between separate channels leading to the electrodes. On each channel, digitally-controlled mixers tune the RF amplitude (and bias-tees, also digitally-controlled, apply DC voltages to the electrodes to fine-tune the static field throughout the experimental sequence). The envelope of the RF pulse is shaped by an arbitrary waveform generator (33521A, Agilent Technologies) controlling mixers on each channel, so as to create a smooth pulse whose amplitude has a trapezoidal shape over time, fulfilling the adiabatic condition on its activation and extinction. A phase-shifter on channel 2 sets the relative phase between electrodes 1 and 2, in order to be able to only have σ_+ polarization at the atoms position. This point is actually crucial, as any residual σ_- polarization could hamper the efficient transfer of population to $|52C\rangle$. The absorption of a σ_- photon removes the atom from the ladder via the $|m, k\rangle \rightarrow |m-1, k+1\rangle$ transition, and it will never reach the circular state. The optimization of the procedure is described below via the measurement of the circular state purity.

III.2.3 Circular state purity

To assess and optimize the performance of the adiabatic passage, we rely on microwave spectroscopy. To already set the stage for interaction measurements, we use here a rearranged array of 6 pairs of atoms. The geometry of the system is drawn in figure III.5 (c). The distance between neighboring pairs is 30 µm, while the distance between two atoms within a pair is 10 µm. To inhibit interactions, we rotate the full array in the $(x - z)$ plane so that the inter-atomic axis is at the angle $\theta_0 = 54.7°$ with the electric and magnetic fields (along x), which define the quantization axis. As explained in chapter 1, in this configuration the dipole-dipole interactions are zero. We also proceed using the ionic detection only, as optical detection of circular states implies going back down to the ground state from the circular levels, which adds technicalities to the sequence and reduces the overall detection efficiency. We only explore the optical detection of circular states once the circularization has been properly optimized through the ionic detection method and once the trapping of Rydberg states is implemented.

The sequence designed to assess the purity is shown in figure III.5 (a). We prepare the rearranged array of cold atoms, then turn the tweezers off and carry out the laser excitation and D-F microwave transition. The electric field is ramped up to branch $|52F\rangle$ to $|52, m = 2, k = -47\rangle$, after which the adiabatic passage is carried out, in version B (the most recent, efficient one). We can then apply a microwave probe pulse or not, and we finally trigger the ionic detection. The whole process, from the ground state to ionization of the circular atoms, takes less than 60 µs. During this time, atoms move by less than 5 µm, which is negligible compared to the electric field structure. The efficiency of the ionic detection is therefore not affected by the free-flight of the atoms in this experiment.

Within a single manifold, high-m states ionize at a significantly higher field than low-ℓ levels, as can be seen in the ionic signals of figure III.1 (b). The first step in optimizing the adiabatic passage is therefore to maximize the time at which we record ions during the ionizing electric field ramp. The fine adjustment of the adiabatic passage parameters (radio-frequency pulse shape, amplitudes and phase for polarization purity, field ramp amplitude and timings) is then done through microwave spectroscopy between the $n=52$ and $n=50$ manifolds.

The relevant level structure is drawn in panel (b): thanks to the first step of rough optimization of the circularization, most atoms end up, after the adiabatic passage, in the three levels of highest m in the manifold, among which $|52C\rangle$. Using the notations of chapter 1, the two levels closest to $|52C\rangle$ are called "elliptical states" and written $|52E^+\rangle$ and $|52E^-\rangle$. An imperfect σ_+ polarization or an insufficient RF power during adiabatic passage lead to populating these elliptical states instead of $|52C\rangle$. The three levels cannot be distinguished via the ionic detection, as their ionization thresholds are almost identical. However, the ionic detection discriminates very well high-m states of different manifolds, as illustrated by the ionization signals of different circular states in figure III.1 (b). We write p_n the counts recorded on average in the time window allotted to the high-m states (among which $|nC\rangle$) of manifold n.

To assess the purity of the circular state preparation, we therefore use a two-photon microwave transfer to $n = 50$, which serves as a probe of the population in the three high-m levels of the 52 manifold.[4] Thanks to their differential Stark shifts, in a field of ~ 2 V/cm, the transitions $|52E^+\rangle \rightarrow |50E^+\rangle$, $|52C\rangle \rightarrow |50C\rangle$ and $|52E^-\rangle \rightarrow |50E^-\rangle$ are each approximately ~ 4 MHz apart. We use this property to estimate the population distribution resulting from the adiabatic passage. For a single microwave frequency, we measure the transfer from $n = 52$ to $n = 50$, defined from the ionic counts as $p_{50}/(p_{50} + p_{52})$. Scanning the frequency of the microwave probe pulse over 10 MHz around the $|52C\rangle \rightarrow |50C\rangle$ frequency (99.279 GHz) yields a spectrum with three peaks, one for each of the three $|52E^+\rangle \rightarrow |50E^+\rangle$, $|52C\rangle \rightarrow |50C\rangle$ and $|52E^-\rangle \rightarrow |50E^-\rangle$ tran-

[4]We choose this specific two-photon transition for various reasons. First, the two ionic arrival time windows for $n = 52$ and $n = 50$ are more separated than those of 52 and 51 or 52 and 53. Moreover, black-body-induced transfers to neighboring manifolds would quickly reduce the contrast of the $n = 52 \rightarrow n = 51$ transition spectrum in this room-temperature setup.

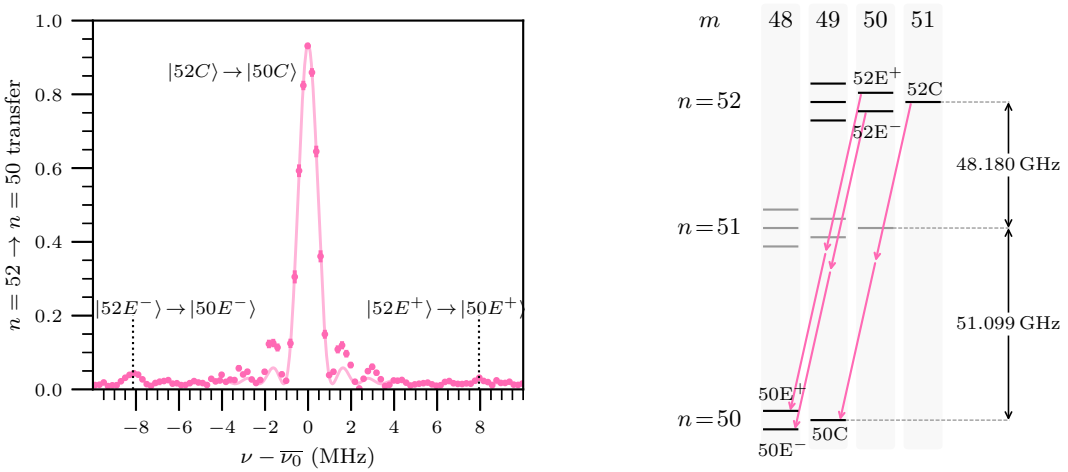

Figure III.5: Spectroscopic probe of the circular state purity. **(a)** Experimental sequence, with the corresponding evolution of the electric field, switched on after the D-F transfer to branch $|52F\rangle$ to the starting level for the circularization. **(b)** Atomic levels involved in the 2-photon microwave probe of the circular state purity. The pink arrows depict the three 2-photon transitions probed in the spectra. **(c)** Geometry of the atomic arrays for this experiment. The tweezer lattice is shown in red dots. The rearranger places atoms on a sub-lattice of six pairs, used for the circular purity measurement. The angle between the quantization axis and the inter-atomic axis is chosen to inhibit interactions within pairs. **(c)** Spectrum of the microwave probe after careful optimization of the adiabatic passage: the elliptical-elliptical peaks are almost indiscernible, indicating a good circular state purity.

sitions. The relative heights of the three peaks are roughly proportional to the population distribution among the three levels at the end of the circularization. We can then precisely optimize the adiabatic passage parameters by maximizing the circular-circular peak while minimizing the two elliptical-elliptical ones.

The optimal purity was reached with a radio-frequency pulse of total duration 4 µs, which comprises the 1 µs ramp times to switch it on and off adiabatically. The electric field ramp has a 0.2 V/cm amplitude and lasts 2 µs. These parameters fulfill the adiabatic conditions previously discussed and are shown in the figure.

The full spectrum obtained after complete optimization of the circularization is plotted in figure III.5 (c). The three peaks are labeled according to their corresponding atomic transitions. We fit each of them with the theoretical line-shape obtained from a square pulse. The microwave probe pulse duration used here is 0.9 µs. We note that the data does not perfectly fit the sinc model, indicating that the pulse duration was slightly different from the optimal π-pulse for the central peak. We can nevertheless

estimate the amplitudes A_-, A_{C-C} and A_+ of the three peaks:

$$A_- = 0.031 \pm 0.003, \quad A_{C-C} = 0.92 \pm 0.02, \quad A_+ = 0.015 \pm 0.004. \tag{III.10}$$

We deduce from these amplitudes the circularization efficiency, corresponding to the ratio between the amplitude of the central peak and the sum of the three amplitudes:

$$\overline{\eta_{52C}} = \frac{A_{C-C}}{A_- + A_{C-C} + A_+}. \tag{III.11}$$

In conclusion, the adiabatic passage is carried out in 4 µs, with a satisfactory efficiency of:

$$\overline{\eta_{52C}} = 0.95 \pm 0.01. \tag{III.12}$$

Some useful information can also be derived from the ionic counts. Over the span of the spectrum, the total number of detected atoms is stable and around $p_{\text{tot}} = p_{50} + p_{52} = 6.4$. This is in good agreement with what we expect, given the limited room-temperature lifetime of circular states. Over the 50 µs delay between their creation and their ionization, the atoms undergo black-body–induced transfers, mainly to their neighboring manifolds. We therefore have significant population transfer from $n = 52$ to $n = 51$ and $n = 53$, and from $n = 50$ to $n = 51$ and $n = 49$ before the ionization. Using the rate equations of appendix A.1 to simulate the population evolution between the manifolds, we estimate that, at 300 K and in 50 µs, 29% of the atoms transfer to a neighboring circular state. We can then deduce the expected number of detected atoms, taking into account the number of rearranged sites (12), the laser, microwave and adiabatic transfer efficiencies (85%, 92% and 95%) and the lifetime of the circular atoms. We get an expected number of atoms of 6.3 on average in each repetition of the sequence. This number matches the one we measure, indicating again near-perfect global efficiency in our ionic detection.

To sum up, the complete circularization protocol takes approximately 10 µs to elevate the single atoms from their ground state to $|52C\rangle$. The laser excitation to $|52D\rangle$ is carried out in less than 1 µs and the microwave transfer to $|52F\rangle$ in 0.5 µs. It then takes 0.5 µs to switch on the electric field diabatically, thus branching $|52F\rangle$ onto the starting level of the circularization, and an additional 1 µs to let the static field settle. Adding the 4 µs of the RF adiabatic passage and some delays between all these events, we get a total duration of 10 µs. The single-atom total preparation efficiency, from ground to circular state, is derived from those of the three successive steps:

$$\begin{aligned} \overline{\eta_{\text{prep}}} &= \overline{\eta_{52D}} \times \overline{\eta_{52F}} \times \overline{\eta_{52C}} \\ &= 0.73 \pm 0.02 \end{aligned} \tag{III.13}$$

Although adequate for experiments on interactions within pairs of atoms, this efficiency is obviously not suitable for the creation of large, defect-free ensembles of circular atoms. Even with some recurrent but time-consuming efforts spent on the

optical pumping and laser excitation optimizations that could bring it to 79%, the efficiency would not be high enough to properly elevate large arrays to circular levels. Let us mention here some prospective ways in which the full circularization could be improved. First, more advanced beam-shaping of the Rydberg lasers [111] could improve the homogeneity of the transfer to Rydberg states. The simple laser excitation π-pulse could be replaced by a stimulated Raman adiabatic passage (STIRAP) [191–193], which is less demanding in terms of parameter optimization. Secondly, a better control of the microwave standing wave pattern in the experiment would reduce the gradient of microwave Rabi frequencies, thus improving the overall D-F transfer. Lastly, known methods of optimal control [194] could replace the radio-frequency adiabatic passage. In such schemes, a circularization fidelity above 96% is reached, through a process that takes about 100 ns. All in all, several techniques could greatly improve the performance of the circularization in this setup and make it adequate for experiments involving defect-free ensembles of tens of circular atoms.

To conclude this part, let us note that the setup allows us to de-circularize and then de-excite the circular atoms back to their ground state. By simply applying the symmetric electric field ramp and the same radio-frequency pulse as in the circularization, the atoms are brought back down to the base of the manifold, after which we can turn off the electric field and apply microwave and laser π-pulses to reach the ground state. With some extra care on the settling of the electric field before the $F - D$ transition, the de-excitation efficiencies are the same as the excitation ones. We will make use of this ability to study the circular atoms through the optical detection scheme, in order to get site-resolved measurements and diagnoses.

III.3 Individually-trapped circular atoms

Having tackled the preparation of circular atoms, we can turn to the matter of their individual trapping, a pre-requisite for appropriate control of their interactions over long timescales. To trap individual circular atoms, we use bottle beams (BoBs), that were already mentioned in chapter 2. We recall that, thanks to a good understanding and control of the SLM phase masks designed for their implementation, the arrays of BoBs we create display low aberrations. The BoBs are defect-free and homogeneous in shape across the 100 µm × 100 µm region of the experiment. To provide more insight into the particular shape of a bottle beam, we start this section by detailing its geometry. We then proceed with the demonstration of the trapping of circular atoms, before discussing the *in situ* characterization of the traps and the coherent manipulation of individual circular atoms within them. All of the data shown here was acquired with the adiabatic passage B, except in the last section where adiabatic passage A was still in use.

III.3.1 Optical trapping of circular states

As explained in the first chapter, Rydberg atoms interact with off-resonant radiation through the ponderomotive effect. In a given intensity distribution $I(\mathbf{r})$, a Rydberg

atom is subjected to the classical potential

$$V(\mathbf{r}) = \frac{e^2}{2m_e c\epsilon_0 \omega^2} I(\mathbf{r}) = h \times 1.52 \text{ MHz}/(\text{mW}\mu\text{m}^{-2}) \times I(\mathbf{r}). \tag{III.14}$$

The second part of the equation is written for a wavelength of 821 nm, as is the case in the experiment. In an inhomogeneous light field, Rydberg atoms are low-field seekers: they are attracted to regions of lowest intensities. The purpose of the bottle beam is therefore to create a field distribution in which a small volume with low intensity is surrounded in all directions by higher intensity. We recall that a single bottle beam is generated by a specific phase pattern on an SLM, where the incoming beam has a 4 mm waist. A π phase-shift over a radius of 3.35 mm induces destructive interference between the inner and outer parts of the beam when focused by the aspheric lens. Adding the lattice-defining phase mask and the aberration correction to the SLM profile ultimately creates arbitrary arrays of such bottle beams, as shown in the image of figure II.4 in the second chapter.

The bottle beam trap

We focus here on the specific geometry of a single bottle beam. Its theoretical intensity profile is plotted in figure III.6, computed using the 16.3 mm focal length of the aspheric lens for size accuracy. The total power is chosen to be 30 mW, a value similar to what we use in most experiments. The axes are set according to the real orientation of the bottle beams in the setup. The direction of propagation is y, while the transverse profile is in the $x - z$ plane. The beam has an elongated shape and cylindrical symmetry, as shown by the 2D cuts of the figure. It is made up of two lobes of high intensity approximately 13 µm apart along y, linked by an outer "tube" of about 3 µm diameter. Three quantities characterize the bottle beam trap: its depth and its two trapping frequencies.

For a power of 30 mW, the trapping depth is estimated to be 60 µK from athe numerical simulation of its shape. This value corresponds to the height of the trapping potential along diagonals in the $y - z$ cut profile. Indeed, at the edges of the high-intensity lobes, the intensity is not as high as in the transverse ring, and this is where leakage is most likely to happen if the bottle beam is not intense enough. In the leakage direction, we estimate that the height of the trap goes as $\sim$2 µK/mW. For comparison, the height of the ring scales with the total power approximately as 3 µK/mW.

To determine the expected trapping frequencies, we fit the intensity profiles of the beam along two axes, shown in white dashed lines in figure III.6. From the two cuts, we get the estimated transverse and longitudinal frequencies:

$$\omega_t = 2\pi \times 21.3 \pm 1.2 \text{ kHz}, \quad \omega_l = 2\pi \times 7.6 \pm 0.2 \text{ kHz}. \tag{III.15}$$

The harmonic approximation holds true for radial distances $r < 1$ µm and longitudinal positions -3 µm $< y < 3$ µm. Further away from these bounds, the intensity distribution deviates from a quadratic shape, as quartic terms become non-negligible. The

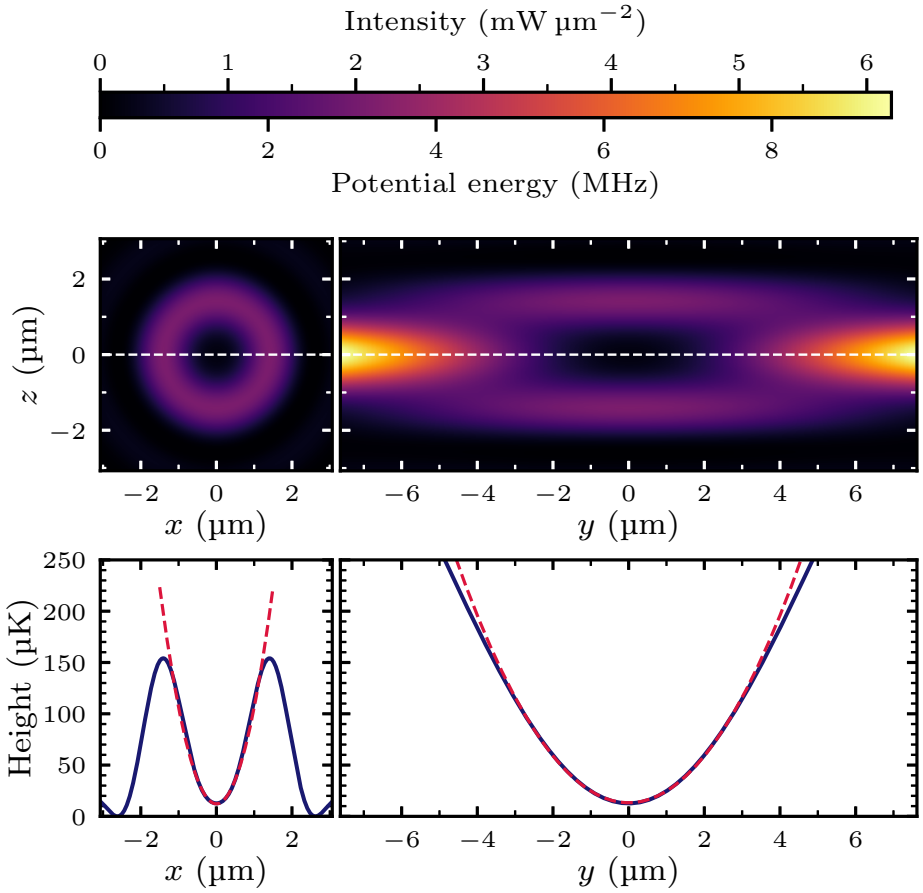

Figure III.6: Bottle beam intensity distribution for 30 mW total power. The harmonic approximation of the profiles are plotted in red dashed lines in the lower panel.

trapping frequencies approximately scale as the square-root of the total power, with potential deviations to this rule because of the trap's imperfect harmonicity. These values are useful to estimate the stability issues for systems of trapped, interacting atoms, as addressed in appendix B.

In the experiment, we are able to create arbitrary arrays of such optical traps. Thanks to a good aberration control, bottle beams have low defects over large, 100 µm-wide arrays. The main limitation of the setup is the number of bottle beams we can implement at once. We are ultimately constrained by the total available power in the laser that generates the three trapping systems (tweezers, moving tweezer and bottle beams). Using trap characterizations presented at the end of this chapter, we estimate that a total of $\sim$ 360 mW can be allotted to the bottle beams. From this value, we infer the expected trapping depths and frequencies as functions of the number of bottle beams implemented, a useful calibration to check the consistency of some experiments. The result is shown in figure III.7, which presents a rough estimation of the depths and transverse frequencies. Adding to the gaussian approximation for the shape of the bottle beams, the SLM diffracting efficiency might slightly depend on the number of traps we create: we suspect that less power goes into the first diffracted order when

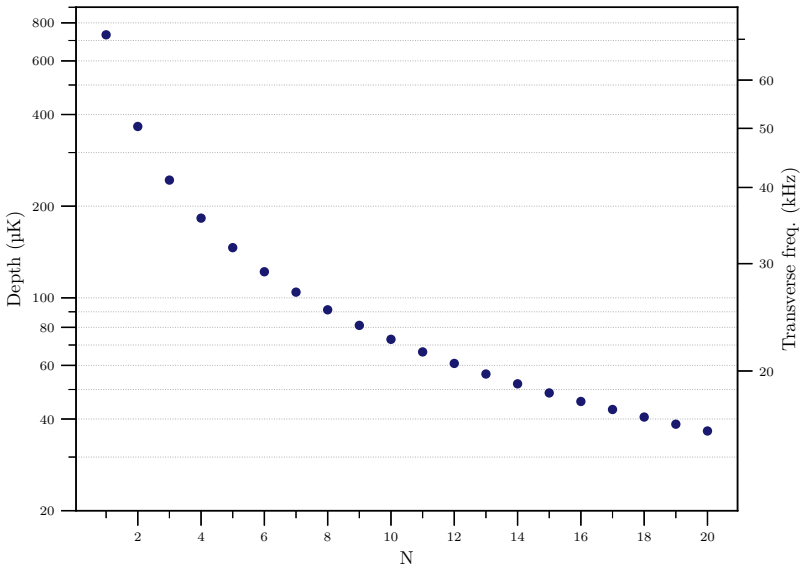

Figure III.7: Computed estimations of the bottle beams' depth and transverse trapping frequency, as functions of the number of sites N generated in the experiment. We plot here the theoretical estimations based on the $\sim$ 360 mW total available laser power and using the scaling laws: $1/N$ for the depth and $1/\sqrt{N}$ for the transverse trapping frequency. However, an-harmonicity in the trap and non-linearity in the SLM diffraction efficiency probably lead to deviations from these indicative values.

we generate 18 BoBs than when we only create two of them. Figure III.7 therefore only provides an indicative assessment of the traps characteristics for different numbers of sites. In the following results, we choose the geometry of the bottle beam array from a trade-off between the available laser power and the atomic temperature. Finally, the bottle beam array is always a sub-lattice of the tweezers, corresponding to the rearranging target. The overlap of the two arrays is regularly adjusted so that the bottle beams are correctly centered onto the tweezers of the target sub-lattice for proper atomic transfer from one trap to another in the experiments.

Demonstration of trapping

To trap circular atoms, and more generally any Rydberg state involved in the experiments, we turn on the bottle beams right after the laser excitation pulse. Low-ℓ Rydberg states, such as $|52D\rangle$ and $|52F\rangle$, also experience the ponderomotive force, just as circular atoms do. The rest of the preparation sequence (microwave transfer and adiabatic passage) is carried out while the atoms are trapped in the bottle beams. We checked that the various preparation steps are not affected by the trapping. No detectable difference was seen in the preparation efficiency whether the Rydberg atoms were trapped or not.

In order to demonstrate that we efficiently capture individual circular atoms, we rely on optical detection. After a variable waiting time τ spent in $|52C\rangle$, during which the atoms are supposedly trapped, we run a second adiabatic passage to de-circularize the atoms. The radio-frequency pulse is the same as before, but the electric field ramp is now the opposite of the one use in the circularization. We then apply a microwave $|52F\rangle \rightarrow |52D\rangle$ π-pulse, turn the electric field off, turn the bottle beams off, and de-excite the atoms to their ground state through the optical transition. At this point, the tweezers are turned back on, and we count the number of recaptured atoms. The full sequence is pictured in figure III.8 (a), in a similar fashion as before. We also run the same acquisition, but without turning on the BoBs.

This experiment constitutes the basis onto which we build the more complex manipulations presented in chapter 4. For its results to be as relevant as possible in subsequent discussions, we carry it out in a similar geometrical configuration as the one used for interaction investigations. The results presented here are therefore not the same as the ones in [123] and [122]. We create here three pairs of atoms, as shown in panel (b) of figure III.8. The rearranger positions the ground-state atoms in the target pairs only, where the six bottle beams are placed. The maximum available amount of power is sent in the six bottle beams, i.e., around 62 mW per trap. Within each pair, the angle between the inter-atomic axis and the quantization axis is equal to θ_0, so that no dipole-dipole interactions between the atoms emerge during the sequence. This specificity is based on investigations presented in chapter 4.

The site-resolved optical data clearly indicates efficient trapping of the circular atoms. Even after a waiting time of several hundred microseconds, recapture is significantly higher than when the atoms are free. The recapture decay is mainly due to black-body-induced transitions to other circular states during the waiting time. The atoms that transfer to neighboring manifolds are not de-excited to their ground state. Even though they might remain trapped in the bottle beams, they result in an inevitable decay of the recapture probability over time. The recapture at the shortest waiting time, of 20 µs, is about 50%. It matches the back-and-forth efficiency of ground-state to circular to ground-state evolution ($\overline{\eta_{\text{prep}}}^2 \simeq 53\%$), and confirms the successful manipulation of the atoms, even in the bottle beams.

To estimate additional losses, we compute the average recapture probability over the six sites and compare it to the theoretical population evolution of $|52C\rangle$, computed numerically for a black-body temperature of 300 K in free space (cf. appendix A.1), taking into account the transfers to elliptical states for improved accuracy. The overlap between the two is shown in panel (d) of figure III.8. The expected evolution is normalized to match the recapture at the shortest waiting time. Over the first $\sim$200 µs, the recapture decay follows the population evolution. After that, we recapture less atoms than we should according to the numerical simulation: at 1 ms waiting time, recapture of trapped atoms is around 3%, when we expect it to be higher than 10%. Some additional exploration would be required to address this issue. In earlier experiments, presented in [122] and [123], we had reached a configuration in which the data

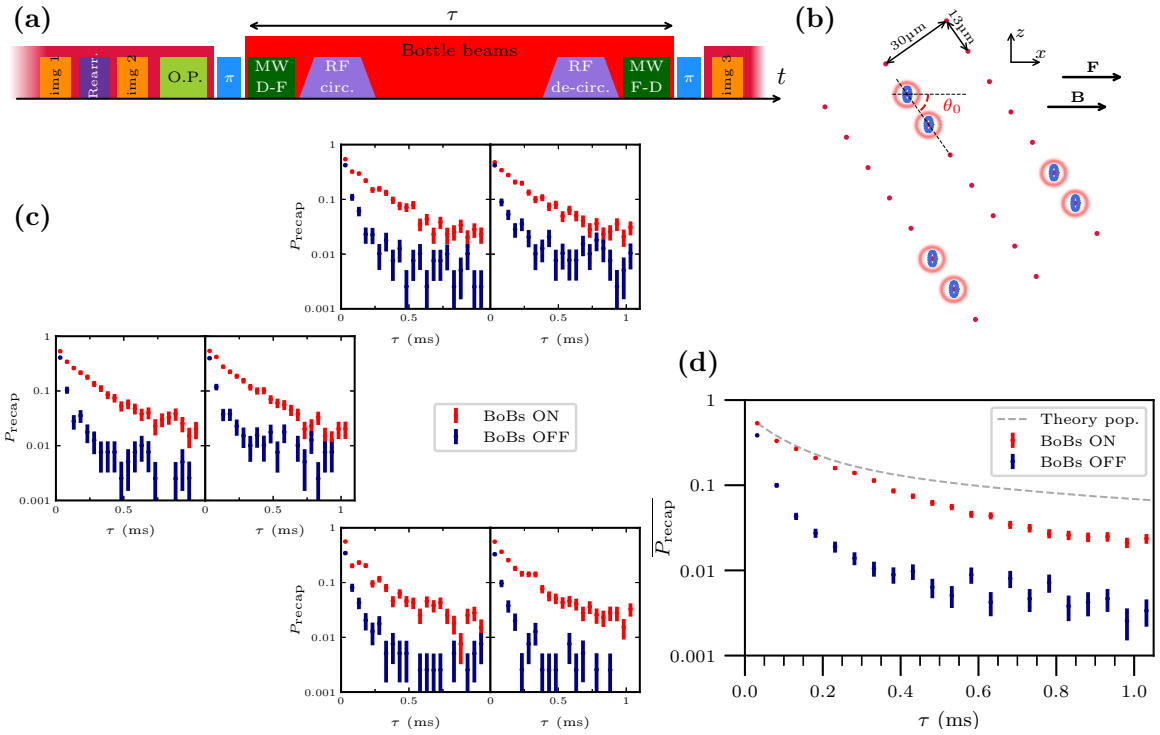

Figure III.8: Demonstration of individual optical trapping of circular atoms. **(a)** Experimental sequence: the bottle beams are activated as soon as the atoms are excited to a Rydberg state, after which they are circularized and left in their traps for a variable delay τ. The atoms are then brought back to their ground state and recaptured in their tweezers. **(b)** Trapping geometry used in this experiment. Three pairs of atoms are implemented, with a spatial arrangement tailored to inhibit interactions between the two atoms of each pair. **(c)** Site-resolved recapture probability, plotted in semi-logarithmic scale, with (red) and without (dark blue) activating the bottle beams. In each site, the evidence of trapping is manifest, with a recapture probability being much larger when the BoBs are turned on. **(d)** Averaged data, compared with the simulated population evolution of $|52C\rangle$ at 300 K. Although the proof of trapping is clear, the comparison with the theoretical population decay reveals some unexpected losses after several hundred microseconds.

followed the theoretical evolution for up to 1 ms of trapping. However, the experiments related to interactions only take place over a much shorter timescale, of tens of microseconds. We therefore do not particularly need to address the unkown decay at long timescales in this work. They could be related to a wrong estimation of the theoretical evolution, as the atoms are not really in a free-space environment. The surrounding structure of electrodes could create a field distribution that enhances the black-body microwave transitions.

III.3.2 Site-resolved coherent manipulation of circular atoms

Now that we have proven the optical trapping of individual circular atoms, we move on to the manipulation and measurement of their internal state while confined inside the bottle beams. Several experiments can be carried out to characterize the trapped circular atoms and check that the ponderomotive action does not affect their properties. These investigations, which study the lifetimes and coherence characteristics of the trapped atoms, are thoroughly described in [123]. Their main conclusion is that the trapping does not modify the single-atom properties in any noticeable way, except for some light-shift induced on microwave transitions at maximal trapping power, when working with a single site.

We only present here the simplest of these experiments, namely the basic driving of the $|52C\rangle \leftrightarrow |50C\rangle$ transition. This is the same transition we addressed earlier to estimate the purity of the circular state preparation. However, we now proceed with trapped atoms and optical detection, instead of the ionic one. Apart from highlighting our ability to act on the atomic levels of the trapped atoms, this new manipulation more importantly demonstrates the site-resolved detection of circular levels, an essential feature of the future quantum simulator. The experimental sequence starts with the preparation of the cold atoms, rearranged into 3 pairs, as in the above trapping experiment. The six atoms are then transferred to $|52C\rangle$ while trapped in their individual bottle beams. The microwave 2-photon pulse to $|50C\rangle$ is applied right after the end of the adiabatic passage. We finally de-circularize the atoms and bring them back to their ground state. Since the adiabatic passage is tailored to the $n = 52$ manifold levels, the atoms transferred to $|50C\rangle$ by the microwave pulse are neither de-circularized nor recaptured in the ground-state tweezers at the end of the sequence. The recapture signal therefore provides a site-resolved, circular state-selective detection method.

The full sequence is shown in figure III.9 (a). By scanning the frequency of the microwave pulse, we first examine the spectrum of the transition, obtained from the computed recapture probability in each site and for each microwave frequency. The six spectra are plotted in (b) and centered on the average resonance frequency $\overline{\nu_0}$. The position of the individual plots follow the general geometry of the atomic arrangement.

The $\sim 50\%$ baseline of the spectra corresponds to the first point, at shortest waiting time, of the trapping experiment, when the recapture reflects the combined efficiencies of the excitation and de-excitation processes. At resonance, the recapture probability drops to a few percents. The origin of the remaining signal can be attributed to a combination of several effects: ground-state atoms that are not excites to Rydberg states and remain in the bottle beams' lobes during the sequence, $|50C\rangle$ atoms that are de-excited back to their ground state, or $|50\rangle$ atoms that undergo black-body transitions to $|52C\rangle$ before the de-excitation. We nonetheless obtain a good contrast on the transition, and therefore good circular-state selectivity with this detection method.

We then drive Rabi oscillations on this transition. The site-resolved data is shown in panel (c) of figure III.9. We measure individual oscillations over 5 periods, with an

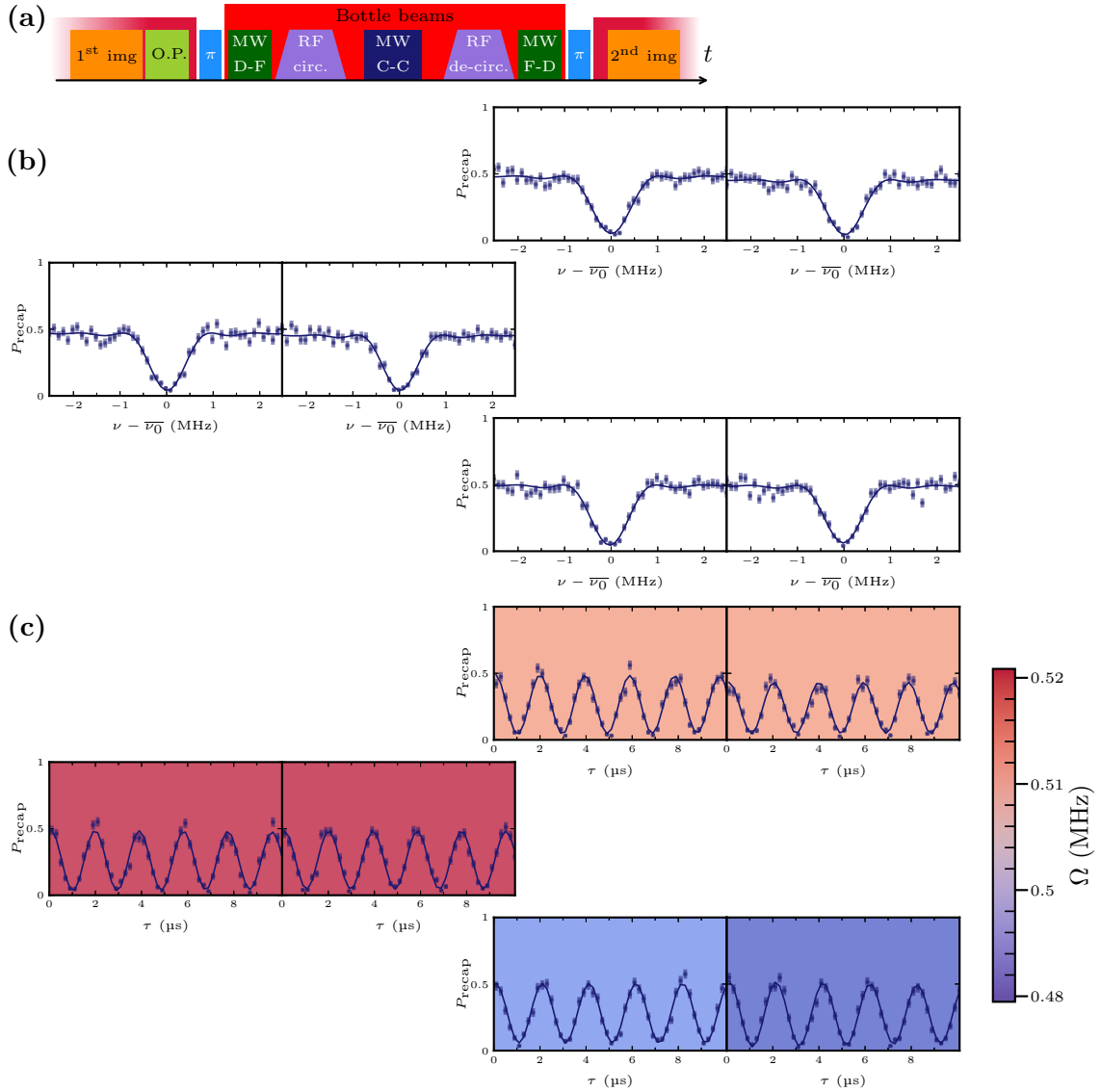

Figure III.9: Circular-circular ($|50C\rangle \rightarrow |50C\rangle$) microwave spectroscopy, with site-resolved detection. **(a)** Experimental sequence, built upon that of the circular-atom trapping experiment. The microwave probe pulse is pictured in dark blue and is followed by the state-selective de-excitation process, so as to optically detect whether each atom was in $|52C\rangle$ or not. **(b)** Individual optical spectra: recapture probability as a function of the microwave frequency. **(c)** Rabi oscillations on the transition. The background color represents the fitted Rabi frequency in each site, thus showing the overall $\sim 7\%$ dispersion in Rabi frequencies because of microwave power gradients.

average Rabi frequency of 0.51 ± 0.01 MHz and no noticeable damping. The individual fitted Rabi frequencies are displayed through the background color of each plot. We recognize here the microwave power gradient first observed when characterizing the $|52D\rangle \rightarrow |52F\rangle$ transition. The atoms of the lower-left part of the experiment display a Rabi frequency about 7% slower than those of the top right corner.

More advanced experiments were carried out on top of this simple microwave spectroscopy. They are all addressed in [123], and we only give here their most important results. By going to longer microwave pulses, we first measured a single-atom damping time of 51 ± 6 µs on the $|52C\rangle \rightarrow |50C\rangle$ oscillations. We then performed Ramsey interferometry experiments with the trapped atoms, still based on the $n = 52 \rightarrow n = 50$ transition. Using the full spatial extent of the trapping region and via the sensitivity of the Ramsey method to dephasing, we measured an electric field variation below 1 mV/cm over the 100 µm × 100 µm extent of the trapping region. Then, working with a single site only, we obtained a characteristic coherence time $T_2 = 61 \pm 8$ µs for a trapped circular atom. This result is compatible with the estimated 0.9 mV/cm electric field noise in the setup, associated with ~ 2 kHz temporal fluctuations on the two-photon transition. We checked that the ponderomotive trapping does not have a detrimental effect on the coherence properties of the atoms. Finally, by triggering the ionic detection of the circular atoms at various instants after their preparation, we reconstructed the population evolution ruled by black-body transfers between manifolds, with and without the bottle beams. No difference was seen in the atomic evolution between the two configurations, and the lifetime of the atoms is therefore not affected by the trapping beams.

Altogether, the measurements presented here, although fundamentally simple, demonstrated the possibility of implementing site-resolved measurements of the coherent manipulation of individual circular atoms. Within the prospect of a quantum simulator based on circular-atom qubits, site-resolution in measurements is a key ingredient to study many-body phenomena. All in all, these results ultimately strengthen our confidence in the long-term success of this project.

III.3.3 *In situ* bottle beam characterization

We conclude this chapter with an *in situ* measurement of the bottle beams' transverse trapping frequency. This experiment is rather tricky to carry out, as it requires a fine adjustment of the traps' positions and results in a low signal-to-noise ratio. We acquired the data presented here for the purpose of Brice Ravon's thesis, before setting up the rearranging beam and with the old version A of the adiabatic passage. However, the conclusions drawn from these results are still valid, since the trap preparation method or optical setup have not evolved since then.

We consider here a non-rearranged array of 3×6 sites. The initial preparation of the ground-state atoms is done as usual, minus the rearranging part. The tweezers are then turned off to proceed with the laser excitation, after which the bottle beams are switched on. The bottle beams are positioned so that their centers have a $+300$ nm offset along x with respect to the ground-state tweezers. Due to this offset, when the bottle beams are turned on, the Rydberg atoms are in non-zero light, with positive potential energy. They start to oscillate within their traps, all in phase, and along the x direction. The rest of the preparation and circularization is done while the atoms

move in their bottle beams. We then implement a release-recapture experiment with the BoBs, as was done with the tweezers. The bottle beams are turned off during a 15 µs delay, and we scan the time at which this is done. If, when switching off the BoBs, the atoms are at the center of their trap with high velocity, they will not be recaptured 15 µs later. However, if they are at one end of their periodic motion as the extinction occurs, with zero velocity but maximal potential energy, they will be recaptured in their BoBs. The total time spent in the bottle beams (before and after the release) is around 200 µs. We finally de-circularize the recaptured atoms and revert to the tweezers. The site-resolved tweezer recapture probability, plotted as a function of the time at which the BoBs are switched off, is shown in figure III.10 (c). Although noisy, each result can be fitted with a damped sinusoidal oscillation. Its frequency is twice the transverse trapping frequency of the bottle beam trap.

The mosaic plot of figure III.10 displays the distribution of trapping frequencies across the array. We find an average value

$$\langle \omega_t \rangle = 2\pi \times (15.7 \pm 0.6) \text{ kHz}. \tag{III.16}$$

One particular outlying trap displays a significantly lower trapping frequency, but the full array is otherwise rather homogeneous. Using the theoretical BoB intensity distribution presented earlier, we can deduce the power effectively input in each bottle beam. From the measured trapping frequencies, we get the average power:

$$\langle P \rangle = 20 \pm 2 \text{ mW}. \tag{III.17}$$

This measurement is in good agreement with the total estimated power sent in the bottle beam array, of about 360 mW. We also conducted the same experiment but with the tweezer-BoB position offset along the z direction, and found similar results. One could finally imagine an identical measurement of the longitudinal frequency ω_l, with an offset along the y axis. However, we expect ω_l to be three times smaller than ω_t. Its measurement would require longer sequences to observe a similar number of oscillations, which would further reduce the signal-to-noise ratio of the data. Furthermore, the estimation of ω_l is not as important as that of ω_t for the scope of this work. We will later address the atomic motion linked to the interactions, which is induced in the $x-z$ plane. The relation between longitudinal motion along y and interactions is only of the second-order kind and will be discarded, as in the formal spin-phonon study of the first chapter. The measurement of the transverse trapping frequency provides enough characterization of the traps for our purposes. Perhaps more generally, it also validates our mastery of holographic optical shaping methods and the precision of the trapping array definition.

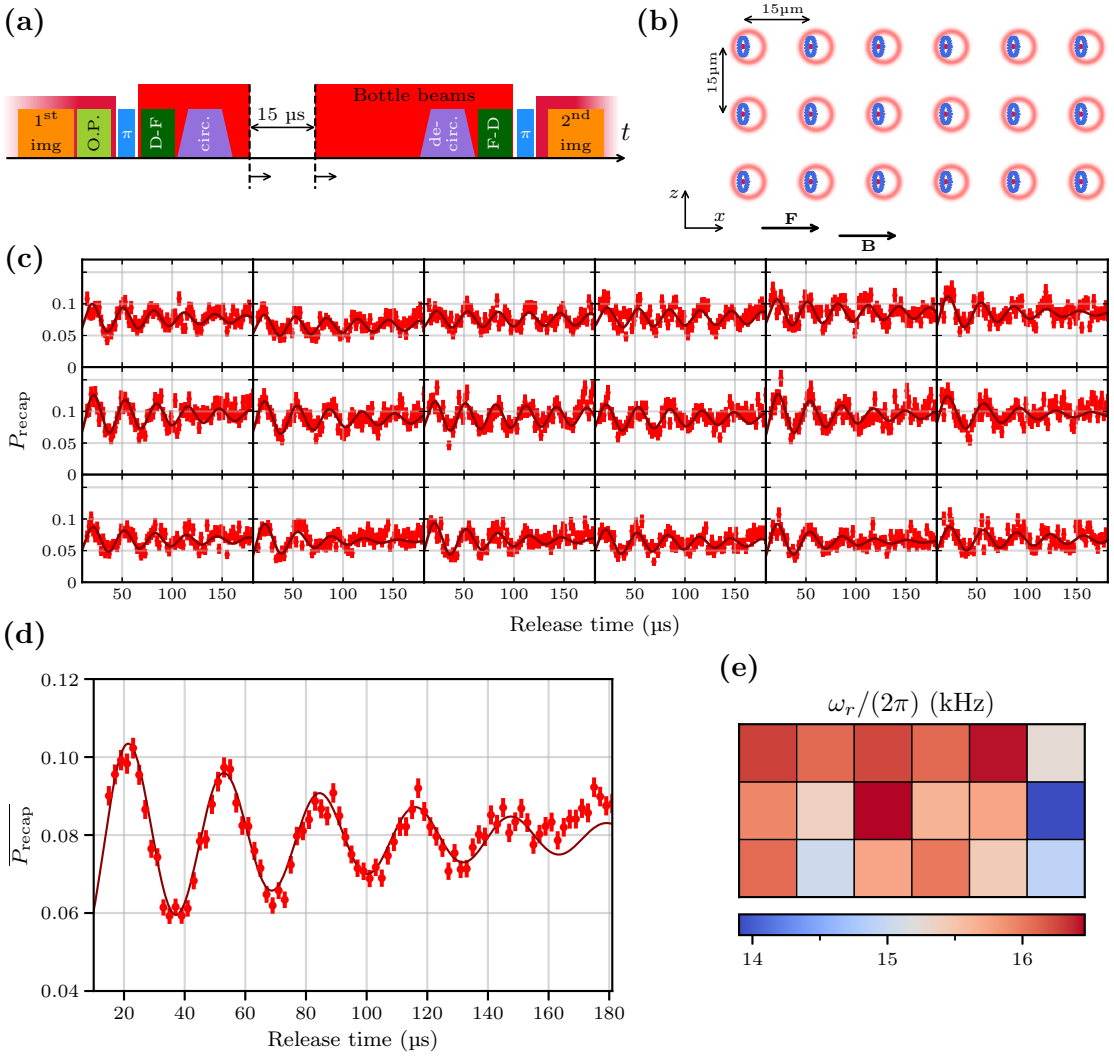

Figure III.10: Measurement of the transverse trapping frequency of the bottle beams. **(a)** Release-recapture sequence, performed while the Rydberg atoms oscillate in their traps thanks to a position offset between the tweezer and BoB arrays. **(b)** Geometry implemented for the measurement. The circular atoms are shown off-centered in their bottle beams to illustrate their initial position when switching on the BoBs. **(c)** Site-resolved recapture data, displaying oscillations that we fit with damped sinusoidal functions. **(d)** Average recapture probability, displaying a clearer oscillation. **(e)** Array of transverse trapping frequencies deduced from the individual results.

Conclusion of chapter 3

The third chapter addressed the "Rydberg" part of the experiment. We presented here the successive processes implemented to excite the atomic lattices to circular levels, along with the specific apparatus and techniques used to trap, manipulate and detect them. The discussion was centered on single-atom results, so as to estimate the overall efficiency of the preparation procedure and to introduce as clearly as possible the several methods that will later be applied to the more complex study of their interactions.

The excitation to circular states is divided in three successive steps, each subject to specific challenges. The three stages go as follows:

1. Two-photon laser excitation to $|52D_{5/2}, m_j = 5/2\rangle$, in 10 G and zero electric field, of unexpectedly low 1.4 MHz Rabi frequency but with satisfactory efficiency $\overline{\eta_{52D}} = 83 \pm 2\%$. Through a careful optimization of the prior optical pumping procedure and a painstaking re-alignment of the two cylindrical excitation beams, it is however possible to reach daily efficiencies higher than 90%.

2. Microwave transfer to $|52F, m = 2\rangle$, still in zero electric electric field and directing magnetic field. Although quite efficient, with a correct transfer of $\overline{\eta_{52F}} = 94 \pm 1\%$ of the atoms, the study of this transition reveals significant microwave power inhomogeneities over the trapping area. After the microwave transfer, the electric field is suddenly ramped up to 2.25 V/cm to branch $|52F\rangle$ onto $|n = 52, m = 2, k = -47\rangle$, the state of the parabolic basis chosen to be the starting point of the subsequent adiabatic passage.

3. Radio-frequency adiabatic transfer, from $|n = 52, m = 2, k = -47\rangle$ to $|52C\rangle$. By ramping the electric field over 0.2 V/cm while applying a radio-frequency field of 225 MHz (and under some adiabatic conditions), the atoms each absorb 49 σ^+-polarized photons and reach the circular level $|52C\rangle$. We probe the efficiency of the adiabatic passage via a two-photon microwave spectroscopy to the $n = 50$ manifold, which yields the circular purity $\overline{\eta_{52C}} = 95 \pm 1\%$.

The whole process takes about 10 µs and has a total cumulative efficiency of around 73%, from ground-state to circular level. To implement and characterize these successive steps, we partly relied on the ionic detection mechanism, a specific sub-system of the setup designed to offer state-resolved detection of the Rydberg atoms, but lacking spatial resolution.

A way to overcome this bottleneck is to rely on the de-circularization of $|52C\rangle$, which leads to a site-resolved – albeit binary – detection of the circular atoms. Through this technique, we are able to measure, in each individual site, whether or not a $|52C\rangle$ atom was present at the outcome of the experimental manipulations. Thanks to this method, we proved that the bottle beams properly trap the circular atoms. Over 200 µs, the atoms are confined in their respective traps and their internal states follow the probabilistic microwave black-body-induced evolution between manifolds. After that, some discrepancy between the data and theory emerges, which is fortunately

irrelevant for the scope of this work, focused on shorter timescales.

We further demonstrated the potential of combining optical detection and circular Rydberg manipulation by presenting the coherent control of circular states, in optical traps, measured with site-resolution. Through a simple microwave spectroscopy of the $|52C\rangle \rightarrow |50C\rangle$ transition, we illustrated the good level discrimination between two circular states offered by the optical detection. At this point, we have arguably created the embryos of the quantum simulator qubits. We can prepare deterministic lattices of circular atoms, coherently drive transitions between two of their circular levels, and detect their internal state with single-site resolution. Although some improvements could be made in the preparation fidelity and trapping efficiency, what we showed in this chapter constitutes a promising set of results and a solid starting point for the study of the interactions.

Chapter IV

Interactions between trapped circular atoms

Having covered the creation of arbitrary, defect-free arrays of trapped circular atoms, we are ready to finally tackle the experimental characterization of their interactions. The fourth chapter describes our most recent results, obtained throughout the major part of my fifth and final year of PhD studies. They address the implementation and measurement of controlled circular-circular interactions. To venture into this new, uncharted territory of circular-Rydberg physics, we decided to simplify our endeavor by two different means. First, we restricted this study to pairs of circular atoms only, so as to characterize the couplings in the most elementary geometric configuration. Secondly, we chose to examine the first-order, resonant dipole-dipole interaction between circular states $|nC\rangle$ and $|(n+1)C\rangle$. As discussed in the first chapter, at atomic distances of several microns, the resonant interactions are of the order of the MHz, whereas the second-order van der Waals interactions are about a hundred times weaker. A spectroscopic characterization of the interactions is therefore easier to carry out in the resonant case, with line splittings and displacements in the MHz range, as compared to tens of kHz in the van der Waals configuration. Moreover, measurements of the pair-state evolution over time also favor the resonant case over the van der Waals one, since the setup currently operates at room-temperature. At 300 K, the lifetime of circular atoms with $n \sim 50$ is of the order of 130 µs. A pair of such states will therefore remain intact for about 65 µs on average, which does not leave enough time to accurately observe pair-state oscillations if the frequency involved is that of the van der Waals interactions.

The interaction regimes explored here are therefore different from those of the long-term circular atom simulator. Their investigation is nonetheless a significant milestone in this context. With this work, we depart from single-atom physics and enter the field of circular atoms in dipole-dipole interactions. With it come several new technical difficulties, that we learn to overcome through these preliminary steps. Furthermore, within the larger global context of quantum simulation efforts, these results can be seen as the first implementation of a new kind of interacting spins, in which the spin states are encoded onto circular Rydberg levels.

All of the results of this last chapter are based on the theory of the resonant, first-order dipole-dipole interaction, introduced in chapter 1. Figure I.4 provides the theoretical framework in which the results presented here can be understood.

The organization of this chapter follows the real progression of our experiments, which allows us to underline the difficulties inherent to the study of circular-circular interactions and to explain the means implemented to overcome them. The data shown in the first experiments was acquired with adiabatic passage A, but we then switched to the settings of adiabatic passage B for improved results. We will signal in the text the moment where version B starts being used.

We start by presenting the specific conditions first chosen to explore the resonant interactions in pairs of circular atoms. We detail the selected geometry and level scheme, and introduce the microwave transition used to probe the relevant coupling. We exhibit the first clear evidence of interactions, first in the frequency domain with microwave spectra, and then in the time domain with driven Rabi oscillations of the pair states. Next, we explore the geometric dependence of the interaction, by varying both the distance between the atoms and the orientation of the pairs with respect to the quantization axis. While doing so, we witnessed some discrepancies between the data and theoretical expectations, explained by atomic motion induced by interactions between the atoms when in low-ℓ states, before the circularization process. This led us to refine the preparation procedure to mitigate these effects and recover data in perfect agreement with the theory. We finally dedicate the last part of this chapter to the observation of spin exchange between two atoms. To reach this result, we implement a site-selective preparation sequence based on the dipole blockade mechanism. Using all the setup's features to their full capacity, we witness the coherent exchange of a spin excitation between two circular atoms, a first step in the realm of circular-atom quantum simulations.

IV.1 Microwave probe of the resonant interaction

IV.1.1 Atomic configuration

As we saw in previous chapters, we are now able to create any arrangement of up to approximately 20 trapped circular atoms. To witness interactions, we focus on pairs of atoms only, which should already exhibit evidences of couplings adjustable via the geometry of the system. The spatial parametrization of a single pair is schematically depicted in figure IV.1. The quantization axis, defined by the orientation of the electric field, is still along x for now. The circular atoms are placed in bottle beams that propagate along y, meaning that they are tightly trapped in the $x-z$ plane and more loosely confined in the y direction. The two geometric parameters that define the interactions within the pair are d, the distance between the two atoms, and θ_{m}, the angle between the inter-atomic axis and the quantization axis. In practice, d corresponds to

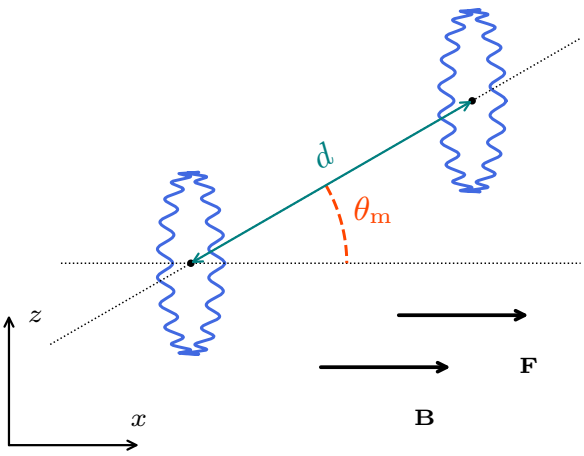

Figure IV.1: Geometric parametrization of the pair interactions for the preliminary microwave spectroscopy experiments. The electric and magnetic fields are along x and define the quantization axis throughout the sequence. The circular atoms are arbitrarily placed with respect to one another via the positions of their traps, which allows us to control and tune both d, the inter-atomic distance, and θ_m, the pair orientation with respect to the quantization axis.

the distance between the two bottle beams' minima. It will be in the 7-16 µm range in all the experiments presented in this chapter to keep the interaction energy close to the MHz. As we have previously seen, a circular atom can move around its trap minimum, so we assume that the inter-atomic distance can fluctuate by hundreds of nanometers around d. To make things clear and maintain consistency with the notations of the rest of the text, we keep d as the distance between the traps minima and write r the actual inter-atomic distance. The versatility of the trapping setup allows us to arbitrarily vary both d and θ_m.

The sequence implemented to probe the pair interactions is pictured in figure IV.2 (a). We proceed with the usual successive steps: the preparation and rearrangement of the ground-state atoms in the desired geometry, their excitation to Rydberg states and their circularization to $|52C\rangle$. The bottle beam array is the same as the tweezer sublattice targeted by the rearrangement procedure. The bottle beams are turned on as soon as the atoms are in $|52D\rangle$ and remain active throughout the rest of the sequence. A microwave pulse of tunable frequency (close to the $|52C\rangle \rightarrow |51C\rangle$ resonance) and with tunable duration is applied right after the circularization procedure. As we will see, it constitutes the probe of the pair interactions. The detection is then carried out by the ionization ramp. We compute, from the ionic signal, the transfer $p_{51}/(p_{51}+p_{52})$ from $|52C\rangle$ to $|51C\rangle$, as a function of the probe pulse parameters (frequency and duration).

To examine the effect of interactions, we implement two different Rydberg trapping schemes, both represented in panel (b) of figure IV.2. The initial ground-state trapping array of tweezers is the same in both cases, and is made of a rectangular lattice of 6×8 sites. In order to establish a reference of the bare, non-interacting $|52C\rangle \rightarrow |51C\rangle$ transition characteristics, the first of the two Rydberg arrangements consists in 12 individual sites, with nearest-neighbors being 25 µm apart. To study interactions, we work with a second design that creates a lattice of 9 pairs of atoms. The pairs are placed so that, within each one, $\theta_{\mathrm{m}} = \pi/2$ and $d = 10$ µm. The minimal distance between two atoms of different pairs is 25 µm. Single-shot images of the ground-state atoms, in both of these configurations and after the rearrangement procedures, are shown in panel (c) of figure IV.2. Given the geometrical analysis of the bottle beams in chapter 3, we expect the depth and transverse trapping frequency of each trap to be ~ 61 µK and ~ 20.6 kHz for the individual atoms configuration (12 BoBs), and ~ 41 µK and ~ 16 kHz for the pairs configuration (18 BoBs).

In these experiments, we restrict the analysis to the evolution of the circular atoms within the $\{|52C\rangle, |51C\rangle\}$ subspace, which we also write $\{|\uparrow\rangle, |\downarrow\rangle\}$. In the field configuration of 10 G and 2 V/cm, the bare single-photon $|52C\rangle \rightarrow |51C\rangle$ transition sits at approximately $\nu_0 = 48.188$ GHz. In the case of a pair of atoms in $|52C, 52C\rangle$, the atomic resonances are displaced by the interactions. As explained in the first chapter, the Hamiltonian of the pair interacting in the direct exchange regime writes

$$\hat{H}/\hbar = \begin{array}{c} \begin{array}{cccc} |\downarrow\downarrow\rangle & |\downarrow\uparrow\rangle & |\uparrow\downarrow\rangle & |\uparrow\uparrow\rangle \end{array} \\ \begin{pmatrix} -\omega_0 & 0 & 0 & 0 \\ 0 & 0 & 2J & 0 \\ 0 & 2J & 0 & 0 \\ 0 & 0 & 0 & \omega_0 \end{pmatrix} \end{array}, \tag{IV.1}$$

where $\omega_0 = 2\pi \times \nu_0$ is introduced to account for the bare energy levels. The Hamiltonian is written here up to first-order in the dipole-dipole interactions, characterized by the pulsation J, which varies with the geometry as:

$$J/(2\pi) = \frac{A(3\cos^2(\theta_{\mathrm{m}}) - 1)}{r^3}. \tag{IV.2}$$

Here, $A = 832$ MHz µm^3 is computed via numerical simulations, so that we can predict the value of J for any configuration (d, θ_{m}). Strictly speaking, second-order van der Waals terms also shift and couple the pair states, but they behave as $1/r^6$ and can be neglected compared to the direct first-order interaction and bare energies. For instance, the level displacement induced on $|\uparrow\uparrow\rangle$ by the van der Waals interaction is about 5 kHz in these conditions. It can clearly be discarded when compared to the other energy scales involved here.

In panel (d) of figure IV.2, we compare the levels schemes of both the interacting (trivial) and non-interacting transitions. In the case of a pair, the initial level $|\uparrow\uparrow\rangle$ is only coupled to the other symmetric eigenstates $|\downarrow\downarrow\rangle$ and $|+\rangle = (|\uparrow\downarrow\rangle + |\downarrow\uparrow\rangle)/\sqrt{2}$, since

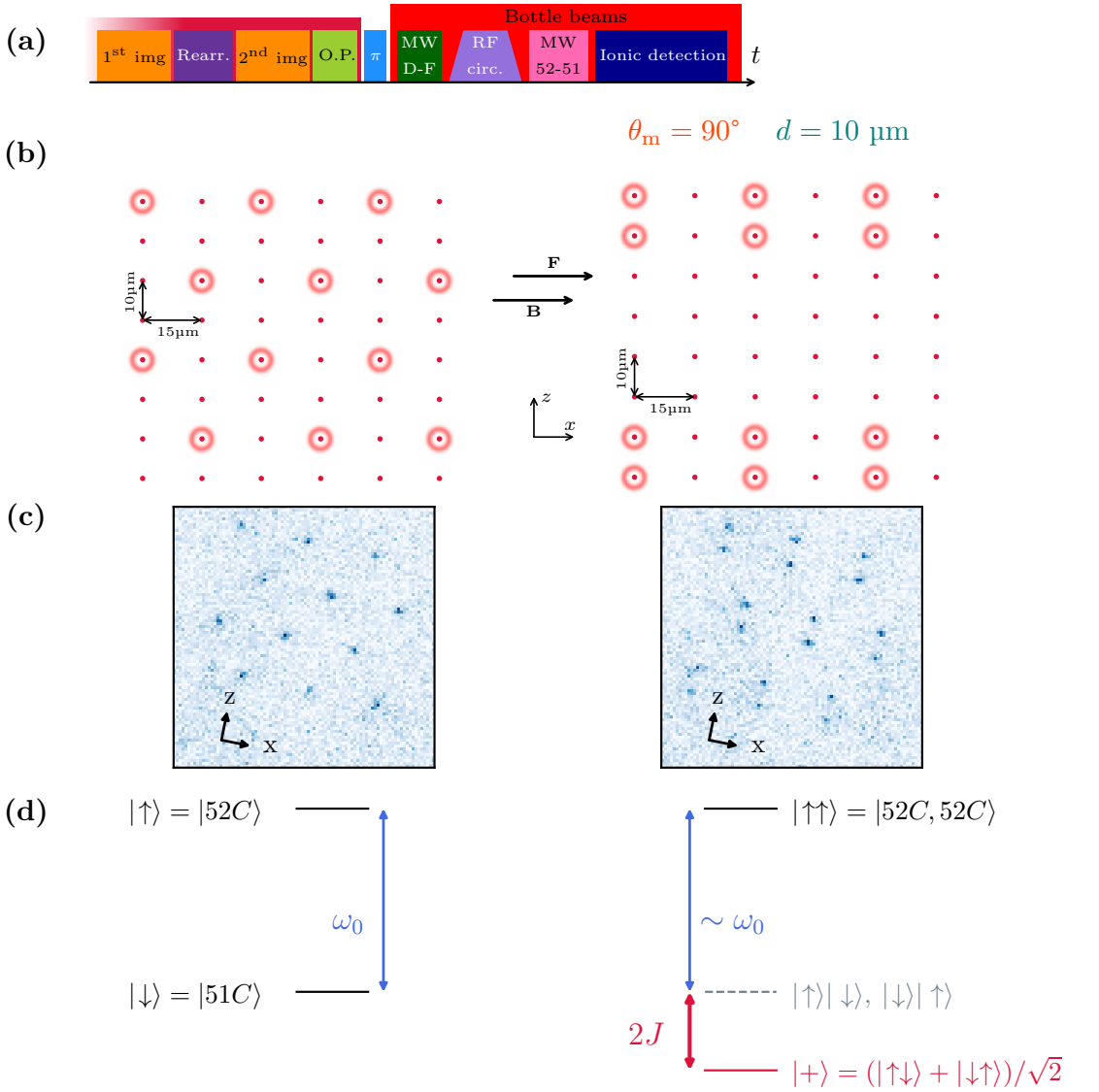

Figure IV.2: Configuration of the microwave spectroscopy experiments designed to probe pair interactions. **(a)** Experimental sequence, starting with the preparation of a rearranged array, followed by the standard successive steps. The microwave probe pulse, of tunable frequency and duration, is pictured in pink. Ionic detection is implemented to compute the outcome of the sequence. **(b)** Drawings of the two trapping schemes used in the sequences. Ground-state tweezers are shown with red dots, while bottle beams are pictured as red torii. The rearrangement targeted in the sequence always corresponds to the bottle-beam sub-lattice. The left scheme implements non-interacting single atoms for reference, while the right one creates pairs of trapped circular atoms. **(c)** Single-shot images of the ground-state atoms in the two geometries. **(d)** Level schemes for both configurations. The pair state $|\uparrow\uparrow\rangle$ is coupled to $|+\rangle$ with a transition pulsation which is close $\omega_0 + 2J$ (up to negligible second-order shifts in the kHz range).

the atoms are symmetrically coupled to the microwave field. The $|\uparrow\uparrow\rangle \rightarrow |+\rangle$ transition that we want to address has a $2J$ frequency shift with respect to the bare transition. Given the geometry ($\theta_{\mathrm{m}} = \pi/2$, $d = 10$ µm), we expect J to be negative (i.e., an attractive interaction) and to be $J = -2\pi \times 0.83$ MHz. This value translates into a 1.67 MHz shift to higher microwave frequencies from the bare transition resonance to the interacting one, as it can be understood from figure IV.2 (d). Given these estimation, a linewidth of about 1 MHz on these spectra should be enough to discern the spectroscopic signature of the interactions.

IV.1.2 Spectroscopic evidence of interactions

We analyze in this section one of the first clear evidences of controlled interactions between circular atoms, acquired in the conditions detailed above. Figure IV.3 shows the result of the microwave spectroscopy probe, displaying the transfer from $n = 52$ to $n = 51$ as a function of the probe pulse frequency, measured by ionic detection, for both the pairs and the single atoms. The horizontal axis is centered on $\overline{\nu_0}$, the bare $|52C\rangle \rightarrow |51C\rangle$ frequency fitted from the single-atom result. The data shown here was generated with microwave pulses of durations 2 µs and 1.3 µs for the single atoms and pairs respectively, with the same power in both cases.

The single-atom transition line displays some features that need to be discussed before moving on to the interaction signal. It is labeled "0" in the following for clear distinction with other peaks. First, it exhibits a significant background, of the order of 15%. It corresponds to the black-body-induced transitions from $n = 52$ to $n = 51$, occurring between the end of the microwave probe and the ionization of the atoms, about 45 µs later. Numerical estimates (cf. appendix A.1) indicate that, after such a delay and at 300 K, an initially pure $|52C\rangle$ population will have transferred by about 12% into $|51C\rangle$, so that $p_{51}/(p_{51} + p_{52}) \simeq 0.15$ at that point. This is in good agreement with the baseline of the spectrum. However, if the initial population were indeed purely $|52C\rangle$, and if the microwave pulse were 100% efficient, we would get a peak reaching $\sim 88\%$ transfer, which is not the case here. The reduced height is probably a combination of imperfections in both purity and microwave transfer efficiency. At the time of these measurements, because of the use of adiabatic passage A, circular single-atom purity was only around 85%, instead of the best achievable 95% with adiabatic passage B. The microwave power inhomogeneity, previously mentioned several times in this text, could account for the rest of the amplitude reduction and explain the total 60% peak height.

The most important information of this graph is the splitting of the bare transition into two lines when working with pairs of circular atoms. We write this frequency splitting $\Delta\nu$. In this case, we obtain two resonance frequencies: one 20 kHz below the bare transition, labeled "1", and the other 1.19 MHz above, labeled "2". The fitting error on the peak frequencies is around 5 kHz in both cases. We identify the high-frequency line as the $|\uparrow\uparrow\rangle \rightarrow |+\rangle$ transition (cf. figure IV.2 [d] for the level scheme). However, the measured $\Delta\nu$ value, of 1.19 MHz, does not properly match the theoretical

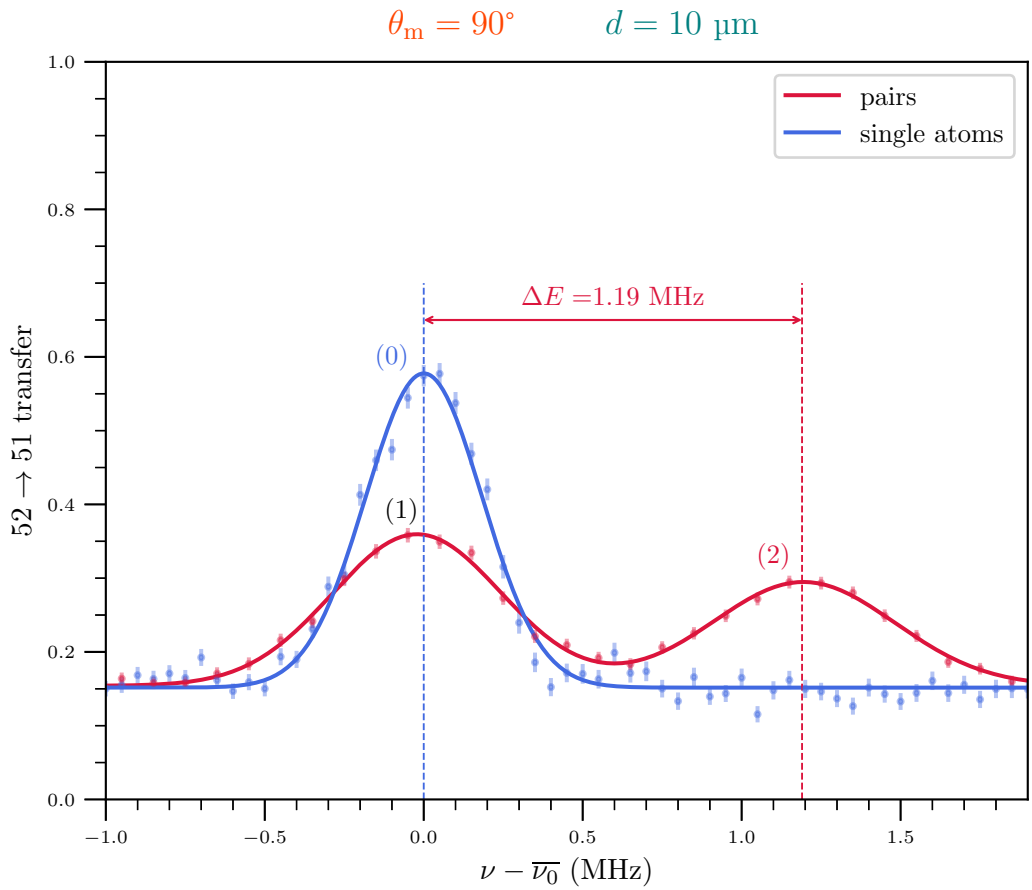

Figure IV.3: Evidence of circular-circular interactions in a microwave spectroscopy experiment: transfer from $n = 52$ to $n = 51$ as a function of the probe pulse frequency. The geometric parameters of the implemented pairs are indicated at the top of the plot. The $\sim 15\%$ background is explained by thermal transfers between multiplicities during the sequence. The reduced height of the single-atom peak accounts for preparation imperfections and microwave power inhomogeneity across the array. We measure a 1.19 MHz splitting between the interacting and non-interacting cases. It is lower than the expected value by 30%, most probably because of undesirable motion in the bottle beams.

1.67 MHz expectation. It implies that, at the time of the microwave probe, the atoms are further apart from one another than expected. The measured value corresponds to an inter-atomic distance of about 11.2 µm, meaning that each atom is off-centered by about 600 nm in its trap during the probe pulse[1]. This hints at unexpected atomic displacements, a first issue that arises when working with interacting atoms. The height of peak 2 is also lower than that of peak 0 because of the intrinsic nature of the pair-state reached. When in $|+\rangle$, we detect $|52C\rangle$ and $|51C\rangle$ with 50% probability each.

[1]The measured interaction strength could also be explained by a distance between BoBs larger than expected. However, given the careful calibrations of the optical system, a 12% error on the inter-site distances is not likely.

It explains why the interaction peak is about half the height of the bare transition one.

We can associate the low frequency peak (peak 1) with two possible transitions. First, it could correspond to the two-photon process $|\uparrow\uparrow\rangle \rightarrow |\downarrow\downarrow\rangle$, via the intermediate state $|+\rangle$. The differential, second-order shift induced by interactions on this transition is estimated to be of about 1 kHz in this configuration, so we expect the 2-photon transition to be resonant at ν_0. Moreover, peak 1 is also associated to occurrences of pairs in which one of the atoms is not initialized in $|52C\rangle$, but in another level $|r\rangle$ instead, because of preparation imperfections. In this case, the properly initialized atom is simply transferred to $|51C\rangle$ at the resonant frequency ν_0: $|\uparrow\rangle|r\rangle \rightarrow |\downarrow\rangle|r\rangle$. Let us note here that we indeed observed a reduced purity when working with geometric configurations made to favor interactions (such as the one studied here). We measured with rectangular lattices of circular atoms that, at $\theta_{\mathrm{m}} = \pi/2$ and when the atoms are 10 µm apart, the circular purity is about 30% lower than that of individual or non-interacting atoms. Peak 1 therefore accounts partly for the diminished circular purity in the interacting regime. This issue constitutes the second difficulty that appears with interactions, after that of the unwanted motion.

Overall, the signal displayed here clearly constitutes an evidence of the circular-circular interactions. Although not exactly in line with theoretical expectations, the atomic behavior we witness here fits our general understanding of the resonant dipole-dipole interactions probed by microwave spectroscopy. Unfortunately, this successful achievement comes at a cost, paid in the form of two different issues created by these very interactions: a reduction in purity and unwanted atomic motion in the traps. We will adress these questions in more details later on, in order to understand their origin and to figure out how to counteract them.

IV.1.3 Driven pair-state Rabi oscillations

To go further with this preliminary experiment, we carry out Rabi oscillations with both the single atoms and the pairs, on the three lines identified above. They allow us to demonstrate a second evidence of circular-circular interactions. The results are displayed in figure IV.4, where we plot the Rabi oscillations of the three peaks. The data was taken with a more powerful microwave field than the one used for the spectroscopy data, so as to drive the transitions faster and measure several oscillations on each line.

We fit the oscillating signals of the bare and interaction transitions (0 and 2 as according to the notations) with a damped sine function and obtain the following Rabi frequencies, labeled according to their respective peaks:

$$\Omega_0 = 2\pi \times (544 \pm 4) \text{ kHz}, \tag{IV.3}$$

$$\Omega_2 = 2\pi \times (699 \pm 9) \text{ kHz}. \tag{IV.4}$$

The pair transition oscillates significantly faster than the single atom one, which is

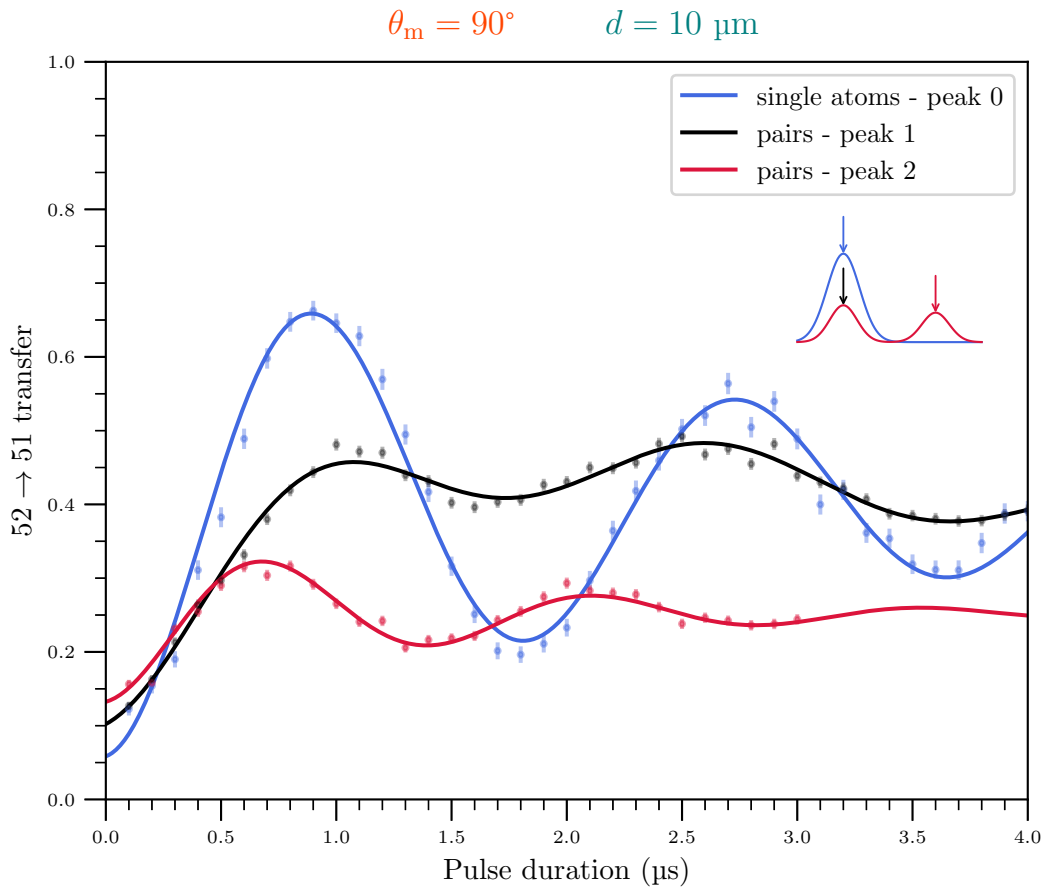

Figure IV.4: Rabi oscillations of each of the three peaks measured in the spectroscopic sequence. The pair-state signal (red) oscillates $\sim \sqrt{2}$ times faster than the single-atom one (blue), further confirming the fact that we drive the $|\uparrow\uparrow\rangle \rightarrow |+\rangle$ transition and that atoms interact as we expect them to. The signal of peak 1 (black) displays a sum of two oscillations, one at the single atom frequency and the other at less than half of that.

another signature of the interaction between the two atoms in the pairs we create. Without interactions, we would only be able to drive pair oscillations between $|\uparrow\uparrow\rangle$ and $|\downarrow\downarrow\rangle$, evolving at the single-atom Rabi frequency Ω_0. The interactions break the regular spacing between $|\uparrow\uparrow\rangle$, $|\downarrow\downarrow\rangle$ and $|+\rangle$ (presence of peak 2), so that we can drive the transition between $|\uparrow\uparrow\rangle$ and the displaced pair state. The faster Rabi frequency Ω_2 confirms that we are driving a transition different from $|\uparrow\uparrow\rangle \rightarrow |\downarrow\downarrow\rangle$. Ultimately, the resonance and Rabi frequencies of line 2 are two sides of a same coin, and both illustrate the presence of interactions within the pairs.

The ratio between the single-atom and pair Rabi frequencies is $\Omega_2/\Omega_0 = 1.29 \pm 0.02$. This is close to the expected theoretical ratio of $\sqrt{2} \simeq 1.414$[2], with a 9% difference only

[2]N entangled particles undergo collective oscillations between the ground state and Dicke states at a rate $\sqrt{N}$ times larger than for a single such particle.

between the two values. The ratio confirms that we address the level $|+\rangle$, in which the two atoms are entangled. The residual 9% error is probably caused, once again, by the microwave power dispersion across the arrays, which induces spatial variations in the Rabi frequencies.

We also fit the Rabi oscillation of peak 1, this time with a sum of two damped sine functions. We obtain the two following Rabi frequencies and respective amplitudes:

$$\Omega_1^{(a)} = 2\pi \times (219 \pm 4) \text{ kHz}, \quad A_1^{(a)} = 0.21 \pm 0.02, \tag{IV.5}$$

$$\Omega_1^{(b)} = 2\pi \times (551 \pm 5) \text{ kHz}, \quad A_1^{(b)} = 0.10 \pm 0.02. \tag{IV.6}$$

Thanks to these values, we can elaborate our understanding of the atomic transitions driven in line 1. We observe that $\Omega_1^{(b)} \simeq \Omega_0$, meaning that peak 1 is partly driven by single-atom transitions, appearing due to rearranger or circularization errors. The other part of this signal oscillates at a slower frequency. Following the above discussion, we attribute this contribution to the 2-photon process $|\uparrow\uparrow\rangle \rightarrow |\downarrow\downarrow\rangle$. It seems to be consistent with the estimation we can make of its Rabi frequency. If we consider $\{|\uparrow\uparrow\rangle, |\downarrow\downarrow\}$ to be an effective two-level system, driven by a two-photon process via the far-detuned intermediate level $|+\rangle$, its Rabi frequency writes $\Omega_{|\uparrow\uparrow\rangle - |\downarrow\downarrow\rangle} = \Omega_2^2/(2\delta)$. Here, δ is the detuning with respect to the intermediate level and we consider that both $|\uparrow\uparrow\rangle \rightarrow |+\rangle$ and $|+\rangle \rightarrow |\downarrow\downarrow\rangle$ have the same Rabi frequency Ω_2, measured on line 2. Using the values of $\delta = 2\pi \times 1.19$ MHz and $\Omega_2 = 2\pi \times 699$ kHz, we estimate:

$$\Omega_{|\uparrow\uparrow\rangle - |\downarrow\downarrow\rangle} = 2\pi \times (205 \pm 5) \text{ kHz}. \tag{IV.7}$$

The computed value matches very well the measured frequency $\Omega_1^{(a)}$ of the slow component in the oscillations, thus confirming that it corresponds to the 2-photon transition $|\uparrow\uparrow\rangle \rightarrow |\downarrow\downarrow\rangle$.

All in all, the Rabi oscillations shown here strengthen our understanding of the atomic behavior in the experimental sequences. They not only provide further proof that the circular atoms interact, but will also allow us, in the next section, to enrich the information provided by the spectra.

IV.1.4 Conclusions on the preliminary data

We complete and sum up here the information that can be inferred from the spectra and Rabi oscillations, to establish a self-consistent diagnosis of the atoms thanks to the measured data. We focus here on the signals acquired with the nine pairs of atoms.

First, as implied in the spectroscopy section, the splitting $\Delta\nu$ between the two peaks (1 and 2) of the spectrum constitutes a precise measurement of the distance between the two atoms at the time of the microwave probe. The numerical model allows us to precisely convert, via equation (IV.2), the measured splitting $\Delta\nu = -2J/(2\pi)$ into an inter-atomic distance, given the angle θ_m. Here, the 1.19 MHz value obtained in this configuration yields:

$$r = 11.18 \pm 0.03 \text{ µm}. \tag{IV.8}$$

We will later use this conversion to probe the variation over time of the inter-atomic distance, or in other words, measure the motion of the circular atoms in their traps.

Secondly, we take advantage of the information deduced from the Rabi oscillations to estimate the purity of the circular atoms in the pairs, i.e, the overall probability of having the two atoms in $|52C\rangle$ in each repetition of the sequence. To do so, we need to compute several quantities. First, thanks to the images acquired throughout the sequences, we estimate that each pair has a probability $P_r \simeq 0.92$ of being correctly prepared by the rearranger[3]. Each pair, in 8% of repetitions, lacks one atom. Occurrences where both atoms are missing after the rearrangement procedure can be neglected. Furthermore, we derive from the single-atom spectrum, taking into account the 85% single-atom purity and the lifetime of $|52C\rangle$, that the microwave probe pulse has an average $\simeq 83\%$ efficiency over the array. Thanks to these values, through a simple numerical toy model of the atomic state evolution[4], we derive a linear relation between the average circular purity[5] in the pairs $\overline{\eta_{52C}}^{(2)}$ and the maximum transfer of peak 2, so that we get the estimation:

$$\overline{\eta_{52C}}^{(2)} = 0.58 \pm 0.02. \tag{IV.9}$$

In other words, for a single pair in this configuration ($d = 10$ µm and $\theta_{\mathrm{m}} = \pi/2$), there is only a 58% chance of successfully carrying out the adiabatic passage with each atoms. We recover here the estimated 30% purity loss, from 85%, that we had roughly measured with evenly-spaced lattices of circular atoms. The ability to directly estimate the purity from these simple signals will be used to assess the impact of the interactions on the atomic preparation, in the various configuration that we will test out.

To conclude, the spectroscopy data is not only relevant to reveal the existence of circular-circular interactions, but also useful to derive other effects caused by the proximity between the atoms. We estimated that, in this geometry, the probability to circularize the atoms is significantly reduced and some non-negligible displacements are induced in the traps. These effects are most probably caused by the coupling between the atoms during their preparation: the resonant, circular-circular interactions only appear with the microwave probe, and cannot impact the position of the atoms or their purity at the time of the measurement. We will get back to these issues later to present the solution we found to solve them. For now, we push the exploration of the behavior of the resonant dipole exchange a bit further than in the preliminary data presented so far.

[3]This is lower than the 98% success rate for each pair presented at the end of chapter 2. In the experiments presented here, the rearranging procedure was not performing at its optimal efficiency and was in need of a slight re-calibration. To circumvent this issue, we could post-select the data to only keep the ionic results of sequence repetitions in which the rearranger had properly worked, but the ionic detection software unfortunately does not allow this level of detailed analysis.

[4]We take into account the various experimental efficiencies (rearranger, excitation to low-ℓ states, microwave probe transition), and use numerical estimations of black-body-induced transfers between manifolds.

[5]We remind that the circular purity is the fraction of atoms properly excited to $|52C\rangle$ by the radio-frequency adiabatic passage.

IV.2 Geometric tunability of the interactions

We now turn to the geometric dependence of the interactions. We implement here the same experimental sequence as above, based on microwave spectroscopy from $n = 52$ to $n = 51$, but with varying geometries. We do so by changing the lattices used and their orientation, so as to measure the line splitting, and therefore J, as a function of the two geometric parameters d and θ_{m}.

IV.2.1 Distance dependence

We start with the measurement of the interaction as a function of the distance between the two circular atoms. We keep $\theta_{\mathrm{m}} = \pi/2$ as in the previous settings, so that the relationship between the line splitting $\Delta\nu$ and the distance writes $\Delta\nu = -2J/(2\pi) = 2A/d^3$.

In order to reduce the displacement issue which already appeared in the preliminary data, we now work with a single pair of circular atoms. It allows us to send the maximal available optical power in each bottle beam, making them as tightly confining as possible. With approximately 200 mW in each trap, we expect their depth and trapping frequency to be ~ 400 µK and ~ 50.5 kHz. The 2-atom configuration also avoids potential couplings to other atoms of neighboring pairs, and eliminates the effects of the microwave power spatial inhomogeneity. We still use the rearranging procedure to deterministically create, for each repetition of the sequence, a single pair of trapped circular atoms, placed along the vertical direction z. The inter-atomic distance d is varied by simply changing the spacing for each acquisition, via the SLM phase masks. For a given d, we perform the spectroscopy experiment detailed above, in which we record the $n = 52 \rightarrow n = 51$ transfer driven by the microwave pulse, as a function of its frequency.

The 2-atom spectra, obtained for d ranging from 8 µm to 16 µm are shown in figure IV.5 (a). We overlap them with the single-atom spectrum, where no interactions come into play and whose central frequency is taken as the x-axis origin. The span of each frequency scan is centered on peak 2, the transition towards $|+\rangle$, whose resonance frequency changes with d. We clearly see this peak appear and move to higher frequencies as the distance gets shorter. We also witness its contrast decreasing significantly when the interaction gets larger, in line with a reduction in circular-state purity when the atoms are prepared closer to one another.

For each spectrum, we fit the data with a gaussian peak and retrieve the frequency splitting $\Delta\nu$ with respect to the single-atom reference peak. In figure IV.5 (b), we plot $\Delta\nu$ as a function of d, in log-log scale. We also plot the result of the same experiment, but conducted with four pairs of trapped circular atoms instead of one, and the single point obtained in section (1.2) with 9 pairs. The overlap of the three configurations underlines the importance of the trapping strength as the interactions grow. Overall, the data is in good agreement with the power-law behavior of the interaction as a function of distance. With a single pair of atoms, the measurements match the expected

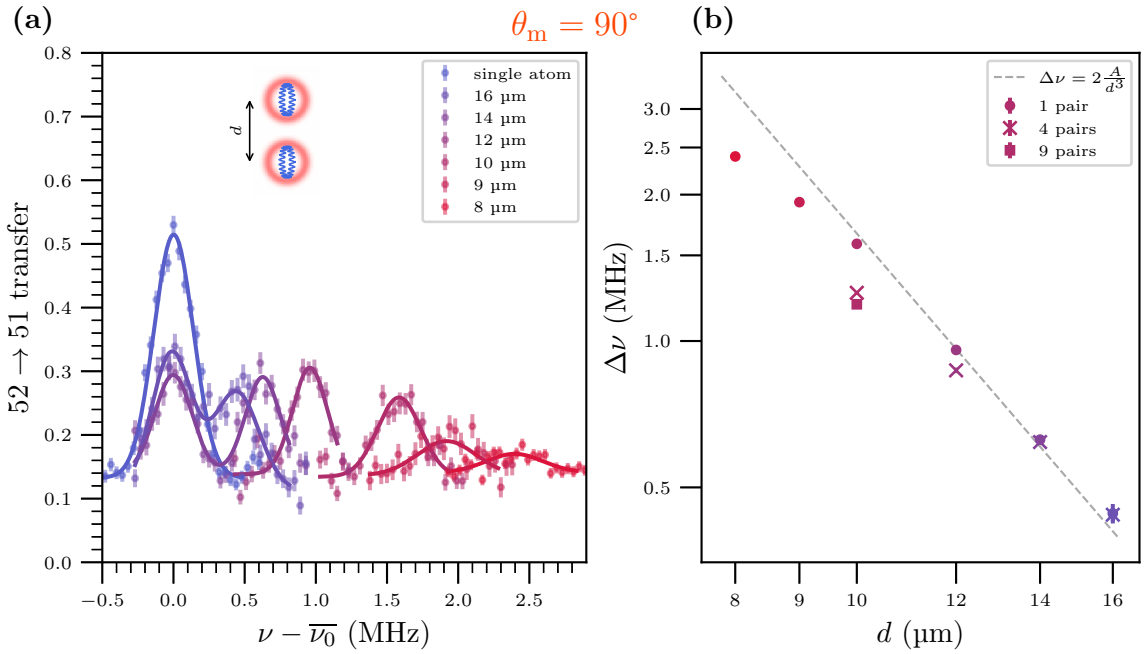

Figure IV.5: Resonant dipole interaction as a function of the inter-atomic distance. **(a)** Spectra of the $|\uparrow\uparrow\rangle \rightarrow |+\rangle$ transition, each obtained with a single pair of circular atoms for maximal trapping strength, and for distances ranging from 8 µm to 16 µm. The x-axis is centered on the resonant frequency of the single-atom, non-interacting configuration, also plotted here (in blue). As the distance is reduced, the interactions grow, so that the interaction line shifts to higher frequencies. Its contrast also drops, because of reduced circular purity when the atoms are prepared close to one another. **(b)** Interaction energy $\Delta\nu = -2J/(2\pi)$ as a function of d. Several trapping configurations are plotted: data acquired with a single pair (the spectra on the right panel), data taken with four pairs of traps, and the preliminary data obtained with 9 pairs. The error bars are smaller than the data points.

values for distances larger than 10 µm. Below that, deviations to the theory appear and indicate that, in strongly-interacting configurations, the atoms do not remain at their trap's centers. With four pairs, i.e., four times less trapping depth, the discrepancy with the theory emerges as soon as $d = 12$ µm.

Overall, we clearly recover here the $1/r^3$ behavior of the resonant dipole interaction. Although deviations from the theory occur when the atoms are close to each other, the measured distance dependence matches the expectations, and further confirms our understanding of the system. Conversely, these results show that, by changing the inter-atomic distance, one is able to tune the circular-circular resonant dipole interactions.

IV.2.2 Angular dependence

We now turn to the variation of J with θ_{m}, which we investigate experimentally in the same manner as above. We still work with a single pair, but this time with fixed inter-atomic distance $d = 13$ µm. We vary θ_{m}, the angle between the inter-atomic axis and the quantization axis, by rotating the trapping arrays (tweezers and bottle beams) in the (x, z) plane. For each value of θ_{m}, we acquire the microwave probe spectrum, fit the interaction line (peak 2) with a gaussian shape, and compute its distance with the non-interacting, single-atom transition frequency $\overline{\nu_0}$.

The recorded spectra are presented in figure IV.6 (a). They demonstrate the change of sign of the interaction as the angle θ_{m} goes from 0 to 90°, with the line shifting from a resonance frequency lower than $\overline{\nu_0}$ to one higher than $\overline{\nu_0}$. Importantly, at $\theta_{\mathrm{m}} \simeq 60°$, peak 2 almost merges with peak 1 at ν_0, and we essentially recover the single-atom spectrum. This corresponds to the interactions vanishing at $\theta_{\mathrm{m}} = \theta_0 \simeq 54.7°$, as mentioned in chapter 1. In other words, close 60°, we mostly get single-atom transitions from $|52C\rangle$ to $|51C\rangle$.

In figure IV.6 (b), we plot the measured splitting as a function of θ_{m}. As in the distance study, the data approximately fits the theoretical prediction. The general behavior matches the $(3\cos^2(\theta_{\mathrm{m}}) - 1)$ evolution, but with deviations at the largest interaction strengths, when the angle gets close to 0°. Still, without any other experimental refinements, we are able to control the sign of the interactions via simple rotations of the trapping systems.

We conducted here the first characterization of resonant dipole interactions between circular atoms. Their behavior matches the theoretical predictions, up to discrepancies in the strongest interaction regimes, when θ_{m} is lower than $\sim \pi/4$ or when the inter-atomic distance is shorter than ~ 10 µm. So far, these deviations prevent any fine control of the interactions, which is problematic for the examination of many-body phenomena with more than a mere pair of atoms. The next part of this work is therefore dedicated to understanding these deviations, in order to ultimately get rid of them.

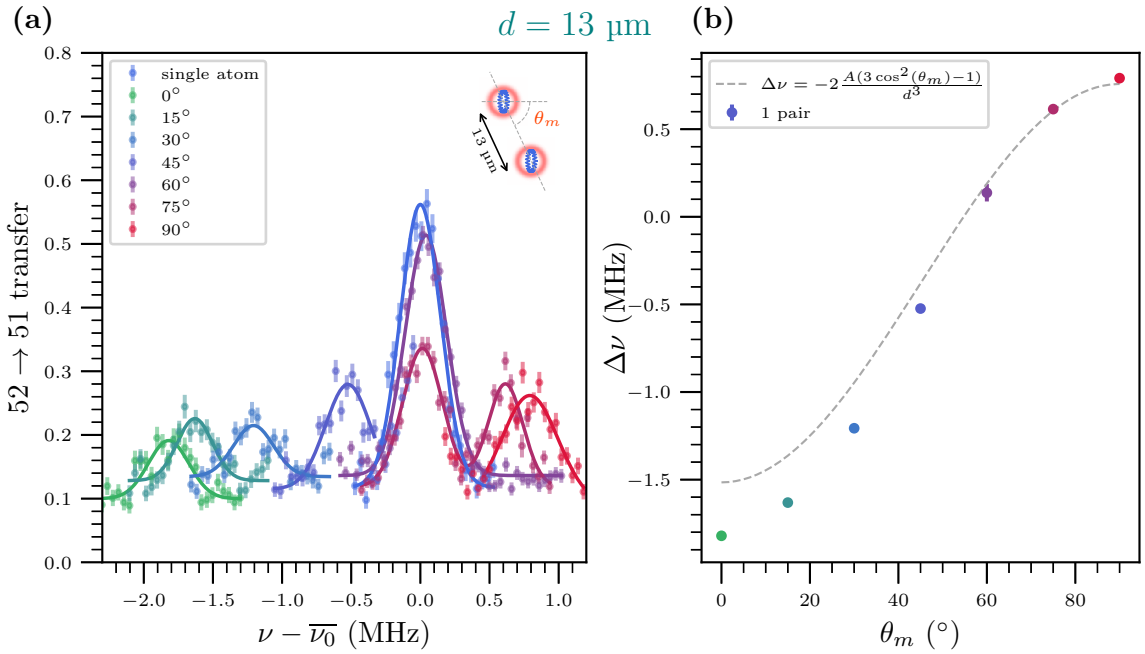

Figure IV.6: Resonant dipole interaction as a function of the angle between the quantization axis and the inter-atomic axis, for $d = 13$ µm. **(a)** Spectra of the $|\uparrow\uparrow\rangle \rightarrow |+\rangle$ transition, each obtained with a single pair of circular atoms, for θ_m ranging from 0° to 90°. The x-axis is once again centered on $\overline{\nu_0}$, and the single-atom $|\uparrow\rangle \rightarrow |\downarrow\rangle$ spectrum is also plotted here (in blue). **(b)** Measured interaction energy $\Delta\nu = -2J$ as a function of θ_m, and overlapped with the theoretical expected behavior. For most data points, the error bar is smaller than the pictured symbol. In the strongest interaction regimes, the data deviates once more from the expected values because of induced atomic displacements.

IV.3 Improved atomic preparation for error elimination

To go any further with this experimental platform, we need to understand and mitigate the deleterious effects witnessed with strong interactions. The irregularities we observed in the data presented here suggest that, in strongly interacting geometries, the atomic positions deviate from the centers of their traps. The spectra only give us a snapshot of the inter-atomic distance at the time of the microwave pulse, but the atoms could very well oscillate over several hundred nanometers around their equilibrium positions over time, which would prevent a proper control of their interactions in the pairs, let alone in larger ensembles. Moreover, the strongly interacting regimes appear to reduce the quality of the circular state preparation, which is not acceptable for prospects of quantum simulations with larger number of atoms.

To tackle this issue, we first design a numerical model of the interacting pairs, describing their evolution throughout the Rydberg preparation. By comparing its results to the data, we identify the source of errors as the low-ℓ interactions emerging

right before the circularization. We then implement a new, refined atomic preparation to mitigate these interactions and recover data in excellent agreement with theoretical expectations, even in strongly-interacting regimes.

IV.3.1 Preparation errors in strongly-interacting regimes

We try in this section to characterize the effects we witnessed more comprehensively, so as to understand their origin and eliminate them. To do so, we implement additional experimental investigations that we couple to numerical simulations.

The deleterious effects cannot be attributed to the circular-circular interactions, as those only emerge at the time of the microwave pulse, which constitutes the probe of the system. We therefore suspect that the errors originate from dipole-dipole interactions between the atoms before the adiabatic passage. Indeed, when the electric field $\mathbf{F}$ is ramped up to branch $|52F\rangle$ to the starting level of the circularization, the "classical" atomic dipole goes from zero to a large value of about $4000(ea_0)$, as per the Stark effect and parabolic basis discussions of chapter 1. The dipole is then shrunk back to zero by the adiabatic passage, which brings the atom to $|52C\rangle$, where no static dipole is apparent. The evolution of a single static dipole during the preparation is visualized in figure IV.7, where we represent its different values throughout the evolution from $|52F\rangle$ to $|52C\rangle$.

During the time that the atoms spend in low-ℓ states, they can therefore strongly interact through classical dipole-dipole interactions. Although trapped, these low-ℓ interactions can induce significant motion, which we believe is the origin of the deviations from the theory that we saw via the microwave spectroscopy of the circular-circular interactions, in figure IV.5 for instance. Moreover, nothing prevents cross-talk between the two atoms during the adiabatic passage. Spatial proximity between the two atoms could very well affect the circularization itself, and therefore explain the purity reduction. In other words, we suspect that the low-ℓ interactions induce position and preparation errors, which we then witness when probing the circular-circular interactions.

To corroborate this hypothesis, we implement a numerical model simulating the atomic evolution from the electric field onset until the end of the sequence, based on a semi-classical approach. We consider two atoms, each trapped in a harmonic potential approximating the bottle beam, of estimated trapping frequency 50.5 kHz (2 BoBs – see fig. III.7 of chapter 3). The atomic state of each atom is described by the two vectors $\mathbf{J}_a$ and $\mathbf{J}_b$, introduced in chapter 1. We remind that, in static parallel fields $\mathbf{F}$ and $\mathbf{B}$ and per equations (I.27) and (I.28), these angular momenta precess around the quantization axis. The atomic dipole, in manifold n, is also written

$$\mathbf{d} = \frac{3}{2} n e a_0 (\mathbf{J}_a - \mathbf{J}_b). \tag{IV.10}$$

To simulate the evolution of the internal state of the atoms, we neglect the quantum defects and assume a purely hydrogenic behavior. We consider that the two atoms are

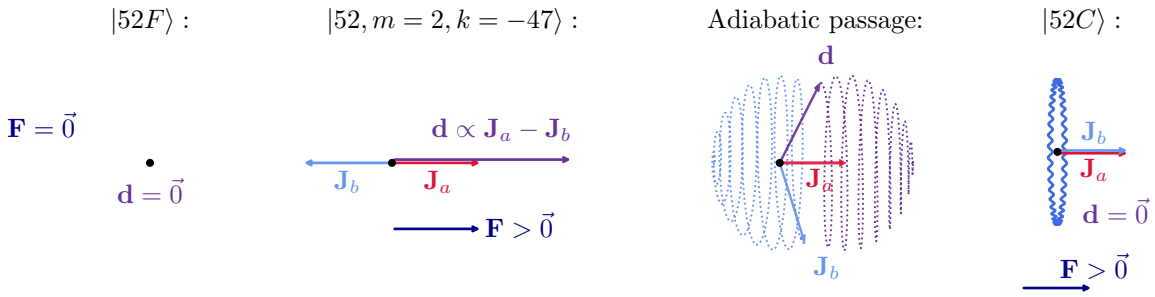

Figure IV.7: Simplified evolution of the classical atomic dipole $\mathbf{d}$ throughout the preparation of a single atom. The atom is excited to $|52F\rangle$ in zero electric field, such that the static dipole only emerges when ramping $\mathbf{F}$ up, to branch the low-ℓ state onto the state $|52, m = 2, k = -47\rangle$ of the manifold, written in the parabolic basis. Then, the dipole is independent of $\mathbf{F}$ and proportional to $\mathbf{J}_a - \mathbf{J}_b$. During the circularization, $\mathbf{d}$ shrinks while precessing around the quantization axis as $\mathbf{J}_b$ evolves (m_b grows) to reach the circular state, where the static dipole is zero (up to first order in $\mathbf{F}$). We suspect that the interactions between the classical dipoles of the two atoms in the pair lead to significant motion, induced before the adiabatic passage.

initially in the level $|m_a = J, m_b = -J\rangle$ of the parabolic basis, where $J = (n-1)/2$. It is the level at the very bottom of the manifold[6]. We recall that, during the adiabatic passage, the $\mathbf{J}_b$ angular momentum, of constant norm, rotates over time to reach the circular state $|m_a = J, m_b = J\rangle$, as shown in figure IV.7. In the numerical model, we simultaneously implement the two actions governing the behavior of the internal state of the two atoms. First, we simulate the effect of the radio-frequency field and of the electric field ramps, described by Hamiltonian (I.30) in chapter 1. The adiabatic passage parameters (timings, electric field ramp amplitude, RF power) are taken to match the real time evolution of the electric field and RF Rabi frequency in the experiment. Secondly, we simultaneously simulate the interactions between the angular momenta of the two atoms throughout the preparation, via the dipole-dipole Hamiltonian:

$$\hat{V}_{\mathrm{dd}} = \frac{1}{4\pi\varepsilon_0 r^3}\left(\frac{3}{2}nea_0\right)^2 \{ \left(\hat{\mathbf{J}}_a^{(1)} - \hat{\mathbf{J}}_b^{(1)}\right)\cdot\left(\hat{\mathbf{J}}_a^{(2)} - \hat{\mathbf{J}}_b^{(2)}\right) - 3\left[\left(\hat{\mathbf{J}}_a^{(1)} - \hat{\mathbf{J}}_b^{(1)}\right)\cdot\mathbf{e}\right]\left[\left(\hat{\mathbf{J}}_a^{(2)} - \hat{\mathbf{J}}_b^{(2)}\right)\cdot\mathbf{e}\right]\}. \tag{IV.11}$$

Here, $\mathbf{e}$ is the unit vector along the inter-atomic axis, and the 1 and 2 indices designate the atoms. Using Ehrenfest theorem, we can then write the system of coupled differential equations ruling the evolution of $\mathbf{J}_a$ and $\mathbf{J}_b$ for both atoms [136]. Thanks to the symmetry of the coupling, the atoms are interchangeable and will undergo the same evolution, which simplifies the model. The system and its equations are presented in more details in appendix A. We solve these equations numerically, which allows us to estimate the purity of the atoms (equation (A.8) of the dedicated appendix) in the

[6]It technically does not correspond to the actual starting point of the adiabatic passage but constitutes a good approximation of it.

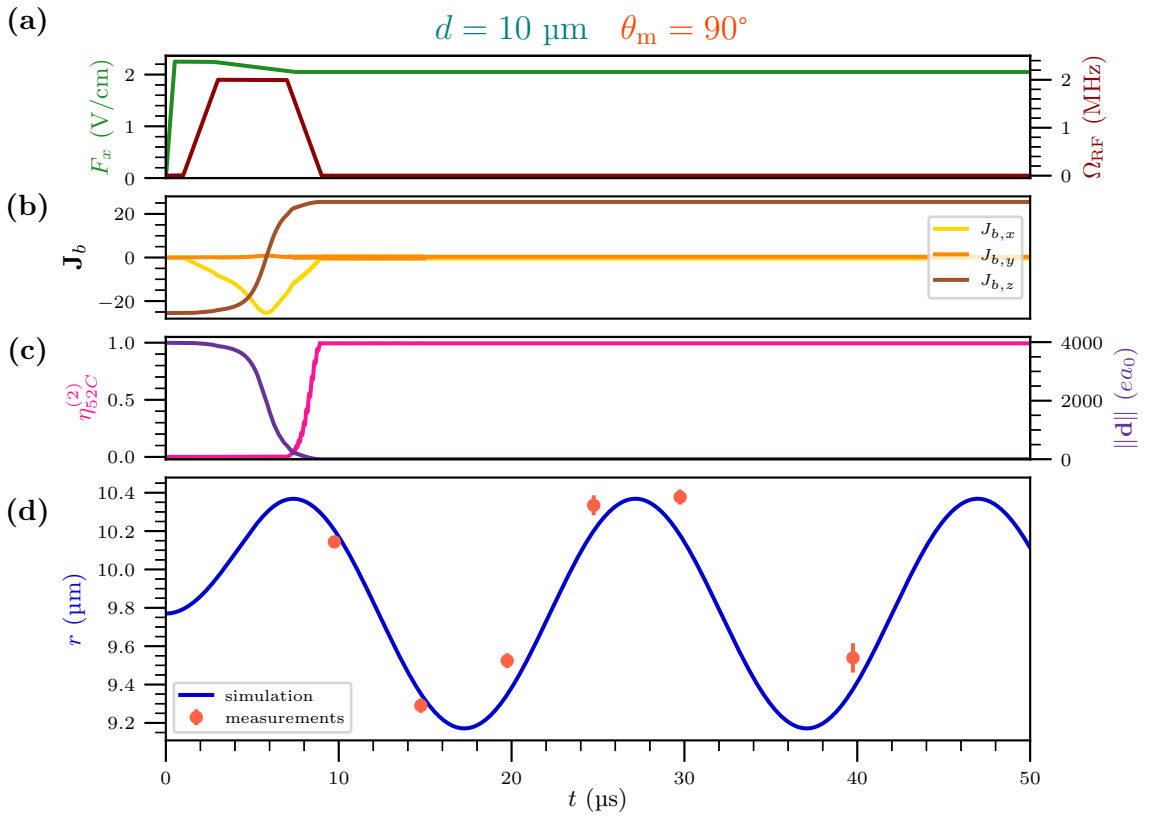

Figure IV.8: Numerical simulation of the motion and state evolution, for a pair of atoms, with $d = 10$ µm and $\theta_m = \pi/2$. **(a)** Input electric field and RF Rabi frequency evolution, replicating the ones of the real experimental sequences. Here, the electric field ramp is decreasing to match the old settings of the procedure, used in the measurements of this section. **(b)** Components of $\mathbf{J}_b$, for one of the atoms, in the rotating frame. During the circularization, $J_{b,z}$ changes sign to reach the circular level. **(c)** Circular state purity for each atom within the pair, which grows to 1 as the adiabatic passage ends. The atomic dipole, on the other hand, shrinks to zero. **(d)** Simulated motion and real measurements of the atomic distance. The excellent agreement confirms the validity of the numerical model.

pair at the end of the adiabatic passage, for any geometric configuration. The result for $d = 10$ µm and $\theta_m = \pi/2$ is shown in figure IV.8 (a)-(c). There, we plot (a) the simulated electric field and RF Rabi frequency ramps, (b) the evolution over time of the three components of $\mathbf{J}_b$ for either one of the atoms, and (c) the atomic dipole $\mathbf{d}$ and probability to be in $|52C\rangle$, $\eta^{(2)}_{52C}$, again for either one of the atoms. According to the numerical results, in this configuration, the pair circularization seems to be working properly, with no interaction-induced loss in purity.

Within the same numerical model, we simulate the atomic motion during the preparation by a simple mechanical description of the force exerted on each atom, derived from the classical version of the dipole-dipole interaction (IV.11). The energy

is strongest right as the dipoles emerge, when the electric field is turned on, before the adiabatic passage. This is when the motion is initiated, as pictured in the simulation of the atomic distance r over time in panel (d) of figure IV.8.

We compare the simulated motion with a real measurement of the inter-atomic distance at several instants in the sequence. To do so, we carry out the acquisition of the interaction spectrum of the pair, in the ($d = 10$ µm, $\theta_{\mathrm{m}} = \pi/2$) configuration, and we vary the time at which we apply the microwave probe pulse. This provides a direct measurement of the atomic distance over time, computed from the position of peak 2 in each acquisition (relative to the position of a single-atom reference line). The distance is computed by inverting equation (IV.2), which yields, in the current geometry, $r = (2A/\Delta\nu)^{1/3}$.

The experimental results match the simulated evolution very well, as shown in figure IV.8 (d). It must be noted that the simulation was run with an inter-trap distance of 9.8 µm instead of 10 µm. It is the only parameter adjusted to match the data, and could be explained by a slight 2% error in the distance calibration of the SLM phase masks. We recall here a remark we made when introducing the definition of the trapping arrays in chapter 2, where we signaled the possibility of a slight error in the camibration of the magnification of the trapping optical path. We potentially witness here such a misestimation, most probably in the aspheric lens' focal length. Nevertheless, the excellent agreement between the experimental data and the numerical results indicates that we have properly identified the source of motion and the origin of the deviations initially observed.

IV.3.2 Inhibition of low-ℓ interactions

We ultimately want to get rid of the unwanted motion induced by the low-ℓ interactions, so as to recover circular-circular interactions in agreement with the designed atomic geometries. To do so, we take advantage of two things: the geometric dependence of the classical dipole-dipole interactions and the fine three-dimensional control of the electric field allowed by the setup. Let us state that, from now on, the circularization adiabatic passage corresponds to the one described in chapter 3, its recent and most efficient version. Its obsolete, less-efficient settings were only used in preliminary data of this chapter, presented up until here.

As explained in the previous section, we associate the motion-inducing low-ℓ interactions to the attraction or repulsion between two classical dipoles. They emerge when the electric field is ramped up after the microwave transfer to $|52F\rangle$ and disapear during the adiabatic passage. By writing θ_{p} the angle between the quantization and interatomic axes during the preparation stages of the experiment, the classical interaction energy for a pair writes:

$$V_{\mathrm{dd}} = \frac{1}{4\pi\varepsilon_0}\frac{\|\mathbf{d}\|^2}{r^3}\left[1 - 3\cos^2(\theta_{\mathrm{p}})\right], \tag{IV.12}$$

(a) Before adiabatic passage: **(b)** After adiabatic passage: **(c)** After **F** rotation:

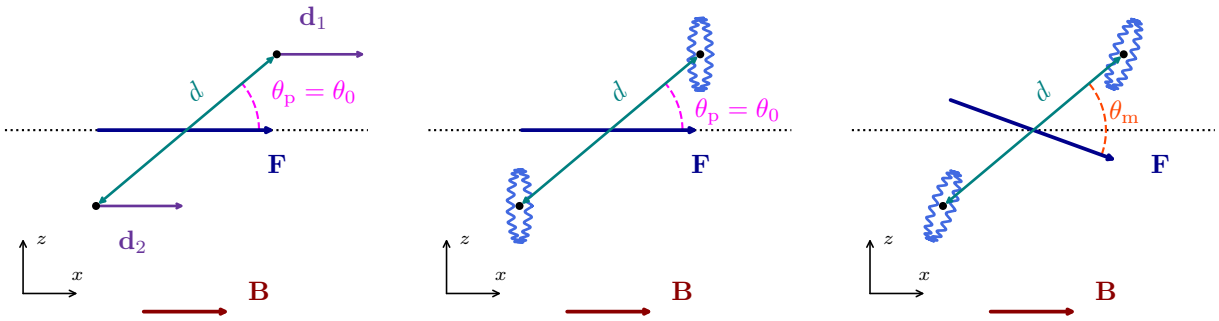

Figure IV.9: Improved preparation procedure. **(a)** The low-ℓ atoms of the pair are positioned with the *preparation* angle $\theta_{\rm p} = \theta_0$ so that their classical dipoles do not interact and no motion is initiated. **(b)** Configuration at the end of the adiabatic passage, with the quantization axis still along x. **(c)** System after the rotation of **F** in the $(x-z)$ plane by an arbitrary angle, so as to reach any *measurement* angle $\theta_{\rm m}$.

where $\|\mathbf{d}\|$ is the norm of the dipole exhibited by each of the two atoms, computed from (IV.10). Interestingly, the interaction energy vanishes when $\theta_{\rm p} = \theta_0 \simeq 54.7°$, an angle already introduced for circular-circular interactions and used in several experiments.[7] By conducting the atomic preparation with $\theta_{\rm p} = \theta_0$, we can inhibit the low-ℓ interactions and make sure that no atomic motion emerges in the bottle beams. We can do so by setting the pairs at that precise angle with the x axis, along which the electric field is directed throughout the circularization. We do this via the trapping array design, as in several of the experiments carried out with non-interacting circular atoms in chapter 3. The geometry is pictured in figure IV.9 (a) and (b). In (a), we schematically represent, for a single pair, the classical dipoles displayed by the atoms in $|52, m = 2, k = -47\rangle$, as the electric field has been switched on. The second panel represents the pair of circular atoms in $|52C\rangle$ at the end of the adiabatic passage, with which we want to investigate the circular-circular interactions.

[7] This is the same angle at which circular atoms in the $\{|nC\rangle, |(n+1)C\rangle\}$ configuration do not interact, as first mentioned in chapter 1. The fact that low-ℓ levels and circular states share the same θ_0 feature is not a priori trivial. On the one hand, low-ℓ atoms display a classical dipole, *aligned* with the directing electric field, which defines the quantization axis. On the other hand, the interaction energy in the $|+\rangle$ and $|-\rangle$ states of the circular pair can be seen as that of dipoles rotating like clock hands, in the plane *perpendicular* to the electric field, as discussed in the geometrical interpretation of the resonant dipole-dipole case in the first chapter. In the circular case, the averaging of the interactions over the clock hands rotation leads to the same angular dependence as classical dipoles aligned with **F**, up to the global sign of the interaction.

To not be restrained to the measurement angle $\theta_m = \theta_0$, we then make use of the electric field control allowed by the sets of electrodes in the setup (see figure II.2 of chapter 2 for the depiction of the electrodes). Up until now, we only worked with an electric field – and quantization axis– aligned with the x-axis of the setup. However, the four RF and two Stark electrodes allow, via the input of DC voltages, to control the static electric field in the three spatial directions. With careful calibrations, we are therefore able to rotate $\mathbf{F}$ in the $(x-z)$ plane, so as to change the orientation of the quantization axis. These calibrations, based on atomic measurements, are presented in appendix C. By rotating $\mathbf{F}$ after the circularization, we can switch to any desired measurement angle θ_m to probe the circular-circular interactions. The process is drawn in panel (c) of figure IV.11, where we show the change in quantization axis due to the field rotation. It takes less than two microseconds to rotate the field, and the precision granted by the electrodes ensures that it keeps the same norm independently of its orientation (but not necessarily *during* its rotation). The magnetic field, however, is kept parallel to the x-axis and never rotated. We therefore have to keep in mind that, when $\mathbf{F}$ is no longer aligned with $\mathbf{B}$, the Zeeman effect will shift the probed transitions by an amount proportional to the projection of $\mathbf{B}$ onto the quantization axis, i.e., $\mathbf{F}$. This is due to the fact that the Stark shift always remains much larger than the Zeeman effect, which ensures that the quantization axis follows the orientation of $\mathbf{F}$.

With this new preparation procedure, we should be able to cancel the atomic motion witnessed in strongly-interacting geometries. By choosing $\theta_p = \theta_0$ via the trapping lattice design and then setting θ_m to any angle thanks to the field rotation, we can now explore any circular-circular interaction geometry without having to deal with unwanted preparation errors. We took advantadge of this new preparation to re-optimize the adiabatic passage, and that is when we set up its more efficient B version, presented in chapter 3. The rest of the experiments presented in this chapter were carried out with the recent, upgraded version of the circularization.

IV.3.3 Motion control

We confirm the validity of the new preparation procedure through new measurements of the atomic motion, as carried out in the section before last. We work here with three pairs of atoms and maximal laser power in the BoBs, so that the expected trapping frequency is approximately $\omega_t = 2\pi \times 25$ kHz. In each pair, the inter-trap distance is $d = 13$ µm.

We run three experiments, each one with a different preparation angle θ_p. To explore the full range of low-ℓ interactions available, we choose: (i) $\theta_p = \theta_0$, where any motion should be prevented, (ii) $\theta_p = 0$, where the interaction is strongest and attractive, and (iii) $\theta_p = \pi/2$, where the interaction is weaker but repulsive. These angles are set from the design of the trapping array, so that in all three cases the circularization is carried out in standard fashion, with the electric field, i.e., quantization axis, along x. We then probe the inter-atomic distance over time via the $|\uparrow\uparrow\rangle \rightarrow |+\rangle$

spectroscopy. We remind that we compute the distance at the time of the microwave probe pulse from the frequency difference between peak 1 and peak 2, which provides here a result averaged over the three different pairs. To be able to do so in the case $\theta_{\mathrm{p}} = \theta_0$, we rotate $\mathbf{F}$ after the circularization to reach $\theta_{\mathrm{m}} = \pi/2$. In the other two configurations, we keep the field as it is, along x, as their geometries already yield measurement configurations in which we can properly conduct the microwave spectroscopy.

The data measured in each configuration is shown in figure IV.10, where we plot the computed atomic distance as a function of the microwave pulse time. The pulses used were 4 µs-long, and we take the center of the pulse as the time of each point. The x-axis origin is the time at which the electric field is switched on in the experimental sequence. We overlap onto each dataset a numerical simulation of the corresponding atomic evolution, computed using the semi-classical model described earlier. As in the previous example of such a simulation, the only parameter empirically adjusted here is the inter-trap distance, taken to be 12.75 µm instead of 13 µm to match the common average value of the three sets of data. We recognize here the same $\sim 2\%$ error in the lattice definition as noted earlier. Other than that, all the parameters of the simulations (sequence timings, interaction geometry, trap frequency, initial atomic level) are pre-defined in agreement with the corresponding experimental conditions. The numerical output matches the data, as can be seen in the three sets of results plotted in figure IV.10.

In the $\theta_{\mathrm{p}} = \theta_0$ geometry, the simulation predicts, as expected, a constant inter-atomic distance over time. We indeed measure a quasi-vanishing motion in this configuration, with some residual excursions of less than 100 nm away from the baseline. They might be due to an imperfect angular calibration of the trapping array, in line with the 2% error in the trapping system's magnification. We nevertheless obtain a clearly reduced motional amplitude compared to the initial $\theta_{\mathrm{p}} = \pi/2$ preparation (cf. figure IV.8), where the oscillations extended to more than 12% of the inter-trap distance. The new preparation method is definitely accurate in preventing unwanted atomic motion, and should allow a more precise investigation of the circular-circular interactions.

Conversely, in the $\theta_{\mathrm{p}} = 0$ and $\theta_{\mathrm{p}} = \pi/2$ cases, we measure significant oscillations of r over time. Both measurements are, again, in good agreement with the *ab initio* simulations. As expected from the $[1 - 3\cos^2(\theta_{\mathrm{p}})]$ term in the expression of the dipole-dipole energy, the $\theta_{\mathrm{p}} = 0$ case leads to an amplitude twice as large as the $\theta_{\mathrm{p}} = \pi/2$ configuration. The signs of the initial interaction (repulsive or attractive) also concur with the theory. These results explicitly show the fine control on the atomic motion brought about by the choice of the preparation geometry, which is ultimately independent of the measurement geometry thanks to the field rotation.

In conclusion, we are able to not only prevent any motion of circular atoms, but also to control it. This new possibility opens up interesting prospects, that we unfortunately do not have time to tackle in the present work. Through a longer waiting

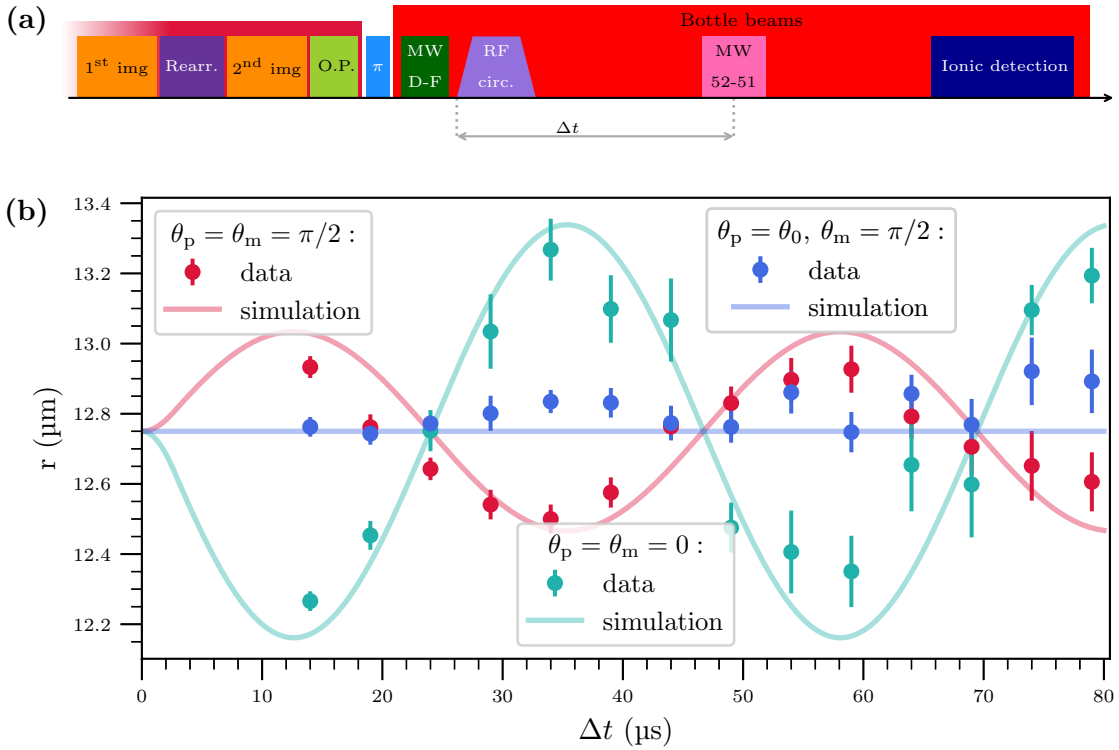

Figure IV.10: Control and characterization of the atomic motion, in three different preparation geometries, and for three pairs of atoms. **(a)** Experimental sequence. **(b)** Overlap of the data and numerical results. The origin of the x-axis is the initial activation of the electric field, after the microwave $D \to F$ transfer. For each measurement (dots), we run an *ab initio* numerical simulation (solid lines) of the corresponding configuration. The $\theta_p = \theta_0$ case leads to a quasi-vanishing motion, as expected. In the two other cases, significant motion is induced and matches the simulations with good agreement.

time in the low-ℓ interacting states, one could imagine exciting motional modes of larger amplitude. With more than two atoms, we might also excite more complex states of motion. It will also be interesting to see the interplay between motion and circular-circular interactions in this system. The spin-phonon model elaborated in the first chapter is directly linked to these ideas. The level of experimental control reached with these results could hopefully lead to explicit implementations of the cat states or thermometry proposals that we introduced with this theoretical system in chapter 1.

IV.3.4 Unperturbed interactions

Equipped with the new distinction between preparation geometry and measurement geometry, we return to the investigation of the spatial dependence of the circular-circular interactions. From now on, we keep $\theta_p = \theta_0$, so that the atomic motion is kept at a minimum and does not perturb the subsequent characterizations. For the rest

of the analyses presented here, we also systematically take into account magnification error of the optical trapping setup that the motion measurements revealed. Our best empirical estimate of its value, derived from the data, is -2.3%. For a user-defined inter-trap distance d, we now compute the corresponding interactions using the corrected value αd, where $\alpha = 0,977$.

Distance dependence

We start with the renewed measurement of the distance dependence in the resonant dipole-dipole interaction. We still work with three pairs of atoms, and set the measurement angle to $\theta_{\mathrm{m}} = \pi/2$ through the rotation of $\mathbf{F}$ after the end of the adiabatic passage. We therefore recover the same measurement conditions as in section IV.2.1, but without any atomic motion. For distances ranging from 8 to 16 µm, we acquire the two-peak microwave spectrum of the system. The spectra are plotted in figure IV.11 (a). In each acquisition, the frequency scan range spans the two peaks (1 and 2) but, for clarity purposes, we plot peak 1 for the 15 µm configuration only. Peak 2 is however shown for all distances. The microwave pulse duration and power are adjusted in each configuration so that the spectra always take the same amount of time to record. At large distances, a long pulse allows good discrimination between peak 1 and peak 2 over the short range of frequencies they span. The 16 µm spectrum is for instance acquired with a pulse duration of 4.3 µs. At short distances, peak 2 is further away from peak 1: a shorter pulse with more microwave power allows to still have good peak definition but with larger frequency steps, and thus the same total acquisition time. At 8 µm, we therefore use a 0.9 µs microwave duration. These adjustments explain the different line-widths of the spectra.

Except for the 9 µm and 10 µm configurations, the height of peak 2 remains constant and above 30%, indicating a good circular purity independently of the geometry. Thanks to the preparation process at $\theta_{\mathrm{p}} = \theta_0$, which not only inhibits motion but also prevents any interaction-induced defects in the circularization, we recover a good purity regardless of the measurement geometry.

In panel (b) of figure IV.11, we plot the interaction energy, computed from the peak separation of the spectra, as a function of the inter-trap distance. With this new atomic preparation, we get a much better agreement between data and theory than in the first version of the experiment. Only one point, at strongest interactions, falls just below the theoretical expected value. We recall that we take into account the $\alpha = 0.977$ correction factor to compute the theoretical interaction energies from the distances. By including this slight correction in the theory-data comparison, we obtain a perfect agreement between the two.

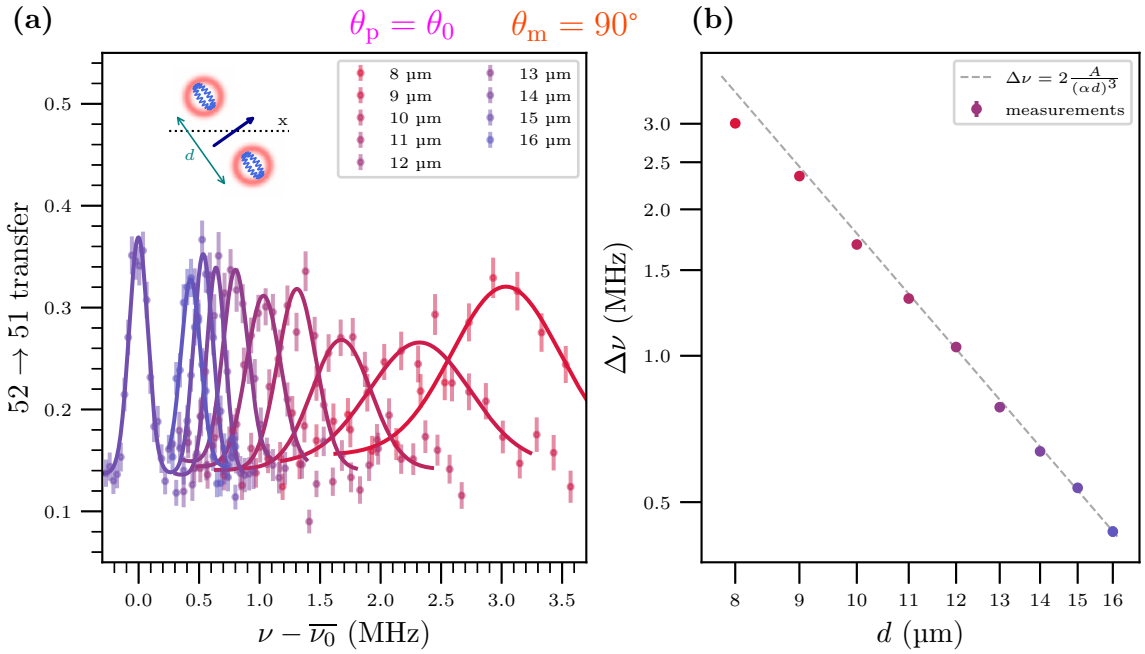

Figure IV.11: Measurement of the circular-circular interaction as a function of the inter-atomic distance, with a preparation tailored to inhibit atomic motion and using three identical pairs of trapped atoms. **(a)** Microwave spectra of the $|\uparrow\uparrow\rangle \rightarrow |+\rangle$ transition for different distances. For each configuration, we only plot the interaction-dependent peak, labeled 2 in the previous sections. Peak 1 of the 15 µm configuration is plotted to show the position of the frequency reference $\overline{\nu_0}$, taken as the x-axis origin. The inset illustrates, with a single pair, the geometry implemented for the microwave measurement, after rotating the electric field. **(b)** Computed interaction energy $\Delta\nu$, as a function of the inter-trap distance. The data follows the expected theoretical evolution (dashed grey line, computed by taking into account $\alpha = 0.977$) with excellent agreement. The errorbars are smaller than the markers.

Angular dependence

We now switch to the examination of the angular dependence. We set the distance to 13 µm and still use three pairs of atoms. The preparation is done with $\theta_p = \theta_0$, but we scan the measurement angle θ_m from 0 to $\pi/2$ via the rotation of **F** executed before the microwave probe pulse. The recorded spectra are shown in figure IV.12 (a). As in the distance experiment, to avoid overcrowding the figure we plot peak 1 for only one of the geometric configurations, while peak 2 is plotted for all of them. The x-axis origin is, once more, the shared position of peak 1.

We subtracted here on all spectra an additional, angle-dependent global frequency shift caused by the angle between the quantization axis and the magnetic field. As we change the orientation of **F** in each of the measurements, the projection of **B** onto the quantization axis changes accordingly. The angle changes result in different Zeeman effects in the different configurations. The Zeeman shift acts on both peaks, ranges

from 0 to 10 MHz, and goes as the cosine of the angle between **F** and **B**, as verified with the raw spectra. We subtracted the shift, irrelevant in this study, to properly overlap the spectra and focus on their interaction-induced features only.

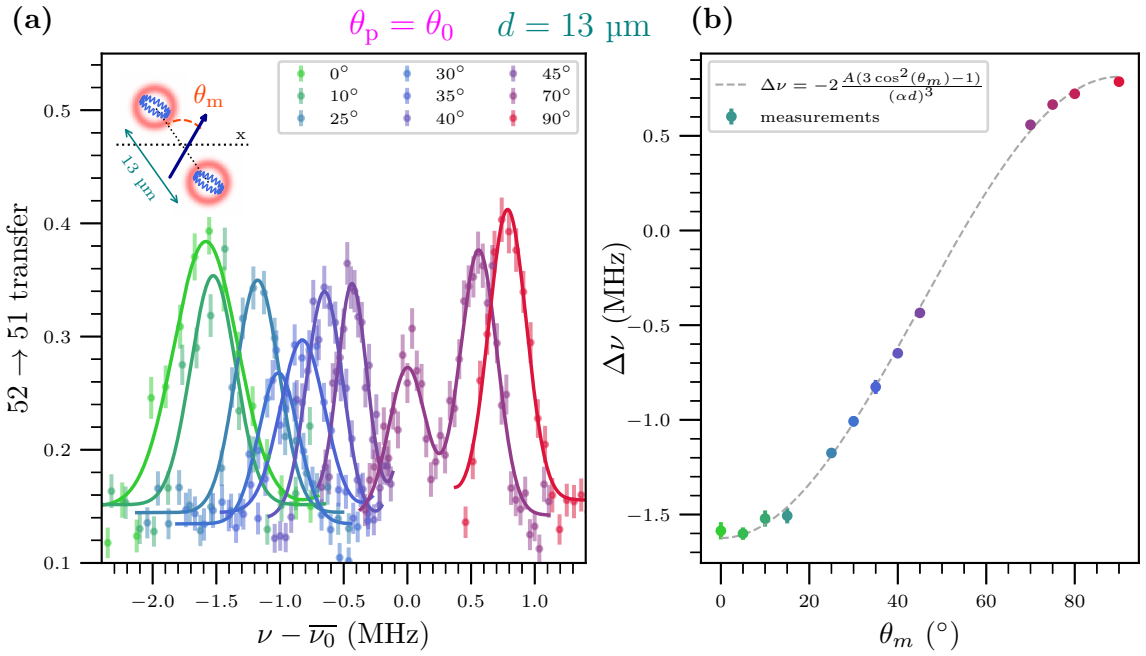

Figure IV.12: Measurement of the circular-circular interaction as a function of the pair orientation, performed with 3 pairs of atoms, $\theta_p = \theta_0$, and with a fixed distance $d = 13$ µm. **(a)** Microwave spectra of the $|\uparrow\uparrow\rangle \to |+\rangle$ transition for different angles θ_m. For each configuration, we only plot the interaction-dependent peak, except for $\theta_m = 70°$, where we also show peak 1, taken as the common frequency origin $\overline{\nu_0}$. The inset shows the geometry of a single pair. **(b)** Computed interaction energy $\Delta\nu$, as a function of θ_m. The data follows the expected theoretical evolution (dashed grey line) with perfect agreement when taking into account the minor α magnification error.

While acquiring this data, we witnessed that the microwave efficiency is strongly dependent on the orientation of the quantization axis. When θ_m is close to 20° we can barely make out the peaks, even at maximal microwave power. We suspect that locally, because of specific patterns of microwave modes in the electrode-covered sapphire structure, in some directions their is no σ^+ polarization. Such a polarization strictly prevents any transfer between $|52C\rangle$ and $|51C\rangle$, a σ^+ transition. Along other directions, the local polarization is a mixture of different states and the microwave transfer works appropriately. The issue is linked to the power inhomogeneities mentioned several times in this work. Having a microwave horn shining radiation through one of the windows creates, between the gilded electrodes, a complex distribution of power and polarization, that we have no control over[8]. It is therefore harder to draw any conclusion on the circular pair purity from the height of the peaks shown here.

[8]In the future version of the setup, the horn will be placed in the vacuum chamber as close to the atoms as possible, in order to minimize these effects.

And again, the widths of the peak differ between the various configurations because of the adjusted pulse durations, set to take a constant acquisition time while keeping correct peak definition.

The recorded interaction energies are plotted as a function of θ_{m} in panel (b) of figure IV.11. Measurements are missing close to 20° because of the unfavorable microwave polarization in that configuration, and close to θ_0 because of vanishing interactions, which make the two peaks indiscernible. In the rest of the θ_{m} values implemented, the agreement with the theory is, again, perfect.

Thanks to the inhibition of the low-ℓ interactions, we now implement interactions between circular atoms with great precision. We successfully characterized here controlled dipole-dipole interactions between circular atoms. Through deterministic changes in the lattice definitions, and therefore in the geometry of the system, we are able to finely strengthen, weaken, and change the sign of the resonant-dipole couplings exhibited in the pairs of circular atoms, and their behavior perfectly matches the theoretical predictions.

IV.4 Spin exchange between two circular atoms

Now that we have a good understanding of how to master pair interactions, we undertake one last experiment. We demonstrate here the observation of spin exchange between two circular atoms in the $\{|51C\rangle, |52C\rangle\}$ spin space, once more written $\{|\downarrow\rangle, |\uparrow\rangle\}$. By bringing together all of the setup's functionalities presented so far and then some, we are indeed able to witness several cycles of coherent excitation transfer between two atoms. Although these results do not uncover any new feature of circular-circular interactions, they constitute an important proof of principle on the path towards full-scale quantum simulations, which will necessarily rely on the observation of energy exchanges within larger ensembles of atoms.

The idea is straightforward: we want to initialize a pair of circular atoms in state $|\uparrow\downarrow\rangle$ and then measure its evolution over time. In the eigenbasis of the interacting pair, the initial state vector writes:

$$|\psi(0)\rangle = \frac{1}{\sqrt{2}}\left(|+\rangle + |-\rangle\right) \tag{IV.13}$$

According to the system's eigenenergies (cf. equation (IV.1) and figure IV.2 [d]), the pair then evolves as

$$|\,\psi(t)\rangle = \frac{1}{\sqrt{2}}\left(e^{-i2Jt}|+\rangle + e^{i2Jt}|-\rangle\right), \tag{IV.14}$$

which we revert to the measurement basis

$$|\psi(t)\rangle = \cos(2Jt)|\uparrow\downarrow\rangle - i\sin(2Jt)|\downarrow\uparrow\rangle. \tag{IV.15}$$

From the amplitudes, we deduce that the probability to measure $|\uparrow\downarrow\rangle$ oscillates over time with frequency $4J$, perhaps the most basic result in the most basic sytem in

quantum mechanics.

Its implementation with circular Rydberg atoms is however a lot less trivial. With the setup in its current configuration, we can create pairs of circular atoms with good preparation fidelity, control their interactions, keep them still for several hundred microseconds with optical traps, and measure their probability to be in $|52C\rangle$ with single-site resolution, as demonstrated in the last part of chapter 3. The tricky additional requirement that arises here is the spin state initialization. Until now, we had no way of discriminating atoms in the preparation protocols, which is what we now need to do to prepare $|\uparrow\downarrow\rangle$. To overcome this issue, we take advantage of the dipole blockade mechanism. We detail this new technique in the next section, before moving on to the presentation of the results.

IV.4.1 Pair state preparation via the dipole blockade mechanism

In order to prepare the state $|\uparrow\downarrow\rangle$ in a pair, we use a third, auxilliary atom, in charge of singling out one atom of the pair via the dipole blockade mechanism. We activate or inhibit the dipole blockade through the orientation of the electric field. By orientating $\mathbf{F}$ along specific axes, we can switch the dipole blockade on and off, which allows us to implement a sequence of events leading to the preparation of $|\uparrow\downarrow\rangle$.

To carry it out, we first prepare 3 circular atoms in $|\uparrow\rangle = |52C\rangle$, labeled A, B and C, placed at the vertices of a flattened triangle, and each trapped in a bottle beam. The atomic arrangement is shown in figure IV.13 (a). The end goal is to observe the spin exchange with the pair made up of atoms A and B. Atom C will be used to blockade A during the preparation. We set the geometry so that A and C are 20 µm apart[9], and the angle between their inter-atomic axis and the x axis is θ_0. When $\mathbf{F}$ is along x, i.e., throughout the circularization and de-circularization, A and C cannot interact. Atom B is 40 µm away from A, on the opposite side of C. Its angular position with respect to A is set by various constraints in the regularity of the underlying tweezer lattice. When $\mathbf{F}$ is parallel to x, A and B are coupled, with an interaction frequency $4J/(2\pi) = 99.0$ kHz. Atoms B and C are separated by 57 µm, so that their interaction is $4J/(2\pi) = 25.4$ kHz when the electric field is along x. With this geometry in mind, we can now go over the successive preparation steps, pictured in the four panels of figure IV.13:

1. All three atoms are initialized in $|52C\rangle$ following the standard procedure. The electric field is along x, C and A do not interact, while A and B do. Their interaction strength is however relatively small, so that the motion induced during the preparation is very limited ($\sim$ 10 nm amplitude according to simulations). This is the configuration drawn in panel (a).

[9] We give the distances as the user-defined ones in the trapping system, but we make sure to take the -2% magnification error into account when estimating the actual interaction energies.

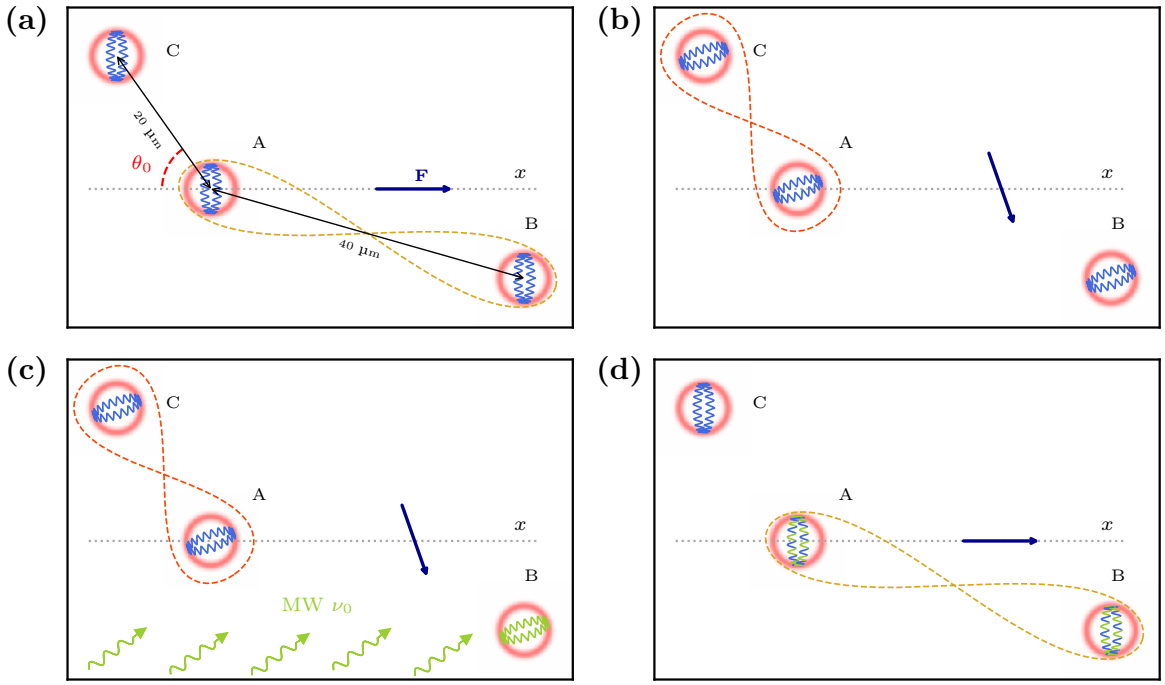

Figure IV.13: Dipole-blockade-based preparation for site selectivity. **(a)** Three atoms are initially prepared in $|\uparrow\rangle$ (blue wavefunctions). At the end of the circularization ($\mathbf{F} \parallel x$), A and B interact weakly (yellow dotted line connecting them). A and C are placed so that, in this field configuration, their interaction is inhibited. **(b)** Rotation of the elecric field to prevent A-B interactions, while A and C are coupled (red dotted line). **(c)** A microwave pulse (green arrows) transfers atom B to $|\downarrow\rangle$ (green wavefunction), while A and C, being in the dipole-blocakde regime, each remain in $|\uparrow\rangle$. The microwave pulse parameters also prevent the two-photon process to $|\downarrow\downarrow\rangle$. **(d)** $\mathbf{F}$ is rotated back to x, A and C no longer interact, while A and B start evolving from $|\uparrow\downarrow\rangle$ (blue and green wavefunction).

2. The electric field is rotated to inhibit interactions between A and B, as shown in panel (b). Atoms A and C interact, with an energy $2J/(2\pi) = 396$ kHz.

3. A 14 µs-long microwave pulse, set on the single-atom $|52C\rangle \rightarrow |51C\,\rangle$ transition frequency ν_0, is applied to the atoms. Atom B, whose interaction with A is inhibited, is transferred to $|\downarrow\rangle$. Atom A is in the dipole blockade regime, due to its interaction with C. Their one-photon transition $|\uparrow\uparrow\rangle \rightarrow |+\rangle$ lies 396 kHz away from the microwave pulse frequency, whose duration imposes a spectral width of less than 80 kHz (checked in preliminary tests). This transition thus cannot take place. The two-photon $|\uparrow\uparrow\rangle \rightarrow |\downarrow\downarrow\rangle$ transfer is also negligible. Assuming that it is an effective two-level system with far-detuned (396 kHz) indetermediate level $|+\rangle$, we estimate its Rabi frequency to be 3.2 kHz. The microwave pulse, although resonant on the two-photon process, is therefore too short to significantly adress it. All in all, A and C each remain in $|\uparrow\rangle$, while atom B is transfered to $|\downarrow\rangle$. This is depicted in panel (c) of the figure.

4. The field is rotated back to its initial angle, along x. This is done in 0.5 µs, a short timescale compared to the interaction energy of A and B (99.0 kHz, i.e., a $\sim$ 10 µs characteristic time). Their interaction is therefore switched on in a diabatic manner, so that the interacting system is properly initialized in $|\uparrow\downarrow\rangle$. In this field configuration, A and C no longer interact.

We then let the atoms evolve for a variable amount of time, after which we carry out the de-circularization and recapture in the tweezers. Only atoms in $|\uparrow\rangle$ can be de-excited back to their ground state and recaptured, so that we obtain an effective measurement of the spin levels. A recapture event signals that the atom was in $|\uparrow\rangle$, while no recapture means that the atom was in another state – most probably $|\downarrow\rangle$ in the case of atoms A and B at short timescales.

IV.4.2 Observation of coherent spin exchanges

With this preparation in mind, we move on to the presentation of the results. In figure IV.14 (c), we display the recapture probabilities for atoms A and B, cast as $P_\uparrow$, the probability to measure $|\uparrow\rangle$, as functions of the waiting time Δt. The waiting time is taken as the delay between the end of the second field rotation (i.e., when the interaction between A and B is switched on), and the center of the de-circularizing radio-frequency pulse (when the atoms being de-excited are no longer in a circular state and the resonant spin exchange stops). Panel (a) of the figure illustrates the timings of the sequence and the definition of Δt. In the anlysis of the recapture signal, we post-process the data to discard repetitions in which the rearranging process made a mistake and did not properly initialize the system of three atoms.

The data shows clear oscillations in $P_\uparrow(A)$ and $P_\uparrow(B)$, with opposite phases. We fit each of them with the following function:

$$f(t) = y_0 + \alpha e^{-t/\tau_\mathrm{L}} + \beta e^{-t/\tau_\mathrm{C}} \cos\left(2\pi\nu t\right). \tag{IV.16}$$

The first exponential term accounts for the black-body radiation-induced decay. The time constant τ_L is not a fitting parameter, it is empirically taken as the average of the lifetimes of $|52C\rangle$ and $|51C\rangle$: $\tau_\mathrm{L} = 138$ µs. The oscillating term also has an exponential pre-factor, which covers the loss of coherence over time, i.e., the decay in oscillation amplitudes. The fitting routine yields the two decay rates $\tau_\mathrm{C}^{(A)} = 43 \pm 9$ µs and $\tau_\mathrm{C}^{(B)} = 36 \pm 7$ µs. Both times are shorter than the estimated pair lifetime, of about 70 µs, indicating the presence of decoherence effects. The coupling strength J being independent of the static electric and magnetic fields, the decoherence might be explained by other effects, such as residual couplings to atom C or undesirable outcomes of the microwave preparation pulse. The spin-motion interplay addressed in chapter 1 could also explain the loss of contrast over time. However, given the 6 µK atomic temperature and weak interaction strength, numerical simulations indicate that this effect should not be visible at such timescales.

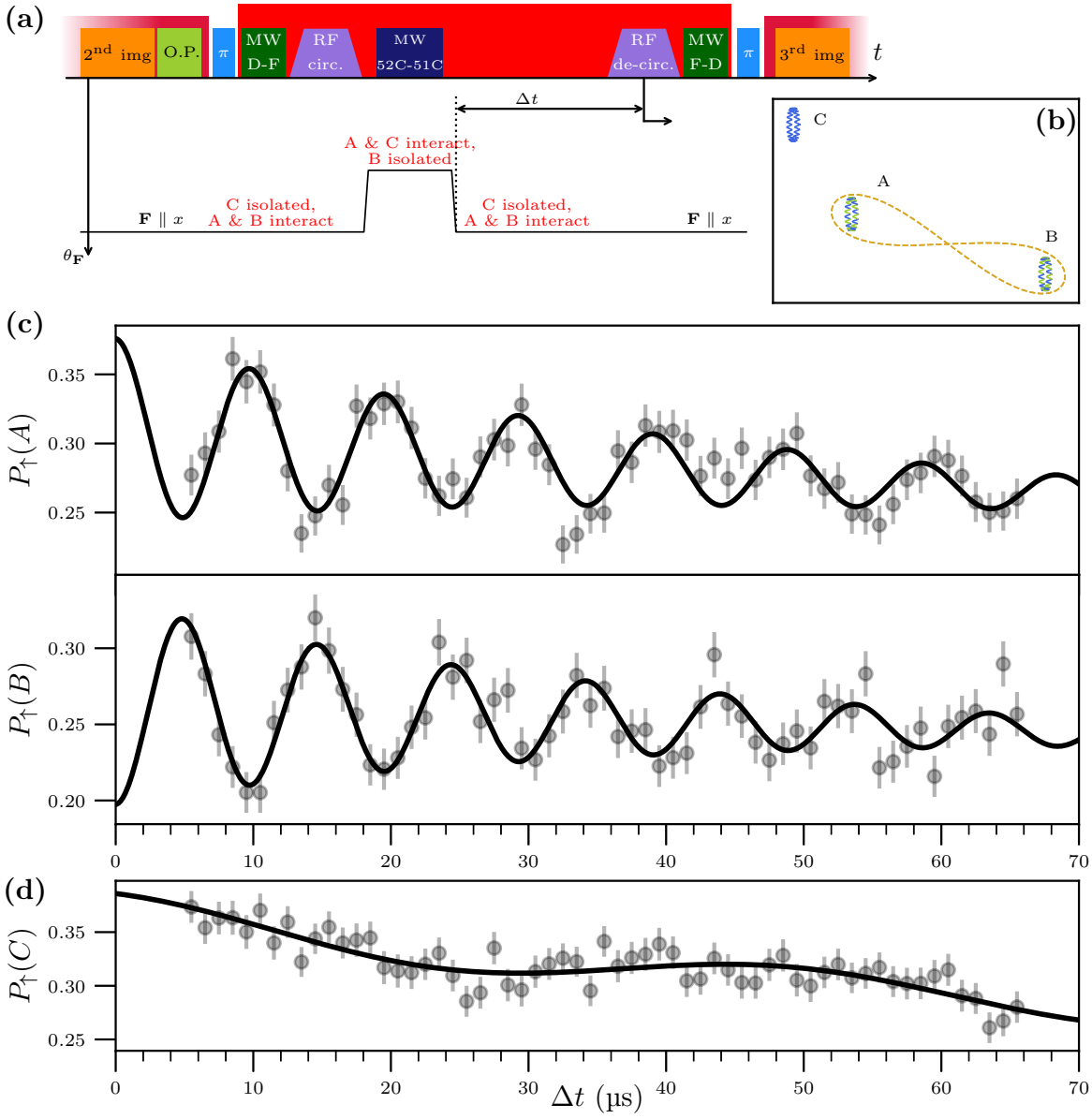

Figure IV.14: Spin exchange between two circular atoms interacting in the resonant dipole regime. **(a)** Depiction of the experimental sequence, where the rearranger is not shown. The orientation of the electric field is plotted to illustrate its change of orientation to prepare atom B in $|\downarrow\rangle$, thanks to the dipole-blockade enacted on A by atom C. **(b)** Representation of the arrangement of the atoms. Atom C has an auxilliary role in the sequence, it is only used to shift A out of resonance when shining the microwave field. **(c)** Recapture probabilities for atoms A and B as functions of the waiting time Δt. We overlap the data (dots) with fit functions (solid lines). The results clearly show more than a dozen spin exchanges between the two circular atoms. **(c)** Recapture probability for atom C, indicating residual interactions between A and C during the evolution.

More importantly, we find the common oscillation frequency to be $\nu = 102.2 \pm 0.5$ kHz. It is in excellent agreement with the predicted value $4J/(2\pi) = 99.0$ kHz. The results indicate that we have properly witnessed the coherent spin exchange taking place in the pair.

We plot in panel (d) the recapture probability of atom C. We also fit it with the function of equation (IV.16), but now taking $\tau_{\mathrm{L}} = \tau_{52C} = 140$ µs, the lifetime of $|52C\rangle$ only. The result shows that the black-body radiation-induced decay is modulated by slow oscillations at 20.3 ± 0.6 kHz. The frequency is of the order of the A-C interaction, where we expect $4J/(2\pi) = 25.2$ kHz. The fact that we observe this oscillation indicates that the interaction between atoms A and C is not totally negligible in the evolution of the system.

A more in-depth analysis would have to be carried out to explain all the features of the data and the quantities obtained from the fitting results. At first glance, the initial recapture of atom A matches that of the circular-atom trapping experiment, discussed in chapter 3. The 20% initial recapture of atom B is harder to explain without additional, more detailed considerations. By taking into account the circularization and de-circularization success rates, the microwave pulse efficiency and other error-inducing technicalities (e.g., the residual A-C interaction, the effect of the de-circularization on $|51C\rangle$, etc), and with a less empirical fitting routine, one should be able to explain the various features of the plots.

These results are still at their preliminary stage and we unfortunately lack the time to address them in more details in the context of this thesis. They nonetheless constitute a satisfying achievement. We basically observed two circular atoms, separated by a distance equivalent to the diameter of a human hair, exchange a single photon in a back and forth manner. Perhaps more pragmatically, the experiment of this last section proves the feasibility of using circular atoms to emulate spin systems – although extremely basic ones at this stage.

Conclusion of chapter 4

We presented in this final chapter the main results of this thesis, dedicated to the measurement and control of interactions between circular atoms. The investigations were conducted with pairs of atoms individually trapped in optical beams. We thoroughly explored their resonant dipole-dipole interactions in the $\{|51C\rangle, |52C\rangle\}$ spin states.

The microwave spectroscopy of the $|\uparrow\uparrow\rangle \rightarrow |+\rangle$ transition proved to be an efficient technique to probe and characterize the interaction regime in any geometry (d, θ_{m}). It not only provided a direct proof of the coupling between the two atoms, but also yielded useful information on the state of the pair at the time of the measurement. Thanks to a simple toy model of the atomic evolution, one can derive from the microwave spectra (and their corresponding Rabi oscillations) the atomic positions and state purity. The study of the variations of the interaction energy with the geometrical parameters of the system followed the general expected behavior, but highlighted preparation errors induced in strongly-interacting regime.

Thanks to a semi-classical simulation, we attributed these errors to dipole-dipole interactions occurring when the atoms are in low-ℓ states before the circularization procedure. The numerical results predicting atomic motion matched the one we measured through the microwave probe. We were able to overcome this bottleneck by exciting the pairs to circular states while in an interaction-inhibiting geometry. The subsequent rotation of the electric field nonetheless allowed us to explore any circular-circular interaction regime. We then demonstrated precise control of the resonant dipole-dipole interactions, still relying on the microwave spectroscopy to do so. Incidentally, the precision of the measurements revealed a small error in the magnification of the optical trapping setup. The distances between the lattice sites are actually 2% shorter than what we aim for when designing the SLM phase masks. The measured discrepancy is attributed to a slight misestimation of the aspheric lens' focal length. Far from being detrimental, this minor error and the fact that we are able to discern it further prove the quality of the optical trapping system.

The refined preparation protocol, where the quantization axis is not the same in the excitation and measurement phases of the experiments, allowed us to demonstrate control over the motion of the atoms in their traps. Through various preparation geometries, we were able to exhibit different regimes of motion. The data is in excellent agreement with numerical simulations, proving both our good understanding of the phenomena at stake and the fine atomic control allowed by the setup's functionalities.

The observation of coherent spin exchange between two circular atoms concluded the investigation addressed here. By taking advantage of the dipole blockade volume induced by a third, auxilliary atom, we recorded the evolution of a pair initially prepared in $|52C, 51C\rangle$. We witnessed several cycles of spin exchange, in excellent agreement with the expected interaction frequency. Although at a preliminary stage, these last results unequivocally lay the foundations for a future circular-atom quantum simulator.

Conclusion

I presented in this dissertation the experimental investigation of dipole-dipole interactions between optically-trapped circular Rydberg atoms. Thanks to our new setup, designed to create arbitrary arrays of circular atoms in a room-temperature environment, we were able to implement, control and measure the resonant exchange coupling exhibited within pairs of such atoms, individually trapped in bottle beams. The experimental technicality and promising results discussed here undeniably lay the groundwork for the long-term goal of creating a quantum simulator based on circular atoms. Over the course of my five-year PhD studies, we successfully bridged the gap between theoretical proposal [117] and experimental implementation, although the setup in its current state is still far from its desired capabilities. Nevertheless, one could argue that, by observing cycles of resonant spin exchange between two trapped circular atoms, we technically implemented a quantum simulation of the simplest imaginable spin system.

We were able to reach the conclusions presented here through an exhaustive upgrade of our setup, coupled to the development of new technical skills, the design of several tailor-made software and in conjunction with refined theoretical predictions and numerical modeling. This long-term project, of which we showed here some of the first outcomes, will hopefully bolster the renewed interest in circular atoms in the context of quantum simulation efforts [116, 195], almost exactly a hundred years after Niels Bohr received his Nobel Prize for his first intuition of these remarkable atomic states.

We dedicated the first chapter of this dissertation to the formal introduction of circular Rydberg atoms, their individual properties and the main characteristics of their interactions. The circular states, distinguished by their large principal quantum number and maximal orbital and magnetic angular momenta, are best understood from the standpoint of the parabolic basis and in the hydrogenic approximation. This formalism is tailored to the description of the Rydberg manifolds of alkali atoms evolving in static electric and magnetic fields. Within this framework, we underlined the distinctive features of individual circular Rydberg atoms, specifically focusing on state $|52C\rangle$, the level we work with in the experiments. Their strong dipole couplings, almost exclusively to other circular states and in the microwave domain, justify their use as spin-encoding levels for simulations. This peculiar level structure also accounts for their lifetimes, outstanding among other Rydberg levels but highly dependent on black-body radiation. The third important property of circular atoms we addressed here is their sensitivity to the ponderomotive force, which enables their individual

optical trapping.

When two circular atoms are close to each other, they interact via the dipole-dipole coupling. Two possible behaviors then emerge, depending on the specific levels involved. On the one hand, if the atoms are in two dipole-coupled states, the interaction is of the first order kind, and leads to the direct, spin exchange regime. On the other hand, if the atoms are in levels that are not dipole-coupled, their coupling is ruled by second-order processes, called the van der Waals regime. The two configurations display energy scales that differ by several orders of magnitude. Although the second one is the target regime of our proposed quantum simulation platform, we focused here on the direct exchange interaction, because of experimental constraints and as our first step in the field of trapped, interacting Rydberg atoms.

To carry out the experimental investigation of said interactions, we rely on the functionalities of our new setup, which we presented in the second chapter of this work. Among its many features, the electric-field control apparatus and the optical trapping system are of crucial importance. Thanks to standard laser-cooling techniques (magneto-optical trapping, optical molasses, adiabatic cooling), we create homogeneous arrays of individually-trapped atoms, with 65% single-site initial loading probability and cooled to 5 µK. We recently added a rearranging beam to the experiment, used to move the loaded atoms between static tweezers, so as to reach arbitrary, defect-free in our atomic lattices.

In chapter 3, we presented some of the first results of this thesis, on the trapping and manipulation of individual circular Rydberg atoms. We started with the description of the excitation procedure to transfer ground-state atoms to $|52C\rangle$, which has a 73% success rate and is performed in about 10 µs. Thanks to our site-resolved optical detection method, we then proved that the atoms, while in the circular state, stay confined in their individual bottle beams. We wrapped up chapter 3 by discussing two experiments that demonstrate other applications of the optical detection to circular state manipulations. We notably implemented the coherent transfer of the atoms between two circular states, which we detect with single-site resolution.

Equipped with arbitrary arrays of trapped $|52C\rangle$ atoms, we finally tackled in chapter 4 the experimental study of the dipole-dipole coupling between circular states. We restricted our investigations to the case of pairs of atoms and to the resonant, first-order interaction regime. Via a microwave spectroscopy probe of the pair transitions, we explicitly demonstrated the emergence of circular-circular interactions, matching the expected theoretical predictions. To implement highly-controlled interactions, we however need to inhibit any atomic motion that can be induced in the traps during the preparation procedure. We therefore circularize the pairs of atoms in a geometrical configuration that prevents any interaction. Then, once the atoms are properly brought to $|52C\rangle$, we rotate the quantization axis to be able to scrutinize any targeted interaction geometry, without the presence of perturbative motion. With this upgraded preparation protocol, the atomic motion is completely de-correlated from the circular-circular interaction configuration we want to probe.

We concluded the fourth chapter with the time-resolved observation of spin exchanges between two circular atoms, still in the resonant, first order interaction regime. Using a third atom and its Rydberg blockade volume, we are able to initialize the pair in $|51C, 52C\rangle$ and record its subsequent evolution, which matches the expected behavior with good accuracy.

Throughout this dissertation, we stressed the importance of several technical features that underlie the scientific achievements on circular atom manipulation and circular-circular interactions. These technicalities correspond to various ingredients that make up the recipe for an efficient quantum simulation platform. In that context, we can mention the following accomplishments: the creation of arbitrary spin geometries (thanks to the rearranging beam), the implementation of long-lived spin-1/2 elements (in the form of individually-trapped circular atoms) interacting in a highly controlled fashion (via the geometry of the dipole-dipole interactions), measurable with site resolution (thanks to the optical detection) and individually addressable for state initialization (through the dipole blockade trick). All in all, by overcoming these various technical challenges, we explicitly demonstrated the feasibility of using circular atoms for quantum simulation experiments.

Although much work is still required to reach advanced simulation schemes, this new setup already opens up interesting investigation prospects, that can be directly built upon these first results. Following the results of the fourth chapter, the resonant spin exchange could be implemented in larger ensembles of atoms. With the straightforward tool of microwave spectroscopy at hand, it seems feasible to probe couplings within groups of three or more atoms, which should display clear signs of interactions in the same fashion as a pair. The driven Rabi oscillations of N atoms, for instance, should display, under the right conditions, oscillations at $\sqrt{N}$ times the frequency of the single-atom ones. Thanks to the dipole blockade preparation, we could also imagine observing the propagation of a single spin excitation in a chain of circular atoms, through a careful choice of the geometry.

Furthermore, the investigation of van der Waals interactions could also be within reach in this current experimental platform. We should indeed be able to reach a precision in our microwave spectroscopy which falls into the scale of second-order van der Waals couplings, where interaction-induced energy shifts in pair states are of the order of 10 kHz at our standard inter-atomic distances. The van der Waals interactions display a richer behavior than the resonant regime. It exhibits both longitudinal and transverse spin couplings, where the resonant case only feature the latter. Importantly, these couplings depend on the static electric and magnetic field. Witnessing such van der Waals interactions and checking their dependence on the static fields would constitute significant achievements.

The motional state of the circular atoms took on an unexpectedly important role in this work, whether through the theoretical spin-phonon model of the first chapter [124] or in obtaining the main experimental results of chapter four. The investigation of spin and motion interplay could also be pushed further in the near future, whether to probe the temperature of the circular atoms or to create motional Schrödinger cat states, as

proposed in chapter 1.

Finally, one could envision the realization of quantum non-destructive (QND) measurements of circular states in our setup, as proposed in [116]. It is possible to find, in the right field conditions, two low-ℓ Rydberg states that are dipole-coupled at the same frequency as two circular states. To measure the state of an atom in these circular levels, we can then use an ancillary atom placed in the low-ℓ levels. Through the resonant interaction between the two atoms, the state of the low-ℓ atom can be made dependent on that of the circular one. If one of the low-ℓ levels is laser-coupled to the ground state, the optical detection of the ancillary atom then yields a QND measurement of the circular atom. The trapping and individual addressing requirements for such a scheme are more involved than what we are currently doing, but should be within reach for our system.

Various technical improvements will nevertheless have to be eventually undertaken in our current platform. We mention them here, following the order of their respective timescales, as prospective evolutions of the setup that should allow it to reach its full potential. First, short-term improvements of the circularization protocol might be considered. As mentioned at the end of chapter 3, other atomic excitation techniques could lead to a circular preparation efficiency greater than the current one, and more suitable for larger ensembles of atoms. In the coming years, the setup will then be transferred to a cryogenic environment, which will allow us to fully harness the properties of circular atoms, by getting rid of most of the black-body-induced decays. With longer lifetimes, the proper implementation and investigation of van der Waals interactions should be immediately within reach in a cryostat. Finally, by adding a plane capacitor around the atoms [119], individual lifetimes of the order of the minute could be achieved, at which point the investigation of unexplored many-body phenomena should become accessible.

From that perspective, the achievements we presented here are only the first of many steps on the road to novel quantum simulations. And in that sense, the completion of this PhD was not really an end in itself, but hopefully an important beginning.

Appendix A

Numerical models

In our experimental work, we constantly rely on numerical simulations to predict and corroborate results. The different programs that run these simulations cover a large scope of applications and vary widely in complexity. They range from simple Python scripts used to estimate atomic transition frequencies based on open-source libraries [95], to intricate Monte-Carlo simulations of single-atom motion in tweezers or bottle beams, to extensive diagonalization of pair Hamiltonians for interaction energy computations, to *ab initio* electric field estimations. We choose to discuss here only two such numerical models. We first present the simulation of circular-state evolution under black-body transfers, as the estimated lifetime of $|52C\rangle$ is omnipresent in discussions throughout this work. We then detail the semi-classical model used to strengthen the main results of this thesis and which is useful for understanding parts of chapter 4. It emulates low-ℓ dipole-dipole interactions in realistic experimental conditions, and allows us to estimate the evolution of both the internal and external degrees of freedoms of the atoms during experimental sequences.

A.1 Lifetime of circular atoms

To analyze experimental data, we often need to estimate the black-body-induced decay of circular atoms to neighboring manifolds. To do so, we compute the statistical evolution of circular population over time, driven by spontaneous emission, absorption and stimulated emission processes. A single circular level $|nC$ is dipole-coupled to mainly six other states, pictured in A.2: its adjacent elliptical levels $|nE^+\rangle$ and $|nE^-\rangle$, the circular levels of the nearest manifolds $|(n-1)C\rangle$ and $|(n+1)C\rangle$, and two elliptical levels of the $n+1$ manifold, $|(n+1)E^-\rangle$ and $|(n+1)E^{--}\rangle$ (not pictured in the figure)[1]. The natural radiative rates of transfer to any of these levels $|r\rangle$ are given by the Einstein coefficient $\Gamma^{(0)}_{nC-r} = 4\alpha\omega^3|\langle r|\hat{\mathbf{r}}|nC\rangle|^2/(3c^2)$ [139]. From the frequency dependency of these rates, we first neglect the transitions to $|nE^{\pm}\rangle$, whose frequencies lie in the radio-frequency range, compared to microwave transitions to the $n \pm 1$ manifolds. Then, the computation of the dipole matrix elements indicates that the transitions to the elliptical states $n+1$ can also be neglected when compared to circular-circular couplings.

[1]State $|nC\rangle$ is also technically coupled to high-ℓ levels of other $n+q$, $q>1$ manifolds, but the couplings are negligible.

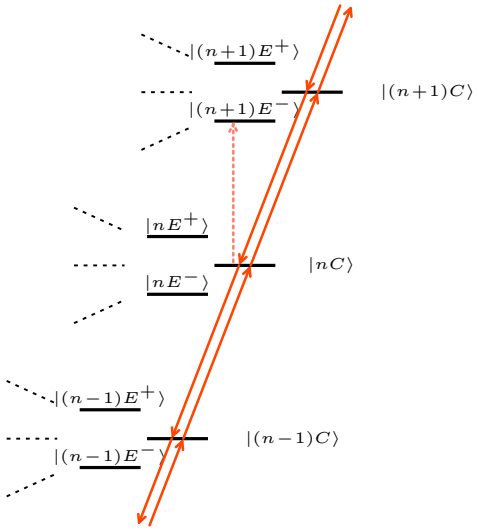

Figure A.1: Most significant dipole-allowed transitions between circular states that contribute to black-body population decay. The circular-circular transitions (orange arrows) have the strongest dipole matrix elements. The π transition between $|nC\rangle$ and $|(n+1)E^-\rangle$ (pink dotted arrow) has a rate that is barely 10% of that of $|nC\rangle \rightarrow |(n+1)C\rangle$, and is discarded in the computations. Other transitions to elliptical states (not pictured here) are completely negligible.

In our numerical model, we therefore only consider transitions between adjacent circular states. We want to estimate the population evolution, starting from any statistical distribution within circular levels and for a given black-body temperature. We write $\nu_{n,n\pm1}$ the microwave transition frequencies between circular levels and $\Gamma_n^{(0)}$ the natural spontaneous emission rate of circular level $|nC\rangle$, computed from the Einstein coefficient:

$$\Gamma_n^{(0)} = \frac{4\alpha(2\pi\nu_{n-1,n})^3}{3c^2}|\langle(n-1)C|\hat{\mathbf{r}}|nC\rangle|^2. \tag{A.1}$$

The absrption and stimulated emission rates of this transition are then computed from:

$$\Gamma_n^{(1)} = s(\nu_{n-1,n})\Gamma_n^{(0)}, \tag{A.2}$$

where $s(\nu_{n-1,n})$ is the average mode of photons in the relevant mode, given by Planck's law:

$$s(\nu) = \frac{1}{e^{h\nu/k_BT}-1}. \tag{A.3}$$

We write p_{nC} the population in level $|nC\rangle$. From the discussed transition processes, the population evolution over an infinitesimal time dt writes, for state $|nC\rangle$:

$$\begin{aligned} p_{nC}(t+\mathrm{d}t) - p_{nC}(t) = &-(\Gamma_n^{(0)} + \Gamma_n^{(1)}) p_{nC}(t)\mathrm{d}t \\ &- \Gamma_{n+1}^{(1)} p_{nC}(t)\mathrm{d}t \\ &+ (\Gamma_{n+1}^{(0)} + \Gamma_{n+1}^{(1)}) p_{(n+1)C}(t)\mathrm{d}t \\ &+ \Gamma_n^{(1)} p_{(n-1)C}(t)\mathrm{d}t. \end{aligned} \tag{A.4}$$

The four successive terms correspond, respectively, to: the spontaneous and stimulated emission to $n-1$, the absorption to $n+1$, the spontaneous and stimulated emission from $n+1$, the absorption from $n-1$.

We can therefore write a system of coupled differential equations ruling the evolution of the circular populations that we can solve numerically. To estimate the lifetime of $|52C\rangle$, we consider all circular states from $|48C\rangle$ to $|56C\rangle$, restraining the population transfers to these 9 states. We check *a posteriori* that the edge levels are not significantly populated during the evolution, which would indicate that the subspace considered is too small and should include additional circular levels. We set the initial population to pure $|52C\rangle$ and numerically compute the evolution over 1000 µs for a temperature of 300 K. The result is shown in figure A.2, where, in the left panel, we plot all the states' computed populations, and in the right-hand panel focus on $|52C\rangle$ at shorter timescales. We see that, as t reaches 1 ms, population in $|56C\,\rangle$ and $|48C\rangle$ becomes significant, indicating that more levels should be taken into account for longer simulations.

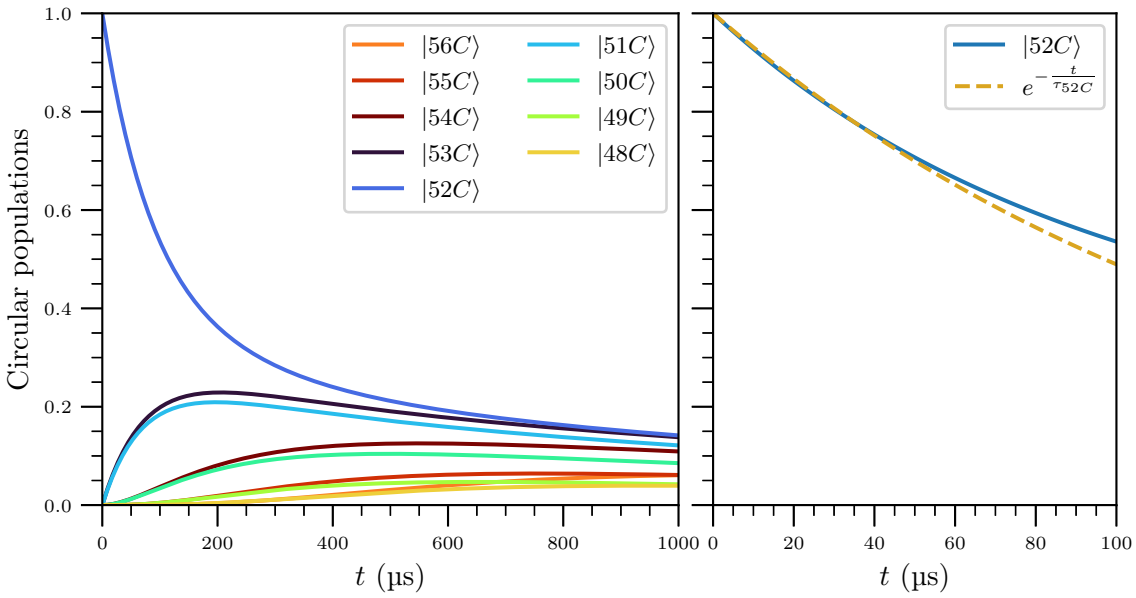

Figure A.2: Simulated population evolution for an initially pure $|52C\,\rangle$ system, at 300 K. The $|52C\rangle$ population is halved in approximately 150 µs. Although the decay process is multi-exponential, we can fit the evolution at short timescales with a simple exponential model (right panel).

To extract a quantitative characterization of the lifetime of $|52C\rangle$, we fit the first 50 µs of its evolution with a basic exponential decay. At longer times, the population strongly deviates from this model, but most of the experiments presented in this work occur at short timescales, within the initial 50 µs duration. In this approximation, we obtain the 300 K lifetime:

$$\tau_{52C} = 140.3 \pm 0.4 \text{ µs}. \tag{A.5}$$

This is the estimate we use throughout the main text to derive information from the results of the measurements.

We finally carry out the same simulation, but starting from $|51C\rangle$, the other circular state of interest in the scope of this work. In this case, the same procedure yields the room-temperature lifetime:

$$\tau_{51C} = 135.4 \pm 0.4 \text{ µs}. \tag{A.6}$$

A.2 Simulation of low-ℓ interactions

The interactions between Rydberg atoms that take place throughout their preparation play a key role in the discussions of chapter 4. We detail here the semi-classical model that allows us to predict these interactions and their effects on the atoms.

A.2.1 Single-atom model

We describe each atom in the hydrogenic approximation, by neglecting the quantum defects, and in a static directing electric field making the parabolic basis the relevant one for computations. The internal atomic state is described by the two angular momenta $\hat{\mathbf{J}}_a = (\hat{\mathbf{L}} - \hat{\mathbf{A}}/2)$ and $\hat{\mathbf{J}}_b = (\hat{\mathbf{L}} - +\hat{\mathbf{A}}/2)$, where $\hat{\mathbf{A}}$ is the symmetric Runge-Lenz vector (see chapter 1). Within the manifold of principal quantum number n, these angular momenta have a magnitude $J_a = J_b = J = (n-1)/2$. Taking z as the quantization axis, the quantum eigenstates of the atom are $|m_a, m_b\rangle$, and the total magnetic quantum number is therefore $m = m_a + m_b$. The lowest-lying state of the manifold is therefore $|J, -J\rangle$, while the circular state of interest is $|J, J\rangle$. For $\sigma = a, b$, the ladder operators $\hat{J}_{\sigma,\pm} = \hat{J}_{\sigma,x} \pm i\hat{J}_{\sigma,y}$ increase or decrease m_σ by single units.

From the definitions of $\hat{\mathbf{J}}_{a,b}$, we get the definition of the atomic dipole moment from the angular momenta:

$$\hat{\mathbf{d}} = (3nea_0/2)(\hat{\mathbf{J}}_a - \hat{\mathbf{J}}_b). \tag{A.7}$$

One can also show [135] that P_C, the probability to be in the circular state, writes:

$$P_C = \left(\frac{(1 + J_{a,z}/J)(1 + J_{b,z}/J)}{4}\right)^{2J}, \tag{A.8}$$

where $J_{a(b),z}$ are the expectations values of $\hat{J}_{a(b),z}$.

In colinear static fields $\mathbf{F}$ and $\mathbf{B}$ that define the quantization axis z, the single-atom Hamiltonian writes:

$$\hat{H} = -(\omega_S - \omega_Z)\hat{J}_{a,z} + (\omega_S + \omega_Z)\hat{J}_{b,z}, \tag{A.9}$$

where $\omega_Z = \mu_B B_z/\hbar$ and $\omega_S = (3nea_0/2)F_z/\hbar$ are respectively the Zeeman and Stark frequencies. By adding a σ^+-polarized radio-frequency field of frequency $\omega_{\mathrm{RF}}/(2\pi)$, which drives the $m_b \to m_b \pm 1$ transitions, the single-atom Hamiltonian becomes:

$$\hat{H} = -\omega_a \hat{J}_{a,z} - \Delta_b \hat{J}_{b,z} + \Omega_b(\hat{J}_{b,+} + \hat{J}_{b,-}), \tag{A.10}$$

where $\Delta_b = -\omega_b + \omega_{\mathrm{RF}}$ and $\Omega_b \propto F$ is the Rabi frequency of the $\hat{J}_{b,\pm}$ transitions. Using the Ehrenfest theorem and the canonical commutation relations

$$[\hat{J}_{a(b),\alpha}, \hat{J}_{a(b),\beta}] = i\hbar\epsilon_{\alpha\beta\gamma}\hat{J}_{a(b),\gamma}, \tag{A.11}$$

we obtain the equations ruling the evolution of the expectation values $\mathbf{J_a}$, in the frame rotating at ω_{RF}:

$$\begin{aligned}\frac{dJ_{a,x}}{dt} &= \omega_a J_{a,y},\\ \frac{dJ_{a,y}}{dt} &= -\omega_a J_{a,x},\\ \frac{dJ_{a,z}}{dt} &= 0,\end{aligned} \tag{A.12}$$

and those of $\mathbf{J_b}$:

$$\begin{aligned}\frac{dJ_{b,x}}{dt} &= \Delta_b J_{b,y},\\ \frac{dJ_{b,y}}{dt} &= -\Delta_b J_{b,x} - 2\Omega_b J_{b,z}\\ \frac{dJ_{b,z}}{dt} &= 2\Omega_b J_{b,y}.\end{aligned} \tag{A.13}$$

To numerically simulate the evolution of the atom during the circularization, we will initialize the atomic state as $|J, -J\rangle$. According to the equations, $\mathbf{J_a}$ will remain constant and aligned with z, while $\mathbf{J_b}$ will precess around a vector $\mathbf{\Omega} = (2\Omega_b, 0, -\Delta_b)$. In this picture, the inversion of the detuning that occurs during the RF adiabatic passage takes a more visual interpretation, as it drives $\mathbf{J_b}$ from one pole of the Bloch sphere to the other. We depict in figure A.3 the evolution of the angular momenta, from $|J, -J\rangle$ to $|nC\rangle$, through the adiabatic passage.

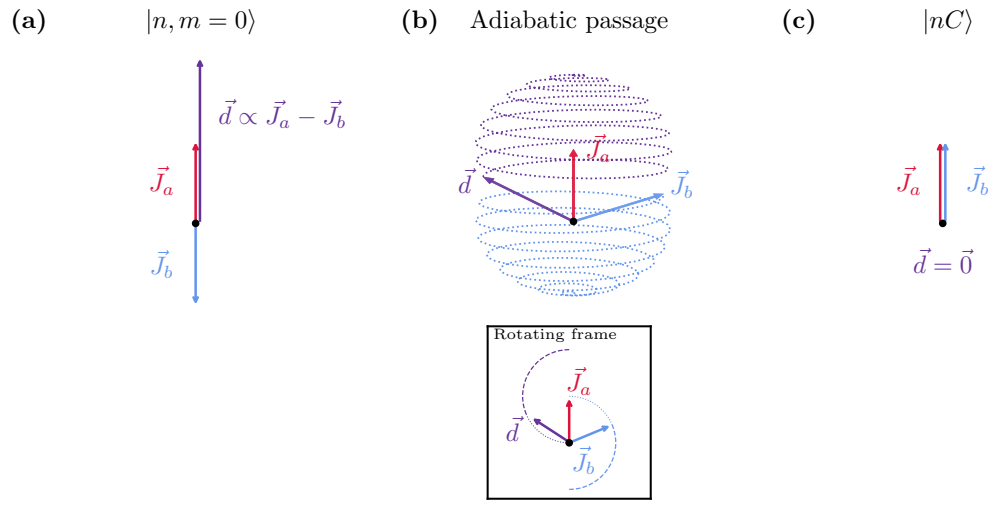

Figure A.3: Simplified representation, in the hydrogenic picture, of the angular momenta and dipole moment **(a)** before, **(b)** during and **(c)** after the circularizing adiabatic passage. In the circularization stage, we show the rotation of $\mathbf{J}_b$ from pole to pole as the detuning changes (over microseconds) and its rotation at ω_{RF} around the quantization axis. For clarity, we however do not display the part of its motion that precesses around $\mathbf{\Omega}$ at the Ω_b timescale.

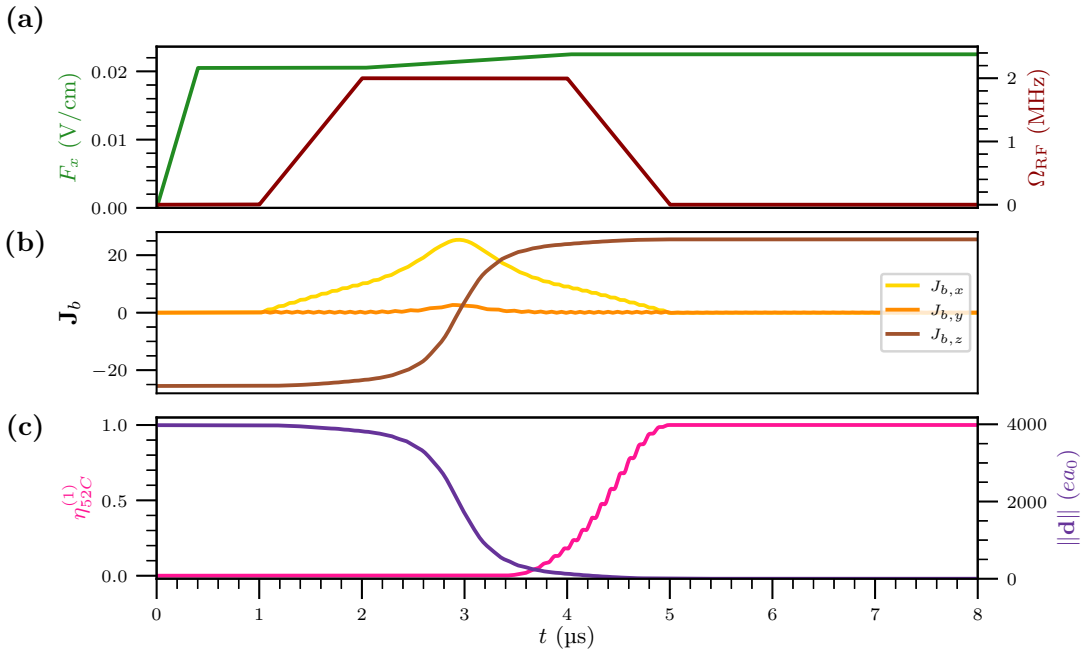

Figure A.4: Numerical simulation of the single-atom evolution during the adiabatic passage, following equations (A.12) and (A.13). **(a)** Simulated time-evolution of the RF Rabi frequency and electric field amplitude, corresponding to their real experimental implementation – as presented in chapter 3. **(b)** Expectation values for the three components of $\mathbf{J_b}$, in the frame rotating at the RF frequency. **(c)** Atomic dipole moment and single-atom circular state purity $\eta^{(1)}_{52C}$, which corresponds to P_C.

We solve the differential equations numerically, by making sure to have $\Delta_b(t)$ and $\Omega_b(t)$ vary as in the adiabatic passage's field and RF amplitude evolutions in the experiments. We obtain the simulated circularization plotted in figure A.4 using the real parameters of the setup and for the $n = 52$ manifold. The atomic dipole moment only starts decreasing midway through the adiabatic passage, while the probability to be in $|52C\rangle$ rises to 1 at the end of the process.

A.2.2 Pair evolution

We now consider two atoms undergoing the same adiabatic passage and each trapped in a harmonic potential of frequency ω_t. We label them with the indices $i = 1, 2$. The goal of the simulation is two-fold. We first want to estimate the impact on the purity of the spatial proximity between the atoms. We also want to simulate the interaction-induced atomic motion. We carry on with a semi-classical approach. We tackle the computation of the internal state of the atoms via Ehrenfest theorem, as in the single-atom picture. We however simulate the motion in a fully classical manner, via the interaction energy of the two atoms and the resulting evolution of the atomic positions in their traps.

As in the main text, we consider that a distance d separates the two traps. We write r the distance between the two atoms and consider that they are in the $x-z$ plane, with z the quantization axis. We denote by θ the angle between the inter-atomic axis and the quantization axis. The unit vector along the inter-atomic axis is then $\mathbf{e} = (\sin\theta, 0, \cos\theta)$.

Simulation of the internal degree of freedom

As per the dipole-dipole interaction formula, the coupling between the two angular momenta of the two atoms writes:

$$\begin{aligned}\hat{V}_{\mathrm{dd}} = \frac{1}{4\pi\varepsilon_0 r^3}\left(\frac{3}{2}nea_0\right)^2 \{ &\left(\hat{\mathbf{J}}_a^{(1)} - \hat{\mathbf{J}}_b^{(1)}\right)\cdot\left(\hat{\mathbf{J}}_a^{(2)} - \hat{\mathbf{J}}_b^{(2)}\right) \\ &- 3\left[\left(\hat{\mathbf{J}}_a^{(1)} - \hat{\mathbf{J}}_b^{(1)}\right)\cdot\mathbf{e}\right]\left[\left(\hat{\mathbf{J}}_a^{(2)} - \hat{\mathbf{J}}_b^{(2)}\right)\cdot\mathbf{e}\right]\}.\end{aligned} \tag{A.14}$$

By developing this expression and applying once more the Ehrenfest theorem, we can write the system of differential equations coupling the expectation values of the four angular momenta (two per atom). By writing $\mathcal{A} = (3nea_0/2)/(4\pi\varepsilon_0 r^3)$, we get the following equations, valid in the reference frame:

$$\begin{aligned}\frac{dJ_{a,x}^{(1)}}{dt} = \mathcal{A}\{ &-(1-3\sin^2\theta)J_{a,y}^{(1)}(J_{a,z}^{(2)} - J_{b,z}^{(2)}) \\ &+ J_{a,z}^{(1)}(J_{a,y}^{(2)} - J_{b,y}^{(2)}) \\ &+ 3\cos\theta\sin\theta J_{a,y}^{(1)}(J_{a,x}^{(2)} - J_{b,x}^{(2)})\},\end{aligned} \tag{A.15}$$

$$\begin{aligned}\frac{dJ_{a,y}^{(1)}}{dt} = \mathcal{A}\{ &-(1-3\sin^2\theta)J_{a,z}^{(1)}(J_{a,x}^{(2)} - J_{b,x}^{(2)}) \\ &+ (1-3\cos^2\theta)J_{a,x}^{(1)}(J_{a,z}^{(2)} - J_{b,z}^{(2)}) \\ &+ 3\cos\theta\sin\theta J_{a,z}^{(1)}(J_{a,z}^{(2)} - J_{b,z}^{(2)}) \\ &- 3\cos\theta\sin\theta J_{a,x}^{(1)}(J_{a,x}^{(2)} - J_{b,x}^{(2)})\},\end{aligned} \tag{A.16}$$

$$\begin{aligned}\frac{dJ_{a,z}^{(1)}}{dt} = \mathcal{A}\{ &-(1-3\sin^2\theta)J_{a,y}^{(1)}(J_{a,x}^{(2)}-J_{b,x}^{(2)}) \\ &- J_{a,x}^{(1)}(J_{a,y}^{(2)}-J_{b,y}^{(2)}) \\ &- 3\cos\theta\sin\theta J_{a,y}^{(1)}(J_{a,z}^{(2)}-J_{b,z}^{(2)})\}.\end{aligned} \tag{A.17}$$

The $\mathbf{J_b}$ equations are obtained by inverting a and b in the above expressions. The interaction being symmetric for the two atoms, the coupling equations of atom 2 are exactly the same, up to the inversion $1 \leftrightarrow 2$. This feature simplifies the resolution. Since the two atoms undergo the same evolution, we constantly have $\mathbf{J}_{a(b)}^{(1)} = \mathbf{J}_{a(b)}^{(2)}$. The system is then reduced to the computation of only two angular momenta $\mathbf{J}_a$ and $\mathbf{J}_b$, each coupled to itself and to the other. By adding the single-atom equations (written in the frame rotating at the RF frequency), we obtain a set of differential equations that we can solve numerically. Let us note that, in the coupling equations, the inter-atomic distance is r and is allowed to change over time, to account for the atomic motion.

Simulation of the external degree of freedom

Modeling the motion of the atoms is simpler. We treat this part of the problem in a classical picture. In this context, the interaction energy between the two atoms writes

$$V_{\mathrm{dd}} = \frac{1}{4\pi\varepsilon_0 r^3}\left\{\mathbf{d}^{(1)}\cdot\mathbf{d}^{(2)} - 3\left(\mathbf{d}^{(1)}\cdot\mathbf{e}\right)\left(\mathbf{d}^{(2)}\cdot\mathbf{e}\right)\right\} \tag{A.18}$$

At any given time during the circularization, the atomic dipole moment of the atoms writes

$$\mathbf{d}^{(i)} = \begin{pmatrix} d_\perp\cos\alpha_{\mathrm{RF}} \\ d_\perp\sin\alpha_{\mathrm{RF}} \\ d_\parallel \end{pmatrix} \tag{A.19}$$

The components $d_\perp$ and $d_\parallel$ are defined by the norm of the dipole and can be computed from $\mathbf{J}_a$ and $\mathbf{J}_b$. They evolve at the timescale of the adiabatic passage, i.e., over fractions of microseconds (see figure A.4). The oscillating terms in the x and y components accounts for the precession of the dipole around the quantization axis, driven by that of $\mathbf{J}_b$. The angle α_{RF} evolves at the RF frequency of 225 MHz, i.e. at the nanosecond scale. For each instant at which we compute the classical dipole-dipole interaction energy, we therefore average the oscillations of the x and y components of the dipoles. When doing so after some re-writing of equation (A.18), we get:

$$V_{\mathrm{dd}}(t) = \frac{1}{4\pi\varepsilon_0 r^3}(1-3\cos^2\theta)(d_\parallel(t)^2 - d_\perp(t)^2/2) \tag{A.20}$$

We note that the angular dependency in the equation indicates that, at $\theta = \theta_0 \simeq 54,7°$, no motion is induced. The motion occurs along the inter-atomic axis, in the $x-z$ plane. Thanks to the simplified energy formula, we can numerically simulate the evolution of r, the inter-atomic distance, during and after the adiabatic passage. We take into account the harmonic trapping potential of each atom, so that the equation of motion of r, the inter-atomic distance, writes:

$$\frac{d^2r}{dt^2} = -\omega_t^2 r(t) - \frac{1}{\mu}\frac{dV_{\mathrm{dd}}}{dr}(t). \tag{A.21}$$

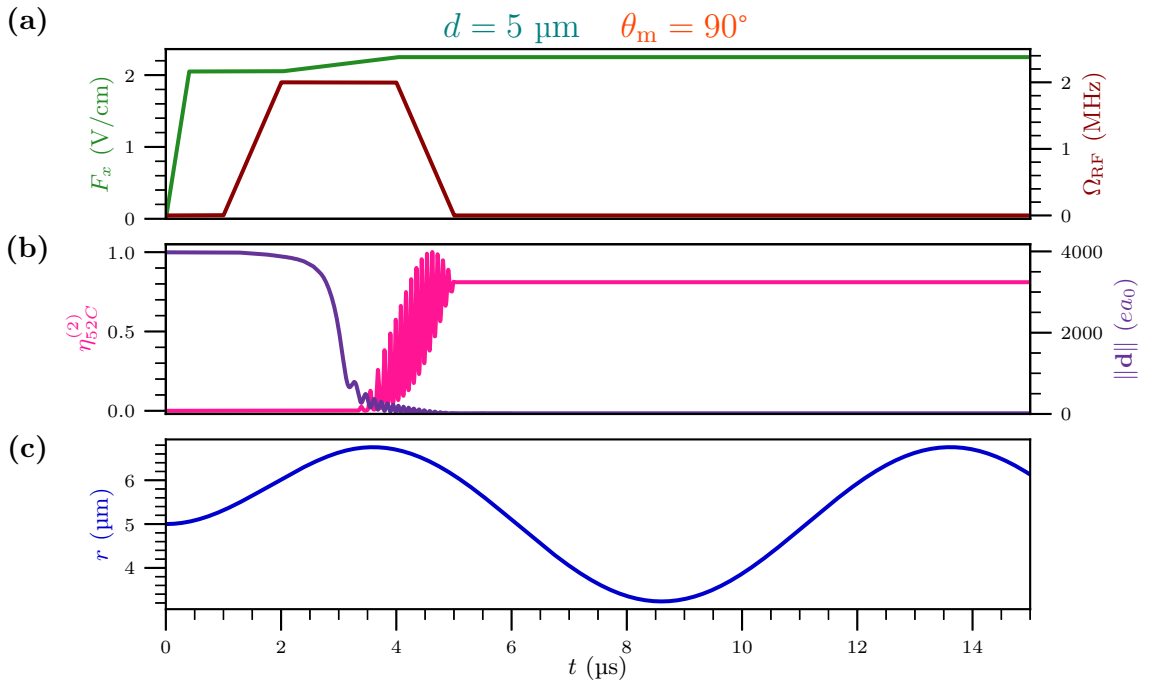

Figure A.5: Numerical simulation of the pair evolution during the adiabatic passage. **(a)** Time-evolution of the simulated RF Rabi frequency and electric field amplitude. **(b)** Atomic dipole moment of each atom and pair circular-state purity $\eta^{(2)}_{52C}$, i.e., probability for each atom to be in $|52C\rangle$. The interactions hinder the proper circularization as $\eta^{(2)}_{52C}$ caps at 80%. **(c)** Simulated atomic motion: variation of the inter-atomic distance r over time. The trapping frequency of the traps is set to 100 kHz.

Here, $\mu = M/2$ is the reduced mass of the pair of atoms, and $V_{\mathrm{dd}}(t)$ evolves over time according to the circularization and angular momenta interactions.

Once the motion is coupled to equations (A.15), (A.16), and (A.17) (where the single-atom adiabatic evolution should be added), we obtain the full description of the pair during the circularization, with the interaction-induced effects taken into account. We show in figure A.5 the result of a numerical resolution of the system. To force the emergence of interaction phenomena, we take a short inter-trap distance of 5 µm, but tightly trap the atoms in $\omega_t = 2\pi \times 100$ kHz potentials. In this case, the interactions prevent the circularization from reaching a good circular purity in the pair. The pair preparation efficiency $\eta^{(}_{52C}2)$ only rises to 81% at the end of the process, when the same procedure applied to single atoms is estimated to reach a 100% purity (cf. figure A.4). The simulation also predicts a significant motion, with an inter-atomic distance varying by microns despite the tight trapping potentials. The motion is kicked-off by the strong low-ℓ interactions before the adiabatic passage. It results in oscillations of r at the trapping frequency for the rest of the evolution. In chapter 4 of the main text, we make use of this numerical model on several occasions to explain the measured phenomena. We mostly rely on it to estimate the motion of the atoms and corroborate its real measurements.

Appendix B

Stability of the spin-phonon system

Within the framework of chapter 1, the effective potentials exerted on the relative position of two circular atoms trapped in harmonic wells write, for each of the two pair states $|+X\rangle$ and $|-X\rangle$:

$$V_{\pm}(x) = \frac{1}{2}\mu\omega^2 x^2 + \hbar U_m(x)(\pm 2J - \Delta), \tag{B.1}$$

where x is the relative position $x = x_2 - x_1$, μ the reduced mass and $U_m(x) = (1 + x/d)^{-m}$ accounts for the distance-dependence of the interaction. The distance between the two traps is d, while J and Δ are the interaction coefficients in the given configuration. They depend on the geometry of the system, on the static fields and on the subspace of atomic levels considered. We recall that, if the states evolve in $\{|nC\rangle, |(n+1)C\rangle\}$, Δ is negligible compared to J, which goes as $1/r^3$, i.e., $m = 3$. If the atomic subspace is $\{|nC\rangle, |(n+2)C\rangle\}$, both coefficients are comparable and $m = 6$.

The second term in $V_{\pm}$ diverges as $1/r^m$. If large and negative, this contribution can dominate the quadratic term of the trapping potential. More precisely, if the interaction is attractive and too strong compared to the trapping potential, the atoms will not be confined to their traps and will collapse onto each other. In this case, the effective potential does not display a local minimum. We study in this appendix such instabilities and try to quantify them so as to be able to avoid them experimentally.

We focus here on the experimental conditions close to the ones implemented in the experiments of this thesis. We take $n' = n + 1$, so that the atoms interact in the direct exchange regime, and we make the approximation $\Delta \simeq 0$ accordingly. To remain within the scope of our study on the spin-phonon system, we also take the quantization axis to be orthogonal to the inter-atomic axis: the atoms are positioned as two plates next to each other on a table. The stability conditions derived here, with this strong interaction configuration, can be easily adapted to other geometries and interaction regimes. In particular, the van der Waals interactions are weaker and should therefore lead to less demanding stability conditions.

In the considered system, we have $J < 0$ (cf. figure I.4 at $\theta = \pi/2$). Of the two effective potentials, only V_+ then displays a negative divergence. We therefore study

this potential only, as no instability issue will arise with V_-. Given the hypotheses on the system, the problematic effective potential writes:

$$V_+(x) = \frac{1}{2}\mu\omega^2 x^2 - \frac{2\hbar|J|}{(1+x/d)^3}. \tag{B.2}$$

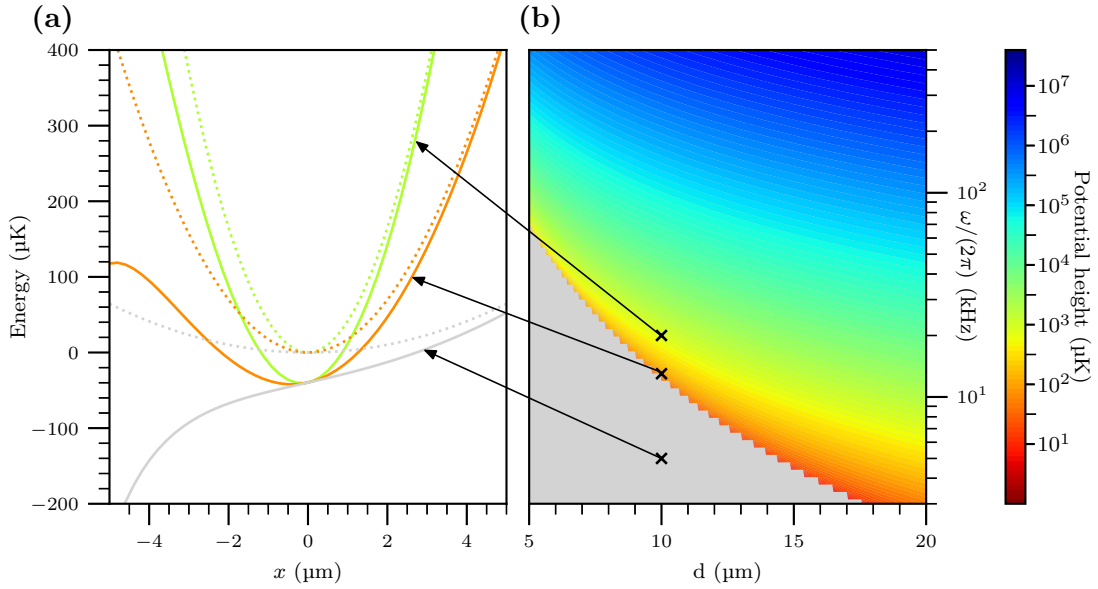

Figure B.1: Stability of the spin-phonon system, in the $\Delta n = 1$ and $\theta = \pi/2$ regime. **(a)** Bare harmonic traps (dotted lines) and effective potentials V_+(solid lines), plotted as functions of the relative distance between the two atoms x, for three configurations illustrating the different behaviors of the system. At large trapping frequency (green), the interaction does not affect the shape of the trap at the relevant scales. In the intermediate regime (orange), the effective potential displays a "wall" of a few hundred µK. For a low trapping frequency (grey), the effective potential cannot trap atoms. **(b)** Map of the wall height as a function of d and ω. The grey region indicates where the system is fully unstable. Experimental parameters should always be taken outside of this region.

Close to $x = -d$, the second term always dominates and $V_+ \to -\infty$. The trapping potential is then characterized, for negative values of x, by a "wall" height. For weak interactions and large trapping frequencies, this wall is extremely high and the trapping potential can be considered fully harmonic. When both terms of V_+ are comparable, the wall can be of reduced amplitude. Knowing its height is crucial for implementations of such experiments. The temperature of the atoms should always be lower than this wall height to prevent them from escaping. Finally, if the interaction is too strong compared to the trapping strength, the effective potential does not even display a local minimum and the atoms are not trapped at all. This configuration should be avoided altogether experimentally. The three possibilities are plotted in figure B (a), where we show both the bare harmonic trap and its associated effective potential V_+ as functions of x. The graphs are computed with $d = 10$ µm and for three different

trapping frequencies of 5 kHz, 10 kHz and 20 kHz. In panel (b), we plot the wall height as a function of both ω and d. The instability domain, where no trapping can occur, is filled in grey. This plot reveals the highly sensitive character of the system's stability, especially with respect to ω. For an increase of the trapping frequency by a factor 2 or 3, the growth of the wall height can be ten-fold. These results, computed numerically, roughly indicate the geometrical parameters that guarantee the stability of the system. These conditions are important to properly manage experiments on interactions. It is for instance quite useful to know, given an atomic temperature, an inter-atomic distance and an interaction strength, the requirement on the trapping frequency (and through it on the laser power per trap) to avoid losses or the collapse of the system.

To be more quantitative, we can also derive analytically the condition on the spin-motion coupling to avoid the unstable regime. Through basic math on V_+, we find that the critical coupling for which the local minimum disappears is:

$$g_c = 3.4\times10^{-3} \times \sqrt{\frac{\omega}{|J|}}. \tag{B.3}$$

We remind that the coupling g is defined as $g = x_0/d$, with x_0 the spatial extent of the ground state in the harmonic trap. The numerical factor is dimensionless and comes from the mathematical manipulations. From this critical coupling, we can express in a more convenient way the instability condition. Re-writing it using d and ω only, we obtain the critical trapping frequency for a given distance:

$$\omega_c = 3.3\times10^{-4} \times \frac{\sqrt{|J|}}{d}. \tag{B.4}$$

This equation gives a practical lower-bound on the trapping frequency that should be used in a specific configuration. For instance, in this direct-exchange setup with $n = 51$, $n' = 52$, $d = 10$ µm and $J = -2\pi \times 830$ kHz, the critical trapping frequency is $\omega_c = 2\pi \times 12$ kHz.

These considerations can easily be extended to other configurations, when $\theta = 0$ for instance (stronger interaction) or when $\Delta n = 2$ (weaker interaction). However, in real experimental setups, the traps are never harmonic. Some extra care has to be added to these stability conditions, to take into account the finite character of the real trapping potentials. These estimations nevertheless remain helpful when the trap can be accurately approximated by a harmonic well over a large region surrounding its center, as it is the case in our experiments with bottle beams.

Appendix C

Electric field control

The electric field plays a central role in all of the experiments carried out in this thesis. Among the electric field properties required for proper atomic manipulations, we can cite: a precise control of its value in the three spatial dimensions, low temporal noise, good homogeneity, i.e., low gradients across the whole atomic manipulation volume, fast temporal response, and the possibility to reach high values to ionize the Rydberg atoms. We address in this appendix some of the technical features of the setup designed to meet these requirements.

C.1 Numerical model

We recall in figure C.1 the set of 12 electrodes surrounding the volume where the experiments take place: 2 Stark electrodes, 2 Stark support electrodes, 4 radio-frequency electrodes, 2 lens-holding electrodes and the 2 ITO-coated lenses themselves. A Simion simulation predicts the field response to any configuration of potentials applied to the 12 electrodes. We use it to choose the voltages that need to be applied to the electrodes to reach a specific field configuration. In practice, we control the field with only 6 electrodes: the 2 Stark and 4 RF ones. The other components mainly impact the field gradients and are not convenient to use to set precise **F** values.

To make the estimation of the field more intuitive, we work with linear combinations of voltages applied to the electrodes, instead of considering each of them independently. We define 6 voltage components: V_{ref}, V_0, V_+, V_x, V_y, V_z. V_{ref} is the sum of the 6 electrodes. It corresponds to a global potential shift. The component V_0 is the sum of the 4 RF electrodes and produces a quadrupolar field in the $x-y$ plane (cf. the legend of figure C.1 for the definition of the axes). V_+ is another combination of the RF electrodes, in which two of their voltages are counted positively and the two others negatively. It creates a quadrupolar field in the $y-z$ plane. V_x creates a field in the x direction and corresponds to a positive voltage on the Stark $+x$ electrode and a negative one on the Stark $-x$ electrode. V_y creates a field along y, and is defined by a positive voltage on the two $+y$ RF electrodes and a negative one on the two $-y$ RF electrodes. Finally, V_z creates a vertical electric field, and corresponds to a positive voltage on the two higher RF electrodes and a negative one on the two lower ones.

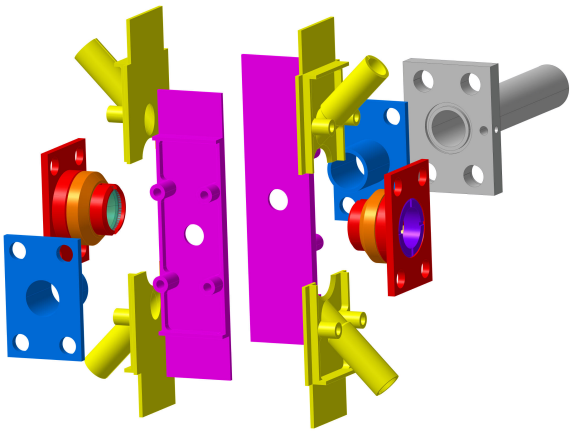

Figure C.1: Exploded view of the electrodes involved in the electric field control. We mainly act on the two Stark electrodes (pink) and four RF electrodes (yellow) to control $\mathbf{F}$ during the experimental sequences. Other components are set to constant values chosen to minimize field gradients in the region of the atoms. The x-axis goes through the Stark electrodes, the y-axis goes through the two lenses (in their red supports), and the z-axis is along the vertical.

We give in table C.1 the simulated electric field response to 1 V being applied on each of the defined voltage components.

Table C.1: Field response at the center of the setup, for 1 V applied on each voltage component. All other electrodes are grounded.

Voltage component	Field response ($\mathrm{V\,cm^{-1}}$)			Gradient response ($\mathrm{V\,cm^{-2}}$)		
	F_x	F_y	F_z	$\partial_x \|\mathbf{F}\|$	$\partial_y \|\mathbf{F}\|$	$\partial_z \|\mathbf{F}\|$
V_{ref}	0	0	0	0.145	−0.111	0
V_0	0	0	0	−0.857	0.849	0
V_+	0	0.142	0	0	0.252	1.149
V_x	−0.818	0	0	0.138	0	0
V_y	0	−0.787	0	0	0.252	0
V_z	0	0	−0.548	0	0	−0.049

This prediction allows us to easily figure out the 6 voltages that *a priori* best reach any given field configuration. In the regular field settings implemented for experiments, we predict a field gradient of -0.138 V/cm/cm in the x-direction in the setup. Across the $\sim$ 100 µm-wide trapping region where we manipulate atoms, this amounts to field variations of 1.38 mV/cm. They are of the same order as the field noise (see below) and we therefore do not try to reduce the gradients any further.

C.2 Electrical setup and LV/HV switch

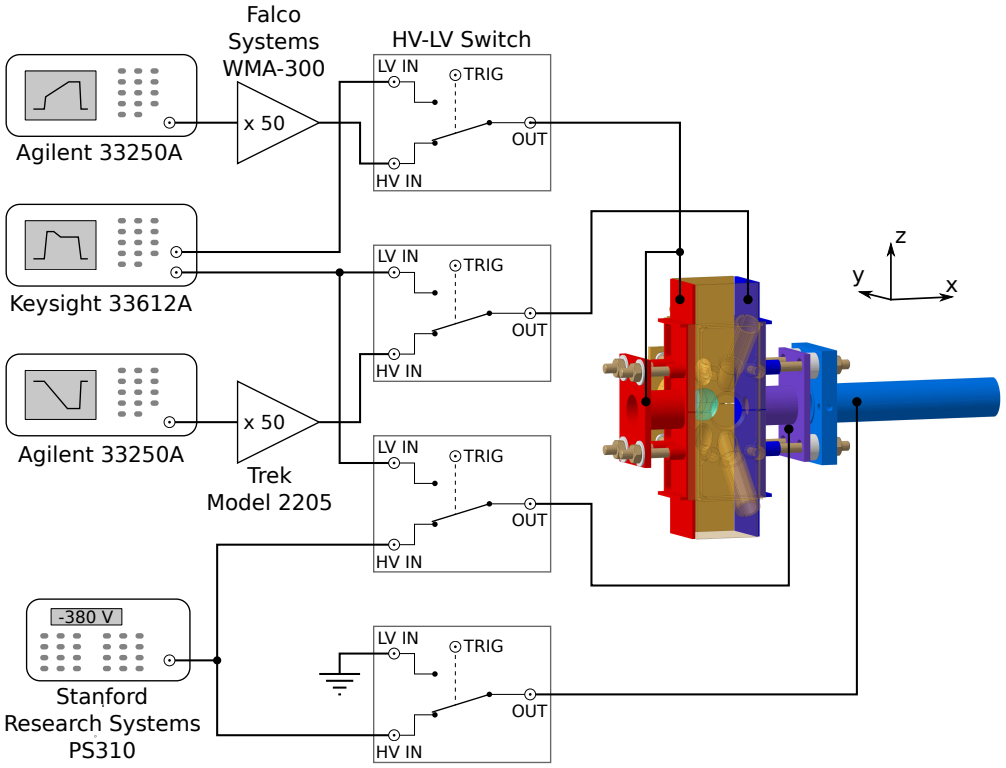

Figure C.2: Electrical circuitry and instruments controlling the Stark electrodes system. Tailored-made switch circuits allow to go from a low-voltage control to high fields for the ionic detection. The guiding tube (shown in blue) is also subjected to a high potential during the ionic detection.

Many technical elements are involved in the control of the 6 central electrodes. The 4 DC voltages applied to the RF electrodes are set via bias-tees placed in their radio-frequency circuitry. Each of them is independently controlled from a computer-controlled digital-to-analog converter (DAC), with a potential range of -10 V to +10 V. The instruments controlling the Stark electrodes are more intricate. Their electrical scheme is represented in figure C.2. They are the electrodes onto which high voltages are applied to ionize the atoms. They should therefore allow two different modes of operation: low-noise, precise, low-field control for atomic manipulation, and high-field (hundreds of Volts) control for the ionization part of the experiments. Electrical circuits designed in-house by Brice Ravon are used to switch between the two regimes. The technical details regarding their components and operation can be found in his thesis [123]. Digitally-controlled triggers signal the switches between low and high voltages. In both cases, the temporal variation of the potentials can be arbitrarily defined thanks to arbitrary waveform generators. They allow, for instance, the definition of both the electric field ramps used in the circularization adiabatic passage and the ionization ramps.

C.3 Field measurements and calibrations

To measure the real value of the electric field in the setup, we use *in situ* atomic measurements. We rely on the microwave spectroscopy of the $|52C\rangle \rightarrow |53E^+\rangle$ transition. With $\Delta m = 0$, its frequency is insensitive to the magnetic field. However, the elliptical level $|53E^+\rangle$ has a linear Stark shift of 101.72 MHz/(V/cm), so that the resonance frequency of the transition yields the value of the electric field norm. A small differential quadratic Stark shift of 0.42 MHz/(V/cm)^2 also shifts the transition. The level structure involved in the spectroscopy is shown in figure C.3 (a). A typical spectrum of the transition is plotted in panel (b) of the same figure.

To thoroughly calibrate the field response, we start by studying the resonance frequency as a function of the V_x component of the voltage settings. Thanks to the numerical model of the electrodes, we roughly cancel the field in the y and z directions. We then measure the resonance frequency of the transition as a function of V_x. We concert the measured frequencies to electric field values thanks to the Stark shift coefficients of the transition. The end result is plotted in the first graph of figure C.3 (c). We oberve a linear relationship between the field response F_x and the applied voltage V_x, as the quadratic shift of the transition is negligible in this range of values.

We then carry out the same procedure with V_y and V_z. We derive, using the now known F_x component, the values of F_y and F_z as functions of the applied voltages. The results are also plotted in figure C.3 (c). We fit each of the three results with linear functions, which yield the precise field calibration needed to carry out the experiments.

We also use this transition to estimate the field noise. By tuning the microwave power so that the transition $\pi - pulse$ occurs at for a pulse duration of 12 µs, we measure a linewidth of 89 ± 5 kHz. We do this with $\mathbf{F}$ aligned with x, the configuration most prominent in the experiments. From the linewidth, we derive the amplitude of the F_x fluctuations in the setup: 0,9 mV/cm. It corresponds to a differential voltage noise of about 1.6 mV on the Stark electrodes, which is compatible with the 1.2 mV precision of their waveform generators.

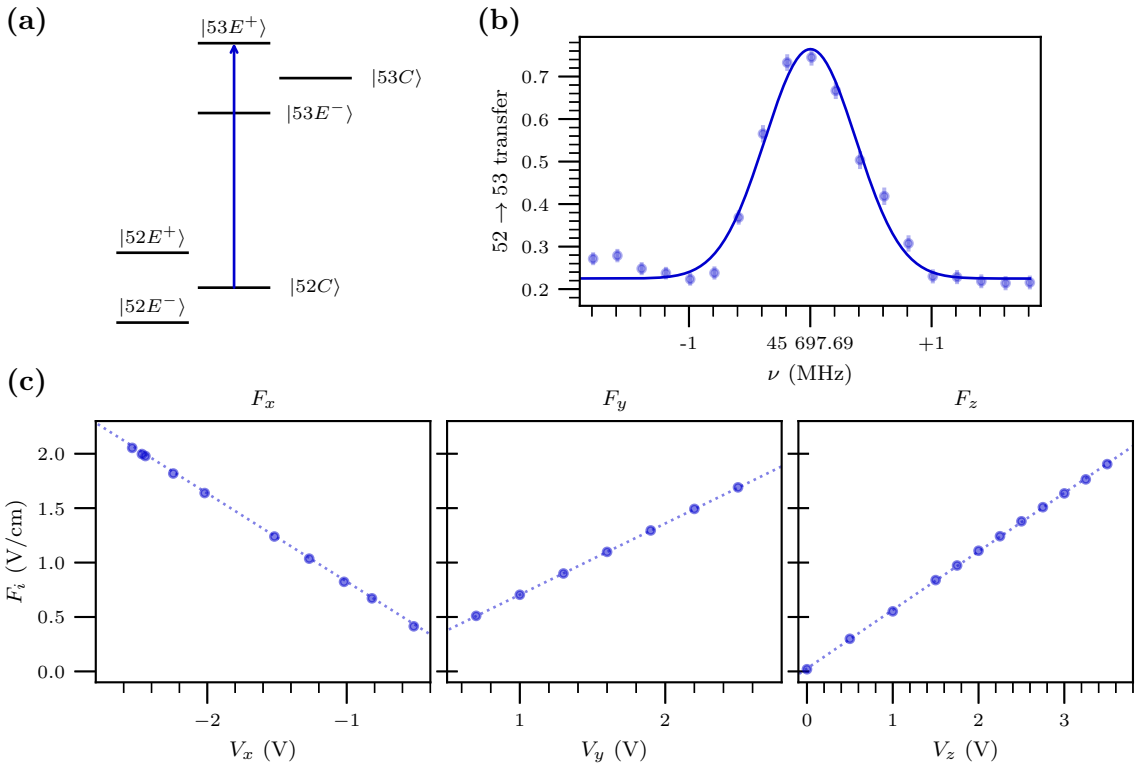

Figure C.3: Electric field measurement and calibration. **(a)** Level structure of the atomic transition used to probe the electric field. **(b)** Example of a $|52C\rangle \rightarrow |53E^+\rangle$ microwave spectrum. Knowing the linear and quadratic Stark shift of the transition, the resonance frequency provides a precise estimation of the electric field's norm. **(c)** Calibration of the field response, in the three directions, as functions of the applied potential components. F_x is measured with the other components *a priori* set to zero, while F_y and F_z are then reconstructed thanks to the knowledge of F_x.

Appendix D

Laser systems

Our experiments essentially rely on the manipulation of light to control atoms. In daily operations, over ten different laser beams are used to prepare and carry out measurements on the atoms, each with its own specific wavelength, size and power. Most of them must have a stable frequency, that sometimes needs to be dynamically controllable. This appendix gives an overview of the optical systems designed and built to meet the needs of the experiment. The figures shown here are reproduced from B. Ravon's PhD dissertation [123], with whom I worked on the design, assembly and optimization of most of the laser systems. They can be divided in three categories:

- The ground-state lasers: they address various transitions in the hyperfine structure of the D_2 line of Rb for ground-state manipulation of the atoms.
- The trapping laser: it generates the three trapping beams of the experiment (tweezers, bottle beams and moving tweezer).
- The Rydberg lasers: their purpose is to excite the ground-state atoms to Rydberg levels. They must be both powerful and finely stabilized in frequency.

The trapping and Rydberg lasers are both new systems in our setup. The ground-state laser scheme had been implemented years ago for past experiments but was recently completely rebuilt and improved to fit the current needs of the setup. I personally set up from scratch the Rydberg lasers and the cavity locking scheme, through which we stabilize the frequency of the lasers. The trapping laser system is rather simple and depicted in figure II.3 of chapter 2. We detail here the organization of the ground-state and Rydberg lasers and their locking scheme.

D.1 Ground-state laser system

Three different lasers are involved in the ground-state manipulations of the atoms: the "MOPA", the "repumper" and the "spectro", as per their given names in the lab. Figure D.1 summarizes their respective frequencies with respect to the D_2 transition of Rb. We show in figure D.2 simplified drawings of their optical schemes.

The "spectro" laser is a Toptical DL Pro, locked through the external cavity onto the $5S_{1/2}, F = 2 \rightarrow 5P_{3/2}, F' = 3$ transition. It is used, through two beat-lock setups, as a frequency reference for the other two ground-state lasers. From the "spectro" laser, we also generate two beams used in the experiments:

- The "probe" beam: used at low power for the optical pumping of the atoms and at higher power to kick them when needed (in the light-shift and Raman spectroscopy experiments). Its frequency is tunable via a double-pass AOM [196].
- The "Raman F2" beam, used in the Raman spectroscopy measurements. In the same manner as the probe, a double-pass AOM tunes its frequency.

The "repumper" laser is also a Toptica DL Pro. It is frequency-locked, through the "spectro" reference, on the $F = 1 \rightarrow F' = 2$ transition. Three beams are generated from this laser:

- The "static repumper": with fixed frequency set on $F = 1 \rightarrow F' = 2$, it is overlapped with the cooling beams to avoid loosing atoms to the dark state $F = 1$ during the cooling process.
- The "tunable repumper": with adjustable frequency thanks to a double-pass AOM, this beam is used to re-pump trapped atoms. The tunable frequency allows us to compensate for the light-shift generated by the tweezers on the transition. It is involved in the measurement of the trap depths and in the optical pumping of the atoms. It is overlapped with the "probe" beam before reaching the experiment.
- The "Raman F1" beam, of tunable frequency, used in the Raman spectroscopy measurements.

Finally, the "MOPA" laser is a Toptica TA 100, outputting 1 W of laser power. Thanks to a specific beat-lock scheme using the "spectro" as a reference, its frequency is quickly tunable over tens of MHz around the $F = 2 \rightarrow F' = 3$ transition. It is used to cool the atoms when its frequency is set to its MOT or molasses values. It also makes the atoms fluoresce for their imaging. Three beams are derived from it:

- Two 2D-MOT beams, of fixed frequency and sent to the 2D-MOT structure for the initial transverse cooling of the atoms.
- One 3D-MOT beam, of tunable frequency, divided into 6 different beams via a Schäfter-Kirchhoff cluster system, in order to create the six cooling/imaging beams.

D.2 Rydberg lasers system

To excite atoms to Rydberg states via a two-photon transition, we operate two lasers setups, one emitting light at 420 nm (blue Rydberg beam) and the other at 1015 nm (red Rydberg beam). Their optical designs are shown in figure D.3. Both are titanium-sapphire lasers (Equinox + SolsTiS, MSquared), in which a 532 nm pump laser feeds the titanium-sapphire system.

In the 1015 nm system, an output of small power is sent to the external locking ultra-stable cavity to stabilize its frequency via a Pound-Drever-Hall (PDH) scheme. The main 2 W output of the laser goes through a double-pass AOM for fine frequency tuning before being sent to the experiment.

For the blue beam, the wavelength of the titanium-sapphire output is set at 840 nm. Again, a small fraction of its light is dedicated to its frequency stabilization via a PDH scheme through the external ultra-stable cavity. Its main output is then doubled in frequency (ECD-X, MSquared) to create 420 nm light of fixed wavelength, with a total power of 2 W.

Both beams are specifically shaped by cylindrical lenses before reaching the atoms to maximize their intensity in the plane of the atomic arrays.

D.3 Laser locking scheme

The "spectro" and both Rydberg lasers are stabilized in frequency on an ultra-stable cavity through the Pound-Drever Hall (PDH) method [197]. For each laser, its output dedicated to the lock has its frequency modulated by an Electro-Optical Modulator (EOM). The EOMs produce the modulation needed to generate the locking signal at the required frequency. The three beams are overlapped before being sent into the cavity. Their reflections are recorded onto three photo-diodes, which feed the electronics of the feedback loops. The optical design of the locking system is depicted in figure D.1.

The "spectro", once properly locked, is used to stabilize the frequencies of the "repumper" and "MOPA". The "repumper" is beat-locked onto the "spectro" with a fixed offset of 6.914 GHz to reach its appropriate hyperfine transition. The "MOPA" is also beat-locked onto the "spectro", but with a tunable frequency spanning several tens of MHz around a 200 MHz offset. Its frequency is dynamically controlled during experiments to switch from the MOT to the molasses and imaging frequencies.

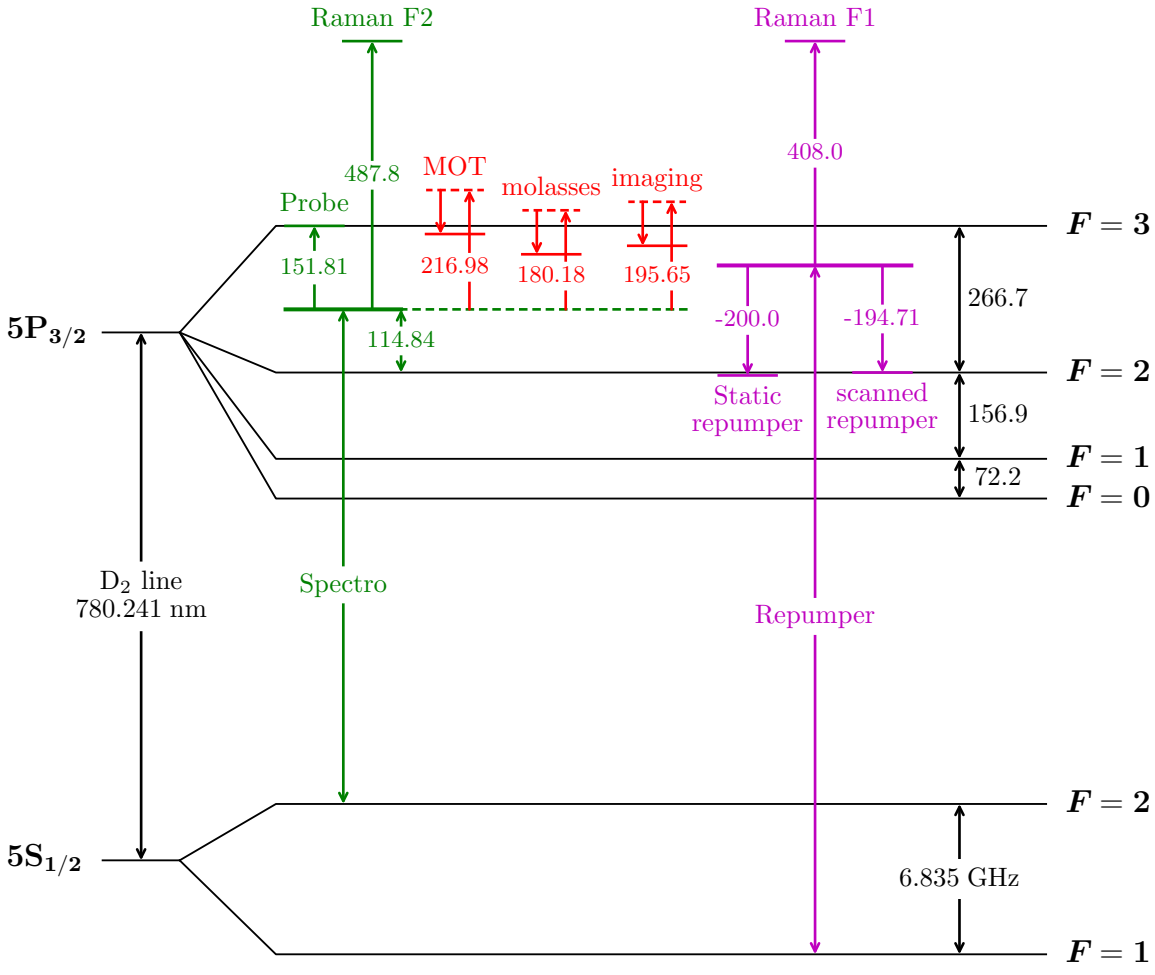

Figure D.1: Level structure of ^{87}Rb D_2-line and relative frequencies of the "ground-state lasers". Owing to its particular locking scheme, the main MOPA laser beam (represented with a dashed red line) has its frequency tuned dynamically during the experimental sequence. We represent the frequency (relative to the "spectro" laser) of the relevant beams during the corresponding parts of the sequence as a solid red line. Unless otherwise specified, the frequencies are expressed in MHz.

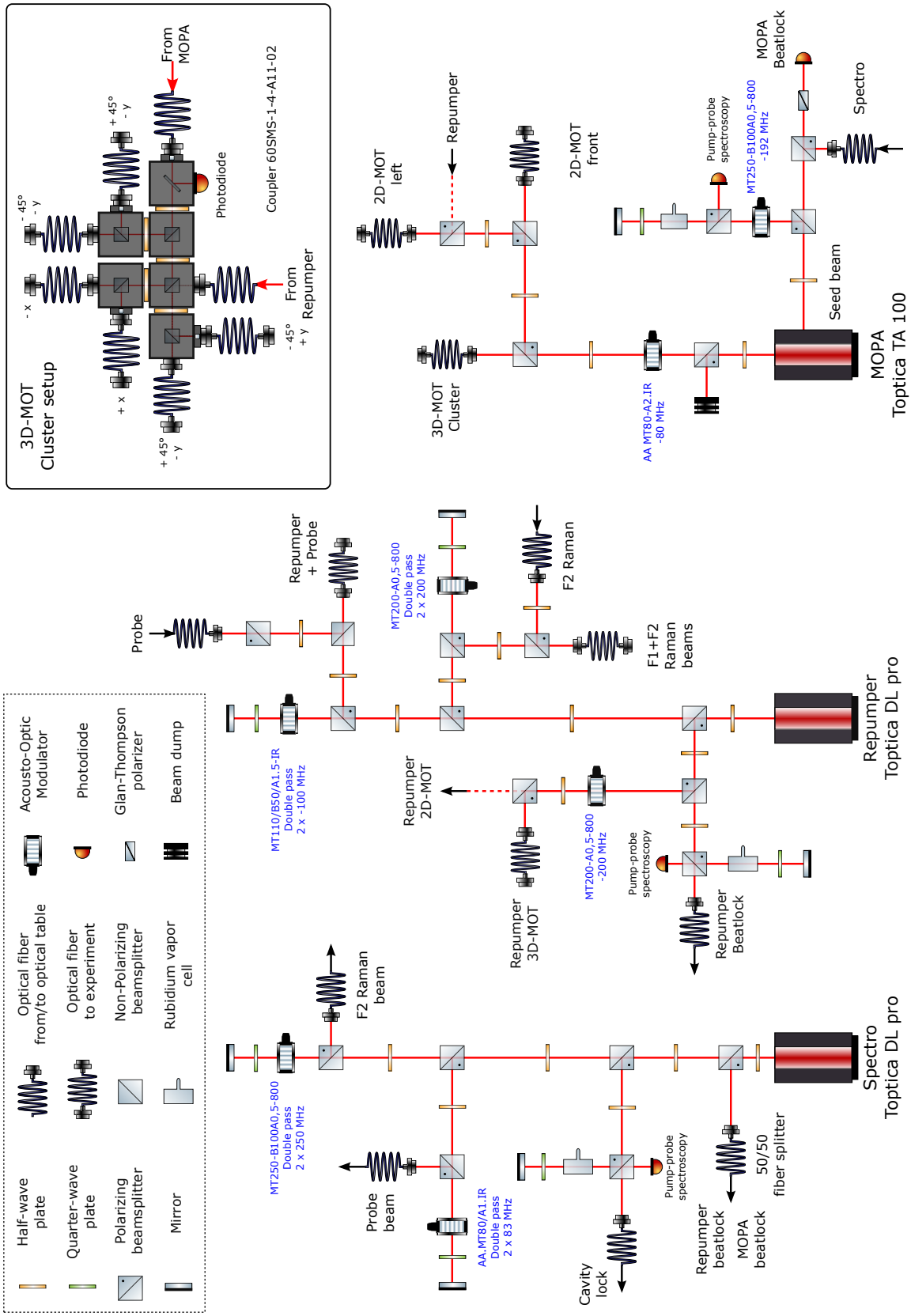

Figure D.2: Laser system for the ground-state beams.

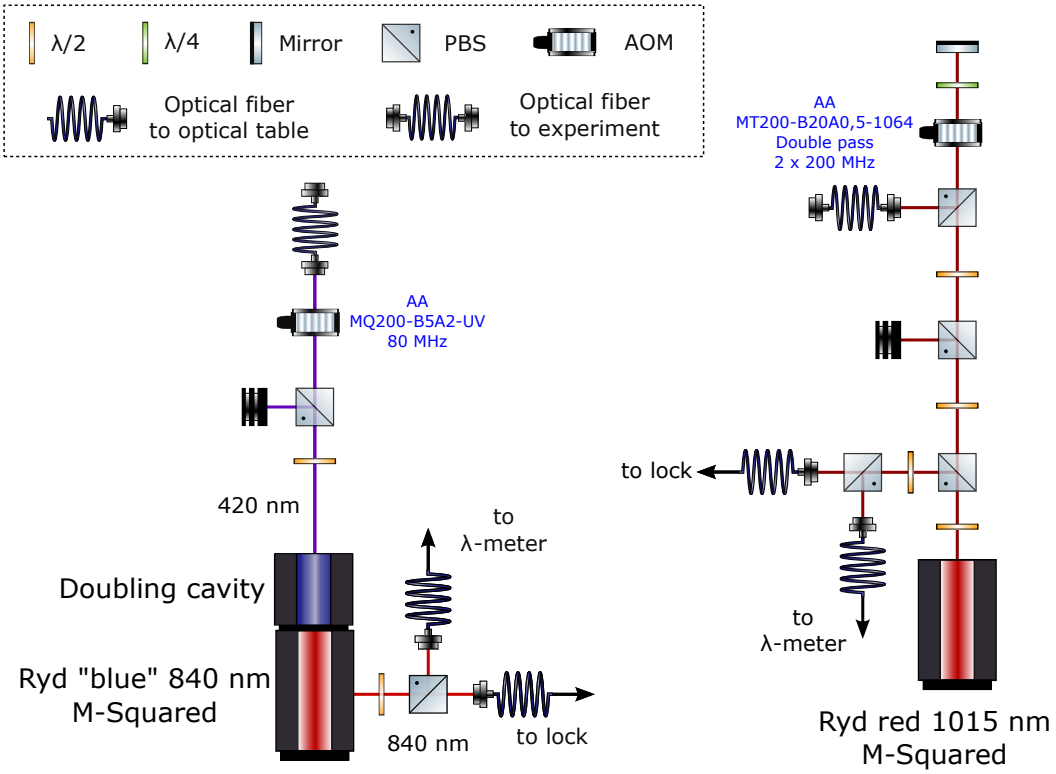

Figure D.3: Laser system for the Rydberg excitation beams.

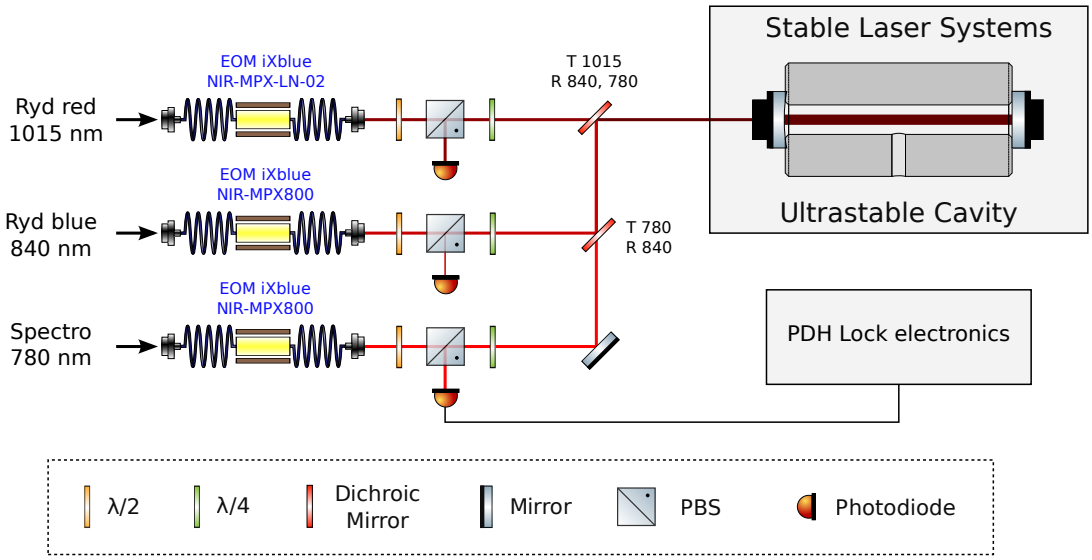

Figure D.4: Pound-Drever-Hall locking scheme of the Rydberg lasers and of the "spectro" laser on an ultra-stable cavity.

Appendix E

Raman spectroscopy

To assess the performance of the optical pumping to $|5S_{1/2}, m_F = +2\rangle$, we implement a Raman spectroscopic measurement. We present here its experimental sequence and the results it produced regarding the purity of the ground-state hyperfine population after optimization of the optical pumping.

The experiment involves several of the ground-state beams, some of them already mentioned in the main text. A description of their respective laser systems can be found in appendix D. The "probe" propagates along the quantization axis x (defined by B_x). It is set on resonance with the $F = 2 \rightarrow F' = 3$ transition and is σ^+-polarized. At low power and for tweezer-trapped atoms, it is used to optically pump the atoms into $|5S_{1/2}, m_F = +2\rangle$ via cycles of σ_+ excitation and random σ_+, σ_-, π decay. At higher power, it is used to kick the $F = 2$ atoms out of their trapping region when turning the traps off. The "tunable repumper", set at resonance on the $F = 1 \rightarrow F' = 2$ transition, avoids the loss of atoms to $F = 1$ during the optical pumping. The two Raman beams, named "Raman F1" and "Raman F2", couple $|5S_{1/2}, F = 1\rangle$ and $|5S_{1/2}, F = 2\rangle$ via a two-photon process through the intermediate state $5P_{3/2}$. They co-propagate at 45° in the $y - z$ plane of the experiment, along one of the cooling beams, with the same circular polarization. The Raman F1 beam is blue-detuned by 759 MHz with respect to $F = 1 \rightarrow F' = 1$ and the Raman F2 beam by 602 MHz with respect to $F = 2 \rightarrow F' = 2$. Both of their frequencies are tunable thanks to double-pass AOMs. Figure E.1 (b) shows a recap of the level structure in the D_2 line, along with the Raman transitions implemented here. The two-photon process addresses the 6 different σ transitions between $F = 1$ and $F = 2$, corresponding to 4 different frequencies shown in various colors in the level structure.

The experimental sequence, including the preliminary optical pumping stage, is pictured in figure E.1 (a). To help understand the purpose of each event, the $5S_{1/2}$ hyperfine level population is also schematically drawn at various moments in the sequence, for a Raman transfer from $|F = 2, m_F = 2\rangle$ to $|F = 1, m_F = 1\rangle$. Right after the first image and for the rest of the sequence, the magnetic field is set to 7 G, which defines the quantization axis and lifts the level degeneracy via the Zeeman effect. We consider the initial atomic population to be evenly spread between the m_F sub-levels of $5S_{1/2}$. The series of events then goes as follows:

1. Optical pumping: with the "probe" and "repumper" beam turned on during 400 µs, the atoms are pumped to $m_F = +2$. The "repumper" is left on for a slightly longer time to make sure that the $F = 1$ population is empty at the end of the process.

2. Raman pulse: the two Raman beams are turned on for 4 µs. If their frequencies are resonant with one of the Raman transitions, the corresponding atoms are transfered from $F = 2$ to $F = 1$.

3. Kick: the tweezers are turned off and the "probe", set on resonance with the non-light-shifted $F = 2 \rightarrow F' = 3$ transition, kicks the $F = 2$ atoms out of their trapping region. We therefore only recapture at the end of the sequence the atoms that were in $F = 1$, i.e., those that underwent a Raman transition.

By plotting the recapture probability as a function of the frequency of one of the Raman beams (the other being fixed), we obtain a snapshot of the hyperfine level population resulting from the optical pumping. When the optical pumping is not properly optimized, we observe four peaks, corresponding to the four Raman transition frequencies of the six σ allowed transitions. The four peaks are plotted in various colors in figure E.1 (c). Incidentally, the regular spacing between the four peaks gives a direct measurement of the magnetic field strength. In the spectrum shown here, the origin of the x-axis corresponds to the frequency at which the peaks collapse when the magnetic field goes to zero. The respective heights of the four peaks are related to the population distribution in the $F = 2$ sub-levels. The right-most peak is directly proportional to the occupancy of $m_F = +2$. To optimize the optical pumping efficiency, we therefore maximize the height of that peak. The best optical pumping configuration we could reach produced the blue spectra of the figure. In this configuration, the "probe" and "repumper" pulses last approximately 400 µs and their respective intensities are around 0.02 mW/cm^2 and 200 mW/cm^2. While tuning the optical pumping parameters, we also monitored the heating it induces on the atoms, via the dedicated experiment presented in the main text. In the final configuration, the optical pumping process raises the atomic temperature by 9 µK.

By fitting the two high-frequency peaks with Lorentzian line shapes, we get the amplitudes $A_{m=2} = 0.72 \pm 0.01$ and $A_{m<2} = 0.018 \pm 0.002$. From them, we deduce the purity of the $m_F = +2$ sub-level, i.e., the efficiency of the optical pumping $\overline{\eta_{\mathrm{OP}}} = A_{m=2}/(A_{m=2} + A_{m<2})$. We evaluate it and find:

$$\overline{\eta_{\mathrm{OP}}} = 0.97 \pm 0.01. \tag{E.1}$$

This level of purity was reached after a meticulous optimization of all the relevant parameters: "probe" and "repumper" powers, frequencies, pulse durations and beam positions. However, these settings are quite sensitive. The very low power of the "probe" is subject to fluctuations (due to its optical fiber or polarization fluctuations). Changes on inhomogeneities in the trap depths also alter the efficiency, as the optimal "probe" frequency depends on the tweezer-induced light-shift. Although careful re-optimization allows us to reach the best purity presented here, its value in daily experiments lies around 90%.

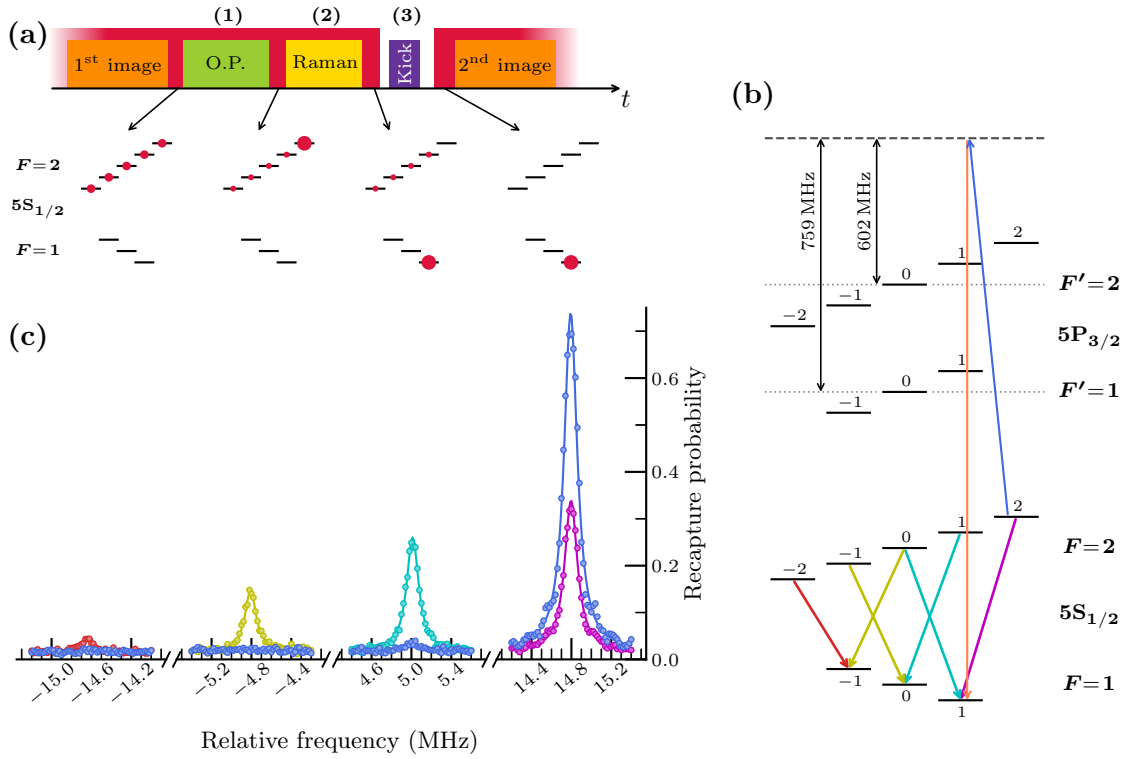

Figure E.1: Raman spectroscopy experiment. **(a)** Sequence of events for Raman spectroscopy. The evolution of the population within the Zeeman sub-levels of $5S_{1/2}$ is shown below when the Raman transition is resonant with $|F = 2, m_F = 2\rangle \rightarrow |F = 1, m_F = 1\rangle$. **(b)** Level structure and Raman transitions involved in the experiment. The six accessible Raman transitions are shown in various colors. **(c)** Raman spectra measured before (various colors) and after (blue) optimization of the optical pumping to $m_F = 2$. The origin of the frequency axis corresponds to the position where the four peaks merge when the magnetic field is zero.

Remerciements

Les résultats présentés dans ce texte constituent le dénouement de cinq laborieuses années de travail, que je n'aurais pu affronter sans la présence et le soutien de celles et ceux qui m'entourent. C'est avec émotion que je souhaite donc adresser ici à ces personnes mes plus sincères remerciements, pour leur sollicitude et leur amitié à travers ces années de thèse.

Je tiens en premier lieu à remercier Jean-Michel Raimond, mon directeur de thèse. Il y a six ans de cela, en tant que professeur, Jean-Michel a su me transmettre son engouement pour la physique atomique et les interactions lumière-matière. Ses cours passionants ont indéniablement contribué à mettre les atomes circulaires sur mon chemin. Son enthousiasme, ses encouragements, son pragmatisme et sa remarquable acuité physique ont ensuite été de vrais moteurs dans l'accomplissement de ce travail.

J'adresse également mes remerciements à Michel Brune et Clément Sayrin, respectivement directeur de laboratoire et chef de ce projet, pour leur accompagnement tout au long de cette thèse. L'association de leurs visions globales de cette expérience, de leur impressionnante technicité et de leur profonde connaissance de la physique moderne a permis d'aboutir aux données présentées ici et continuera, j'en suis sûr, à produire d'admirables résultats.

Une très grande part de ma gratitude va à mes collègues, aux côtés desquels j'ai eu le privilège d'œuvrer sur ce projet. Je tiens ainsi à remercier chaleureusement Rodrigo Cortiñas, qui m'a accueilli à mon arrivée dans l'équipe en 2018. Faisant preuve d'une grande pédagogie à mon égard, il m'a méticuleusement enseigné pendant près d'un an le contrôle complet de l'expérience. Je lui suis profondément reconnaissant pour la confiance qu'il a su rapidement m'accorder et pour son irréductible entrain dans la conduite des opérations. Merci également à Maxime Favier, qui a officié en tant que post-doctorant sur ce projet au moment de la refonte de l'expérience. Son expertise et sa bienveillance ont été fondamentaux dans le renouvellement de notre dispoditif expérimental. C'est en revanche avec Brice Ravon que j'ai passé le plus clair de mon temps au laboratoire. Je ne peux résumer ici en quelques mots ni le nombre gigantesque d'heures passées ensemble en salle d'expérience, aussi bien dans l'euphorie que dans le désespoir, ni l'admiration que j'ai pour Brice et sa minutie exceptionnelle, qui a été cruciale dans le déroulé de ce projet. Je tiens uniquement à souligner notre rare complémentarité dans le travail, qui a rapidement évolué en une véritable complicité amicale, ce qui nous a permis d'avancer dans ce projet, bon an mal an mais toujours

côte à côte. Je le remercie donc pour ces innombrables moments partagés, qui resteront vivement et éternellement gravés dans ma mémoire. Yohann Machu, arrivé un an après moi dans l'équipe, a été un autre élément clé dans la réussite de ce projet. Faisant preuve d'une immense résilience et d'un incroyable sens pratique, il a réussi à concevoir et mettre en œuvre, à lui seul, notre système de piégeage optique hors pair. Tout comme Brice, Yohann est devenu au fil du temps un ami précieux sur qui j'ai pu me reposer pendant ces années de thèse. Je mesure toute la chance que j'ai eu de travailler avec ces personnes brillantes, passionnées et passionnantes, et je doute de pouvoir retrouver un jour des collègues d'une si grande qualité. Je tiens également à remercier Andrés Durán-Hernández qui nous a rejoints, armé de son grand enthousiasme, alors que mon passage sur l'expérience touchait à sa fin, et avec qui nous avons œuvré à la mise en route du système de réarrangement des atomes. Une partie des résultats exposés ici ont par ailleurs étés acquis par Yohann et Andrés, tandis que j'entamais la rédaction de ce manuscrit, ce qui ajoute une dimension particulière à la reconnaissance que j'ai à leur égard.

Hors du temps de travail, ma vie au laboratoire a été façonnée par les moments passés avec de nombreuses autres personnes, au premier rang desquelles figure Léa Lachaud, de l'équipe strontium. Léa, je souhaite te témoigner l'immense joie et le profond réconfort que j'ai eus à te retrouver pour nos rituels quotidiens, au sein du Collège de France ou dans les rues avoisinantes. Merci de m'avoir faire rire, de m'avoir écouté, de m'avoir fait réfléchir ; merci pour les cigarettes et merci d'être devenue si essentielle à ces années des thèse. Je garderai également en mémoire les repas, cafés et bières partagés avec les autres doctorants et chercheurs de l'institut de physique: Arthur, Rémi, Haiteng, Andrea, Angelo, Sébastien, Igor, Brice B., et les plus jeunes, à qui je souhaite de grands succès dans leurs thèses respectives.

Ce travail n'aurait enfin pas vu le jour sans le soutien inconditionnel de mes proches. Je remercie ainsi tout particulièrement et du fond du coeur ma famille – mes parents, mon frère et ma soeur – pour leurs encouragements, leur patience et leur accueil indéfectible en Bretagne. Ce qu'il reste de mon infinie gratitude va à mes ami.e.s, rencontré.e.s à Vitré (Agathe, Emmanuelle, Marion), à New-York (Fanny, Fleur, Manon, Margaux), à Versailles (Anne-Claire, Armand, Côme, Clément, Hippolyte, Pierre H., Salomé, Victor), à Palaiseau (Alexandra, Émilie, Félix, Gustave, Marguerite, Mathieu, Pierre B., Sylvain, Vincent), ou à Paris (Élise, Romi et leurs normaliens). Je vous redis ici, à chacune et à chacun, la chance, le bonheur et la fierté que j'ai de cheminer à vos côtés !

Mezzanine du 5^{e} étage, Collège de France, 17 Octobre 2023

References

[1] Serge Haroche and Jean-Michel Raimond. *Exploring the Quantum: Atoms, Cavities, and Photons*. Oxford University Press, Aug. 2006. ISBN: 9780198509141. DOI: 10.1093/acprof:oso/9780198509141.001.0001.

[2] N. Bohr Dr. phil. "I. On the constitution of atoms and molecules". In: *The London, Edinburgh, and Dublin Philosophical Magazine and Journal of Science* 26.151 (1913), pp. 1–25. DOI: 10.1080/14786441308634955. eprint: https://doi.org/10.1080/14786441308634955.

[3] Randall G. Hulet and Daniel Kleppner. "Rydberg Atoms in "Circular" States". In: *Phys. Rev. Lett.* 51 (16 Oct. 1983), pp. 1430–1433. DOI: 10.1103/PhysRevLett.51.1430.

[4] J. Liang et al. "Circular Rydberg-state spectroscopy". In: *Phys. Rev. A* 33 (6 June 1986), pp. 4437–4439. DOI: 10.1103/PhysRevA.33.4437.

[5] M. Brune et al. "Quantum Rabi Oscillation: A Direct Test of Field Quantization in a Cavity". In: *Phys. Rev. Lett.* 76 (11 Mar. 1996), pp. 1800–1803. DOI: 10.1103/PhysRevLett.76.1800.

[6] M. Brune et al. "Observing the Progressive Decoherence of the "Meter" in a Quantum Measurement". In: *Phys. Rev. Lett.* 77 (24 Dec. 1996), pp. 4887–4890. DOI: 10.1103/PhysRevLett.77.4887.

[7] E. Hagley et al. "Generation of Einstein-Podolsky-Rosen Pairs of Atoms". In: *Phys. Rev. Lett.* 79 (1 July 1997), pp. 1–5. DOI: 10.1103/PhysRevLett.79.1.

[8] G. Nogues et al. "Seeing a single photon without destroying it". In: *Nature* 400.6741 (July 1, 1999), pp. 239–242. ISSN: 1476-4687. DOI: 10.1038/22275.

[9] Sébastien Gleyzes et al. "Quantum jumps of light recording the birth and death of a photon in a cavity". In: *Nature* 446.7133 (Mar. 2007), pp. 297–300. ISSN: 1476-4687. DOI: 10.1038/nature05589.

[10] Samuel Deléglise et al. "Reconstruction of non-classical cavity field states with snapshots of their decoherence". In: *Nature* 455.7212 (Sept. 1, 2008), pp. 510–514. ISSN: 1476-4687. DOI: 10.1038/nature07288.

[11] P. G. Merli, G. F. Missiroli, and G. Pozzi. "On the statistical aspect of electron interference phenomena". In: *American Journal of Physics* 44.3 (Mar. 1976). _eprint: https://pubs.aip.org/aapt/ajp/article-pdf/44/3/306/11843743/306_1_online.pdf, pp. 306–307. ISSN: 0002-9505. DOI: 10.1119/1.10184.

[12] Alain Aspect, Jean Dalibard, and Gérard Roger. "Experimental Test of Bell's Inequalities Using Time-Varying Analyzers". In: *Phys. Rev. Lett.* 49 (25 Dec. 1982), pp. 1804–1807. DOI: 10.1103/PhysRevLett.49.1804.

[13] W. Neuhauser et al. "Localized visible Ba^+ mono-ion oscillator". In: *Phys. Rev. A* 22 (3 Sept. 1980), pp. 1137–1140. DOI: 10.1103/PhysRevA.22.1137.

[14] Warren Nagourney, Jon Sandberg, and Hans Dehmelt. "Shelved optical electron amplifier: Observation of quantum jumps". In: *Phys. Rev. Lett.* 56 (26 June 1986), pp. 2797–2799. DOI: 10.1103/PhysRevLett.56.2797.

[15] C. Monroe et al. "Demonstration of a Fundamental Quantum Logic Gate". In: *Phys. Rev. Lett.* 75 (25 Dec. 1995), pp. 4714–4717. DOI: 10.1103/PhysRevLett.75.4714.

[16] D. M. Meekhof et al. "Generation of Nonclassical Motional States of a Trapped Atom". In: *Phys. Rev. Lett.* 76 (11 Mar. 1996), pp. 1796–1799. DOI: 10.1103/PhysRevLett.76.1796.

[17] John M. Martinis, Michel H. Devoret, and John Clarke. "Energy-Level Quantization in the Zero-Voltage State of a Current-Biased Josephson Junction". In: *Phys. Rev. Lett.* 55 (15 Oct. 1985), pp. 1543–1546. DOI: 10.1103/PhysRevLett.55.1543.

[18] John M. Martinis, Michel H. Devoret, and John Clarke. "Experimental tests for the quantum behavior of a macroscopic degree of freedom: The phase difference across a Josephson junction". In: *Phys. Rev. B* 35 (10 Apr. 1987), pp. 4682–4698. DOI: 10.1103/PhysRevB.35.4682.

[19] Nicolas Schlosser et al. "Sub-poissonian loading of single atoms in a microscopic dipole trap". In: *Nature* 411.6841 (June 1, 2001), pp. 1024–1027. ISSN: 1476-4687. DOI: 10.1038/35082512.

[20] P. Michler et al. "A Quantum Dot Single-Photon Turnstile Device". In: *Science* 290.5500 (2000), pp. 2282–2285. DOI: 10.1126/science.290.5500.2282. eprint: https://www.science.org/doi/pdf/10.1126/science.290.5500.2282.

[21] Charles Santori et al. "Triggered Single Photons from a Quantum Dot". In: *Phys. Rev. Lett.* 86 (8 Feb. 2001), pp. 1502–1505. DOI: 10.1103/PhysRevLett.86.1502.

[22] Christian Kurtsiefer et al. "Stable Solid-State Source of Single Photons". In: *Phys. Rev. Lett.* 85 (2 July 2000), pp. 290–293. DOI: 10.1103/PhysRevLett.85.290.

[23] Rosa Brouri et al. "Photon antibunching in the fluorescence of individual color centers in diamond". In: *Opt. Lett.* 25.17 (Sept. 2000), pp. 1294–1296. DOI: 10.1364/OL.25.001294.

[24] Frank Arute et al. "Quantum supremacy using a programmable superconducting processor". In: *Nature* 574.7779 (Oct. 2019), pp. 505–510. ISSN: 1476-4687. DOI: 10.1038/s41586-019-1666-5.

[25] Andrew D. Ludlow et al. "Optical atomic clocks". In: *Rev. Mod. Phys.* 87 (2 June 2015), pp. 637–701. DOI: 10.1103/RevModPhys.87.637.

[26] T. L. Nicholson et al. "Systematic evaluation of an atomic clock at 2×10^{-18} total uncertainty". In: *Nature Communications* 6.1 (Apr. 2015), p. 6896. ISSN: 2041-1723. DOI: 10.1038/ncomms7896.

[27] N. Huntemann et al. "Single-Ion Atomic Clock with 3×10^{-18} Systematic Uncertainty". In: *Phys. Rev. Lett.* 116 (6 Feb. 2016), p. 063001. DOI: 10.1103/PhysRevLett.116.063001.

[28] W. F. McGrew et al. "Atomic clock performance enabling geodesy below the centimetre level". In: *Nature* 564.7734 (Dec. 2018), pp. 87–90. ISSN: 1476-4687. DOI: 10.1038/s41586-018-0738-2.

[29] Juan Yin et al. "Satellite-based entanglement distribution over 1200 kilometers". In: *Science* 356.6343 (June 2017), pp. 1140–1144. DOI: 10.1126/science.aan3211.

[30] Ji-Gang Ren et al. "Ground-to-satellite quantum teleportation". In: *Nature* 549.7670 (Sept. 2017), pp. 70–73. ISSN: 1476-4687. DOI: 10.1038/nature23675.

[31] Oak Ridge National Laboratory. *Press release - Frontier supercomputer debuts as world's fastest, breaking exascale barrier*. May 2022. URL: https://www.ornl.gov/news/frontier-supercomputer-debuts-worlds-fastest-breaking-exascale-barrier.

[32] Richard P. Feynman. "Simulating physics with computers". In: *International Journal of Theoretical Physics* 21.6 (June 1982), pp. 467–488. ISSN: 1572-9575. DOI: 10.1007/BF02650179.

[33] I. M. Georgescu, S. Ashhab, and Franco Nori. "Quantum simulation". In: *Rev. Mod. Phys.* 86 (1 Mar. 2014), pp. 153–185. DOI: 10.1103/RevModPhys.86.153.

[34] Leticia Tarruell and Laurent Sanchez-Palencia. "Quantum simulation of the Hubbard model with ultracold fermions in optical lattices". In: *Comptes Rendus Physique* 19.6 (2018), pp. 365–393. ISSN: 1631-0705. DOI: https://doi.org/10.1016/j.crhy.2018.10.013.

[35] S. Blundell. *Magnetism in Condensed Matter*. Oxford Master Series in Condensed Matter Physics. OUP Oxford, 2001. ISBN: 978-0-19-850591-4.

[36] W. S. Bakr et al. "Probing the Superfluid–to–Mott Insulator Transition at the Single-Atom Level". In: *Science* 329.5991 (2010), pp. 547–550. DOI: 10.1126/science.1192368. eprint: https://www.science.org/doi/pdf/10.1126/science.1192368.

[37] T. Hensgens et al. "Quantum simulation of a Fermi–Hubbard model using a semiconductor quantum dot array". In: *Nature* 548.7665 (Aug. 2017), pp. 70–73. ISSN: 1476-4687. DOI: 10.1038/nature23022.

[38] Michael Schreiber et al. "Observation of many-body localization of interacting fermions in a quasirandom optical lattice". In: *Science* 349.6250 (Aug. 2015), pp. 842–845. DOI: 10.1126/science.aaa7432.

[39] R. Harris et al. "Phase transitions in a programmable quantum spin glass simulator". In: *Science* 361.6398 (2018), pp. 162–165. DOI: 10.1126/science.aat2025. eprint: https://www.science.org/doi/pdf/10.1126/science.aat2025.

[40] G. Semeghini et al. "Probing topological spin liquids on a programmable quantum simulator". In: *Science* 374.6572 (Dec. 2021), pp. 1242–1247. DOI: 10.1126/science.abi8794.

[41] Xi-Wang Luo et al. "Quantum simulation of 2D topological physics in a 1D array of optical cavities". In: *Nature Communications* 6.1 (July 2015), p. 7704. ISSN: 2041-1723. DOI: 10.1038/ncomms8704.

[42] Luca D'Alessio et al. "From quantum chaos and eigenstate thermalization to statistical mechanics and thermodynamics". In: *Advances in Physics* 65.3 (2016), pp. 239–362. DOI: 10.1080/00018732.2016.1198134. eprint: https://doi.org/10.1080/00018732.2016.1198134.

[43] C. J. Turner et al. "Weak ergodicity breaking from quantum many-body scars". In: *Nature Physics* 14.7 (July 2018), pp. 745–749. ISSN: 1745-2481. DOI: 10.1038/s41567-018-0137-5.

[44] J. Smith et al. "Many-body localization in a quantum simulator with programmable random disorder". In: *Nature Physics* 12.10 (Oct. 2016), pp. 907–911. ISSN: 1745-2481. DOI: 10.1038/nphys3783.

[45] C. Monroe et al. "Programmable quantum simulations of spin systems with trapped ions". In: *Rev. Mod. Phys.* 93 (2 Apr. 2021), p. 025001. DOI: 10.1103/RevModPhys.93.025001.

[46] M. G. Raizen et al. "Ionic crystals in a linear Paul trap". In: *Phys. Rev. A* 45 (9 May 1992), pp. 6493–6501. DOI: 10.1103/PhysRevA.45.6493.

[47] Lowell S. Brown and Gerald Gabrielse. "Geonium theory: Physics of a single electron or ion in a Penning trap". In: *Rev. Mod. Phys.* 58 (1 Jan. 1986), pp. 233–311. DOI: 10.1103/RevModPhys.58.233.

[48] D. Porras and J. I. Cirac. "Effective Quantum Spin Systems with Trapped Ions". In: *Phys. Rev. Lett.* 92 (20 May 2004), p. 207901. DOI: 10.1103/PhysRevLett.92.207901.

[49] Pengfei Wang et al. "Single ion qubit with estimated coherence time exceeding one hour". In: *Nature Communications* 12.1 (Jan. 2021), p. 233. ISSN: 2041-1723. DOI: 10.1038/s41467-020-20330-w.

[50] T. P. Harty. "High-Fidelity Preparation, Gates, Memory, and Readout of a Trapped-Ion Quantum Bit". In: *Physical Review Letters* 113.22 (2014). DOI: 10.1103/PhysRevLett.113.220501.

[51] P. Jurcevic et al. "Quasiparticle engineering and entanglement propagation in a quantum many-body system". In: *Nature* 511.7508 (July 2014), pp. 202–205. ISSN: 1476-4687. DOI: 10.1038/nature13461.

[52] J. Smith et al. "Many-body localization in a quantum simulator with programmable random disorder". In: *Nature Physics* 12.10 (Oct. 2016), pp. 907–911. ISSN: 1745-2481. DOI: 10.1038/nphys3783.

[53] C. Kokail et al. "Self-verifying variational quantum simulation of lattice models". In: *Nature* 569.7756 (May 2019), pp. 355–360. ISSN: 1476-4687. DOI: 10.1038/s41586-019-1177-4.

[54] Thomas Monz et al. "Realization of a scalable Shor algorithm". In: *Science* 351.6277 (2016), pp. 1068–1070. DOI: 10.1126/science.aad9480. eprint: https://www.science.org/doi/pdf/10.1126/science.aad9480.

[55] Cornelius Hempel et al. "Quantum Chemistry Calculations on a Trapped-Ion Quantum Simulator". In: *Phys. Rev. X* 8 (3 July 2018), p. 031022. DOI: 10.1103/PhysRevX.8.031022.

[56] B.D. Josephson. "Possible new effects in superconductive tunnelling". In: *Physics Letters* 1.7 (1962), pp. 251–253. ISSN: 0031-9163. DOI: https://doi.org/10.1016/0031-9163(62)91369-0.

[57] B. D. Josephson. "The discovery of tunnelling supercurrents". In: *Rev. Mod. Phys.* 46 (2 Apr. 1974), pp. 251–254. DOI: 10.1103/RevModPhys.46.251.

[58] Morten Kjaergaard et al. "Superconducting Qubits: Current State of Play". In: *Annual Review of Condensed Matter Physics* 11.1 (Mar. 2020), pp. 369–395. ISSN: 1947-5454. DOI: 10.1146/annurev-conmatphys-031119-050605.

[59] Frank Arute et al. "Quantum supremacy using a programmable superconducting processor". In: *Nature* 574.7779 (Oct. 2019), pp. 505–510. ISSN: 1476-4687. DOI: 10.1038/s41586-019-1666-5.

[60] L. Tian. "Circuit QED and Sudden Phase Switching in a Superconducting Qubit Array". In: *Phys. Rev. Lett.* 105 (16 Oct. 2010), p. 167001. DOI: 10.1103/PhysRevLett.105.167001.

[61] Oliver Viehmann, Jan von Delft, and Florian Marquardt. "Observing the Nonequilibrium Dynamics of the Quantum Transverse-Field Ising Chain in Circuit QED". In: *Phys. Rev. Lett.* 110 (3 Jan. 2013), p. 030601. DOI: 10.1103/PhysRevLett.110.030601.

[62] Yuanwei Zhang et al. "Quantum phases in circuit QED with a superconducting qubit array". In: *Scientific Reports* 4.1 (Feb. 2014), p. 4083. ISSN: 2045-2322. DOI: 10.1038/srep04083.

[63] A. Morvan et al. "Formation of robust bound states of interacting microwave photons". In: *Nature* 612.7939 (Dec. 2022), pp. 240–245. ISSN: 1476-4687. DOI: 10.1038/s41586-022-05348-y.

[64] Jan-Michael Reiner et al. "Emulating the one-dimensional Fermi-Hubbard model by a double chain of qubits". In: *Phys. Rev. A* 94 (3 Sept. 2016), p. 032338. DOI: 10.1103/PhysRevA.94.032338.

[65] P. Roushan et al. "Chiral ground-state currents of interacting photons in a synthetic magnetic field". In: *Nature Physics* 13.2 (Feb. 2017), pp. 146–151. ISSN: 1745-2481. DOI: 10.1038/nphys3930.

[66] Ruichao Ma et al. "A dissipatively stabilized Mott insulator of photons". In: *Nature* 566.7742 (Feb. 2019), pp. 51–57. ISSN: 1476-4687. DOI: 10.1038/s41586-019-0897-9.

[67] P. Roushan et al. "Spectroscopic signatures of localization with interacting photons in superconducting qubits". In: *Science* 358.6367 (Dec. 2017), pp. 1175–1179. DOI: 10.1126/science.aao1401.

[68] Immanuel Bloch, Jean Dalibard, and Sylvain Nascimbène. "Quantum simulations with ultracold quantum gases". In: *Nature Physics* 8.4 (Apr. 2012), pp. 267–276. ISSN: 1745-2481. DOI: 10.1038/nphys2259.

[69] Christian Gross and Immanuel Bloch. "Quantum simulations with ultracold atoms in optical lattices". In: *Science* 357.6355 (Sept. 2017), pp. 995–1001. DOI: 10.1126/science.aal3837.

[70] Florian Schäfer et al. "Tools for quantum simulation with ultracold atoms in optical lattices". In: *Nature Reviews Physics* 2.8 (Aug. 2020), pp. 411–425. ISSN: 2522-5820. DOI: 10.1038/s42254-020-0195-3.

[71] Waseem S. Bakr et al. "A quantum gas microscope for detecting single atoms in a Hubbard-regime optical lattice". In: *Nature* 462.7269 (Nov. 2009), pp. 74–77. ISSN: 1476-4687. DOI: 10.1038/nature08482.

[72] Markus Greiner et al. "Quantum phase transition from a superfluid to a Mott insulator in a gas of ultracold atoms". In: *Nature* 415.6867 (Jan. 2002), pp. 39–44. ISSN: 1476-4687. DOI: 10.1038/415039a.

[73] Jonathan Simon et al. "Quantum simulation of antiferromagnetic spin chains in an optical lattice". In: *Nature* 472.7343 (Apr. 2011), pp. 307–312. ISSN: 1476-4687. DOI: 10.1038/nature09994.

[74] Maxwell F. Parsons et al. "Site-resolved measurement of the spin-correlation function in the Fermi-Hubbard model". In: *Science* 353.6305 (Sept. 2016), pp. 1253–1256. DOI: 10.1126/science.aag1430.

[75] B. K. Stuhl et al. "Visualizing edge states with an atomic Bose gas in the quantum Hall regime". In: *Science* 349.6255 (Sept. 2015), pp. 1514–1518. DOI: 10.1126/science.aaa8515.

[76] M. Mancini et al. "Observation of chiral edge states with neutral fermions in synthetic Hall ribbons". In: *Science* 349.6255 (Sept. 2015), pp. 1510–1513. DOI: 10.1126/science.aaa8736.

[77] J. Struck et al. "Tunable Gauge Potential for Neutral and Spinless Particles in Driven Optical Lattices". In: *Phys. Rev. Lett.* 108 (22 May 2012), p. 225304. DOI: 10.1103/PhysRevLett.108.225304.

[78] J. Struck et al. "Engineering Ising-XY spin-models in a triangular lattice using tunable artificial gauge fields". In: *Nature Physics* 9.11 (Nov. 2013), pp. 738–743. ISSN: 1745-2481. DOI: 10.1038/nphys2750.

[79] Jae-yoon Choi et al. "Exploring the many-body localization transition in two dimensions". In: *Science* 352.6293 (June 2016), pp. 1547–1552. DOI: 10.1126/science.aaf8834.

[80] Antoine Browaeys and Thierry Lahaye. "Many-body physics with individually controlled Rydberg atoms". In: *Nature Physics* 16.2 (Feb. 2020), pp. 132–142. ISSN: 1745-2481. DOI: 10.1038/s41567-019-0733-z.

[81] M. Morgado and S. Whitlock. "Quantum simulation and computing with Rydberg-interacting qubits". In: *AVS Quantum Science* 3.2 (May 2021). 023501. ISSN: 2639-0213. DOI: 10.1116/5.0036562. eprint: https://pubs.aip.org/avs/aqs/article-pdf/doi/10.1116/5.0036562/14572456/023501_1_online.pdf.

[82] Thomas F. Gallagher. *Rydberg Atoms*. Cambridge Monographs on Atomic, Molecular and Chemical Physics. Cambridge: Cambridge University Press, 1994. ISBN: 978-0-521-02166-1.

[83] Silvia Bergamini et al. "Holographic generation of microtrap arrays for single atoms by use of a programmable phase modulator". In: *J. Opt. Soc. Am. B* 21.11 (Nov. 2004), pp. 1889–1894. DOI: 10.1364/JOSAB.21.001889.

[84] F. Nogrette et al. "Single-Atom Trapping in Holographic 2D Arrays of Microtraps with Arbitrary Geometries". In: *Phys. Rev. X* 4 (2 May 2014), p. 021034. DOI: 10.1103/PhysRevX.4.021034.

[85] R. Dumke et al. "Micro-optical Realization of Arrays of Selectively Addressable Dipole Traps: A Scalable Configuration for Quantum Computation with Atomic Qubits". In: *Phys. Rev. Lett.* 89 (9 Aug. 2002), p. 097903. DOI: 10.1103/PhysRevLett.89.097903.

[86] M Schlosser et al. "Fast transport, atom sample splitting and single-atom qubit supply in two-dimensional arrays of optical microtraps". In: *New Journal of Physics* 14.12 (Dec. 2012), p. 123034. DOI: 10.1088/1367-2630/14/12/123034.

[87] P. Huft et al. "Simple, passive design for large optical trap arrays for single atoms". In: *Phys. Rev. A* 105 (6 June 2022), p. 063111. DOI: 10.1103/PhysRevA.105.063111.

[88] Manuel Endres et al. "Atom-by-atom assembly of defect-free one-dimensional cold atom arrays". In: *Science* 354.6315 (2016), pp. 1024–1027. DOI: 10.1126/science.aah3752. eprint: https://www.science.org/doi/pdf/10.1126/science.aah3752.

[89] Hyosub Kim et al. "In situ single-atom array synthesis using dynamic holographic optical tweezers". In: *Nature Communications* 7.1 (Oct. 2016), p. 13317. ISSN: 2041-1723. DOI: 10.1038/ncomms13317.

[90] Woojun Lee, Hyosub Kim, and Jaewook Ahn. "Three-dimensional rearrangement of single atoms using actively controlled optical microtraps". In: *Opt. Express* 24.9 (May 2016), pp. 9816–9825. DOI: 10.1364/OE.24.009816.

[91] Daniel Barredo et al. "An atom-by-atom assembler of defect-free arbitrary two-dimensional atomic arrays". In: *Science* 354.6315 (2016), pp. 1021–1023. DOI: 10.1126/science.aah3778. eprint: https://www.science.org/doi/pdf/10.1126/science.aah3778.

[92] C. S. E. van Ditzhuijzen et al. "Spatially Resolved Observation of Dipole-Dipole Interaction between Rydberg Atoms". In: *Phys. Rev. Lett.* 100 (24 June 2008), p. 243201. DOI: 10.1103/PhysRevLett.100.243201.

[93] L. Béguin et al. "Direct Measurement of the van der Waals Interaction between Two Rydberg Atoms". In: *Phys. Rev. Lett.* 110 (26 June 2013), p. 263201. DOI: 10.1103/PhysRevLett.110.263201.

[94] R. Celistrino Teixeira et al. "Microwaves Probe Dipole Blockade and van der Waals Forces in a Cold Rydberg Gas". In: *Phys. Rev. Lett.* 115 (1 June 2015), p. 013001. DOI: 10.1103/PhysRevLett.115.013001.

[95] N. Šibalić et al. "ARC: An open-source library for calculating properties of alkali Rydberg atoms". In: *Computer Physics Communications* 220 (2017), pp. 319–331. ISSN: 0010-4655. DOI: https://doi.org/10.1016/j.cpc.2017.06.015.

[96] J M Kosterlitz. "The critical properties of the two-dimensional xy model". In: *Journal of Physics C: Solid State Physics* 7.6 (Mar. 1974), p. 1046. DOI: 10.1088/0022-3719/7/6/005.

[97] H. Schempp et al. "Correlated Exciton Transport in Rydberg-Dressed-Atom Spin Chains". In: *Phys. Rev. Lett.* 115 (9 Aug. 2015), p. 093002. DOI: 10.1103/PhysRevLett.115.093002.

[98] Sylvain de Léséleuc et al. "Observation of a symmetry-protected topological phase of interacting bosons with Rydberg atoms". In: *Science* 365.6455 (2019), pp. 775–780. DOI: 10.1126/science.aav9105. eprint: https://www.science.org/doi/pdf/10.1126/science.aav9105.

[99] Xie Chen et al. "Symmetry-Protected Topological Orders in Interacting Bosonic Systems". In: *Science* 338.6114 (2012), pp. 1604–1606. DOI: 10.1126/science.1227224. eprint: https://www.science.org/doi/pdf/10.1126/science.1227224.

[100] P. Scholl et al. "Microwave Engineering of Programmable XXZ Hamiltonians in Arrays of Rydberg Atoms". In: *PRX Quantum* 3 (2 Apr. 2022), p. 020303. DOI: 10.1103/PRXQuantum.3.020303.

[101] F. Robicheaux and J. V. Hernández. "Many-body wave function in a dipole blockade configuration". In: *Phys. Rev. A* 72 (6 Dec. 2005), p. 063403. DOI: 10.1103/PhysRevA.72.063403.

[102] M. D. Lukin et al. "Dipole Blockade and Quantum Information Processing in Mesoscopic Atomic Ensembles". In: *Phys. Rev. Lett.* 87 (3 June 2001), p. 037901. DOI: 10.1103/PhysRevLett.87.037901.

[103] E. Urban et al. "Observation of Rydberg blockade between two atoms". In: *Nature Physics* 5.2 (Feb. 2009), pp. 110–114. ISSN: 1745-2481. DOI: 10.1038/nphys1178.

[104] Henning Labuhn et al. "Tunable two-dimensional arrays of single Rydberg atoms for realizing quantum Ising models". In: *Nature* 534.7609 (June 2016), pp. 667–670. ISSN: 1476-4687. DOI: 10.1038/nature18274.

[105] Sylvain de Léséleuc et al. "Accurate Mapping of Multilevel Rydberg Atoms on Interacting Spin-1/2 Particles for the Quantum Simulation of Ising Models". In: *Phys. Rev. Lett.* 120 (11 Mar. 2018), p. 113602. DOI: 10.1103/PhysRevLett.120.113602.

[106] Vincent Lienhard et al. "Observing the Space- and Time-Dependent Growth of Correlations in Dynamically Tuned Synthetic Ising Models with Antiferromagnetic Interactions". In: *Phys. Rev. X* 8 (2 June 2018), p. 021070. DOI: 10.1103/PhysRevX.8.021070.

[107] Hyosub Kim et al. "Detailed Balance of Thermalization Dynamics in Rydberg-Atom Quantum Simulators". In: *Phys. Rev. Lett.* 120 (18 May 2018), p. 180502. DOI: 10.1103/PhysRevLett.120.180502.

[108] Woojun Lee et al. "Coherent and dissipative dynamics of entangled few-body systems of Rydberg atoms". In: *Phys. Rev. A* 99 (4 Apr. 2019), p. 043404. DOI: 10.1103/PhysRevA.99.043404.

[109] Hannes Bernien et al. "Probing many-body dynamics on a 51-atom quantum simulator". In: *Nature* 551.7682 (Nov. 2017), pp. 579–584. ISSN: 1476-4687. DOI: 10.1038/nature24622.

[110] Yunheung Song et al. "Quantum simulation of Cayley-tree Ising Hamiltonians with three-dimensional Rydberg atoms". In: *Phys. Rev. Res.* 3 (1 Mar. 2021), p. 013286. DOI: 10.1103/PhysRevResearch.3.013286.

[111] Sepehr Ebadi et al. "Quantum phases of matter on a 256-atom programmable quantum simulator". In: *Nature* 595.7866 (July 2021), pp. 227–232. ISSN: 1476-4687. DOI: 10.1038/s41586-021-03582-4.

[112] Pascal Scholl et al. "Quantum simulation of 2D antiferromagnets with hundreds of Rydberg atoms". In: *Nature* 595.7866 (July 2021), pp. 233–238. ISSN: 1476-4687. DOI: 10.1038/s41586-021-03585-1.

[113] Ivaylo S. Madjarov et al. "High-fidelity entanglement and detection of alkaline-earth Rydberg atoms". In: *Nature Physics* 16.8 (Aug. 2020), pp. 857–861. ISSN: 1745-2481. DOI: 10.1038/s41567-020-0903-z.

[114] J. T. Wilson et al. "Trapping Alkaline Earth Rydberg Atoms Optical Tweezer Arrays". In: *Phys. Rev. Lett.* 128 (3 Jan. 2022), p. 033201. DOI: 10.1103/PhysRevLett.128.033201.

[115] R Cardman et al. "Photoionization of Rydberg atoms in optical lattices". In: *New Journal of Physics* 23.6 (June 2021), p. 063074. DOI: 10.1088/1367-2630/ac07ca.

[116] Sam R. Cohen and Jeff D. Thompson. "Quantum Computing with Circular Rydberg Atoms". In: *PRX Quantum* 2 (3 Aug. 2021), p. 030322. DOI: 10.1103/PRXQuantum.2.030322.

[117] T. L. Nguyen et al. "Towards Quantum Simulation with Circular Rydberg Atoms". In: *Phys. Rev. X* 8 (1 Feb. 2018), p. 011032. DOI: 10.1103/PhysRevX.8.011032.

[118] Daniel Kleppner. "Inhibited Spontaneous Emission". In: *Phys. Rev. Lett.* 47 (4 July 1981), pp. 233–236. DOI: 10.1103/PhysRevLett.47.233.

[119] H. Wu et al. "Millisecond-Lived Circular Rydberg Atoms in a Room-Temperature Experiment". In: *Phys. Rev. Lett.* 130 (2 Jan. 2023), p. 023202. DOI: 10.1103/PhysRevLett.130.023202.

[120] T. Cantat-Moltrecht et al. "Long-lived circular Rydberg states of laser-cooled rubidium atoms in a cryostat". In: *Phys. Rev. Res.* 2 (2 May 2020), p. 022032. DOI: 10.1103/PhysRevResearch.2.022032.

[121] R. G. Cortiñas et al. "Laser Trapping of Circular Rydberg Atoms". In: *Phys. Rev. Lett.* 124 (12 Mar. 2020), p. 123201. DOI: 10.1103/PhysRevLett.124.123201.

[122] Brice Ravon et al. *Array of Individual Circular Rydberg Atoms Trapped in Optical Tweezers*. 2023. arXiv: 2304.04831 [quant-ph].

[123] Brice Ravon. "Preparation and trapping of individual circular Rydberg atoms for quantum simulation". PhD thesis. Université Paris Sciences et Lettres, Dec. 2022.

[124] Paul Méhaignerie et al. "Spin-motion coupling in a circular-Rydberg-state quantum simulator: Case of two atoms". In: *Phys. Rev. A* 107 (6 June 2023), p. 063106. DOI: 10.1103/PhysRevA.107.063106.

[125] E. Schrödinger. "An Undulatory Theory of the Mechanics of Atoms and Molecules". In: *Phys. Rev.* 28.6 (Dec. 1, 1926), pp. 1049–1070. ISSN: 0031-899X. DOI: 10.1103/PhysRev.28.1049.

[126] Albert Messiah. *Quantum Mechanics*. OCLC: 874097814. Dover Publications, 2014. ISBN: 978-0-486-78455-7.

[127] G. E. Uhlenbeck and S. Goudsmit. "Spinning Electrons and the Structure of Spectra". In: *Nature* 117.2938 (Feb. 1926), pp. 264–265. ISSN: 0028-0836, 1476-4687. DOI: 10.1038/117264a0.

[128] Jean Hare. "Etude théorique et expérimentale des atomes de Rydberg circulaires: vers une mesure directe de la constante de Rydberg en unités de fréquence". PhD thesis. Université Pierre et Marie Curie - Paris VI, Dec. 1991.

[129] M. J. Seaton. "Quantum defect theory I. General formulation". In: *Proc. Phys. Soc.* 88.4 (Aug. 1966). Publisher: IOP Publishing, pp. 801–814. ISSN: 0370-1328. DOI: 10.1088/0370-1328/88/4/302.

[130] K. Afrousheh et al. "Determination of the ^{85}Rb ng-series quantum defect by electric-field-induced resonant energy transfer between cold Rydberg atoms". In: *Phys. Rev. A* 74 (6 Dec. 2006), p. 062712. DOI: 10.1103/PhysRevA.74.062712.

[131] Wenhui Li et al. "Millimeter-wave spectroscopy of cold Rb Rydberg atoms in a magneto-optical trap: Quantum defects of the ns, np, and nd series". In: *Phys. Rev. A* 67 (5 May 2003), p. 052502. DOI: 10.1103/PhysRevA.67.052502.

[132] Jianing Han et al. "Rb nf quantum defects from millimeter-wave spectroscopy of cold ^{85}Rb Rydberg atoms". In: *Phys. Rev. A* 74 (5 Nov. 2006), p. 054502. DOI: 10.1103/PhysRevA.74.054502.

[133] Hans A. Bethe and Edwin E. Salpeter. *Quantum Mechanics of One-And Two-Electron Atoms*. Softcover reprint of the original 1st ed. 1977 édition. New York: Kluwer Academic/Plenum Publishers, Apr. 30, 1977. 370 pp. ISBN: 978-0-306-20022-9.

[134] Arno Bohm. *Quantum Mechanics: Foundations and Applications*. Softcover reprint of the original 3rd ed. 1993 edition. New York: Springer, July 27, 2001. 707 pp. ISBN: 978-0-387-95330-4.

[135] Adrien Facon. "Chats de Schrödinger d'un atome de Rydberg pour la métrologie quantique". Theses. Université Pierre et Marie Curie - Paris VI, Dec. 2015.

[136] Andreas Kruckenhauser et al. "High-dimensional SO(4)-symmetric Rydberg manifolds for quantum simulation". In: *Quantum Science and Technology* 8.1 (Dec. 2022), p. 015020. DOI: 10.1088/2058-9565/aca996.

[137] M. J. Englefield and L. C. Biedenharn. "Group Theory and the Coulomb Problem". In: *American Journal of Physics* 42.3 (Mar. 1974), pp. 263–264. ISSN: 0002-9505. DOI: 10.1119/1.1987669. eprint: https://pubs.aip.org/aapt/ajp/article-pdf/42/3/263/11911095/263_1_online.pdf.

[138] Daniel A. Steck. "Rubidium 87 D Line Data". In: (Jan. 1, 2003).

[139] T. F. Gallagher and W. E. Cooke. "Interactions of Blackbody Radiation with Atoms". In: *Phys. Rev. Lett.* 42 (13 Mar. 1979), pp. 835–839. DOI: 10.1103/PhysRevLett.42.835.

[140] H. Friedrich. *Theoretical Atomic Physics*. Graduate Texts in Physics. Springer International Publishing, 2017. ISBN: 9783319477671.

[141] Kelly Cooper Younge, Sarah Elizabeth Anderson, and Georg Raithel. "Adiabatic potentials for Rydberg atoms in a ponderomotive optical lattice". In: *New Journal of Physics* 12.2 (Feb. 2010), p. 023031. DOI: 10.1088/1367-2630/12/2/023031.

[142] P. Avan et al. "Effect of high frequency irradiation on the dynamical properties of weakly bound electrons". In: *J. Phys. France* 37.9 (Sept. 1, 1976). Publisher: Société Française de Physique, pp. 993–1009. ISSN: 0302-0738, 2777-3396. DOI: 10.1051/jphys:01976003709099300.

[143] Claude Cohen-Tannoudji, Bernard Diu, and Franck Laloë. *Quantum Mechanics*. Wiley, 1977, p. 1524.

[144] Rodrigo Gastón Cortiñas. "Laser trapped Circular Rydberg atoms for quantum simulation". PhD thesis. Université Paris sciences et lettres, May 5, 2020.

[145] Tigrane Cantat-Moltrecht. "Atomes de Rydberg en interaction : des nuages denses d'atomes de Rydberg à la simulation quantique avec des atomes circulaires". PhD thesis. Ecole Normale Supérieure, Paris ; PSL Research University, Jan. 11, 2018.

[146] R. J. Baxter. "Exactly Solved Models in Statistical Mechanics". In: *Integrable Systems in Statistical Mechanics*, pp. 5–63. DOI: 10.1142/9789814415255_0002. eprint: https://www.worldscientific.com/doi/pdf/10.1142/9789814415255_0002.

[147] Jacques Des Cloizeaux and Michel Gaudin. "Anisotropic Linear Magnetic Chain". In: *Journal of Mathematical Physics* 7.8 (Dec. 2004), pp. 1384–1400. ISSN: 0022-2488. DOI: 10.1063/1.1705048. eprint: https://pubs.aip.org/aip/jmp/article-pdf/7/8/1384/11001022/1384_1_online.pdf.

[148] C. N. Yang and C. P. Yang. "One-Dimensional Chain of Anisotropic Spin-Spin Interactions. I. Proof of Bethe's Hypothesis for Ground State in a Finite System". In: *Phys. Rev.* 150 (1 Oct. 1966), pp. 321–327. DOI: 10.1103/PhysRev.150.321.

[149] C. N. Yang and C. P. Yang. "One-Dimensional Chain of Anisotropic Spin-Spin Interactions. II. Properties of the Ground-State Energy Per Lattice Site for an Infinite System". In: *Phys. Rev.* 150 (1 Oct. 1966), pp. 327–339. DOI: 10.1103/PhysRev.150.327.

[150] C. N. Yang and C. P. Yang. "One-Dimensional Chain of Anisotropic Spin-Spin Interactions. III. Applications". In: *Phys. Rev.* 151 (1 Nov. 1966), pp. 258–264. DOI: 10.1103/PhysRev.151.258.

[151] Josef Kurmann, Harry Thomas, and Gerhard Müller. "Antiferromagnetic long-range order in the anisotropic quantum spin chain". In: *Physica A: Statistical Mechanics and its Applications* 112.1 (1982), pp. 235–255. ISSN: 0378-4371. DOI: https://doi.org/10.1016/0378-4371(82)90217-5.

[152] Yasuhiro Hieida, Kouichi Okunishi, and Yasuhiro Akutsu. "Anisotropic antiferromagnetic spin chains in a transverse field: Reentrant behavior of the staggered magnetization". In: *Phys. Rev. B* 64 (22 Nov. 2001), p. 224422. DOI: 10.1103/PhysRevB.64.224422.

[153] O. Breunig et al. "Spin-$\frac{1}{2}$ XXZ Chain System Cs_2CoCl_4 in a Transverse Magnetic Field". In: *Phys. Rev. Lett.* 111 (18 Oct. 2013), p. 187202. DOI: 10.1103/PhysRevLett.111.187202.

[154] B. Grenier et al. "Longitudinal and Transverse Zeeman Ladders in the Ising-Like Chain Antiferromagnet $BaCo_2V_2O_8$". In: *Phys. Rev. Lett.* 114 (1 Jan. 2015), p. 017201. DOI: 10.1103/PhysRevLett.114.017201.

[155] Amit Dutta et al. "Quantum phase transitions in transverse field spin models: from statistical physics to quantum information". In: (2015). arXiv: 1012.0653 [cond-mat.stat-mech].

[156] F D M Haldane. "'Luttinger liquid theory' of one-dimensional quantum fluids. I. Properties of the Luttinger model and their extension to the general 1D interacting spinless Fermi gas". In: *Journal of Physics C: Solid State Physics* 14.19 (July 1981), p. 2585. DOI: 10.1088/0022-3719/14/19/010.

[157] Thierry Giamarchi. *Quantum Physics in One Dimension*. Oxford University Press, Dec. 2003. ISBN: 9780198525004. DOI: 10.1093/acprof:oso/9780198525004.001.0001.

[158] F C Alcaraz and A L Malvezzi. "Critical and off-critical properties of the XXZ chain in external homogeneous and staggered magnetic fields". In: *Journal of Physics A: Mathematical and General* 28.6 (Mar. 1995), p. 1521. DOI: 10.1088/0305-4470/28/6/009.

[159] Eytan Barouch and Barry M. McCoy. "Statistical Mechanics of the XY Model. II. Spin-Correlation Functions". In: *Phys. Rev. A* 3 (2 Feb. 1971), pp. 786–804. DOI: 10.1103/PhysRevA.3.786.

[160] Pierre Pfeuty. "The one-dimensional Ising model with a transverse field". In: *Annals of Physics* 57 (1970), pp. 79–90.

[161] C. J. Turner et al. "Weak ergodicity breaking from quantum many-body scars". In: *Nature Physics* 14.7 (May 2018), pp. 745–749. DOI: 10.1038/s41567-018-0137-5.

[162] D. Bluvstein et al. "Controlling quantum many-body dynamics in driven Rydberg atom arrays". In: *Science* 371.6536 (Mar. 2021), pp. 1355–1359. DOI: 10.1126/science.abg2530.

[163] Joonhee Choi et al. "Probing Quantum Thermalization of a Disordered Dipolar Spin Ensemble with Discrete Time-Crystalline Order". In: *Phys. Rev. Lett.* 122 (4 Feb. 2019), p. 043603. DOI: 10.1103/PhysRevLett.122.043603.

[164] Rahul Nandkishore and David A. Huse. "Many-Body Localization and Thermalization in Quantum Statistical Mechanics". In: *Annual Review of Condensed Matter Physics* 6.1 (2015), pp. 15–38. DOI: 10.1146/annurev-conmatphys-031214-014726. eprint: https://doi.org/10.1146/annurev-conmatphys-031214-014726.

[165] G. Semeghini et al. "Probing topological spin liquids on a programmable quantum simulator". In: *Science* 374.6572 (2021), pp. 1242–1247. DOI: 10.1126/science.abi8794. eprint: https://www.science.org/doi/pdf/10.1126/science.abi8794.

[166] S. Weber et al. "Experimentally Accessible Scheme for a Fractional Chern Insulator in Rydberg Atoms". In: *PRX Quantum* 3 (3 July 2022), p. 030302. DOI: 10.1103/PRXQuantum.3.030302.

[167] Serge Haroche and Jean-Michel Raimond. *Exploring the Quantum: Atoms, Cavities, and Photons*. Oxford University Press, Aug. 2006. ISBN: 9780198509141. DOI: 10.1093/acprof:oso/9780198509141.001.0001.

[168] Andrew J. Kerman et al. "Beyond Optical Molasses: 3D Raman Sideband Cooling of Atomic Cesium to High Phase-Space Density". In: *Phys. Rev. Lett.* 84 (3 Jan. 2000), pp. 439–442. DOI: 10.1103/PhysRevLett.84.439.

[169] Ingemar Bengtsson and Karol Zyczkowski. *Geometry of Quantum States: An Introduction to Quantum Entanglement*. Cambridge University Press, 2006. DOI: 10.1017/CBO9780511535048.

[170] R. G. Cortiñas et al. "Laser Trapping of Circular Rydberg Atoms". In: *Phys. Rev. Lett.* 124 (12 Mar. 2020), p. 123201. DOI: 10.1103/PhysRevLett.124.123201.

[171] T. Cantat-Moltrecht et al. "Long-lived circular Rydberg states of laser-cooled rubidium atoms in a cryostat". In: *Phys. Rev. Res.* 2 (2 May 2020), p. 022032. DOI: 10.1103/PhysRevResearch.2.022032.

[172] Dorian Grosso. "Des atomes froids pour sonder et manipuler des photons piégés". These de doctorat. Paris 6, Dec. 1, 2017.

[173] J.W. Goodman. *Introduction to Fourier Optics*. McGraw-Hill physical and quantum electronics series. W. H. Freeman, 2005. ISBN: 9780974707723.

[174] R. W. Gerchberg and W. O. Saxton. "A Practical Algorithm for the Determination of Phase from Image and Diffraction Plane Pictures". In: *Optik* 35.2 (1971), pp. 237–246.

[175] Peng Xu et al. "Trapping a single atom in a blue detuned optical bottle beam trap". In: *Opt. Lett.* 35.13 (July 2010), pp. 2164–2166. DOI: 10.1364/OL.35.002164.

[176] Harold J. Metcalf and Peter Van Der Straten. *Laser Cooling and Trapping*. New York: Springer-Verlag New York Inc., Nov. 1, 1999. 339 pp. ISBN: 978-0-387-98747-7.

[177] Rudolf Grimm, Matthias Weidemüller, and Yurii B. Ovchinnikov. "Optical Dipole Traps for Neutral Atoms". In: *Advances In Atomic, Molecular, and Optical Physics*. Ed. by Benjamin Bederson and Herbert Walther. Vol. 42. Academic Press, Jan. 1, 2000, pp. 95–170. DOI: 10.1016/S1049-250X(08)60186-X.

[178] N. Schlosser, G. Reymond, and P. Grangier. "Collisional Blockade in Microscopic Optical Dipole Traps". In: *Phys. Rev. Lett.* 89 (2 June 2002), p. 023005. DOI: 10.1103/PhysRevLett.89.023005.

[179] Ingolf V. Hertel and Claus-Peter Schulz. *Atoms, Molecules and Optical Physics 1: Atoms and Spectroscopy*. 2015th edition. Heidelberg Berlin: Springer, Nov. 13, 2014. 726 pp. ISBN: 978-3-642-54321-0.

[180] J. Dalibard and C. Cohen-Tannoudji. "Laser cooling below the Doppler limit by polarization gradients: simple theoretical models". In: *J. Opt. Soc. Am. B* 6.11 (Nov. 1989), pp. 2023–2045. DOI: 10.1364/JOSAB.6.002023.

[181] Claude Cohen-Tannoudji and Alfred Kastler. "I Optical Pumping". In: ed. by E. Wolf. Vol. 5. Progress in Optics. Elsevier, 1966, pp. 1–81. DOI: https://doi.org/10.1016/S0079-6638(08)70450-5.

[182] J. D. Thompson et al. "Coherence and Raman Sideband Cooling of a Single Atom in an Optical Tweezer". In: *Phys. Rev. Lett.* 110 (13 Mar. 2013), p. 133001. DOI: 10.1103/PhysRevLett.110.133001.

[183] M. D. Barrett, J. A. Sauer, and M. S. Chapman. "All-Optical Formation of an Atomic Bose-Einstein Condensate". In: *Phys. Rev. Lett.* 87 (1 June 2001), p. 010404. DOI: 10.1103/PhysRevLett.87.010404.

[184] Roy Jonker and A. Volgenant. "A shortest augmenting path algorithm for dense and sparse linear assignment problems". In: *Computing* 38 (1987), pp. 325–340.

[185] J. E. Bresenham. "Algorithm for computer control of a digital plotter". In: *IBM Systems Journal* 4.1 (1965), pp. 25–30. DOI: 10.1147/sj.41.0025.

[186] Alain Aspect. *Quantum Optics I (lecture notes*. Jan. 2015.

[187] Brice Ravon et al. *Array of Individual Circular Rydberg Atoms Trapped in Optical Tweezers*. 2023. arXiv: 2304.04831 [quant-ph].

[188] Gilbert Grynberg Claude Cohen-Tannoudji Jacques Dupont-Roc. "The Dressed Atom Approach". In: *Atom—Photon Interactions*. John Wiley and Sons, Ltd, 1998. Chap. 6, pp. 407–514. ISBN: 9783527617197. DOI: https://doi.org/10.1002/9783527617197.ch6. eprint: https://onlinelibrary.wiley.com/doi/pdf/10.1002/9783527617197.ch6.

[189] Jean-Michel Raimond. *Atoms and Photons (lecture notes - ENS/ICFP)*. Jan. 2016.

[190] Jan R. Rubbmark et al. "Dynamical effects at avoided level crossings: A study of the Landau-Zener effect using Rydberg atoms". In: *Phys. Rev. A* 23 (6 June 1981), pp. 3107–3117. DOI: 10.1103/PhysRevA.23.3107.

[191] Gerard Higgins et al. "Coherent Control of a Single Trapped Rydberg Ion". In: *Phys. Rev. Lett.* 119 (22 Nov. 2017), p. 220501. DOI: 10.1103/PhysRevLett.119.220501.

[192] T. Cubel et al. "Coherent population transfer of ground-state atoms into Rydberg states". In: *Phys. Rev. A* 72 (2 Aug. 2005), p. 023405. DOI: 10.1103/PhysRevA.72.023405.

[193] Sylvain de Léséleuc et al. "Observation of a symmetry-protected topological phase of interacting bosons with Rydberg atoms". In: *Science* 365.6455 (2019), pp. 775–780. DOI: 10.1126/science.aav9105. eprint: https://www.science.org/doi/pdf/10.1126/science.aav9105.

[194] Arthur Larrouy et al. "Fast Navigation in a Large Hilbert Space Using Quantum Optimal Control". In: *Phys. Rev. X* 10 (2 June 2020), p. 021058. DOI: 10.1103/PhysRevX.10.021058.

[195] Florian Meinert et al. "Indium tin oxide films meet circular Rydberg atoms: Prospects for novel quantum simulation schemes". In: *Phys. Rev. Res.* 2 (2 May 2020), p. 023192. DOI: 10.1103/PhysRevResearch.2.023192.

[196] E. A. Donley et al. "Double-pass acousto-optic modulator system". In: *Review of Scientific Instruments* 76.6 (June 2005). Publisher: American Institute of Physics, p. 063112. ISSN: 0034-6748. DOI: 10.1063/1.1930095.

[197] R. W. P. Drever et al. "Laser phase and frequency stabilization using an optical resonator". In: *Appl. Phys. B* 31.2 (June 1, 1983), pp. 97–105. ISSN: 1432-0649. DOI: 10.1007/BF00702605.

Paul MÉHAIGNERIE **6 Octobre 2023**

Sujet : Interactions entre atomes de Rydberg circulaires piégés pour la simulation quantique

Résumé : Les atomes de Rydberg circulaires, de par leur long temps de vie et fortes interactions dipolaires ajustables, sont des candidats prometteurs pour l'implémentation de simulations quantiques dans des régimes jusqu'à présent hors d'atteinte. Un nouveau paradigme de simulateur quantique, basé sur un encodage des qubits dans des états circulaires, implémenterait ainsi un hamiltonien XXZ de spins 1/2 dont les paramètres seraient ajustables dynamiquement et sur une large gamme de valeurs. Cette thèse traite des premières étapes dans la construction de ce simulateur quantique. Nous présentons tout d'abord la réalisation de réseaux bi-dimensionnels, à géométrie arbitraire, d'atomes de Rydberg circulaires piégés optiquement. Nous préparons dans ce but un tableau d'atomes de rubidium ultra-froids, piégés individuellement dans des pinces optiques. Un faisceau additionnel de position ajustable nous permet de réarranger les atomes au sein du tableau, afin d'implémenter la géométrie voulue de façon déterministe. Nous excitons ensuite les atomes vers l'état circulaire n=52, tout en les piégeant à ce stade dans des faisceaux creux par le biais de la force pondéromotrice. Ces capacités expérimentales nous ont permis de mesurer, pour la première fois, les interactions dipolaires entre atomes circulaires, au sein de paires d'atomes piégés côte à côte. Nous avons vérifié le bon accord de ces mesures avec les attentes théoriques et mis en évidence leur variation en fonction de la géométrie du système. Cette étude expérimentale est couplée à une investigation du mouvement des atomes circulaires au sein de leurs pièges.

Mots clés : atomes froids, atomes de Rydberg, pinces optiques, interactions dipolaires, simulation quantique

Subject : Interactions between trapped circular Rydberg atoms for quantum simulation

Abstract: Circular Rydberg atoms, with their long lifetimes and adjustable strong dipolar interactions, are promising candidates for the implementation of quantum simulations in regimes that were previously out of reach. A new quantum simulator paradigm, based on qubits encoded in circular states, would implement an XXZ spin-1/2 Hamiltonian with dynamically adjustable parameters over a wide range of values. This thesis addresses the preliminary steps in constructing such a quantum simulator. First, we present the realization of two-dimensional arrays of optically-trapped circular Rydberg atoms with arbitrary geometries. For this purpose, we prepare arrays of ultra-cold rubidium atoms, individually trapped in optical tweezers. An additional beam with adjustable position allows us to rearrange the atoms within the array to implement the desired geometry in a deterministic manner. We then excite the atoms to the circular state with principal quantum number n=52, while trapping them in hollow beams using the ponderomotive force. These experimental capabilities allowed us to control and characterize, for the first time, the dipolar interactions between circular states, within pairs of individually trapped atoms. We showed the good agreement of these measurements with theoretical expectations and highlighted their variation depending on the system's geometry. This experimental study is coupled to an investigation of the motion of the circular atoms within their traps.

Keywords : cold atoms, Rydberg atoms, optical tweezers, dipole interactions, quantum simulation